Dissertation

submitted to the
Combined Faculties of the Natural Sciences and Mathematics
of the Ruperto-Carola-University of Heidelberg, Germany,
for the degree of
Doctor of Natural Sciences

Put forward by

Aida Ahmadi

born in Tehran, Iran

Oral examination: January 10th, 2020

IN SEARCH OF DISKS IN HIGH-MASS STAR FORMATION

Aida Ahmadi

Referees: Prof. Dr. Henrik Beuther
Prof. Dr. Cornelis P. Dullemond

Zusammenfassung

Diese Dissertationsschrift handelt von der Suche und Charakterisiertung von Scheiben in massereichen Sternentstehungsgebieten. Die vorgestellte Arbeit ist Teil des CORE Beobachtungsprogrammes, welches interferometrische Beobachtungen des NOrthern Extended Millimetre Array (NOEMA) von 20 massereichen, protostellaren Objekten im 1,3 mm Wellenlängenbereich nutzt. Eine detaillierte Auswertung der W3 (H_2O) Sternentstehungsregion untersucht den Zerfall in zwei heiße Kerne, welche 2300 AE voneinander entfernt liegen und von einer dichten und rotierenden circumbinären Gaswolke umgeben sind. Beobachtungen mit höherer Auflösung zeigen, dass in jedem Kern eine rotierende, scheibenartige Struktur mit Ausflüssen entlang der Rotationsachsen eingebettet ist. Untersuchungen der Stabilität dieser scheibenartigen Strukturen bestätigen, dass diese gravitativ instabil sind, was diese anfällig für eine Fragmentierung der Scheiben macht. Um die zugrundeliegenden Unsicherheiten abschätzen zu können, haben wir synthetische Beobachtungen einer hochauflösenden, dreidimensionalen Strahlungs- und Hydrodynamiksimulation erzeugt, welche zur Fragmentierung einer massereichen Scheibe unter verschiedenen Inklinationen und Entfernungen führen. Wir beobachteten, dass in schlecht aufgelösten Beobachtungen die Kinematik von differenziell rotierenden Scheiben derer von starren Scheiben ähnlich sieht, was zu einem Überschätzen der Sternmasse führt. Trotz der ungenügenden Auflösung beobachten wir weiter, dass die Stabilitätsanalyse die Scheibenfragmentierung ungeachtet der Unsicherheiten korrekt vorhersagt. Untersuchungen der gesamten CORE Stichproben zeigen in den meisten Quellen Rotationssignaturen im dichten Gas orthogonal zu bipolaren Molekülausflüssen. Beim Modellieren der Besetzungszustände verschiedener Rotationsübergänge des Dichtgasindikators CH_3CN finden wir typischerweise warme (~200 K) Scheibenkandidaten. Beim Anwenden der robusten Stabilitätsanalyse finden wir überwiegend massereiche stellare Objekte, welche aufgrund des hohen Scheiben-zu-Sternmassenverhältnisses schon früh in ihrer Entstehung anfällig für Scheibenfragmentierung sind. Da die meisten massereichen Sterne Begleiter haben, scheint die Scheibenfragmentierung ein wichtiger Mechanismus zu sein unter welchem solche Systeme entstanden sein könnten.

Abstract

This thesis is dedicated to the search and characterization of disks in high-mass star formation. The work presented is part of the CORE survey, a large observational program making use of interferometric observations from the NOrthern Extended Millimetre Array (NOEMA) for a sample of 20 high-mass protostellar objects in the 1.3 millimetre wavelength regime. An in-depth analysis of the W3 (H_2O) star forming region examines its fragmentation into two hot cores, separated by 2300 au and engulfed in a rotating circumbinary envelope of dense gas. Higher resolution observations reveal that embedded within each core is a rotating disk-like structure with outflows being ejected along the disk rotation axes. Studying the stability of the disk-like structures confirms that they are gravitationally unstable and prone to disk fragmentation. In an effort to understand the uncertainties involved, we created synthetic observations of a high-resolution 3D radiation-hydrodynamic simulation that leads to the fragmentation of a massive disk at different inclinations and distances. We find that the kinematics of differentially rotating disks resemble rigid-body-like rotation in poorly resolved observations, leading to overestimation of protostellar masses. Despite the lack of resolution, we find that the stability analysis correctly predicts disk fragmentation regardless of the uncertainties. Studying the kinematics of the full CORE sample, we find rotational signatures in dense gas perpendicular to bipolar molecular outflows in most regions. Modelling the level populations of various rotational transitions of the dense gas tracer CH_3CN, we find the disk candidates to be on average warm (~200 K). Applying the robust stability analysis, we find that most high-mass young stellar objects are prone to disk fragmentation early in their formation due to high disk to stellar mass ratio. Since most high-mass stars are found to have companions, disk fragmentation seems to be an important mechanism by which such systems may be formed.

Dedicated to my parents for all their sacrifices
and to Micah for holding my hand along the way

تقدیم به پدر و مادر عزیزم
به خاطر
تمام از خود گذشتگی‌ها

"Within the cradle of a burning core,
You wither down and find yourself well worn;
As untold pressures crush and shape and bore,
Your substance is assaulted, broke and torn.

Then just as you think you can take no more,
Through flames and righteous heat you are reborn;
An all-consuming diamond in the sky,
Extinguishing all other lights nearby.

We map and chart your growth and range through space,
And mark your height against the kitchen door;
Creating patterns through which we can trace
Your progress against those who came before.

But all your truths and stats are out of place,
You do not fit the charts that we speak for;
And now we see that you do not belong,
Is everything we knew about you wrong?"

– Sam Illingworth –

Contents

List of Figures v

List of Tables ix

1 Introduction 1
- 1.1 Star formation in a nutshell . . . 1
- 1.2 High-mass stars . . . 3
- 1.3 Barriers to high-mass star formation . . . 4
  - 1.3.1 Jeans fragmentation . . . 5
  - 1.3.2 Radiation pressure . . . 6
  - 1.3.3 Disk fragmentation . . . 7
  - 1.3.4 Other feedback mechanisms . . . 8
- 1.4 The formation of high-mass stars . . . 9
  - 1.4.1 Formation through accretion . . . 9
  - 1.4.2 Formation through collisions . . . 10
- 1.5 Stages of high-mass star formation . . . 10
- 1.6 Disks in high-mass star formation . . . 11
- 1.7 Structure of this thesis . . . 15

2 Observational Techniques 17
- 2.1 Chasing disks in high-mass star formation . . . 17
  - 2.1.1 Continuum . . . 18
  - 2.1.2 Masers . . . 19
  - 2.1.3 Thermal emission . . . 20
- 2.2 Molecular transitions . . . 20
- 2.3 Radiative transfer modelling . . . 24
- 2.4 Interferometry . . . 28
  - 2.4.1 Basic theory . . . 29
  - 2.4.2 Imaging . . . 32

3 IRAM Large Program: CORE 35
- 3.1 Sample selection . . . 35
- 3.2 NOEMA observations and data reduction . . . 36
  - 3.2.1 Spectral line setup . . . 38
  - 3.2.2 Calibration . . . 41
  - 3.2.3 Imaging . . . 43

4 The Curious Case of W3 (H_2O) 45
- 4.1 Motivation . . . 45
- 4.2 Introduction . . . 45
- 4.3 Observations . . . 46
  - 4.3.1 NOEMA observations . . . 46
  - 4.3.2 30-m observations . . . 47
- 4.4 Observational results . . . 47

4.4.1 Continuum emission . . . 47
4.4.2 Line emission . . . 49
4.4.3 Outflow structure . . . 51
4.5 Analysis and discussion . . . 53
4.5.1 Dense gas kinematics . . . 53
4.5.2 Temperature distribution . . . 57
4.5.3 Mass estimates . . . 58
4.5.4 Toomre stability . . . 60
4.5.5 Cooling . . . 64
4.6 Summary and conclusions . . . 65

5 Benchmarking the Method: Linking Simulations and Observations 67
5.1 Motivation . . . 67
5.2 Simulations . . . 68
5.3 Radiative transfer post-processing . . . 72
5.4 Synthetic observations . . . 72
5.4.1 ALMA . . . 72
5.4.2 NOEMA . . . 73
5.5 Analysis and results . . . 74
5.5.1 Continuum maps . . . 74
5.5.2 Kinematics . . . 76
5.5.3 Temperature distribution . . . 82
5.5.4 Mass estimates . . . 83
5.5.5 Toomre stability . . . 89
5.6 Summary and conclusions . . . 95

6 Kinematics and Stability of the CORE Sample 99
6.1 Motivation . . . 99
6.2 Large-scale structure . . . 100
6.2.1 Core fragmentation . . . 100
6.2.2 Kinematics . . . 100
6.3 Dense gas kinematics . . . 103
6.4 Molecular outflows . . . 107
6.5 Temperature distribution . . . 108
6.6 Mass estimates . . . 111
6.6.1 Gas mass . . . 111
6.6.2 Protostellar mass . . . 113
6.7 Disk candidacy . . . 114
6.7.1 Timescales . . . 114
6.7.2 Specific angular momentum . . . 116
6.8 Toomre stability . . . 125
6.8.1 Toomre unstable disks . . . 126
6.8.2 Toomre stable disks . . . 129
6.8.3 General trends . . . 129
6.8.4 Disk thickness . . . 130
6.9 Summary and conclusions . . . 131

7 Summary and Conclusions 135

8 Outlook 139

A Supplemental Material for Chapter 4 **143**
A.1 Moment maps 143
A.2 Toomre Q maps 147

B Supplemental Material for Chapter 6 **149**
B.1 Moment maps 150
B.2 Molecular outflows 152
B.3 XCLASS maps 158
B.4 Specific angular momentum 162

Acronyms **163**

List of Publications **165**

Bibliography **168**

Acknowledgements **177**

List of Figures

1.1 Hubble Space Telescope UV & Chandra X-ray image of Eta Car 4
1.2 Schematic of the volutionary phases in high-mass star formation 12
1.3 Schematic of our current understanding of disk properties around intermediate- to high-mass (proto)stars 14

2.1 Spectral energy distributions of various phases in high-mass star formation . . . 18
2.2 Energy level diagram of CH_3CN 23
2.3 Example spectrum of CH_3CN transitions with *XCLASS* model fits 28
2.4 Schematic showing the setup of an elementary interferometer 30
2.5 Example *uv*-coverage of NOEMA observations 31
2.6 Example of cleaning interferometric observations 32
2.7 NOEMA 1.37 mm continuum maps toward IRAS 21078, imaged with different weightings in *GILDAS* 33

3.1 The NOEMA interferometer located in the French Alps 36
3.2 3-colour images of the CORE sample 38
3.3 Full WideX spectrum of W3 (H_2O) averaged over a $4'' \times 4''$ region 39
3.4 Example spectra showing the frequency range covered by the narrow-band correlator 40

4.1 NOEMA 1.37 mm continuum image toward W3 (H_2O) and W3 (OH) 48
4.2 1.37 mm continuum image toward W3 (H_2O) observed with the A, AB, and ABD configurations of NOEMA 49
4.3 Zeroth & first moment maps of CH_3CN $(12_3 - 11_3)$ for W3 (H_2O) and W3 (OH) 50
4.4 Molecular outflows originating from W3 (H_2O) 52
4.5 Millimetre and centimetre emission maps of W3 (H_2O), showing H_2O maser positions and outflow directions 53
4.6 Position–velocity plots of W3 (H_2O) for a cut going through both embedded cores 54
4.7 First moment maps of CH_3CN $(12_3 - 11_3)$ using only the A-array observations and masked out to show contributions from W3 (H_2O) E and W3 (H_2O) W . 56
4.8 Position–velocity plots of W3 (H_2O) E and W3 (H_2O) W 57
4.9 Column density, velocity offset, full width at half maximum linewidth, and rotational temperature maps of W3 (H_2O) obtained by fitting CH_3CN transitions with *XCLASS* 59
4.10 Mass density map of W3 (H_2O) 61
4.11 Toomre Q map of W3 (H_2O) E and W3 (H_2O) W 62
4.12 Map of β cooling parameter for W3 (H_2O) E and W3 (H_2O) W 65

5.1 Disk surface density maps extracted from the numerical simulation at a snapshot of 12 kyr, inclined to 10°, 30°, 60°, and 80° 70
5.2 The *uv*-coverage of synthetic ALMA and NOEMA observations 73
5.3 1.37 mm continuum images of the model simulations, synthetic ALMA observations, and synthetic NOEMA observations at a distance of 800 pc and 2000 pc and inclinations of 10°, 30°, 60°, and 80° 75

5.4 Integrated intensity (zeroth moment) maps of CH_3CN (12_4–11_4) for the model simulations, synthetic ALMA observations, and synthetic NOEMA observations at a distance of 800 pc and 2000 pc and inclinations of 10°, 30°, 60°, and 80° 78

5.5 Intensity-weighted peak velocity (first moment) maps of CH_3CN (12_4–11_4) for the model simulations, synthetic ALMA observations, and synthetic NOEMA observations at a distance of 800 pc and 2000 pc and inclinations of 10°, 30°, 60°, and 80° 79

5.6 Intensity-weighted peak velocity (first moment) map of CH_3CN ($12_4 - 11_4$) for the model simulations at an inclination of 60° and a distance of 800 pc showing zoomed views of the kinematics of each fragment 80

5.7 Position–velocity plots of CH_3CN ($12_4 - 11_4$) for a cut in the east–west direction across the model simulations, synthetic ALMA observations, and synthetic NOEMA observations at a distance of 800 pc and 2000 pc and inclinations of 10°, 30°, 60°, and 80° 81

5.8 Rotational temperature maps of synthetic ALMA and NOEMA observations at a distance of 800 pc and 2000 pc and inclinations of 10°, 30°, 60°, and 80° . 84

5.9 Face-on view of the disk mid-plane temperature from the model simulations . . 85

5.10 Example of the Keplerian fitting approach to the 6σ outer edge of the PV plot of CH_3CN ($12_4 - 11_4$) for the model simulation inclined to 60° at a distance of 800 pc in order to determine the protostellar mass 88

5.11 Mass estimates from fitting the 6σ edges of the PV diagrams of CH_3CN ($12_4 - 11_4$) for the model simulations, synthetic ALMA observations, and synthetic NOEMA observations at a distance of 800 pc and 2000 pc and inclinations of 10°, 30°, 60°, and 80° 89

5.12 The 'true' Toomre Q map obtained from the model simulations inclined by 10°, 30°, 60°, and 80° 90

5.13 Toomre Q maps of synthetic ALMA and NOEMA observations at a distance of 800 pc and 2000 pc and inclinations of 10°, 30°, 60°, and 80°, corrected for the effect of inclination 92

5.14 Histogram of Q values for model simulations and synthetic ALMA observations at 2000 pc 93

5.15 Toomre Q maps of synthetic ALMA and NOEMA observations at a distance of 800 pc and 2000 pc and inclinations of 10°, 30°, 60°, and 80°, not corrected for the effect of inclination 94

6.1 NOEMA 1.37 mm continuum maps of the CORE sample 101

6.2 Intensity-weighted peak velocity (first moment) maps of $H_2CO(3_{0,3} - 2_{0,2})$ showing the large-scale kinematics of the full CORE sample 102

6.3 Intensity-weighted peak velocity (first moment) maps of CH_3CN ($12_3 - 11_3$) showing the dense gas kinematics for 15 of the 20 sources in the CORE survey 104

6.4 Position–velocity (PV) plots of CH_3CN ($12_3 - 11_3$) along cuts in the direction of rotation for 17 cores in the CORE survey 106

6.5 Rotational temperature maps obtained by fitting CH_3CN transitions with *XCLASS* for 17 cores in the CORE survey 109

6.6 Ratio of free-fall to rotational timescale as a function of disk gas mass, showing most of the sources with CH_3CN velocity gradients are rotationally supported . 116

6.7 Specific angular momentum radial profiles for a high-resolution numerical simulation of a high-mass core having formed a massive disk that is feeding the central protostar, inclined to 10°, 30°, 60°, and 80°, their synthetic ALMA observations at 2000 pc, and synthetic NOEMA observations at 800 pc and 2000 pc 118
6.8 Specific angular momentum radial profiles for 12 disk candidates in the CORE survey 120
6.9 Toomre Q maps for 15 of the 20 sources in the CORE survey assuming a protostar is located at the position of the continuum peak, accounting for the self-gravity of the disk 127
6.10 Median Q plotted against gas to stellar mass ratio for 17 candidate disks within the CORE survey 130
6.11 Median Q plotted against gas mass and stellar mass for 17 candidate disks within the CORE survey 131
6.12 An estimate for the Gammie disk thickness criterion for the disk candidates withing the CORE survey 132

8.1 The Atacama Large Millimeter Array located on the Chajnantor Plateau in Chile 140
8.2 The Very Larger Telescope Interferometer located on Cerro Paranal in Chile . . 141

A.1 Integrated intensity (zeroth moment) maps of most important lines covered in the narrow-band receiver for W3 (H_2O) and W3 (OH) 144
A.2 Intensity-weighted peak velocity (first moment) maps of most important lines covered in the narrow-band receiver for W3 (H_2O) and W3 (OH) 145
A.3 Intensity-weighted velocity dispersion (second moment) maps of most important lines covered in the narrow-band receiver for W3 (H_2O) and W3 (OH) . . 146
A.4 Toomre Q maps of W3 (H_2O) E and W3 (H_2O) W obtained by assuming two disk-like structures in gravito-centrifugal rotation about the positions of peak continuum emission, each containing a (proto)star with a mass of 5 $M_\odot$ and 15 $M_\odot$ 147

B.1 Integrated intensity (zeroth moment) maps of CH_3CN $(12_3 - 11_3)$ showing the dense gas distribution for 15 of the 20 sources in the CORE survey 150
B.2 Intensity-weighted velocity dispersion intensity (second moment) maps of CH_3CN $(12_3 - 11_3)$ showing the dense gas kinematics for 15 of the 20 sources in the CORE survey 151
B.3 Intensity maps of CO (2–1) emission from IRAM 30-m telescope integrated over the blue and redshifted wings of emission, showing the outflow structure for the full CORE sample 152
B.4 Intensity maps of ^{13}CO $(2-1)$ emission from IRAM 30-m telescope integrated over the blue and redshifted wings of emission, showing the outflow structure . 153
B.5 Intensity maps of ^{13}CO $(2-1)$ emission from merged NOEMA and IRAM 30-m data integrated over the blue and redshifted wings of emission, showing the outflow structure for the full CORE sample 154
B.6 Intensity maps of ^{13}CO $(2-1)$ integrated over the blue and redshifted wings of emission, showing the outflow structure for the full CORE sample 155
B.7 Intensity maps of $C^{18}O$ $(2-1)$ emission from IRAM 30-m telescope integrated over the blue and redshifted wings of emission, showing the outflow structure for the full CORE sample 156
B.8 Intensity maps of SO $(6_5 - 5_4)$ emission from IRAM 30-m telescope integrated over the blue and redshifted wings of emission, showing the outflow structure for the full CORE sample 157

B.9 CH_3CN column density maps obtained by fitting CH_3CN transitions with *XCLASS* for 17 cores in the CORE survey 158
B.10 Maps of velocity offset with respect to the systemic velocity obtained by fitting CH_3CN transitions with *XCLASS* for 17 cores in the CORE survey 159
B.11 Maps of linewidth obtained by fitting CH_3CN transitions with *XCLASS* for 17 cores in the CORE survey 160
B.12 Maps of source size parameter obtained by fitting CH_3CN transitions with *XCLASS* for 17 cores in the CORE survey 161

List of Tables

1.1 Classification of high-mass main sequence stars 5

2.1 Comparison between beam sizes and sensitivities of visibilities imaged with different weightings for IRAS 21078 33

3.1 Positions and properties of the CORE sample 37
3.2 NOEMA correlator units and frequency ranges covered in the CORE survey . 39
3.3 Bright lines covered in the narrow-band correlator setup of CORE 41

4.1 Observations of W3 (H_2O) and W3 (OH) 46
4.2 Details of CLEANed images for W3 (H_2O) 47

5.1 Details of synthetic observations 74
5.2 Summary of temperatures, masses, and Q values for the synthetic observations . 86

6.1 Observational parameters for the disk candidates within the CORE survey . . . 110
6.2 Gas mass estimates for the CORE sample 112
6.3 Summary of results from fitting the PV diagrams of the CORE sample 114
6.4 Fit parameters to the specific angular momentum radial profiles for the best disk candidates in the CORE survey 124
6.5 Overview of mass estimates and Toomre Q results for the best disk candidates in the CORE survey 128

B.1 Fit parameters to different regions of the specific angular momentum radial profiles of the simulations shown in Fig. 6.7 162

CHAPTER 1

Introduction

The field of star formation is one of the oldest in astronomy. This is of no surprise considering the importance of stars in the Universe. From the formation of the first stars, about 180 Myr after the Big Bang (Bowman et al. 2018), which led to the formation of the first galaxies, to the feedback processes with which they continually contribute to the lifecycle of matter in the interstellar medium (ISM), understanding their formation mechanism is of utmost importance. While we orbit an ordinary star in our solar system, we know of the existence of stars more than one hundred times as massive as our Sun. *How do such stars come to exist?*

1.1 Star formation in a nutshell

Stars form within so-called giant molecular clouds (GMCs), which encompass most of the molecular mass of the ISM. GMCs have masses $\gtrsim 10^4\ M_\odot$ and sizes of ~20–100 pc (e.g. McKee & Ostriker 2007; Beuther et al. 2007a) and have a hierarchical structure. Following the definitions of Williams et al. (2000), GMCs consist of 'clumps' of dense gas and dust within which clusters of stars can form. These clumps typically have masses in the range 50–500 $M_\odot$ and sizes that span a few parsecs (Bergin & Tafalla 2007 and references therein). Massive clumps are thought to be the locations where high-mass stars form and have masses between a few 100 to a few $1000 M_\odot$ (Beuther et al. 2007a). On smaller scales, 'cores' are defined as bound structures within which single stars or multi-star systems such as binaries can form.

For a cloud to collapse and form stars, it needs to overcome stabilising forces such as thermal pressure, internal turbulence, magnetic forces, and angular momentum. Considering a simple case of gravity acting against thermal support, the cloud could only collapse if its mass exceeds the Jeans (Jeans 1928) mass,

$$M_J = \left(\frac{\pi\, k_\mathrm{B}\, T_\mathrm{gas}}{\mu\, m_H\, G}\right)^{1.5} \rho^{-0.5} = 0.5 \left(\frac{T_\mathrm{gas}}{10\ \mathrm{K}}\right)^{1.5} \left(\frac{n}{10^4\ \mathrm{cm^{-3}}}\right)^{0.5} M_\odot, \tag{1.1}$$

where k_B is the Boltzmann constant, ρ is the mass density (g cm^{-3}), T_gas is the gas temperature, and n is the number density. When this happens, the cloud can no longer support itself and starts to contract at nearly free-fall velocities. Density increases as material flows deep into the gravitational potential while temperature remains unchanged, making the Jeans mass decrease further. Therefore, different regions can undergo local collapse forming overdensities within the cloud through a process known as fragmentation. This process is supported by observations of

star-forming regions in which star formation typically occurs in clustered environments.

After the collapse of the cloud, a given core moves onto the protostellar phase of evolution. In this phase, the collapsing core transitions from isothermal contraction to adiabatic contraction. This is because at some point as density increases the core becomes opaque to infrared (IR) wavelengths and thermal energy can no longer be dissipated through radiation. Therefore, temperature increases as the core continues to collapse further and the build up of internal pressure continues until hydrostatic equilibrium is reached. At this point, the core seizes to contract further and a so-called first hydrostatic core is formed, with gravity and pressure in balance. Material continues to fall onto the core from larger scales, increasing the density and temperature, hence increasing the Jeans mass and preventing the core from further fragmentation. Once temperatures are high enough (~2000 K), molecular hydrogen dissociates into atomic hydrogen. As a result, thermal energy is lost in the system and a second contraction phase is triggered, leading to the creation of a second hydrostatic core. At this point a so-called protostar is formed. Details of the protostellar collapse phases, namely the first and second collapse can be found in Masunaga et al. (1998) and Masunaga & Inutsuka (2000), respectively, more recently revisited by Bhandare et al. (2018) (also see textbook by Stahler & Palla 2005). As material continues to fall onto the protostar from larger scales, the protostar continues to become hotter through shock heating and hence contracts increasing its density. Once temperatures and densities are high enough, nuclear reactions begin in the core. Initially, deuterium is converted into helium (at temperatures of $\sim 10^6$ K) which allows the core to temporarily stop contracting as the reaction provides the necessary thermal energy. Once the deuterium reservoir is exhausted, the core contracts further, allowing temperatures to increase to about 10^7 K at which point hydrogen fusion begins. Thus, a star is born, starting its journey on the main sequence. The contraction phase before the protostar joins the main sequence is typically referred to as the pre-main-sequence (PMS) phase.

In the main accretion phase, material from the envelope accretes onto the protostar through a disk which forms due to non-zero initial angular momentum of the cloud and envelope. At this stage, bipolar outflows remove excess energy and angular momentum from the system, creating cavities in the envelope. Once the envelope material is depleted, accretion continues through the disk at a lower rate onto the PMS star. Once the star/disk system becomes optically visible, the star will be known as a T Tauri star if its mass is $\lesssim 2\ M_\odot$ or a Herbig Ae/Be star (Herbig 1960) if its mass is $\sim 2-10\ M_\odot$. The star continues to accrete and contract towards the main sequence at which point hydrogen burning begins and the star is surrounded by a protoplanetary disk. The remaining disk is eventually dispersed through photoevaporation and winds.

Because young stars can be strongly affected by their circumstellar material and due to observational difficulties in properly characterizing the various phases a star goes through early-on (e.g. protostar, PMS star, T Tauri star), Strom (1972) coined the term young stellar object (YSO) to refer to such objects whose exact evolutionary phase is unknown. Each distinct phase in the sequence of events described above marks a unique feature in its emitted spectrum, known as the spectral energy distribution (SED). During the main accretion phase, the SED resembles that of a modified blackbody that peaks in the far-IR or submillimeter with the emission attributed to cold dust. YSOs in this phase of evolution are classified as Class 0 sources and have extremely high visual extinctions due to their embedded nature within the infalling envelope of gas and

dust (Andre et al. 1993). This class of YSOs are already powering highly collimated outflows. As material continues to accrete from the envelope onto the disk, the opening angle of the outflow increases and the star becomes visible in the mid and near-IR. This Class I object has a spectral energy distribution that is broader than a blackbody, peaking in the far-IR (Lada 1987). Once envelope material is depleted and infall stops, only a thin disk remains which allows the star to become visible. In this Class II phase, the dusty disk produces substantial IR emission and the SED has a flat shape. Eventually, the disk is dissipated (or coagulated) and only the central star is left. The SED in this Class III phase is dominated by blackbody radiation from the newly formed star and a very small contribution from whatever is left of the disk.

1.2 High-mass stars

High-mass stars are typically defined to be stars with masses $\gtrsim 8\ M_\odot$. The value of 8 $M_\odot$ is not an exact threshold but it roughly corresponds to the mass at which the (dynamical) free-fall timescale of a collapsing gas condensation, also known as a core, equals the (thermal) Kelvin-Helmholtz timescale. If such objects become even more massive, they have to accrete while nuclear fusion has already started at their interiors which has severe implications for their formation. Varying parameters such as the accretion rate would in fact result in a slightly different threshold value (Palla & Stahler 1993). Another reason for the convention of using 8 $M_\odot$ to distinguish between high-mass stars and their lower mass counterparts is their subsequent evolution. Massive stars[1] evolve beyond core carbon burning phase and produce most of the heavy elements in the Universe, particularly alpha process elements such as oxygen, neon, magnesium and silicon. For solar abundances, stars with $M_*/M_\odot > 8$ end their lives through a supernova type II explosion. Therefore, massive stars significantly contribute to the chemical evolution of the ISM and the galaxy. Not only do high-mass stars enrich the Universe with heavy elements through their ultimate deaths, but they also dominate the turbulent energy input into the ISM via powerful stellar winds and radiation forces. Figure 1.1 shows, as an example, the binary stellar system η Car with a mass more than 100 times that of our Sun, energetically losing mass in episodic events shedding metal-rich shells producing the famous *Homunculus Nebula* we see today (Smith & Morse 2019). Considering the vast extent of such episodes, it is clear that high-mass stars affect not only subsequent star and planet formation in their local environments, but also the evolution of their host galaxies.

Using the Morgan-Keenan spectral classification of stars, high-mass stars span the OB-type regime (Morgan & Keenan 1973). Table 1.1 roughly summarizes the spectral classification of high-mass main sequence stars for logarithmic mass ranges (Zinnecker & Yorke 2007). With a luminosity of $\sim 1.5 \times 10^3\ L_\odot$, roughly corresponding to a B3 type star with an effective temperature of 17 500 K (Crowther 2005), the peak of the SED for high-mass stars lies in the ultraviolet (UV) wavelength range; therefore, the emitted photons are energetic enough to ionize the surrounding gas and lead to the creation of expanding H II regions which also affect their surroundings and can trigger subsequent star formation. We will come back to this point later as it has important implications in the formation of high-mass stars.

[1]While the word 'massive' corresponds to any object that possesses mass regardless of its magnitude, we will use the term 'massive' analogous to 'high-mass' in this thesis.

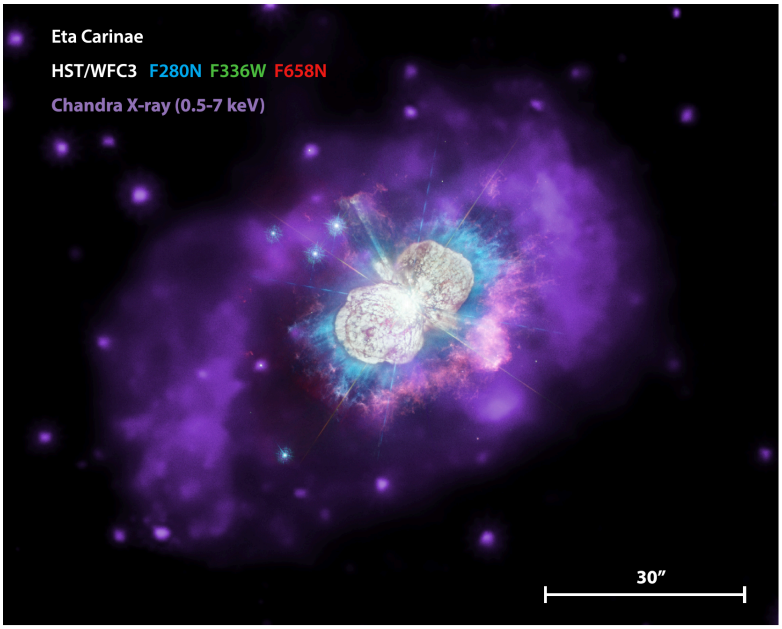

Figure 1.1: X-ray image of η Car obtained from Chandra X-ray Observatory shown in purple, combined with a 3-colour Hubble Space Telescope image with blue tracing Mg II emission in the UV regime, while green and red corresponding to near-UV continuum and N IIemission from Smith & Morse (2019). The size of the scalebar in the bottom right corresponds to a physical scale of ~0.33 pc. With a mass more than 100 times that of our Sun, η Car has been episodically losing mass in energetic events producing the nebula we see today.

The number of stars formed out of a collapsing molecular cloud and their masses once they enter the main sequence phase in their evolution is described by a probability distribution function known as the initial mass function (IMF) (Salpeter 1955; Scalo 1986; Kroupa 2002; Chabrier 2003). The IMF is typically presented as the number of stars per logarithmic mass bin, $\mathrm{d}N/\mathrm{d}\log(M)$, which has a lognormal shape for masses below ~ 1 $M_\odot$, peaks at about 0.3 $M_\odot$ and has a power-law tail with a slope of –1.3 (Salpeter 1955) on the high-mass end. The origin and universality of the IMF is an open question in the field (e.g. Bastian et al. 2010; Hennebelle & Chabrier 2011) that goes beyond the scope of this thesis. Moreover, the exact power-law slope of the IMF on the high-mass end is also uncertain, with a number of studies finding lower values for the slope (e.g. Weisz et al. 2015; Rybizki & Just 2015). Nevertheless, using a Salpeter slope, for every O/WR-type star one would expect to find about 9 stars with masses 16–64 $M_\odot$, 17 stars with masses 8–16 $M_\odot$, and more than 1100 stars with masses less than 8 $M_\odot$ (Zinnecker & Yorke 2007). As a result of their rareness, high-mass stars are typically found at farther distances than sites of low-mass star formation.

1.3 Barriers to high-mass star formation

While the formation of stars has been a topic of debate for many years (see reviews by Shu et al. 1987; Andre et al. 2000; McKee & Ostriker 2007; Bergin & Tafalla 2007), there exist problems with simply scaling up low-mass star formation to explain the formation of high-mass stars. Therefore, before introducing the current theories of high-mass star formation, we need

Table 1.1: Classification of high-mass main sequence stars from Zinnecker & Yorke (2007).

Mass	Designation	Spectral type
$8-16\ M_\odot$	Early B-type massive stars	B3V to B0V
$16-32\ M_\odot$	Late O-type massive stars	O9V to O6V
$32-64\ M_\odot$	Early O-type massive stars	05V to O2V [a]
$64-128\ M_\odot$	O/WR-type massive stars	WNL-H [b]

[a)] O2V main sequence stars have been identified by Walborn et al. (2002).
[b)] WNL-H: N-rich late-type Wolf-Rayet (WR) stars, still on the Main Sequence – see Crowther (2007).

to describe the reasons why alternative formation scenarios were needed in the first place. The following is a summary of the major processes which can hinder the formation of massive stars.

1.3.1 Jeans fragmentation

As described in Sect. 1.1, a cloud could only collapse if its mass exceeds the Jeans mass (Eq. 1.1). With the right side of the Jeans equation adjusted to typical temperatures and densities found in star-forming regions, it can be seen that the Jeans mass is very small, on the order of $\sim 1\ M_\odot$. Therefore, one would expect a massive cloud to fragment and form many low-mass stars rather than one or more stars of higher mass.

This issue has been investigated both theoretically and observationally. On the theory side, numerical simulations have shown that indeed forming high-mass stars may be limited by Jeans fragmentation. For example, the work of Dobbs et al. (2005) showed that even by using a steep centrally condensed density profile of $\rho \propto r^{-1.5}$ in an effort to raise the Jeans mass, that centrally condensed $30\ M_\odot$ cores in their simulations would form ~20 stars. Girichidis et al. (2011) studied the importance of the choice of the initial density profile and found that in the case of flat density profiles the cores would fragment heavily, while using steeper density profiles like $\rho \propto r^{-2}$ would allow for a single high-mass star to be formed at the center of the cloud. However, none of these early numerical simulations took into account radiative feedback processes or magnetic forces which can provide support against fragmentation.

Radiation works to increase the Jeans mass by increasing the temperature of the gas. Krumholz (2006) showed that low-mass stars can radiate enough energy to increase gas temperatures in their vicinities by a factor of a few and therefore increase the Jeans mass (Eq. 1.1) by a factor of ~10 and hence allow for the formation of higher mass stars. Furthermore, magnetic fields help suppress fragmentation by providing pressure support: clouds can only collapse if their magnetic flux to mass ratios are below a certain critical value. Additionally, magnetic fields help remove angular momentum from the system through a mechanism called magnetic braking. Magnetic braking occurs as a result of magnetic fields getting twisted as material falls onto the protostar with varying degrees of rotation. This twisting creates a sort of magnetic tension that transports angular momentum outwards, inhibiting the formation of a rotationally flattened disk. In such a scenario, the rotation support is lowered and infall velocities are enhanced as a

result. Commerçon et al. (2011) were one of the first to show the effect of magnetic braking in the case of strong magnetic fields, including radiative processes in their simulations, and proposed that highly magnetized dense cores can serve as seeds for the formation of massive stars. Furthermore, Myers et al. (2013) presented a set of numerical simulations which showed the importance of radiation and magnetic forces in preventing fragmentation.

Observationally, different degrees of fragmentation have been found in different regions of high-mass star formation. As an example, observations of G351.77–0.54, a high-mass star-forming region with a luminosity of ~10^5 $L_\odot$ (Norris et al. 1993), Atacama Large Millimeter Array (ALMA) observations at 690 GHz and a linear resolution of ~130 au[2] resolved four cores (Beuther et al. 2017b). Further observations at 1.3 mm at scales of ~40 au showed further fragmentation of the region into at least 12 more structures with separations and masses consistent with Jeans fragmentation, demonstrating that hierarchical Jeans fragmentation can continue down to such small scales (Beuther et al. 2019). On the other hand, observations of G17.64+0.16, another high-mass star-forming region with a similar luminosity of ~10^5 $L_\odot$ (Lumsden et al. 2013), has shown little to no fragmentation from 400 au (Maud et al. 2018) down to ~40 au scales (Maud et al. 2019). What makes up for this diversity in fragmentation levels?

It is evident that larger samples are needed in order to understand the fragmentation mode of high-mass star-forming regions. Recently, Beuther et al. (2018) presented a sample of 20 such regions for which they found a diversity of fragmentation on few hundred to thousands of au scales[3]. Some regions have substructure down to as many a 20 cores, while others stay singularly dominated. Their analysis attributed this variation to either varying strengths of magnetic forces or different initial density profiles. Further observations of magnetic field strengths in these regions are needed (and are underway) to rule out the former and give some clues to understanding large-scale fragmentation in high-mass star formation.

1.3.2 Radiation pressure

In the inside-out model of star formation described in Sect. 1.1, once gravity dominates over pressure and magnetic forces, the gas collapses in a free-fall time (Spitzer 1978),

$$t_{\rm ff} = \left(\frac{3\,\pi}{32\,G\,\rho}\right)^{0.5} = 4.3\times10^5\left(\frac{n}{10^4\,{\rm cm}^{-3}}\right)^{-0.5}\ {\rm years}, \tag{1.2}$$

which is on the order of a few 100 000 years in regions of high-mass star formation. However, the Kelvin-Helmholtz timescale defined to be the time over which the accumulated gravitational potential energy is radiated away can be written as,

$$t_{\rm KH} = \frac{3\,G\,M_*^2}{5\,R_*\,L_*}, \tag{1.3}$$

[2]This source has a distance ambiguity and for the sake of the argument here we assume it is at a distance of 2.2 kpc (Norris et al. 1993)

[3]These data are the main focus of this thesis.

where M_*, R_*, and L_* are the stellar mass, radius and luminosity. The Kelvin-Helmholtz time is on the order of $10^4 - 10^5$ years for stellar masses of $100 - 10\ M_\odot$, respectively (see Fig. 4 of Zinnecker & Yorke 2007). The fact that Kelvin-Helmholtz time is shorter than that of free-fall means that high-mass stars begin burning hydrogen while still accreting material (Palla & Stahler 1993). This lack of pre-main-sequence phase in the evolution of high-mass stars would mean that intense (ionizing) radiation from the protostar is present in the main accretion phase of the protostar. Such intense radiation pressure exerted on the infalling material can stop accretion altogether.

For many years, the effect of radiation pressure on dust was thought to hinder the formation of stars more massive than ~40 $M_\odot$ (e.g. Larson & Starrfield 1971; Kahn 1974; Wolfire & Cassinelli 1987). Such studies would adopt nearly dust-free cloud conditions and extremely high accretion rates to allow the build-up of enough material onto the protostar to even reach such stellar upper mass limits. Subsequent works showed that the unrealistic restrictions on the dust opacity and accretion rates can be removed if non-spherical accretion flows are considered (e.g. Nakano 1989). In particular, magnetic fields, rotation, or even simple contraction of the cloud could provide such deviations from spherical symmetry. In more recent years, two- and three-dimensional radiation-hydrodynamical simulations of collapsing cores have shown support for disk-mediated accretion in the formation of very massive stars, analogous to the formation of low-mass stars (e.g. Yorke & Sonnhalter 2002; Krumholz et al. 2009; Kuiper et al. 2010, 2011; Kuiper & Yorke 2013; Klassen et al. 2016; Rosen et al. 2016; Kuiper & Hosokawa 2018). In the disk-mediated accretion, the effect of radiation pressure would be reduced as the radiation could escape through the poles along the disk rotation axis, and the disk would be shielded from radiation due to its high optical depth.

1.3.3 Disk fragmentation

Despite the disk-mediated accretion having solved the radiation-pressure problem, high accretion rates ($\gtrsim 10^{-4}\ M_\odot\ \mathrm{yr}^{-1}$) through the disk are still required for the creation of the most massive stars. Gas densities needed to provide such high rates of accretion could induce gravitational instabilities in the disk forcing it to fragment and produce companion objects (Kratter & Matzner 2006). While high densities can induce instabilities in the disk, thermal gas pressure and the shear force as a result of differential rotation of material in the disk can provide added stability against local collapse. The balance between these forces ultimately determines the fate of the disk. Originally introduced by Safronov (1960) and later quantified by Toomre (1964), a disk in Keplerian rotation is unstable against axisymmetric gravitational instabilities when the Toomre Q parameter

$$Q \equiv \frac{c_s\,\Omega}{\pi\,G\,\Sigma} < 1, \tag{1.4}$$

where the stabilising effect of pressure is accounted for in the equation of sound speed c_s, shear is considered in the epicyclic frequency (or angular velocity) Ω of the disk, and the self-gravitational force is represented as the surface density Σ of the disk.

Disks are prone to fragmentation when their mass exceeds 50% of the mass of the entire system (Kratter et al. 2010). Numerical simulations have found that disk fragmentation can

result in the creation of short-period binaries on the scales of hundreds of au (Meyer et al. 2017; 2018). The highest-resolution observations with ALMA that are able to resolve such structures on sub-hundred au scales are also starting to see fragmentation of the disks on these scales (Ilee et al. 2018). Considering the large fraction (> 70%) of OB stars that are found in close binary systems through radial velocity surveys (Chini et al. 2012), it is important to understand the role of disk fragmentation in affecting the observed stellar mass distribution.

For a marginally stable disk ($Q \sim 1$), the locally unstable regions compress as they start to collapse, providing compressional heating in these regions. This increase in the local thermal pressure can counteract the local collapse and put the disk back into a state of equilibrium such that the region will not fragment unless heat can be dissipated on a short timescale. Through numerical simulations, Gammie (2001) and Johnson & Gammie (2003) have introduced a cooling parameter, β, to study the effect of cooling for marginally stable thin disks in gravito-centrifugal equilibrium. In their prescription,

$$\beta = \Omega\, t_{\rm cooling}, \tag{1.5}$$

where the cooling time, $t_{\rm cooling}$, is assumed to be constant and a function of the surface density and internal energy of the disk. If the local collapse needs more than a few orbits, due to a long cooling timescale, a locally collapsing region within the disk can be ripped apart by shear. Therefore, there exists a critical β value below which a locally collapsing region would be rapidly cooling, and if it is sufficiently self-gravitating, it would be prone to fragmentation. Conversely, values above this critical β value would put a marginally stable disk into a self-regulating scenario such that heating acts as a stabilizing force and directly counteracts the cooling rate.

The Gammie cooling criterion is relevant only if the disk is marginally stable, with regions that are locally unstable against axisymmetric gravitational instabilities. A Toomre-stable disk will not fragment regardless of how quickly it may be cooling.

This critical value is determined through numerical simulations and varies depending on the heating and cooling recipes and convergence issues. For an overview of these issues, see Kratter & Lodato (2016), and more recently Baehr et al. (2017). Regardless of the specific numerical simulation issues, it is generally assumed that the critical β value ranges between $1 - 5$.

1.3.4 Other feedback mechanisms

Photoionization

In the later evolutionary stages in the formation of high-mass stars, ionizing flux from the hot star allows the creation of an H II region. When the size of the photoionized region is small enough that the escape speed from its outer boundary is large, the photoionized gas will be trapped and accretion continues. If the accretion rate is not high enough to trap the photoionized region, and if the ionizing flux is powerful, the H II region can expand outwards allowing gas to easily escape, halting further accretion of material onto the star. This effect was first proposed by Walmsley (1995) and a mechanism for accretion in photoionized regions to over come this issue was later proposed by Keto (2003), which we will touch on in Sect. 1.4.1.

Winds

Fast winds can radiate away from the surface of stars when they reach temperatures in excess of ~2.5×10^4 K (Vink et al. 2015 and references therein). While the momentum carried by such winds may not have as significant of an effect as the stellar radiation pressure, the high-velocity nature of such winds can produce shocks against the dense inflow of material accreting onto the star. On a similar note, protostellar jets outflows can also have similar consequences. Temperatures in these shocked regions can get as high as 10^7 K and disrupt accretion.

1.4 The formation of high-mass stars

The two most commonly discussed scenarios in the formation of the most massive stars are 1) formation by accretion of interstellar matter in a turbulent environment and 2) formation by coalescence of low-mass stars. These theories were established as a consequence of the need for overcoming the barriers in the formation of high-mass stars outlined in the previous section. In the following, we briefly introduce each of these mechanisms.

1.4.1 Formation through accretion

The formation of stars through accretion of interstellar matter is the mechanism by which low-mass stars form.

Turbulent core accretion model

The Turbulent Core Accretion Model, also known as the 'Monolithic Collapse Model' was first proposed by McKee & Tan (2002, 2003). In this theory, a single or a bound multiple system of high-mass stars form out of gravitationally bound cores that are supported by turbulence and magnetic fields. The necessary material to build up enough mass in the cores is constantly supplied from the turbulent and pressurized larger-scale cloud. In fact, the rate at which material is accreted from the cloud is the same as the rate at which this material is formed into a star. Turbulent Core models have high accretion rates of ~$10^{-3} M_\odot\,\mathrm{yr}^{-1}$, orders of magnitude higher than accretion rates measured in sites of low-mass star formation. The accretion rates in these models are high enough that sufficient matter is accreted onto the protostar. In order to keep the quasi-equilibrium between turbulence and gravity, either mechanical energy is provided from the large-scale cloud cascading to smaller scales, or is injected from within the cores through outflows and accretion shocks.

Competitive accretion model

Motivated by the fact that the most massive stars tend to be found in the centers of massive clusters, Bonnell et al. (1997; 2001; 2004) proposed that stars in a cluster environment compete to accrete mass from the parental cloud (see also review by Bonnell et al. 2007). This means that the location of the protostar within the cluster is extremely important in providing it with the material it needs to grow. Moreover, the size of each protostar's accretion domain which depends on its initial mass strongly affects how much it can accrete material away from other protostars

in its vicinity. Therefore, the accretion rate is highly variable such that more massive seeds can grow faster. This scenario results in mass segregation whereby the most massive stars form in the center of the cluster with a population of stars of varying masses distributed within the cluster. This scenario can explain why the most massive stars are so rare, as they must have been privileged enough to be seeded in the centers of the most massive clusters where they could accrete as much material as possible from the parental cloud. Variable accretion and mass segregation would also be expected in the case of the Turbulent Core Model if the clump fragments and forms the most massive core at the center, so these observables do not help in differentiating one model from the other.

HII regions

In order to overcome photoionization inhibiting the accretion of enough material onto the protostar, Keto (2003) proposed a scheme in which molecular gas which becomes ionized within the H II region can continue to accrete onto the star via an ionized accretion disk. This is an important mechanism as it removes the need for unrealistically high accretion rates in the earlier phases of high-mass star formation. Observational evidence for such an accretion mechanism has been provided through observations of radio recombination lines (e.g. Keto & Wood 2006; Keto & Klaassen 2008; Klaassen et al. 2018). It is important to note that while the Competitive Accretion Model is often compared against the Turbulent Core Model, accretion through the H II region is a mechanism which can occur in either of the two aforementioned models.

1.4.2 Formation through collisions

Perhaps the most radical theory for the formation of high-mass stars is that of merging and coalescence of lower mass objects in dense clusters (e.g. Bonnell et al. 1998; Portegies Zwart et al. 1999). The problem with such models is that the densities required are high and the time for the collisions to happen is short. Vink et al. (2015) calculate that in a cluster with 10^4 stars pc^{-3}, less than 1 collision between two 1 $M_\odot$ stars will occur over the ~4 Myr lifetime of a massive star. To circumvent these, gas accretion models were introduced to increase the cluster densities as well as gas-free collision models were investigated in order to increase the time available for collisions to take place (see Vink et al. 2015 and references therein). Nevertheless, the conclusions for this formation mechanism are that they are rare and may only be able to explain the formation of the most massive stars in the densest clusters (Zinnecker & Yorke 2007).

1.5 Stages of high-mass star formation

In reality, the formation of massive stars may be possible through a combination of formation scenarios presented in the previous section. For example, observations of Peretto et al. (2006) pointed to a picture of high-mass star formation that is a combination of the Turbulent Core Model (McKee & Tan 2003) and stellar mergers (Bonnell et al. 1998) whereby a very massive turbulent ultra-dense core is formed in the center of a collapsing protocluster through gravitational merging of two or more Class 0 protostellar cores. Regardless of the exact formation scenario, an evolutionary sequence for the formation of high-mass stars has been established.

Following the evolutionary sequence outlined by Beuther et al. (2007a), the initial stage starts with high-mass starless cores (HMSCs), also known as Prestellar Cores, which reside within Infrared Dark Clouds. HMSCs have masses of 100 – 1000 $M_\odot$ and are dense, cold, molecular condensations on the verge of collapse, which in the Turbulent Core Accretion model of McKee & Tan (2003) collapse to form massive protostars. From there, the evolutionary sequence continues to the High-Mass Core stage which encompasses accreting low- to intermediate-mass protostar(s) that are on their way to becoming high-mass star(s). Therefore in this stage the luminosity is expected to be dominated by accretion luminosity. In the transition between accreting intermediate mass protostar stage and accreting high-mass star stage, a 'high-mass protostar' can be defined. There exists some debate over the use of this term, mainly because of the exact definition of 'protostar'. Classically, a protostar is defined to be a hydrostatic object that has not yet begun bruning hydrogen. Zinnecker & Yorke (2007) suggest the term 'high-mass protostar' should not be used since one cannot easily establish observationally when exactly an accreting object starts burning hydrogen. On the other hand, Beuther et al. (2007b) suggest a simpler interpretation such that a 'high-mass protostar' can be defined as a high-mass object that is still in its accretion phase, regardless of whether or not it has already ignited hydrogen in its core. In this thesis, we will adopt the latter definiton for the term 'protostar'.

Next, a high-mass protostellar object (HMPO) is formed. These objects contain within them protostars with masses $> 8\ M_\odot$, therefore, their luminosities become dominated by the hydrogen burning process. Sridharan et al. (2002) observed a sample of 69 HMPO candidates in the centimeter regime and found their bolometric luminosities to be in the range $10^4 - 10^6\ L_\odot$ with a significant fraction still due to accretion processes. Furthermore, HMPOs may harbour hot molecular cores (HMCs) and/or Hypercompact H II (HCH II) region with sizes < 0.01 pc. Temperatures in the HMCs can reach a few hundred Kelvins, evaporating ices from dust grain surfaces hence stimulating a wealth of chemistry at this stage, observable in the (sub)millimeter. HCH II regions can be detected through their strong free-free emission making them bright in the centimeter regime. As described in the previous section, it is possible that accretion is still ongoing within the HCH II phase (Keto 2003). In some cases, Ultracompact H II (UCH II) regions with size < 0.1 pc are present at this stage which likely mark a transition phase after the breakout of the Lyman continuum radiation from the young star (Hoare et al. 2007).

Proposed by Motte et al. (2018), Fig. 1.2 shows a schematic of the evolutionary phases in high-mass star formation similar to what we have just described but including the global hierarchical collapse of the cluster within which massive stars form. In their picture, molecular cloud complexes are defined to have sizes of 100 pc with masses of $10^5 - 10^6\ M_\odot$.

1.6 Disks in high-mass star formation

Of all the formation scenarios presented in the Section 1.4, all but formation through collisions allow for a disk-mediated accretion scenario analogous to low-mass star formation. The existence of disks in the Competitive Accretion Model is also sometimes debated as it is expected that disks could get truncated to smaller sizes in the densest parts of the cluster where the most massive member may be forming through collisions. Moreover, disks are able to overcome some of the

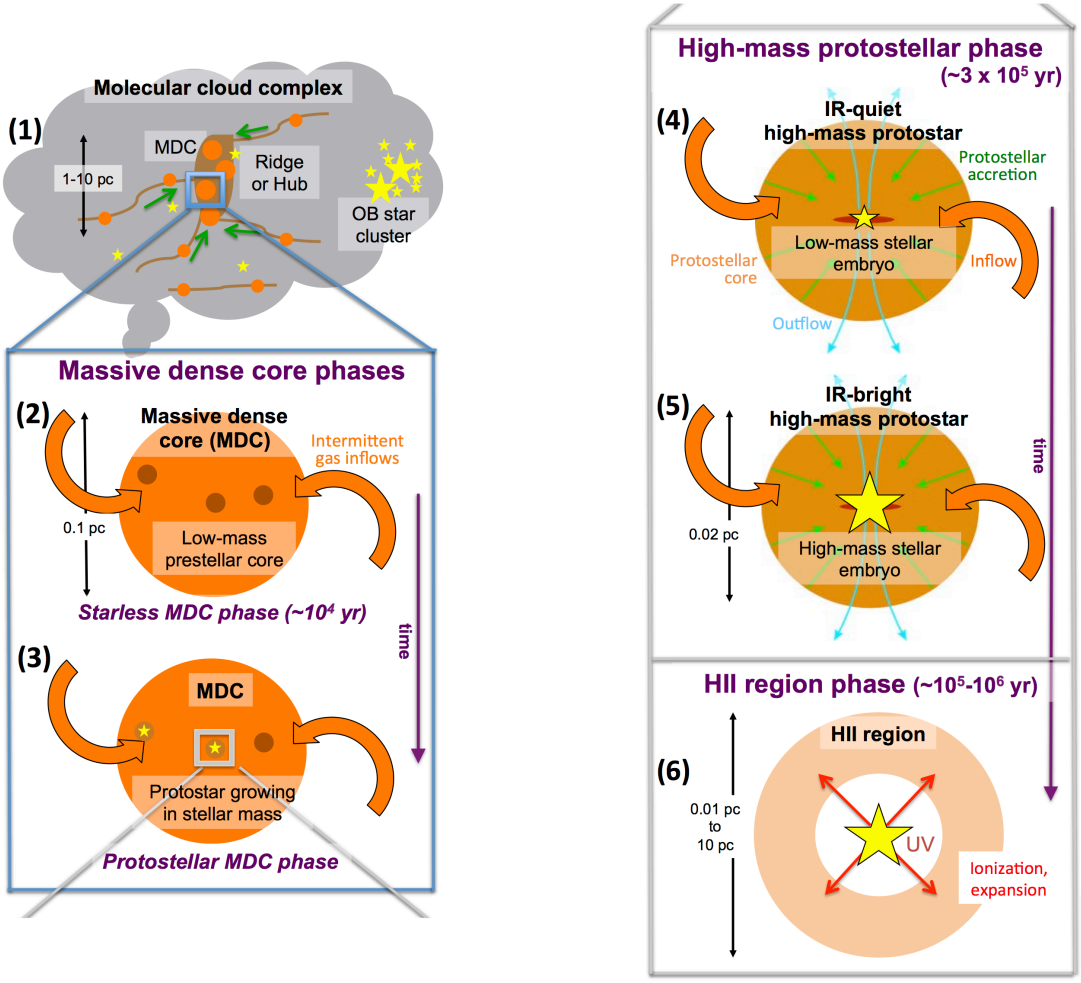

Figure 1.2: Schematic of the evolutionary phases in high-mass star formation, obtained from Motte et al. (2018).

major barriers to high-mass star formation (see Sect. 1.3). In more recent years, two- and three-dimensional radiation-hydrodynamical simulations of collapsing cores have shown support for disk-mediated accretion in the formation of very massive stars, analogous to the formation of low-mass stars (e.g. Yorke & Sonnhalter 2002; Krumholz et al. 2009; Kuiper et al. 2010, 2011; Kuiper & Yorke 2013; Klassen et al. 2016; Rosen et al. 2016; Kuiper & Hosokawa 2018).

While the formation mechanism of high-mass stars through accretion disks is being comprehensively studied theoretically, the observational existence of disks around O- and B-type stars is still elusive. This is in part due to their scarcity, fast evolution, and the fact that high-mass stars form in dense distant clusters, making disentangling individual stellar contributions difficult (see reviews by Cesaroni et al. 2007, Beltrán & de Wit 2016, Motte et al. 2018). Perhaps the best indirect observational evidence for the existence of disks is the ubiquitous observations of collimated bipolar outflows (e.g. Beuther et al. 2002a; Fallscheer et al. 2009; Leurini et al. 2011; Frank et al. 2014; Maud et al. 2015; Sanna et al. 2019), which has also been predicted by theoretical models (e.g. Pudritz et al. 2007; Banerjee & Pudritz 2008; Kölligan & Kuiper 2018). Moreover, as the evolution of a high-mass protostar is quite rapid, the disk-accretion phase can

be expected to occur while the protostar is highly embedded in its prenatal cocoon of gas and dust. With the advent of interferometers in the (sub)millimeter regime it is only in recent years that observations of cold dust and dense gas tracers in these regions have been able to shed light on the existence of disks in the formation of OB-type stars. It should be noted that even on the low-mass end, establishing disks in their earliest Class 0 phase has been challenging (Maury et al. 2019).

It is important to note a significant difference in the exact mechanism with which disks allow the accretion of material onto the (proto)star in the low- versus the high-mass regimes. In low-mass star formation, the exact mechanism with which disk material is thought to accrete onto the low-mass protostar is through the magnetic field lines at points near the stellar poles through a process called magnetospheric accretion (e.g. see Fig. 8.1 of Hartmann 2009). In high-mass stars, the outer layers are radiative rather than convective, therefore accretion is expected to happen through the disk directly.

A review by Beltrán & de Wit (2016) summarizes our current understanding of the properties of accretion disks around young intermediate- to high-mass stars. Figure 1.3 shows a schematic of our current understanding of disk properties around these stars. They refer to large structures for which a rotational velocity field could be established, extending thousands of au in space, as 'toroids' which host a (proto)cluster of stars and are not in an equilibrium state. In contrast, 'true' disks such as those seen in the Class I and II phases of low-mass star formation are expected to be in an equilibrium state whereby the differential Keplerian-like rotation with $V_{\rm rot} \propto R^{-1/2}$, provides support against the gravitational force of the central protostar. Many toroidal like structures have been detected around OB-type protostars (e.g. Beltrán et al. 2005). Furthermore, Keplerian disks around B-type stars have been confirmed by many studies in recent years and the current understanding for the formation of B-type stars is a scaled up version of low-mass star formation.

With the advent of long-baseline interferometry, a hand-full of disk candidates around the most massive stars have recently been detected (Johnston et al. 2015; Ilee et al. 2016, 2018; Chen et al. 2016; Cesaroni et al. 2017; Csengeri et al. 2018; Ahmadi et al. 2018; Maud et al. 2018, 2019; Sanna et al. 2019; Zapata et al. 2019). Of these studies, that of Cesaroni et al. (2017) targeted a sample of 6 YSOs with luminosities $> 10^5\ L_\odot$ with ALMA at 0.2″ to search for disks around O-type stars. They found strong indications of rotation in three of the targets making them good candidates for circumstellar disks while another three were tentative cases and one showed no rotational signatures. They concluded that disk detections around O-type stars must be sensitive to the evolutionary phase of the YSO such that in earlier evolutionary phases confusion with the envelope can hinder the detection and characterization of the disk, and at a later evolutionary phase the molecular component of the disk may have already been destroyed resulting in no detections. Therefore, not only do we need larger number statistics in the search for disks in high-mass star formation, but careful considerations must be given to the evolutionary phase. This is an extremely difficult task considering the already rare existence of O-type stars as well as the short evolutionary timescale for this particular phase in its evolutionary sequence.

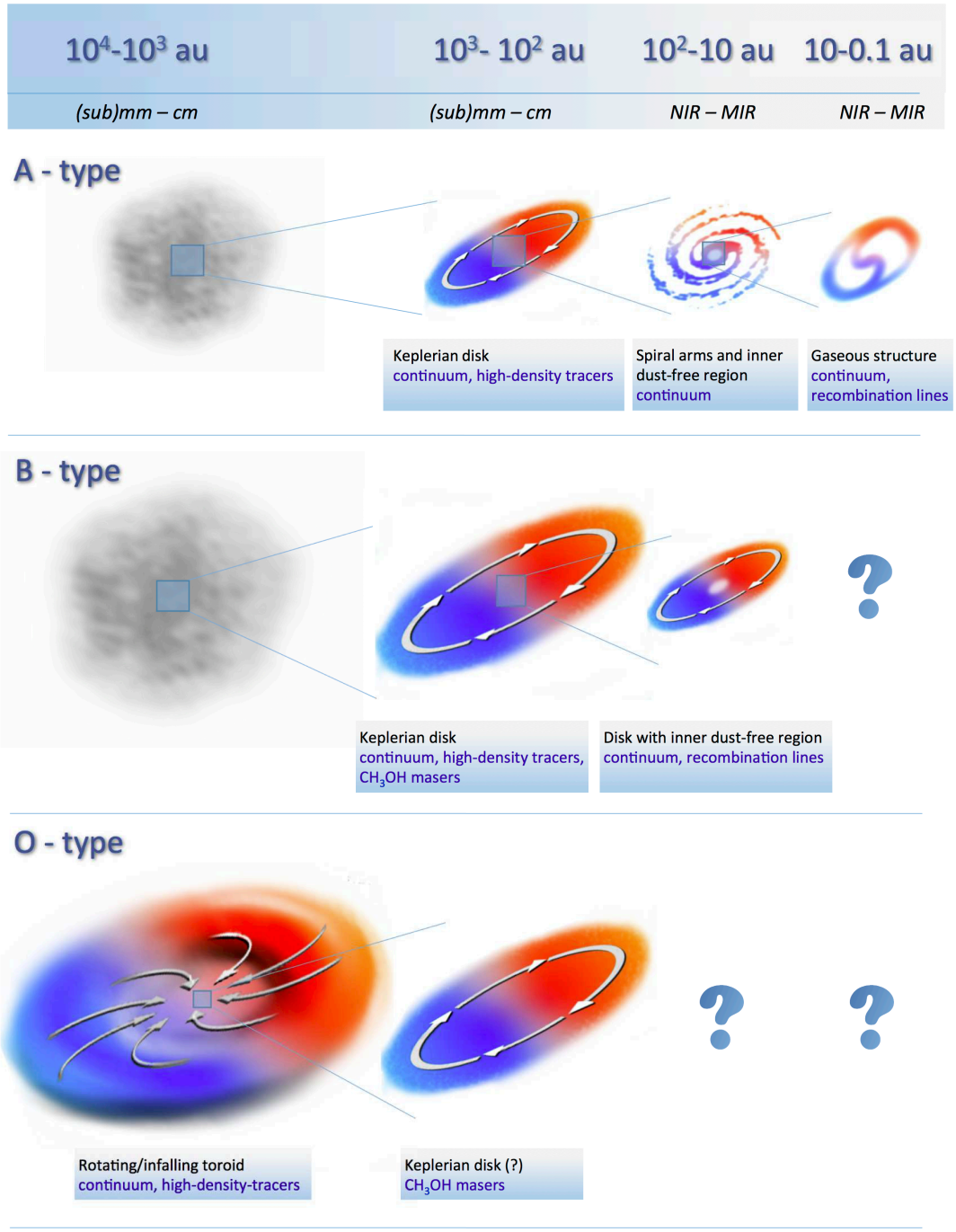

Figure 1.3: Schematic of our current understanding of disk properties around intermediate- to high-mass (proto)stars as presented in Beltrán & de Wit (2016). The columns range from large scales down to small scales from left to right with observing wavelengths listed. The type of tracers used in each case are specified in the boxes.

1.7 Structure of this thesis

In this thesis, we embark on a journey in search of disks around OB-type stars. The aim is to characterize their properties and study their stability against gravitational collapse in order to understand the importance of disk fragmentation in high-mass star formation. The data presented in this thesis is based on a large observational program at Institut de Radioastronomie Millimétrique (IRAM) called CORE (PI: Henrik Beuther, Beuther et al. 2018), using the NOrthern Extended Millimeter Array (NOEMA) interferometer[4] and IRAM 30-m single-dish telescope at 1.3 mm wavelength, targeting 20 high-mass star-forming regions. These data provide the highest possible resolution observations of these well-known regions in the northern sky.

In the following chapter we present some of the observational and modelling techniques used in finding and characterizing such disks. The CORE project and its observational specifications will be introduced in Chapter 3 and our detailed findings for one of the most interesting sources in the sample, W3 (H_2O), will be showcased in Chapter 4. Our interferometric observations of this source show that the core has fragmented into two smaller cores through gravitational core fragmentation, separated by a distance of ~2000 au. We study the detailed kinematics of the rotating structures surrounding each of these cores and calculate their Toomre stability against gravitational collapse. In Chapter 5, we test the caveats involved in using current interferometric observations at 1.3 mm to study the kinematics of high-mass star forming regions. We make use of a state-of-the-art numerical simulations of a very massive fragmenting disk and create synthetic observations to analyze the effects of inclination and resolving power on the derived parameters. In Chapter 6 we apply the benchmarked method to the full CORE sample of 20 objects and draw conclusions about the properties of rotating structures surrounding the most massive stars. A summary is provided in Chapter 7 with a discussion of future works provided in Chapter 8.

[4]Formerly Plateau de Bure Interferometer.

CHAPTER 2

Observational Techniques

In the following chapter, I outline some of the observational techniques and data analysis tools utilized in this thesis. I begin by summarizing the mechanisms by which disks around high-mass YSOs can be identified, and justify the need for interferometric observations in the (sub)millimeter for this effort.

2.1 Chasing disks in high-mass star formation

High-mass stars spend a significant portion of their formation time deeply embedded within their prenatal envelopes of gas and dust. Considering the clustered mode of high-mass star formation in combination with the typical far distances to these objects, it is evident that high angular resolutions are needed to properly resolve these regions. For example, a disk as large as 1000 au in size at a distance of ~2 kpc, typical for high-mass star-forming regions, would have an angular size of 0.5″. Therefore one needs resolving power below this limit to properly characterize such a disk. This is currently only possible by interferometers.

Various methods and tracers can be used to search for disks in high-mass star-forming regions. To aid this endeavour, first and foremost, luminosity cuts can be made to narrow the search to OB-type protostars. Next, YSOs in the correct evolutionary stage, i.e. the protostellar phase must be targeted. In Fig. 2.1 we show example SEDs of various phases in high-mass star formation (introduced in Sect. 1.5). A cold molecular core mainly emits in the far-IR to submillimetre regime as a single greybody (e.g. Rathborne et al. 2005). As infall begins and temperatures increase in the hot molecular core phase, its SED resembles a two-component greybody (e.g. Urquhart et al. 2007). In the massive YSO stage which is a more evolved stage than the hot core phase, accretion is still actively ongoing and radiation from the protostar is absorbed by the surrounding dusty envelope and disk which is then re-emitted in IR wavelengths. Once the star begins to ionize its surroundings, an UCH II is formed whose SED in the IR regime looks similar to a massive YSO, but has significant radio emission due to thermal Bremsstrahlung from the ionized gas. For these objects, the turnover wavelength for thermal Bremsstrahlung emission is roughly at 6 cm (corresponding to a frequency of 5 GHz). For hypercompact H II regions which are smaller and denser than the ultracompact H II, this turnover wavelength is found at lower wavelengths.

The cold molecular core and UCH II phases respectively represent stages that are either too early or late in the formation sequence. In the cold molecular core phase disks have likely not had enough time to be formed, while during the UCH II phase the disk is either highly embedded

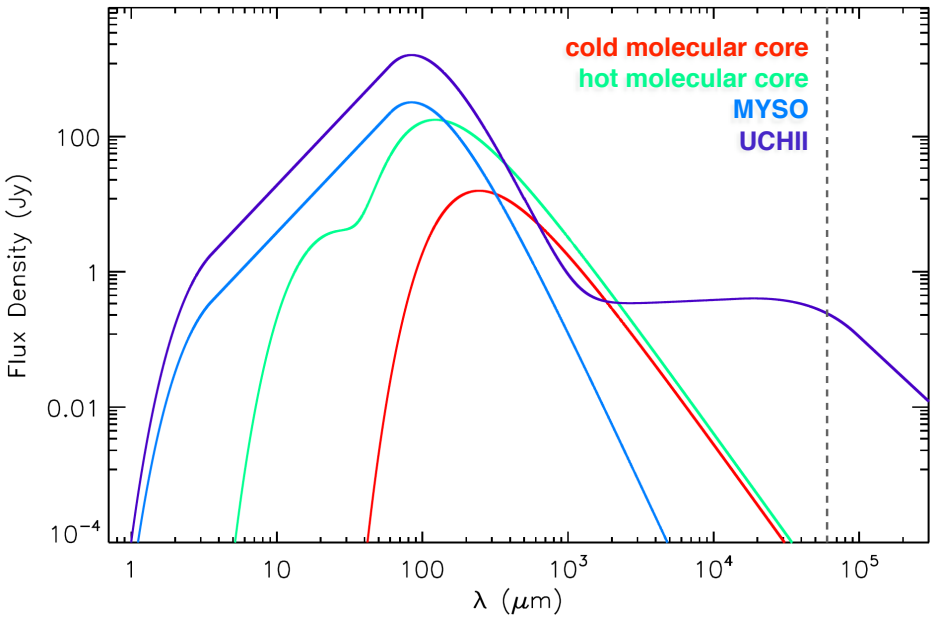

Figure 2.1: Example spectral energy distribution (SED) for a cold molecular core (red), hot molecular core (green), massive young stellar object (blue), and Ultracompact H II region (purple), adapted from Mottram (2008). The vertical dashed line corresponds to the wavelength (6 cm, or 5 GHz) for thermal bremsstrahlung emission from the ionized gas in the UCH II region.

within the ionized medium or it has already been dispersed. Therefore, the aim is to target objects that are in the hot molecular core or massive YSO phase of evolution. To do so, targets can be narrowed down to those that are known to have rich chemistry and/or associated jets/outflows from ancillary observations at lower resolutions. Moreover and especially if such ancillary data are not available, colour cuts can be imposed. A typical strategy is to use a flux ratio of 21 μm emission ($S_{12\mu m}$) over 8 μm flux ($S_{8\mu m}$) of at least 2 (Lumsden et al. 2013). This strategy helps to exclude more evolved regions, since on average they appear redder than the $S_{12\mu m}/S_{8\mu m}$ colour of YSOs. Additionally, H II regions can be excluded by confirming that no free-free emission is present.

Over the years, efforts have been made to establish the presence of disks in high-mass star formation, once reasonable targets have been chosen. The following is a summary of some of the tracers used for this purpose (see reviews by Cesaroni et al. (2007) and Beltrán & de Wit (2016) for a more detailed view)

2.1.1 Continuum

It is evident from Fig. 2.1 that continuum emission from dusty disk regions would peak in the far-IR regime and observations from near-IR to centimetre wavelengths can be useful. Observing most of the far-IR wavelengths from Earth is a fruitless task as the transmission of radiation through the atmosphere is zero in this regime. Observed flux in the near-IR is dominated by scattered light and thermal dust emission exactly at the sublimation temperature of 1500 K while in the mid-IR is dominated by warm temperatures on the order of few hundred Kelvins. There-

fore, near-IR emission is able to probe regions very close to the star and allow the investigation of accretion processes that take place. The best example of such observations is that of a 20 $M_{\odot}$ YSO, IRAS 13481–6124, observed in the K-band (at 2.2 μm) with the AMBER instrument on the Very Large Telescope Interferometer (VLTI) utilising three different three-telescope arrays reaching an angular resolution of 2.4 milliarcsecond resolving physical scales below 10 au (Kraus et al. 2010). Through radiative transfer modelling techniques, these authors concluded that the compact structure that they have observed in continuum emission is consistent with a disk. This finding was further justified by the detection of large-scale bipolar molecular outflows perpendicular to the disk plane.

In the mid-IR, Boley et al. (2013) made use of the two-telescope Mid-infrared Interferometric Instrument (MIDI) instrument on VLTI to observe a sample of 24 massive YSOs in the N-band (8–13 μm). Fitting the visibilities with 2-D geometric models, they derived size, orientation, and elongation of the circumstellar material for a sub-sample of 20 objects. They found that almost all objects showed deviations from spherical symmetry. In general, the compact mid-IR emission is elongated along the direction of the circumstellar disk and perpendicular to the outflow (e.g. S255 IRS3: Zinchenko et al. 2018), but sometimes the illumination footprints of outflow cones can dominate the thermal emission at mid-IR and therefore the elongated nature of the intensity distribution at mid-IR for some sources may be due to outflows rather than the embedded disks (De Buizer et al. 2017), hence the geometric models of the MIDI data are in principle susceptible to both disks and outflow cavity walls (Boley et al. 2013).

Since the bulk of disk material is colder than what the near- and mid-IR regimes can trace, (sub)millimetre observations at high angular resolutions are necessary to obtain a full picture, especially of the outermost regions of the disk and to study the properties of the transition between the infalling envelope and the disk. Sub-arcsecond observations in the (sub)millimetre regime are possible through interferometers such as ALMA and NOEMA interferometers with sensitivities that are sufficient for observing such distant embedded objects. Most recent detections and characterizations of disks around high-mass YSOs mentioned in Sect. 1.6 have been made with the use of these interferometers.

The major downfall of continuum observations in the search for disks in high-mass star formation is due to the fact that disks are deeply embedded within their parental clumps such that decoupling the disk from its surrounding envelope is a difficult task, therefore careful attention must be paid to properly model such observations. Moreover, kinematic information through line observations are needed to confirm such claims, therefore continuum observations alone are never sufficient for this task.

2.1.2 Masers

Gravitational collapse and accretion processes in star-forming regions naturally result in the heating of the environment through IR radiation as well as high-velocity jets/outflows. Such radiative and mechanical energy input can result in population inversions between energy levels in some of the more abundant species like OH, H_2O (water), CH_3OH (methanol), H_2CO, SiO, and NH_3. Observations of the distribution, line of sight velocities, and proper motions of these non-thermal line emissions known as masers are able to trace the physics and kinematics of the

hot dense regions close to protostars. Milli-arcsecond observations of these strong and compact masers have been possible through long-baseline observations (e.g. with Very Long Baseline Interferometry) for some time now. In particular, water masers at 22.2 GHz and Class II methanol masers at 6.7 GHz have been extremely useful in probing conditions in high-mass star-forming regions (e.g. Beuther et al. 2002b; Breen et al. 2010; Moscadelli et al. 2016). These water masers typically trace fast (20–100 km s^{-1}) shocks ejected from massive protostellar jets or winds, while Class II methanol masers tend to trace slower material (1–10 km s^{-1}) usually associated with the disks/envelopes of high-mass YSOs (see proceedings by Moscadelli et al. 2018). Interestingly, accretion outbursts onto two massive protostars have been reported through observations of maser flares in recent years (S255 NIRS3: Caratti o Garatti et al. 2017, NGC6334I-MM1: Hunter et al. 2017).

One of the major downfalls of this technique is the fact that maser emission is sensitive to excitation conditions in the environment, therefore it is often difficult to characterize the physical properties of these regions solely from maser observations. Moreover, while maser observations are powerful in analyzing the kinematics of the regions surrounding high-mass protostars in 3-D, it is often unclear whether they trace rotation, infall, or expansion motions. Typically, ancillary data like observations of jets or molecular outflows are needed in order to confirm which type of motion is being traced by masers.

2.1.3 Thermal emission

Direct evidence for disks around massive YSOs have been achieved through near-IR observations of the CO overtone bands (e.g. Bik & Thi 2004, Wheelwright et al. 2010, Ilee et al. 2013), but these observations probe the inner few astronomical units of the disks where temperatures are >1500 K. To characterize the properties of disks on larger scales where the disk is cooler, observations at longer wavelengths, especially in the (sub)millimetre are needed. Cesaroni et al. (2007) proposed that considering the fact that outflows are ubiquitous in star forming regions of all masses (e.g. Beuther & Shepherd 2005) and with the assumption that disks and outflows have a direct link, the best method for establishing the existence of a disks to first order is to search for small (<0.1 pc) molecular cores at the geometric center of a bipolar jet/outflow with a velocity gradient in dense gas tracers perpendicular to the outflow axis. Knowledge about the jet/outflow axis is especially important as velocity gradients in dense gas tracers can also indicate infall or outflowing motions. This criterion has been used for many of the recent detections using molecular lines (see Sect. 1.6) and the main technique we have used in this thesis as an initial assessment.

2.2 Molecular transitions

According to the *Born-Oppenheimer approximation*, the total molecular wavefunction $\psi_{\rm tot}$ consists of the product of its nuclear, electronic, vibrational, and rotational wavefunctions:

$$\psi_{\rm tot} = \psi_{\rm nuc}\psi_{\rm el}\psi_{\rm vib}\psi_{\rm rot}, \tag{2.1}$$

whereby each state has a different energy separation. The electronic transitions have the highest energy separations and hence are observed in the visible and UV range of the electromagnetic spectrum, while vibrational and rotational transitions are observed in the IR and millimetre regimes, respectively. The observations presented in this thesis are mainly focused in the millimeter regime, hence we are only concerned with rotational transitions.

Molecules can rotate about their three principal axes each of which has its own moment of inertia. Rotational transitions are possible only if the molecule has a permanent dipole or quadrupole moment. The energy levels of the rotational states of a linear diatomic molecule such as CO, the second-most abundant molecule in the ISM, can be calculated by solving the Schrödinger equation of a rigid rotor

$$E_J = \frac{h^2}{8\pi^2 I} J(J+1), \tag{2.2}$$

where J is the rotational quantum number, I is the moment of inertia, and h is the Planck constant. $J = 0$ is the lowest rotational energy state and selection rules for such a molecule with a dipole moment only allow transitions between successive rotational states ($\Delta J = \pm 1$).

Dense gas and outflow tracers

Molecules that best trace outflows are those with small dipole moments which as a result have transitions with low critical densities and are easily excited. Such a molecule is CO and its isotopologue ^{13}CO which is less abundance than its parent species by a factor of 20 to 80 depending on the galactocentric distance (Wilson & Rood 1994). Other outflow tracers are silicon- and sulfur-bearing molecules as they are typically locked onto grains and shocks from outflows can sputter them off the grains. Sputtered off silicon and sulfur then react with oxygen to form SiO and SO in the gas phase, making them excellent outflow tracers (e.g. Chernin & Masson 1993; Schilke et al. 1997), albeit not as widely found and effective as tracers like CO and its isotopologues. On the other hand, to trace dense gas surrounding high-mass YSOs, transitions of rare molecular species that have high excitation temperatures and critical densities can be used. Some of the molecules used for this purpose are NH_3, CH_3CN, $HCOOCH_3$, and $C^{34}S$ (Cesaroni et al. 2007).

A powerful tool in analysing molecular spectra is the use of moment maps to describe in simple terms the properties of a given distribution, in this case a spectral line. The zeroth moment for a given pixel at position (x, y) is the intensity integrated over velocity, v,

$$\mu^0_{x,y} = \int I\,(v,\,x,\,y)\,\mathrm{d}v. \tag{2.3}$$

This moment is typically used to investigate the spatial distribution of the emission. The first moment is the intensity-weighted peak velocity,

$$\mu^1_{x,y} = \frac{1}{\mu^0_{x,y}} \int I\,(v,\,x,\,y) \cdot v\,\mathrm{d}v, \tag{2.4}$$

which describes the intensity-weighted line of sight velocity for that pixel. This moment helps

to establish the nature of the velocity field across the source. For example, a systematic shift in velocity across a source (a velocity gradient) could point to infall, outflow, or rotation. The second moment is the intensity-weighted velocity dispersion,

$$\mu^2_{x,y} = \sqrt{\frac{\int I(v,\ x,\ y)\left(v - \mu^1_{x,y}\right)^2\ \mathrm{d}v}{\mu^0_{x,y}}}, \tag{2.5}$$

which is proportional to the line full width at half maximum (FWHM).

In this thesis, we have primarily made use of the dense gas tracer CH_3CN, as its many transitions allow us to obtain not only kinematical information at different excitation conditions but also knowledge about the excitation conditions like temperatures and densities which is invaluable for studying the stability of the disks. The following is an overview of the CH_3CN molecule.

CH_3CN as a dense gas tracer[1]

A symmetric top molecule like CH_3CN (methyl cyanide) has rotational energy levels that are described with two quantum numbers: J which is the total angular momentum and K, the projection of J onto the symmetry axis of the molecule which can have values $K = 0, 1, ..., J$ (see Boucher et al. 1980). Figure 2.2 shows the energy level diagram of CH_3CN where the levels are grouped into different K-ladders. For $J > K$ state, only downward J transitions within a given K-ladder are allowed. States that have $J = K$ have long radiative lifetimes and are metastable and the lowest J level in each K ladder is $J = K$. It can be seen in Fig. 2.2 that a given J level is shifted to higher energies with increasing K level but the spacing between different J levels is nearly independent of K. This results in radiative transitions from $J + 1 \rightarrow J$ for different Ks to occur at similar frequencies. Higher K transitions occur at lower frequencies due to centrifugal distortion. This is an extremely advantageous property as many transitions can be observed in the same frequency band reducing uncertainties due to data reduction and calibration.

Due to the threefold symmetry of the methyl group (containing CH_3), such molecules can be divided into two distinct groups (A and E, also known as ortho- and para-) depending on whether the hydrogen nuclei have their spins aligned or not. Rotational levels $K = 3n$, where n is an integer, belong to the A species and $K = 3n \pm 1$ belong to the E species. The two groups can be treated as separate species because radiative transitions are only allowed between adjacent J levels within a given K ladder and collisions are very inefficient in changing the spin state. The statistical weight of the A species (except $K = 0$) is twice as large as that of the E species.

In a two-level system under thermal equilibrium, the relative populations of the internal states can be described according to the Boltzmann distribution such that,

$$\frac{n_u}{n_l} = \frac{g_u}{g_l} e^{-E_{ul}/kT_{\mathrm{ex}}}, \tag{2.6}$$

where E_{ul} is the energy separation between the upper (u) and lower (l) levels, T_{ex} is the excitation temperature, n is the number density, and g the degeneracy (or statistical weight) of each level.

[1]This section is in part based on information presented in Loren & Mundy (1984) and Zhang et al. (1998).

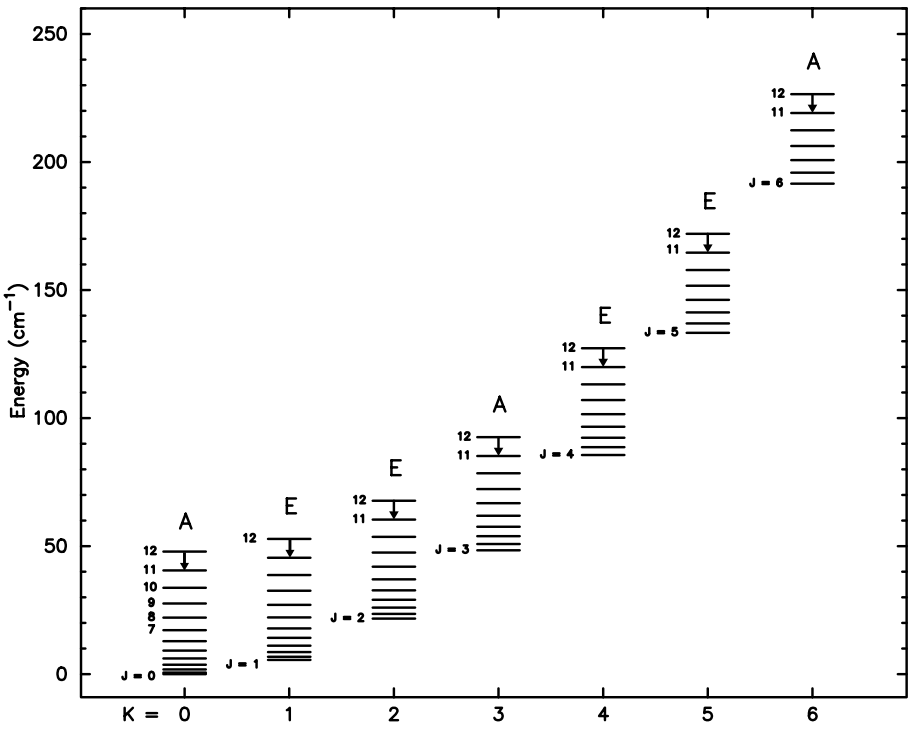

Figure 2.2: Energy level diagram of CH_3CN modified from Chen et al. (2006) showing J levels up to $J = 12$, for the $K = 0 - 6$ ladders. The A and E labels correspond to two independent species of K ladders. The transitions observed at high spectral resolution presented in this thesis are marked by arrows.

When thermal equilibrium is violated, different transitions can have different excitation temperatures. Under the local thermodynamic equilibrium (LTE) assumption which is valid deep within star-forming regions, densities are high enough such that collisional processes determine the level populations and the excitation temperature becomes equal to the kinetic temperature and the molecule is said to be thermalized. There exists a critical density $n_{\rm crit}$, at which collisional de-excitation is equal to the radiative de-excitation. For transitions that have high critical densities, the upper states may become underpopulated if densities are lower than this critical value. In such a case, the molecule is said to be sub-thermalized and the excitation temperature is lower than the kinetic temperature.

One of the main advantages in observing CH_3CN is the fact that radiative processes across K ladders for a given J are forbidden, therefore if the molecule is thermalized the populations in different K levels can provide a measure for the kinetic temperature. According to Loren & Mundy (1984), at densities higher than $10^{6.5}$ cm^{-3} the assumption that CH_3CN is thermalized is valid. Below this density, the excitation temperature of a given transition would overestimate the kinetic temperature. In this thesis, we analyze the spectra of CH_3CN $(12_K - 11_K)$ $K = 0-6$ transitions to investigate the kinematics and physical conditions deep within the cores that form the most massive stars, where LTE is a valid assumption. These transitions have energies $E_u/k = 70 - 325$ K (see Table 3.3), making CH_3CN an excellent thermometer. In the following section we give an overview of radiative transfer methods and introduce the software we use to model the spectra of this molecule.

2.3 Radiative transfer modelling

The radiative transfer equation describes how the intensity of a ray of light with intensity I_ν would change as it travels along a path s through a slab of material. Ignoring scattering effects, the intensity variation along the path can be written as a function of the emissivity coefficient j_ν and absorption coefficient κ_ν of the material:

$$\frac{\mathrm{d}I_\nu(s)}{\mathrm{d}s} = j_\nu(s) - \kappa_\nu(s) \cdot I_\nu(s). \tag{2.7}$$

The absorption coefficient can alternatively be written in terms of optical depth, τ_ν, such that

$$\mathrm{d}\tau_\nu(s) = \kappa_\nu(s)\,\mathrm{d}s. \tag{2.8}$$

The radiative transfer equation can therefore be written as

$$\frac{\mathrm{d}I_\nu(s)}{\mathrm{d}\tau_\nu(s)} = S_\nu(s) - I_\nu(s), \tag{2.9}$$

where the ratio of the emission and absorption coefficients is defined as the source function

$$S_\nu \equiv \frac{j_\nu}{\kappa_\nu}. \tag{2.10}$$

The solution to the radiative transfer equation for a plane-parallel slab of material with a uniform source function can be written as

$$I_\nu(\tau_\nu) = I_\nu^0\, e^{-\tau_\nu} + S_\nu(1 - e^{-\tau_\nu}), \tag{2.11}$$

where $\tau_\nu = 0$ at the surface of the emitting object where the starting intensity is I_ν^0. Therefore, the intensity at a given optical depth along the path is composed of three parts: the attenuation of background radiation, I_ν^0, by the optical depth, the emission from the source S_ν, and the attenuation of the emission over the distance between the emission and the observer.

The difficulty in solving the equation of transfer is that the source function is often a function of intensity, making the equation of transfer nonlinear. Under LTE conditions, the source function is the Planck Function, $B_\nu(T)$:

$$S_\nu = B_\nu(T_{\mathrm{ex}}) = \frac{2h\nu^3}{c^2}\frac{1}{e^{h\nu/k_B T_{\mathrm{ex}}} - 1}, \tag{2.12}$$

where k_B is the Boltzmann constant, and T_{ex} is the excitation temperature. At low frequencies, or high temperatures, the Planck function can be approximated using the Rayleigh Jeans approximation ($h\nu \ll k_{\mathrm{B}}T$) such that

$$B_\nu(T) \simeq \frac{2k\nu^2}{c^2}\,T. \tag{2.13}$$

It is customary in radio astronomy to define the intensity of a body in terms of the equivalent

Rayleigh–Jeans brightness temperature,

$$I_\nu = \frac{2k\nu^2}{c^2} T_\mathrm{B}, \tag{2.14}$$

even if $I_\nu \neq B_\nu$.

When a spectral line is observed, its intensity includes a contribution from the line itself as well as the background continuum, I_ν^0. This contribution is often removed by means of continuum subtraction, therefore the baseline-subtracted spectral line intensity is:

$$\begin{aligned} I_\nu(\tau_\nu) - I_\nu^0 &= I_\nu^0\, e^{-\tau_\nu} + S_\nu(1 - e^{-\tau_\nu}) - I_\nu^0 \\ &= [S_\nu - I_\nu^0]\,(1 - e^{-\tau_\nu}). \end{aligned} \tag{2.15}$$

Therefore, the observed line can be described via

$$J_\nu(T_\mathrm{B}) = [J_\nu(T_\mathrm{ex}) - J_\nu(T_\mathrm{bg})]\,(1 - e^{-\tau_v}), \tag{2.16}$$

where $J_\nu = \frac{1}{4\pi}\int_\Omega I_\nu \,\mathrm{d}\Omega$ is the mean intensity, i.e., the angular average of I_ν over the solid angle Ω, and T_bg is the background temperature. Therefore, if $T_\mathrm{ex} > T_\mathrm{bg}$, the line is observed in emission, and if $T_\mathrm{ex} < T_\mathrm{bg}$ it is observed in absorption against the warmer/brighter background. Written in terms of temperatures, the brightness temperature is,

$$T_\mathrm{B}(v) = \frac{h\nu}{k_\mathrm{B}} \left(\frac{1}{e^{h\nu/k_\mathrm{B}T_\mathrm{ex}} - 1} - \frac{1}{e^{h\nu/k_\mathrm{B}T_\mathrm{bg}} - 1}\right)(1 - e^{-\tau_v}). \tag{2.17}$$

XCLASS: The eXtended CASA Line Analysis Software Suite

We make use of the eXtended *CASA* Line Analysis Software Suite (*XCLASS*[2], Möller et al. 2017) to model the various K ladder transitions of CH_3CN in order to study the physical conditions in the dense regions this tracer is expected to probe. *XCLASS* solves the radiative transfer equation in one dimension for a set of initial conditions (source size, column density, temperature, linewidth, and peak velocity) provided by the user, and through a χ^2 minimization routine changes the initial conditions within ranges that have been provided by the user to obtain the best fit to the observed spectra. *XCLASS* is similar to other spectral line modelling tools like *WEEDS* (Maret et al. 2011) but with the added advantage that it makes use of the optimization package *MAGIX* (Möller et al. 2013) which constrains the model parameters by minimising deviations between the model spectra and the observations using various algorithms. Furthermore, *XCLASS* uses its own locally-saved SQLite3 database, making use of the Cologne Database for Molecular Spectroscopy (CDMS) and Jet Propulsion Laboratory catalogues for obtaining various spectroscopic parameters. The following is a simplified overview of how *XCLASS* solves the radiative transfer equation for a given molecule in order to create synthetic spectra that can be compared with observations[3].

Starting with a given excitation temperature (kinetic temperature in LTE) and column density provided by the user, the program calculates the optical depth of each transitions, t, of a

[2] https://xclass.astro.uni-koeln.de

[3] Detailed derivations and explanations can be found in Möller et al. (2017) and the *XCLASS* user manual.

given line along the line of sight via

$$\tau(\nu) = \sum_t \left[\frac{c^2}{8\pi\nu^2} A_{ul}^t N_{\rm tot} \frac{g_u^t \, e^{-E_l^t/k_{\rm B}\,T_{\rm ex}}}{Q\,(T_{\rm ex})} \left(1 - e^{-h\,\nu^t/k_B\,T_{\rm ex}}\right) \times \phi^t(\nu) \right]. \tag{2.18}$$

The Einstein A_{ul} coefficient, the upper state degeneracy g_u, the energy of the lower state E_l, the partition function $Q(T_{\rm ex})$, and the rest frequency of the transition ν^t, are taken from the stored SQLite3 database. Assuming the broadening of a given line is caused by the thermal motion of the gas, the line profile, $\phi(\nu)$, can be estimated to have a Gaussian profile normalized such that $\int_0^\infty \phi(\nu)\, d\nu = 1$, and is described by the following function

$$\phi(\nu)^t = \frac{1}{\sqrt{2\pi}\,\sigma^t} \cdot e^{-\frac{\left(\nu - \left(\nu^t + \delta\nu_{\rm LSR}^t\right)\right)^2}{2(\sigma^t)^2}}, \tag{2.19}$$

where σ is the standard deviations and $\delta\nu_{\rm LSR}^t$ is the local standard of rest (LSR) frequency of the source. Since the user-provided offset velocity $v_{\rm offset}$ is in units of km s^{-1}, *XCLASS* converts it to frequency units as needed using

$$\delta\nu_{\rm LSR}^t = -\frac{\delta v_{\rm offset}}{c} \cdot \nu^t. \tag{2.20}$$

Furthermore, the standard deviation is calculated with the following equation,

$$\sigma^t = \frac{\frac{\Delta v_{\rm width}}{c} \cdot \left(\nu^t + \delta\nu_{\rm LSR}^t\right)}{2\,\sqrt{2\,\ln 2}}, \tag{2.21}$$

using the user-provided linewidth Δv, which is the line FWHM in velocity units.

Once the optical depth is calculated (Eq. 2.18)[4], *myXCLASS* function creates a synthetic spectrum using Eq. 2.17 with the user-provided kinetic and background temperatures. We assume the background temperature to be that of the cosmic microwave background, about 2.7 K. In the case of single-dish observations, beam dilution will also have to be taken into account such that the observed brightness temperature is

$$T_{\rm obs}(v) = \eta \cdot T_{\rm B}(v), \tag{2.22}$$

where η is the beam filling factor defined as

$$\eta = \frac{\theta_{\rm source}^2}{\theta_{\rm tele}(\nu)^2 + \theta_{\rm source}^2}, \tag{2.23}$$

where $\theta_{\rm source}$ and $\theta_{\rm tele}$ are the source and telescope beam sizes, respectively. For high-resolution observations with an interferometer, the beam size is much smaller than the size of the source and hence $\eta = 1$.

[4]Note that here we have presented a simplified picture, whereas in reality modelling the dusty core layer or any other layer in the fore/background is also possible. In that case, the optical depth of dust would also have to be calculated, assuming a certain dust opacity (e.g. from Ossenkopf & Henning 1994) and a gas-to-dust mass ratio. The source function will also have to be adjusted to include the dust emissivity and absorption coefficients.

Once *myXCLASS* creates a synthetic spectrum with the user-provided initial guesses, it uses the *MAGIX* optimization routine to vary the user-provided parameters within the range specified by the user to find the best fit to the observed spectra through a χ^2 minimization routine. *MAGIX* provides optimization through one or more algorithms which can be nested together and stops when the maximum number of iterations (or the desired χ^2 value) has been reached. One of the main advantages of using *XCLASS* is in the fact that its *myXCLASSMapFit* function can perform the above steps pixel-by-pixel and provide output maps for each of the free parameters the user wishes to model.

Details of our XCLASS modelling

In this thesis, we employ a combination of the Genetic and Levenberg-Marquardt algorithms of *XCLASS*, and an isothermal model such that one temperature is used for reproducing the observed population of CH_3CN lines at each pixel. In the first part of the thesis (Chapter 4), we aim to investigate the properties of rotating structures within the source W3 (H_2O). For this study, we assumed the size of the source to be larger than the interferometer's beam (~0.4″) and therefore set the beam filling factor to one. Our initial fits to the spectra of CH_3CN included the full $K = 0-6$ ladder, along with its $CH_3{}^{13}CN$ $(12_K - 11_K)$ $K = 0-3$ isotopologue, prescribing the $^{12}C/^{13}C$ ratio to be 76 which is consistent with the findings of Henkel et al. (1982) and the calculations of Qin et al. (2015) for W3 (H_2O). The top panel of Fig. 2.3 shows an example of the best-fit spectrum for one pixel, which yielded a high rotational temperature of 835 K. The lower intensities of the low-K lines of CH_3CN compared to the transitions higher on the K-ladder indicates that the low-K transitions are optically thick. Furthermore, the fits to the optically thinner high-K lines are not satisfactory. Repeating the same procedure but only fitting the CH_3CN $(12_K - 11_K)$ $K = 4 - 6$ lines along with the $CH_3{}^{13}CN$ $(12_K - 11_K)$ $K = 0 - 3$ isotopologues results in a better fit to these lines, for a lower rotational temperature of 207 K (see bottom panel of Fig. 2.3).

These findings are in agreement with line fitting analysis of Feng et al. (2015) in Orion KL in which they find that fitting all CH_3CN lines, assuming they are optically thin and in LTE, yields higher temperatures than when fitting them with an optical depth correction (see their Fig. 8). The exclusion of the optically thick and low energy lower K lines along with the inclusion of the ^{13}C isotopologues, although barely detected, allows the software to avoid prioritising the fitting of these optically thick lines and therefore derive the temperature more accurately. This finding is also related to the existence of temperature and density gradients which our one-component model cannot properly reproduce. As lower K lines are more easily excited than the higher K lines, they can probe the temperature in the envelope as well as the disk surface, while the higher K lines are better at tracing the disk and may not be as excited in the envelope. In fact, the reason why the brightness temperature of the low-K lines is lower than the high-K lines may be due to self-absorption of the photons from the warmer inner region by molecules in the cooler envelope material between the disk and the observer. Another explanation can be that the optically thick low-K transitions are more extended and therefore may be partially resolved out.

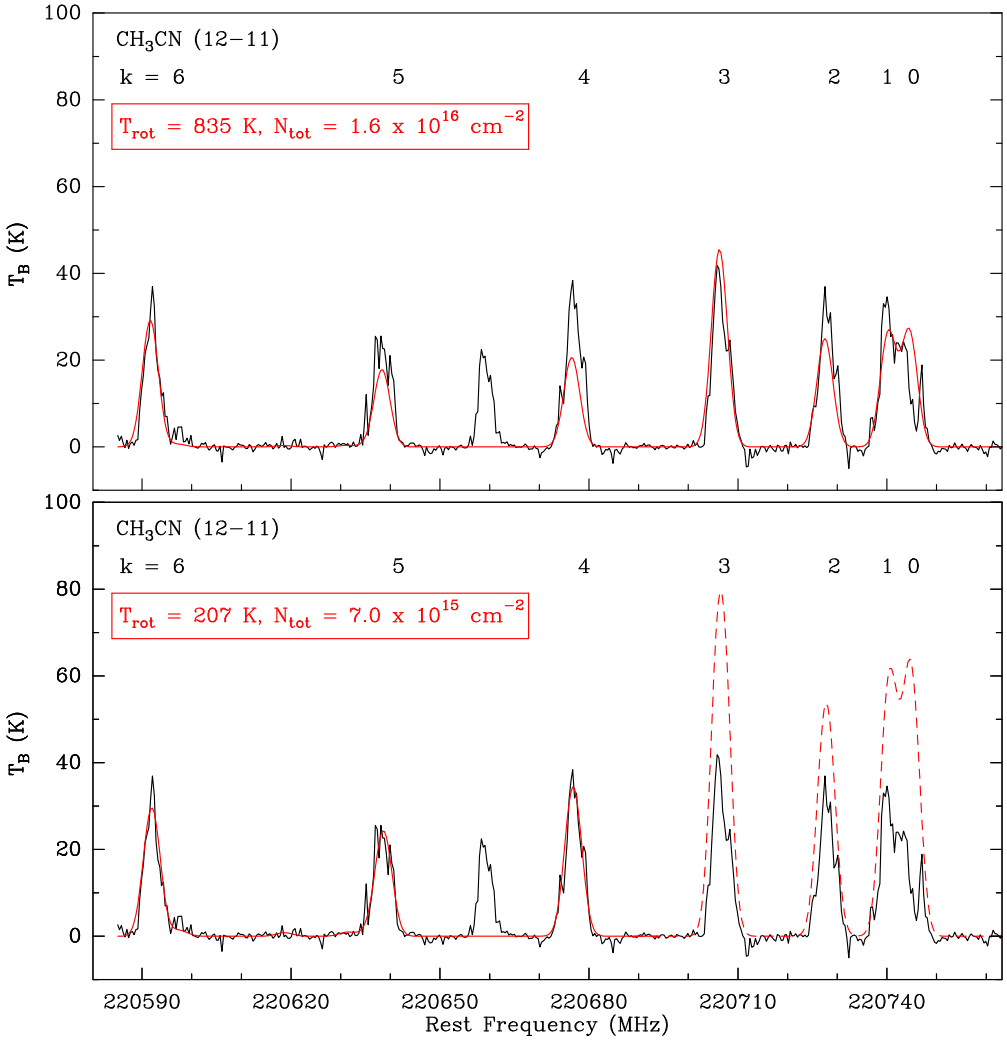

Figure 2.3: *Top*: Spectrum of a given pixel in black along with the *XCLASS* fit for $CH_3CN\,(12_K - 11_K)\,K = 0 - 6$ and $CH_3{}^{13}CN\,(12_K - 11_K)\,K = 0 - 3$ lines in solid red. The corresponding fit parameters are provided in the panel. *Bottom*: Spectrum of the same pixel as above in black with the *XCLASS* fit for $CH_3CN\,(12_K - 11_K)\,K = 4 - 6$ and $CH_3{}^{13}CN\,(12_K - 11_K)\,K = 0 - 3$ in solid red. The dashed red line corresponds to the predicted spectrum for the CH_3CN lines that were not used in the fitting process. This shows that the exclusion of the low-K lines in the fitting process allows *XCLASS* to provide a better fit for the optically-thinner high-K lines. The bright line detected between $K = 4$ and 5 components is C_2H_5CN.

2.4 Interferometry

It is clear that due to the clustered mode of high-mass star formation as well as the typically far distances involved, observations at high angular resolutions are needed in order to properly resolve these regions. The resolving power of a telescope, Θ, is determined by the wavelength at which it is used and the size of the collecting area, i.e. the diameter of the telescope D, such that

$$\Theta \propto \frac{\lambda}{D}. \tag{2.24}$$

In the radio regime with the long wavelengths involved, very large dish sizes would be needed in order to reach high resolutions. For example, in order to reach sub-arcsecond resolutions at 1 mm, a telescope with a diameter of at least 200 m would be needed. At longer wavelengths, for example to observe the 21 cm line at high resolutions, telescopes with diameters of tens of kilometres are needed which is an impossible engineering task to build. To increase the size of the collecting area, several smaller telescopes can be used together to 'simulate' a larger telescope. The resolving power of such an interferometer is then limited by the largest distance between the set of telescopes, which is referred to as the longest baseline. Details of interferometry are complex with many textbooks dedicated to it (e.g. Wilson et al. 2013; Burke & Graham-Smith 2014; Thompson et al. 2017). In the following, I briefly introduce some important interferometric concepts without going into much of the details, and refer to these textbooks for the more technical aspects[5].

2.4.1 Basic theory

The simplest interferometer is one that is comprised of two antennas. Such a system works similar to Young's double slit experiment, such that waves arriving in phase interfere constructively and those arriving out of phase interfere destructively, creating a patter of 'fringes'. Consider two antennas as depicted in Fig. 2.4, where $\vec{b}$ is the vector baseline from antenna 1 to antenna 2, observing a distant source in the direction of $\hat{s}$. Signal from a source that is far away arrives at antenna 1 later than at antenna 2. This so-called geometric delay, τ_g, depends on the path difference between the antennas such that $\tau_g = (\vec{b} \cdot \hat{s})/c$ where c is the speed of light. Assuming the incident radiation is emitted from a point source that is monochromatic, the interferometer can observe it in a narrow frequency range centered on $\nu = \omega/2\pi$ where ω is the angular frequency. Its electric field E can be described according to its amplitude A and phase ϕ, such that $E = Ae^{i\phi}$, and its time-variable electric field is $E_\nu(t) = E\cos(\omega t + \phi)$. The output voltage at antenna 2 is then $V_2 = V\cos(\omega t)$ and is retarded by the geometric delay at antenna 1: $V_1 = V\cos(\omega(t-\tau_g))$. Modern interferometers use correlators which multiply and time average the voltage outputs from each antenna in a pair of antennas. The final output is then

$$R = \langle V_1 V_2 \rangle = \left(\frac{V^2}{2}\right)\cos(\omega\tau_g). \tag{2.25}$$

Since V^2 is proportional to power, the output is dependent on the point-source flux density and the geometric delay, and varies sinusoidally with the change in the source direction (e.g. due to Earth's rotation), creating the so-called 'fringes'. The fringe amplitude is $V^2/2$ and its phase

$$\phi = \omega\tau_g = \frac{\omega}{c} b\cos(\theta), \tag{2.26}$$

which depends on the source position according to

$$\frac{\mathrm{d}\phi}{\mathrm{d}\theta} = \frac{w}{c} b\sin(\theta) = 2\pi\left(\frac{b\sin(\theta)}{\lambda}\right). \tag{2.27}$$

[5]Some other useful resources are lecture notes from various interferometry schools hosted by IRAM, Karl G. Jansky Very Large Array (VLA), and European Southern Observatory (ESO).

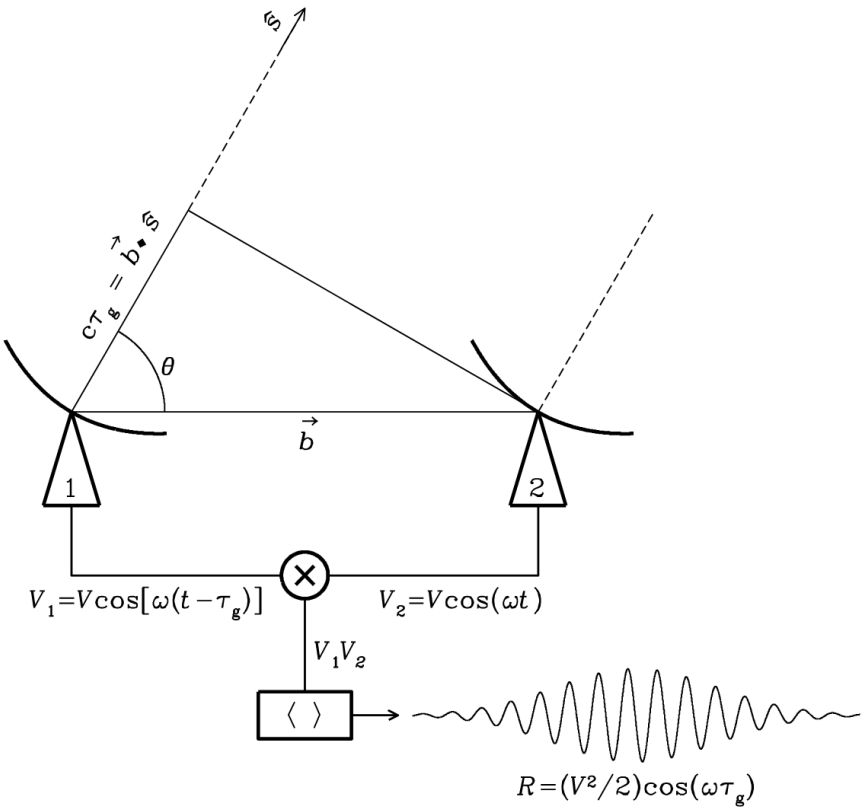

Figure 2.4: Schematic showing the setup of an elementary interferometer, obtained from an NRAO lecture on interferometry (https://www.cv.nrao.edu/course/astr534/Interferometers1.html).

Since the fringe period is $\Delta\phi = 2\pi$, the angular change in source position is $\Delta\theta = \lambda/(b\sin\theta)$. Therefore, fringe phase provides an excellent measure for the source position. Longer baselines resolve smaller scales better and shorter baselines recover larger scales.

In order to observe more complex sources than a point source, many more baselines of different lengths are needed. N antennas provide $N(N-1)/2$ unique baselines. In the observations presented in this thesis, we make use of the NOEMA interferometer with six 15-m antennas[6] and hence 15 baselines. The response of an interferometer to an extended source with a sky brightness distribution $I_\nu(\hat{s})$ can be derived by treating the extended source as a sum of individual point sources and including both the even and odd components of the signal. The latter can be done by including a 90° phase shift in one of the signal paths. Then the correlator output is a complex quantity called 'visibility', given as

$$V_\nu = \int I_\nu(\hat{s}) e^{-2\pi i \vec{b}\cdot\hat{s}/\lambda} \mathrm{d}\Omega, \tag{2.28}$$

which is the Fourier transform of the sky brightness.

In 2D, a coordinate system can be introduced parallel to the plane of the sky, with u giving the

[6]NOEMA is in the process of upgrading to 12 antennas with 10 antennas in operation at the time of writing this thesis. Although our observations spanned a few years in time when the interferometer was upgraded to 8 antennas, the correlator which was used for the high-spectral resolution observations could only process signal from 6 antennas.

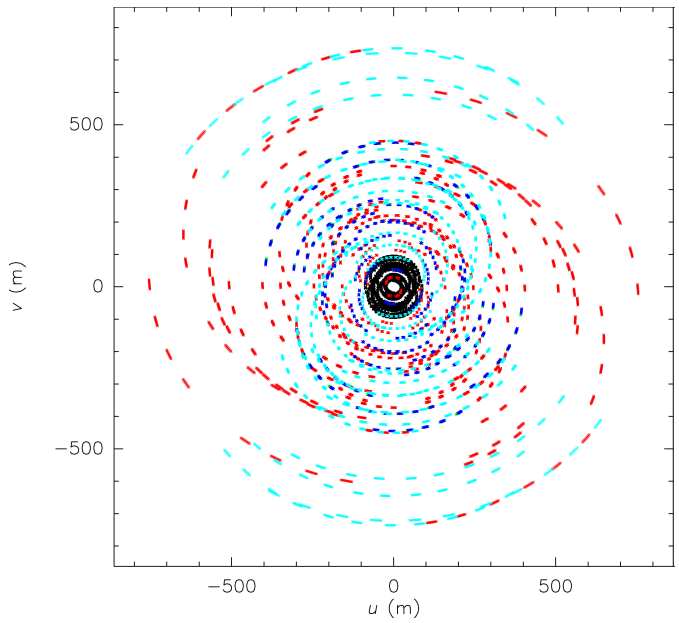

Figure 2.5: Example *uv*-coverage of NOEMA observations with five tracks, two in the A-configuration *(cyan and red)*, two in the B-configuration *(blue and green)*, and one in the D-configuration *(black)*.

east–west and v to the north–south components of the baseline. In this *uv*-plane, each projected baseline (i.e.baseline as seen from the source) traces an ellipse with one telescope at the center of the ellipse, such that $b\sin(\theta) = \sqrt{u^2+v^2}$. Therefore, each pair of antennas provides two points in the *uv*-plane. By observing long periods, Earth's rotation allows more points to be filled in the *uv*-plane. Figure 2.5 shows an example *uv*-coverage of three different configurations of the NOEMA interferometer. The hole in the center corresponds to the shortest distance between two antennas and limits the recovery of large scale structures. The outer boundary of dots sets the resolution limit, limiting information on scales smaller than the resolution element. Holes in the *uv*-plane corresponds to missing 'information', meaning some emission is filtered out. The reason why the curves are disjointed rather than continuously circular is partly because calibrators were being observed regularly as well as the fact that we were observing in track-sharing mode with two sources observed together in one observing session.

Setting parameters l and m as the corresponding sky coordinates, such that $\vec{b}\cdot\hat{s} = ul + vm$, the visibility function can be written as

$$V(u,v) = \int\int T(l,m)e^{2\pi i(ul+vm)}\,dl\,dm \tag{2.29}$$

where $T(l,m)$ is the sky brightness temperature. Since the complex visibility function is the 2D Fourier transform of the sky brightness distribution, then

$$T(l,m) = \int\int V(u,v)e^{-2\pi i(ul+vm)}\,du\,dv. \tag{2.30}$$

2.4.2 Imaging

Because the *uv*-plane is only discretely sampled, the sampled visibility function is a product of the visibility function with a sampling function $S(u,v)$, such that

$$V_S(u,v) = V(u,v) \cdot S(u,v) = \sum_{k=1}^{M} \delta(u-u_k, v-v_k) \cdot V(u_k, v_k). \tag{2.31}$$

The 'point spread function' of an interferometer is called the 'dirty beam', $s(l,m)$, and is the Fourier transform of the sampling function:

$$S(u,v) \xrightarrow{\mathcal{F}} s(l,m). \tag{2.32}$$

The so-called 'synthesized beam' is then a Gaussian fit to the dirty beam, depicting the spatial resolution of the interferometer. Taking the Fourier transform of the sampled visibility function produces the 'dirty image', $T^D(l,m)$:

$$V_S(u,v) \xrightarrow{\mathcal{F}} T^D(l,m). \tag{2.33}$$

Furthermore, the dirty image is the true image convolved with the 'dirty beam':

$$T^D(l,m) = T(l,m) * s(l,m). \tag{2.34}$$

Therefore, Fourier transform of the sampled visibilities gives the 'clean image' convolved with the point spread function. The 'clean image' is an approximation of the true sky brightness. The most commonly used deconvolution algorithm is called 'CLEAN'. This algorithm assumes a priori that the sky brightness consists of a set of point sources. The original version of this algorithm was introduced by Högbom (1974) while another more efficient one was later developed by Clark (1980). Figure 2.6 shows an example of the imaging routine using the *CLARK* algorithm, showing the dirty and clean images with the residual map showing the difference between the two. The field of view shown is roughly the size of NOEMA's primary beam. The primary beam describes an antenna's sensitivity as a function of direction because the antenna response is not

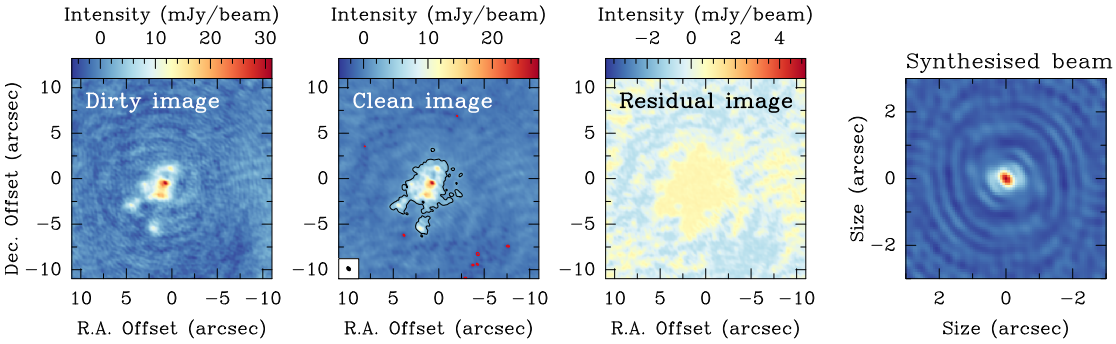

Figure 2.6: Example of cleaning interferometric observations for the continuum image of IRAS21078 at 1.37 mm. Black and red contours in the clean image correspond to 5σ and -5σ levels.

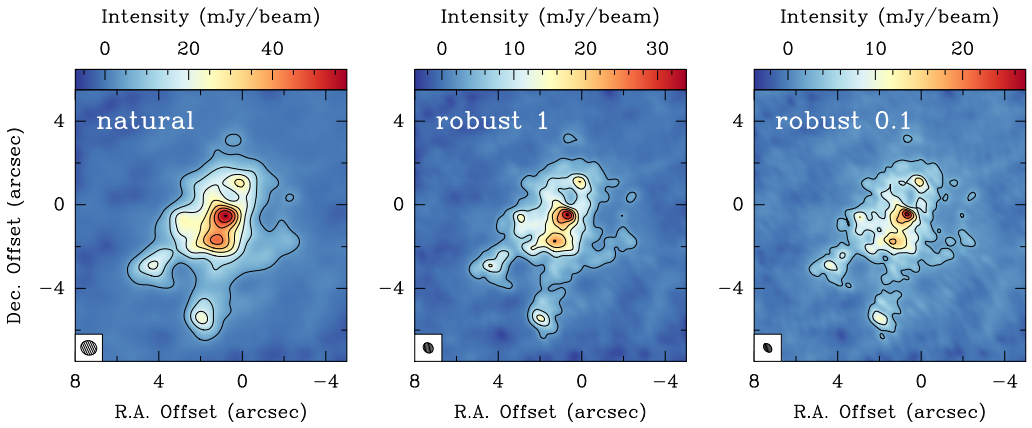

Figure 2.7: NOEMA 1.37 mm continuum maps toward IRAS 21078, imaged with natural (*left*), robust 1 (*middle*), and robust 0.1/uniform (*right*) weightings. Contours start at 5σ and increase in steps of 10σ (see Table 2.1).

uniform across the entire sky. A parabolic dish has its maximum sensitivity towards the direction it is pointing (i.e., the phase center) with sensitivity dropping towards the edges such that the angular distance at which only half of the power is observed FWHM $\approx \lambda/D$. The primary beam of NOEMA at 1.3 mm (220 GHz) with dishes of 15 m in diameter is ~22″.

It is possible to change the angular resolution and sensitivity of the image by introducing a weighting function that modifies the sampling function and therefore changes the size of the synthesized beam. The two extreme weighting functions are natural and uniform weightings. Natural weighting gives more weight to the shorter baselines where the *uv*-plane is better sampled and therefore degrades the resolution but increases the signal-to-noise (S/N) ratio. Uniform weighting does the opposite and upweighs the longer baselines providing higher resolution but noisier images. The so-called Robust (Briggs) weighting parameter is in between the other two with larger robust values leaning towards natural weighting and lower values closer to uniform weighting. While high angular resolutions are needed for the intended science in this work, we do make use of this weighting parameter to help the detection of certain species for sources that are weak in line emission. In Fig. 2.7, we show an example of how changing the weighting parameter affects an observation. The lower the robust parameter, the higher the angular resolution with more substructure recovered, but the noise in the image is higher. The corresponding beam sizes, peak intensities, and root mean square (RMS) noise values are listed in Table 2.1.

Table 2.1: Comparison between beam sizes and sensitivities of visibilities imaged with different weightings for IRAS 21078, shown in Fig. 2.7.

Weighting	Synthesized Beam (″×″, PA)	Peak Intensity (mJy beam^{-1})	RMS Noise (mJy beam^{-1})	S/N Ratio
Natural	0.78″×0.69″, PA=70	57.7	0.8	75
Robust 1	0.53″×0.44″, PA=41	34.0	0.5	65
Robust 0.1	0.48″×0.33″, PA=41	27.2	0.5	59

CHAPTER 3

IRAM Large Program: CORE

Partially based on Ahmadi et al. (2018) and Beuther et al. (2018)

The CORE survey is an IRAM large program (PI: Beuther), making use of the NOEMA interferometer (see Fig. 3.1), at 1.37 mm in both line and continuum emission to study the early phase of star formation for a sample of 20 highly luminous ($L > 10^4\ L_\odot$) star-forming regions at high angular resolution (~0.4″). Observations with the IRAM 30-m telescope are included to complement the interferometric data, allowing us to understand the role of the environment by studying high-mass star formation at scales larger than those covered by the interferometer. The sample selection criteria and initial results from the observed level of fragmentation in the full sample are presented in Beuther et al. (2018), and details of the IRAM 30-m observations and the merging of single-dish with the interferometric observations can be found in Mottram et al. (submitted). In this chapter, we will describe the sample selection method and present our spectral line setup for the interferometric observations (which was presented in Ahmadi et al. 2018) and give an overview of the data reduction scheme used to produce the final data products.

3.1 Sample selection

A few different criteria were used for the selection of the sources. To ensure that the targets are high-mass star forming regions, we made a luminosity cut at $L > 10^4\ L_\odot$, which corresponds to a star with a mass of at least 8 $M_\odot$. To be able to observe the sample at high resolution with good image fidelity, a distance cut at $D < 6$ kpc was enforced and only sources with declination >24° were included to ensure good *uv* coverage. To target the early phase of formation with active accretion, we imposed a colour cut based on $S_{21\mu m}/S_{8\mu m} > 2$ colours from the Red MSX survey[1] (Lumsden et al. 2013) since it is expected that the IR colour evolves from red to blue (see Fig. 2.1). The final sample size was 18 regions with two additional sources (NGC7538 IRS1 and NGC7538 S) which were observed in the past with almost the same setup to which we will refer as the CORE pilot regions (Beuther et al. 2012; Beuther et al. 2013; Feng et al. 2016). Table 3.1 lists the names and positions of the sources, with their properties. The threshold between IR-bright and -dark is defined according to Motte et al. (2007) based on cores in the Cygnus X star-forming region at a distance $D = 1.7$ kpc, such that if a core with a luminosity of 1000 $L_\odot$ has 21 μm flux ($S_{21\mu m}$) below 10 Jy it would be categorized as IR quiet. Therefore regions with

[1] http://rms.leeds.ac.uk/cgi-bin/public/RMS_DATABASE.cgi

Figure 3.1: The NOEMA interferometer (formerly Plateau de Bure Interferometer) located in the French Alps with 10 out of the 12 future antennas commissioned. Photo credits: IRAM/F. Gueth

$S_{21\mu m} < 10\,\mathrm{Jy}\left(\frac{1.7\ \mathrm{kpc}}{D}\right)^2\left(\frac{L}{1000\,L_\odot}\right)$ are classified as IR-dark. As discussed in Beuther et al. (2018) and as we will show in Chapter 6, this criterion is not the best measure for the age of these complex regions. The associated features listed in the table correspond to the presence of various masers and/or centimetre continuum emission as proxy for star formation activity. Figure 3.2 shows an overview of the larger scale environment for the CORE sample with colour corresponding to near- to mid-IR data and single-dish 850 μm continuum in contours (di Francesco et al. 2007).

3.2 NOEMA observations and data reduction

Observations in the 1.3 mm wavelength regime of the CORE project began in June 2014 and finished in January 2017, consisting of a total of more than 400 hours of observations with NOEMA. We observed in three different configurations of the interferometer: A-configuration being the most extended, D-configuration being the most compact array, and B-configuration covering baselines between the two (see Fig. 2.5 for an example of the *uv* coverage). Baselines roughly in the range of 15 – 765 m were covered, therefore the NOEMA observations are not sensitive to structures larger than ~15″ (0.1 pc) at 220 GHz. The exact baseline ranges for all tracks are listed in Table 3 of Beuther et al. (2018). On-source observations were taken in roughly 20-minute increments distributed over an observing run (i.e., a track) and interleaved with observations of various calibration sources. We observed in track-sharing mode meaning two science targets were observed in one track, with one track corresponding to a total of roughly

8 hours of observations. We paired sources with similar positions in the sky together in order to be able to use the same calibrators. With the sources being observed in three different configurations, in total at least three half tracks were observed per sources. To achieve the required sensitivity, depending on the weather conditions, in many cases more tracks were needed.

Table 3.1: Positions and properties of the CORE sample, grouped in track-sharing pairs, adapted from Beuther et al. (2018).

Source	R.A. (J2000.0)	Dec. (J2000.0)	D (kpc)	L ($10^4\,L_\odot$)	IR-bright	a.f.[a]	Ref.[b]
IRAS23151+5912	23:17:21.01	+59:28:47.49	3.3	2.4	+	w	d1, l2
IRAS23033+5951	23:05:25.00	+60:08:15.49	4.3	1.7	–	cm, w	d2, l1
AFGL2591	20:29:24.86	+40:11:19.40	3.3	20.0	+	cm, w	d3, l1
G75.78+0.34	20:21:44.03	+37:26:37.70	3.8	11.0	–	cm, m	d4, l1
S87 IRS1	19:46:20.14	+24:35:29.00	2.2	2.5	+	cm	d5, l1
S106	20:27:26.77	+37:22:47.70	1.3	3.4	+	cm, w	d6, l2
IRAS21078+5211	21:09:21.64	+52:22:37.50	1.5	1.3	–	cm, w	dl1
G100.3779-03.578	22:16:10.35	+52:21:34.70	3.5	1.5	+	w	d1, l2
G084.9505-00.691	20:55:32.47	+44:06:10.10	5.5	1.3	+	w	d2, l2
G094.6028-01.797	21:39:58.25	+50:14:20.90	4.0	2.8	+	w, m	d1, l2
Cep A HW2	22:56:17.98	+62:01:49.50	0.7	1.5	–	cm, w, m	d7, l1
NGC7538IRS9	23:14:01.68	+61:27:19.10	2.7	2.3	+	w	d7, l1
W3(H_2O)	02:27:04.60	+61:52:24.73	2.0	8.3	–	cm, w, m	d8, l2
W3IRS4	02:25:31.22	+62:06:21.00	2.0	4.5	+	cm, w	d8, l1
G108.7575-00.986	22:58:47.25	+58:45:01.60	4.3	1.4	+	w, m	d2, l3
IRAS23385+6053	23:40:54.40	+61:10:28.20	4.9	1.6	–	w	dl2
G138.2957+01.555	03:01:31.32	+60:29:13.20	2.9	1.4	+	cm, w	d2, l1
G139.9091+00.197	03:07:24.52	+58:30:48.30	3.2	1.1	+	cm, w	d2, l1
Pilot study							
NGC7538IRS1	23:13:45.36	+61:28:10.55	2.7	21.0	+	cm, w, m	d7, l1
NGC7538S	23:13:44.86	+61:26:48.10	2.7	1.5	–	w, m	d7, l1

[a)] Associated features (a.f.): cm: cm continuum; w: H_2O maser; m: CH_3OH maser

[b)] References for distances and luminosities:
d1: Choi et al. 2014, d2: Urquhart et al. 2011, d3: Rygl et al. 2012, d4: Ando et al. 2011, d5: Xu et al. 2009, d6: Xu et al. 2013, d7: Moscadelli et al. 2009, d8: Hachisuka et al. 2006, Xu et al. 2006, dl1: Molinari et al. 1996, dl2: Molinari et al. 1998, l1: RMS survey database (http://rms.leeds.ac.uk/cgi-bin/public/RMS_DATABASE.cgi) using SED fitting from Mottram et al. (2011) including Herschel fluxes and the latest distance determination, l2: RMS survey database, using SED fitting from Mottram et al. (2011) updated to the latest distance determination, l3: RMS survey database, calculated from the MSX 21 μm flux using the scaling relation derived by Mottram et al. (2011) and updated to the latest distance determination.

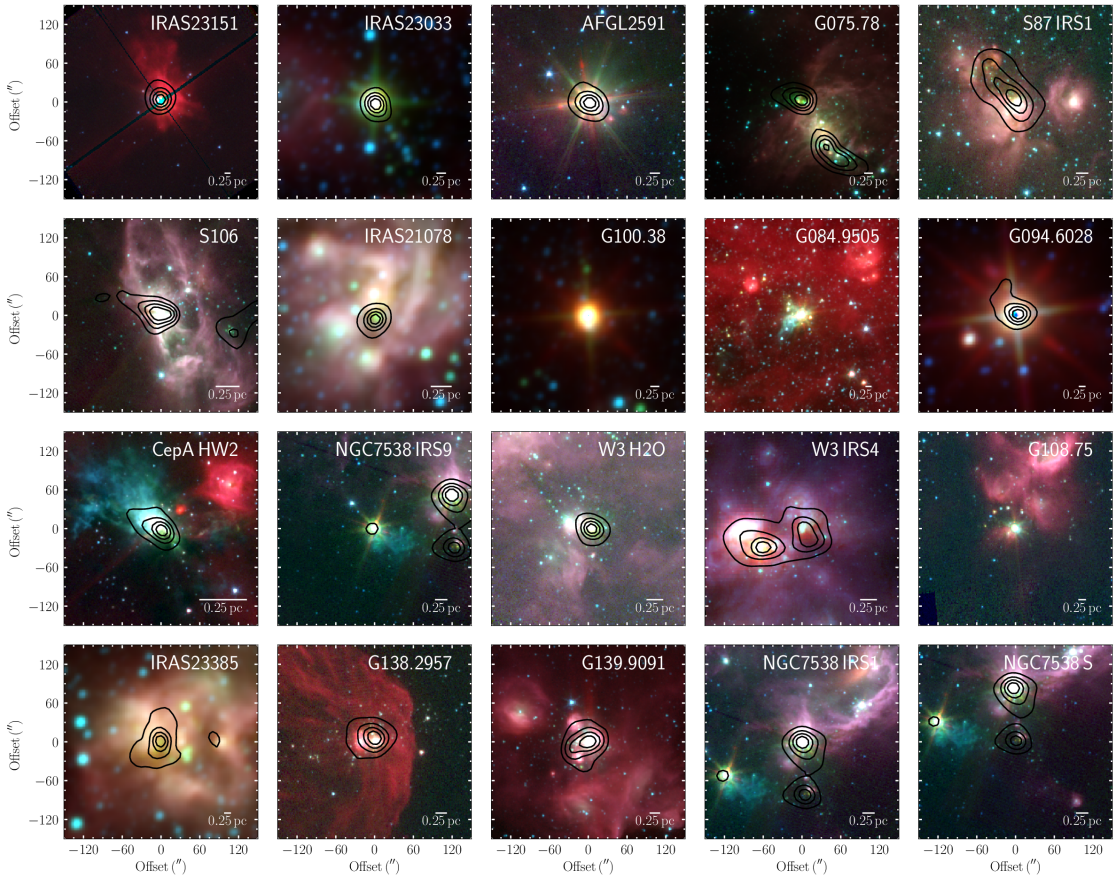

Figure 3.2: 3-color images of the CORE sample from Beuther et al. (2018) with blue, green and red from Spitzer 3.6, 4.5 and 8.0 μm for all sources except IRAS 23033, IRAS21078, G100, G094 and IRAS 23385 for which WISE 3.4, 4.6 and 12 μm data are presented. Furthermore, W3IRS4 uses Spitzer 3.6, 4.5 μm and MSX 8 μm. The contours show SCUBA 850 μm continuum data (di Francesco et al. 2007; contour levels 20, 40, 60, 80% of the peak emission) for all sources except G100, G084 and G108 where these data do not exist.

3.2.1 Spectral line setup

The full CORE sample of 20 regions has been observed with NOEMA using both a narrow- and a wide-band correlator, simultaneously. The wide-band correlator, WideX, has four units, each with 1.8 GHz bandwidth, covering two overlapping ranges in frequency in both horizontal and vertical polarizations (H and V) with a fixed spectral resolution of 1.95 MHz (~2.7 km s^{-1} at 219 GHz). The full coverage of the WideX correlator is shown in Fig. 3.3 for one of the most chemically-rich sources in the sample, W3 (H_2O), with bright lines marked. The narrow-band correlator has 8 units, each with 80 MHz bandwidth and a spectral resolution of 0.312 MHz (~0.43 km s^{-1}), placed in the 1.37 mm wavelength regime. The frequency coverage of the correlator bands are listed in Table 3.2. As explained in the previous section, observations for the CORE survey were performed while the NOEMA intereferometer was being upgraded to include more antennas. Although for some of observations later in the campaign more than six antennas were used, the narrow-band correlator could only process the signal from six antennas; therefore, in cases for which the sources were observed with more than six antennas, the correlator automatically accepts the signal from the antennas that yield the best *uv*-coverage.

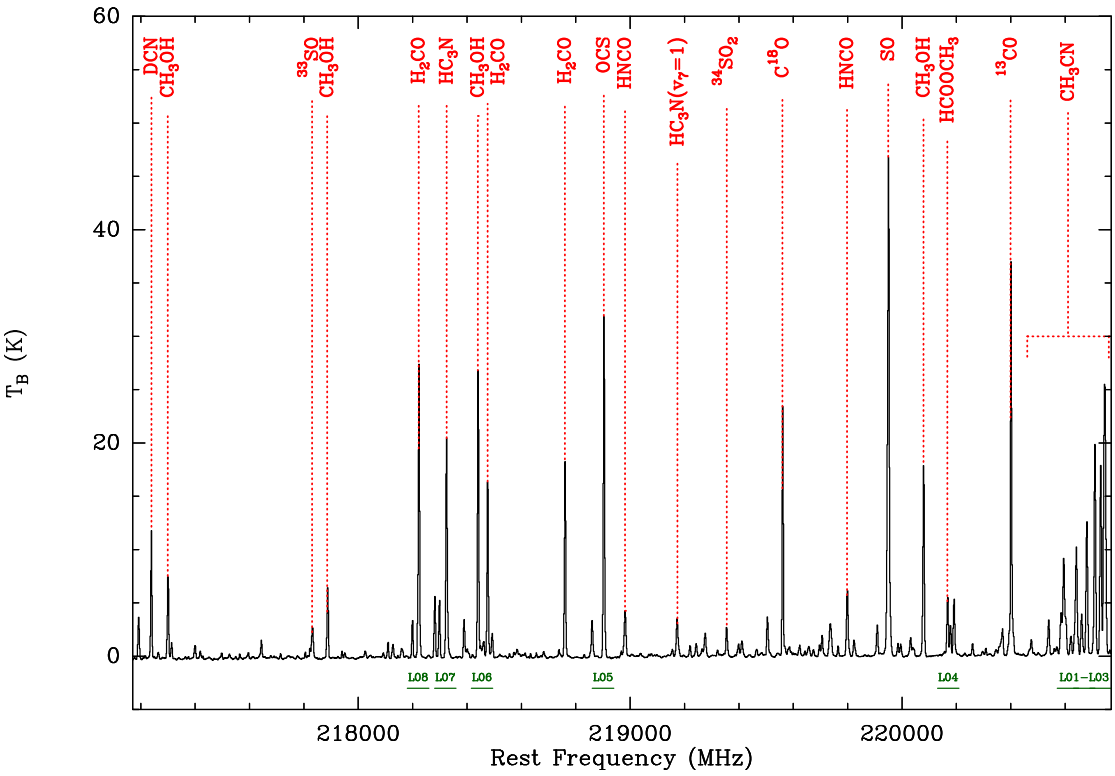

Figure 3.3: Full WideX spectrum of W3 (H_2O) averaged over a $4'' \times 4''$ region encompassing two cores, W3 (H_2O) E and W3 (H_2O) W, showing the chemical-richness of the source. The coverage of the narrow-band correlator units are shown as horizontal green lines and labeled accordingly. The units of the spectrum has been converted from Jy beam^{-1} to K by multiplying the flux by 188 K/Jy under the Rayleigh-Jeans approximation.

Table 3.2: Correlator units and frequency ranges observed with NOEMA.

Correlator	Spectral Unit	Polarization	Frequency Range (MHz)
Narrow-band	L01	H	220 690.6–220 769.7
	L02	H	220 630.6–220 709.7
	L03	H	220 570.6–220 649.7
	L04	H	220 130.6–220 209.7
	L05	H	218 860.6–218 939.7
	L06	H	218 415.6–218 494.7
	L07	H	218 280.6–218 359.7
	L08	H	218 180.6–218 259.7
WideX	L09	H	218 878.6–220 859.5
	L10	V	
	L11	H	217 078.6–219 059.4
	L12	V	

Note: H and V correspond to horizontal and vertical polarizations.

The narrow-band spectral range is shown in Fig. 3.4 for the pixel at the phase center toward W3 (H_2O), with bright lines clearly marked. Important lines covered by the narrow-band receiver are listed in Table 3.3.

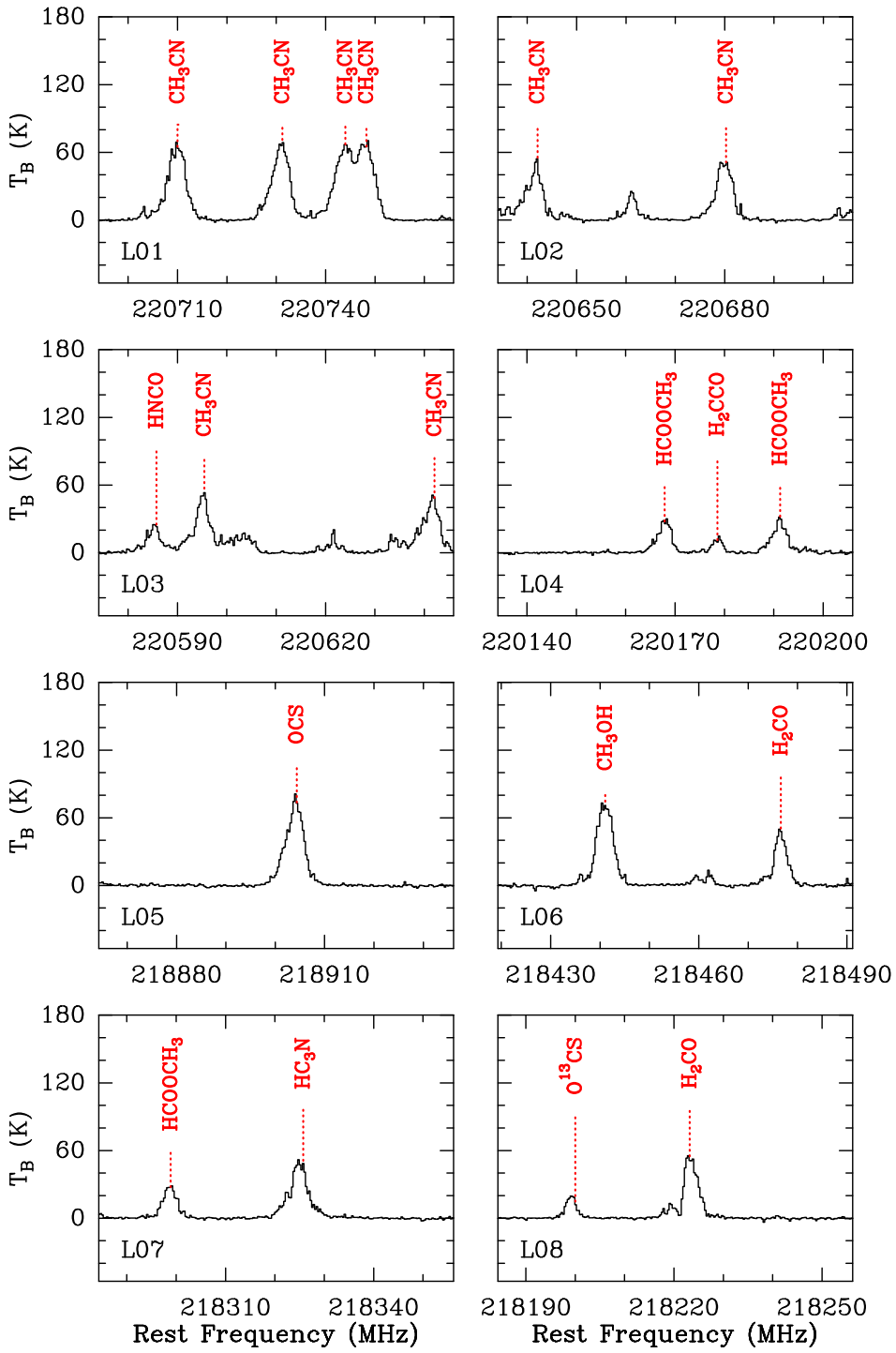

Figure 3.4: Spectra of the frequency range covered by the narrow-band correlator for the pixel at the phase center toward W3 (H_2O). The name of the correlator unit is listed in the bottom left corner of each panel, with some of the detected lines marked.

Table 3.3: Bright lines covered in the narrow-band correlator setup.

Molecule	Transition	Rest Frequency (MHz)	E_u/k (K)
$O^{13}CS$	18–17	218 199.00	99.5
H_2CO	$3_{0,3}$–$2_{0,2}$	218 222.19	21.0
$HCOOCH_3$	$17_{3,14}$–$16_{3,13}$A	218 297.89	99.7
HC_3N	24–23	218 324.72	131.0
CH_3OH	4–3	218 440.05	45.5
H_2CO	$3_{2,2}$–$2_{2,1}$	218 475.63	68.1
OCS	18–17	218 903.36	99.81
$HCOOCH_3$	$17_{4,13}$–$16_{4,12}$E	220 166.89	103.1
H_2CCO	$11_{1,11}$–$10_{1,10}$	220 177.57	76.5
$HCOOCH_3$	$17_{4,13}$–$16_{4,12}$A	220 190.29	103.2
HNCO	$10_{1,9}$–$9_{1,8}$	220 584.75	101.5
CH_3CN	12_6–11_6	220 594.42	325.9
$CH_3^{13}CN$	12_3–11_3	220 599.98	133.1
$CH_3^{13}CN$	12_2–11_2	220 621.14	97.4
$CH_3^{13}CN$	12_1–11_1	220 633.83	76.0
$CH_3^{13}CN$	12_0–11_0	220 638.07	68.8
CH_3CN	12_5–11_5	220 641.08	247.4
CH_3CN	12_4–11_4	220 679.29	183.2
CH_3CN	12_3–11_3	220 709.02	133.2
CH_3CN	12_2–11_2	220 730.26	97.4
CH_3CN	12_1–11_1	220 743.01	76.0
CH_3CN	12_0–11_0	220 747.26	68.9

Note: Rest frequencies and upper energy levels have been obtained from the CDMS (Müller et al. 2001; 2005), with the exception of those for $HCOOCH_3$ transitions which were acquired from the Jet Propulsion Laboratory (Pickett et al. 1998).

3.2.2 Calibration

Calibration of the NOEMA observations was performed with the *CLIC* program of the Grenoble Image and Line Data Analysis Software *GILDAS*[2] package developed by IRAM and Observatoire de Grenoble. As an integral part of the data reduction team, I was responsible for calibrating the data from two track-sharing pairs of sources (5 and 7, sources: G084, G094, W3 (H_2O), W3 IRS4) which was done by following the instructions in the *GILDAS* data reduction cookbook[3]. We always began the calibration process by examining the notes from the astronomer on duty and using the *First Look* task in *CLIC* to get an idea of the observing con-

[2] http://www.iram.fr/IRAMFR/GILDAS
[3] https://www.iram.fr/IRAMFR/GILDAS/doc/pdf/pdbi-cookbook.pdf

ditions, the calibrators used, antenna temperatures, tracking quality and other details of the observations. Then a standard calibration was performed using the pipeline provided by *GILDAS*. The autoflagging routine of *CLIC* was in most cases effective in flagging noisy data, but we re-calibrated the entire dataset offline to carefully asses the quality of each track.

We manually checked the observing order of science targets and calibrators for all sources to make sure that the on-source observations were always wrapped by observations of calibrators. This ensures that all on-source observations can properly be calibrated. In some cases, the science targets were observed at the end of the track in which case they were flagged manually. In most observations more than one phase calibrator was observed. We manually always selected the strongest one and flagged the others. For bandpass calibration, typically strong quasars such as 3C84, 3C273, or 3C454.3 were used. Phases noises varied depending on the weather conditions between 10° and 50°. For a few tracks, especially in the A-configuration where phases were sometimes more unstable, a clear discontinuity was found in the phases. In such cases, we manually fitted the phases by introducing a break point and specifying a certain polynomial degree to be fitted to the phases. This was done by the command *'solve phase /break 'break degree' 'break time' /polynomial 'degree'*, where the break degree is the order of the polynomial derivative that is discontinuous at the observed breaking point, the break time is the time at which the discontinuity is seen, and the degree is the polynomial degree one can fit to the phases. This was an extremely tedious task as one has to be careful not to fit polynomials of very high orders while providing good fits to the phases. It was done on a trial-and-error basis and each time the quality of the calibration output was checked and the best solutions were picked. The absolute flux calibration was done using observations of MWC349 where an absolute model flux of 1.86 Jy at 220 GHz was assumed. For a few tracks this calibrator was not available and instead LKH101 was used as the flux calibrator. The absolute final flux scale is estimated to be correct within 20% (Beuther et al. 2018).

From the calibrated dataset, we created visibility tables called 'uvt tables' in *GILDAS* lingo using the combined set of observations in the A-, B-, and D-array configurations (hereafter ABD) together in one table, ready to be imaged. The continuum was extracted by identifying line-free channels in the range 217 078.6–220 859.5 MHz covered by all four spectral units of the WideX correlator. For the lines covered in the Narrowband correlator, we resampled the visibilities to have 60 channels with the center frequency of each line corresponding to the LSR velocity of the source and a uniform velocity resolution of 0.5 km s^{-1}. Continuum subtraction for the lines was performed in the *uv*-plane, by subtracting the emission in the line-free channels in the spectral unit in which the line was observed. Due to line contamination in spectral unit L03, we used the continuum from spectral unit L02 to remove the continuum from spectral unit L03, under the assumption of there being no significant spectral slope between the two adjacent spectral windows. For the continuum subtraction of the WideX spectra, we subtracted the continuum obtained from line-free channels in all four spectral units. This procedure was done for the entire CORE sample in an automated way. Therefore to determine the line-free parts of the spectra, we used one of the most chemically-rich sources in the sample, W3 (H_2O), as a template for where lines would be expected. This proved to be an effective method.

3.2.3 Imaging

Imaging was performed with the *MAPPING* program of the *GILDAS* software package. As we were interested in achieving the highest possible angular resolution, we CLEANed the cubes using the *CLARK* algorithm (Clark 1980) with a uniform weighting (i.e. robust parameter of 0.1)[4]. The imaging procedure was done in an automated way after fine-tuning the parameters that provided the best images. The total number of iterations for the CLEAN algorithm was set to 5000 with a stopping criteria when the maximum amplitude of the absolute value of the residual image reached 0.01 Jy beam^{-1}. The quality of the resulting images and residuals were checked and we ensured the CLEAN algorithm had converged in all cases. All narrow-band spectra when imaged with the CLARK algorithm and uniform weighting had a negligibly smaller synthesized beam than the continuum images.

I was responsible for providing the final data cubes for the entire CORE sample of 20 sources for all 23 lines covered in the narrowband correlator units (see Table 3.3). In addition, I provided the team with images of the L01-L03 units of the narrowband correaltor stitched together in one data cube order to make modelling the CH_3CN lines easier. All data cubes were imaged with different robust weightings (1, 3, and 5) as well as natural weighting. This aids the detection of certain species for sources that are weak in line emission.

[4]This corresponds to the *CASA* robust weighting with a robustness parameter of –2.

CHAPTER 4

The Curious Case of W3 (H_2O)

Based on Ahmadi et al. (2018)
published in *Astronomy & Astrophysics* (618, A46)

4.1 Motivation

In this chapter, we study the fragmentation and kinematic properties of one particular YSO in the CORE survey: W3 (H_2O). We use this source as a test-bed for what will be expanded in Chapter 6 to the analysis of the kinematics of all disk candidates in our survey. The structure of this chapter is as follows. Section 4.3 presents our spectral line setup within the CORE survey with the details of our observations and data reduction for W3 (H_2O). The observational results are described in Section 4.4. The kinematics, temperature, and stability analysis of W3 (H_2O) are presented in Section 4.5. The main findings are summarized in Section 4.6.

4.2 Introduction

W3 (H_2O), also known as the "Turner-Welch object", resides in the W3 high-mass star-forming region and was initially identified through observations of the dense-gas tracer HCN at 88.6 GHz (Turner & Welch 1984). It is located ~0.05 pc (5″) east of the well-known ultra-compact H II region (UC H II) W3 (OH). The name, W3 (H_2O), stems from the existence of water masers in the vicinity of the source (Dreher & Welch 1981), allowing for an accurate distance measurement of 2.0 kpc for this region (Hachisuka et al. 2006; cf. Xu et al. 2006). The relative proper motions of these masers are further explained by an outflow model oriented in the east-west direction (Hachisuka et al. 2006). A continuum source elongated in the east-west direction and spanning the same extent as the water maser outflow has been observed in sub-arcsecond VLA observations in the radio regime with a spectral index of –0.6, providing evidence for synchrotron emission (Reid et al. 1995; Wilner et al. 1999). This source of synchrotron emission has been characterized by a jet-like model due to its morphology, and the point symmetry of its wiggly bent structure about the center hints at the possibility of jet precession. Moreover, Shchekinov & Sobolev (2004) attribute this radio emission to a circumstellar jet or wind ionized by the embedded (proto)star at this position. Additional radio continuum sources have been detected in the vicinity of the synchrotron jet, the closest of which is to the west of the elongated

Table 4.1: Observations of W3 (H_2O) and W3 (OH).

Observation Date	Configuration	Time On-source (h)	Bandpass Calibrator
2014-Oct-31	D	3.9	3C454.3
2015-Mar-18	A	2.6	3C84
2015-Apr-3	B	0.9	3C84
2015-Apr-6	B	1.3	3C84
2016-Mar-11	A	2.2	3C84

Note: The phase and flux calibrators were 0059+581 and MWC349, respectively, for all observations.

structure and has a spectral index of 0.9 (Wilner et al. 1999; Chen et al. 2006), consistent with a circumstellar wind being ionized by another embedded protostellar source. In fact, the high angular resolution (~0.7″) observations of Wyrowski et al. (1999) in the 1.36 mm band allowed for the detection of three continuum peaks in thermal dust emission, one of which peaks on the position of the water maser outflow and synchrotron jet, and another on the position of the radio continuum source with positive spectral index, confirming the existence of a second source at this position. The detection of two bipolar molecular (CO) outflows further supports the protobinary scenario, suggesting that W3 (H_2O) may be harbouring (at least) two rotating structures (Zapata et al. 2011). The two cores within W3 (H_2O) have individual luminosities on the order of 2×10^4 $L_\odot$, suggesting two 15 $M_\odot$ stars of spectral type B0[1].

4.3 Observations

The spectral setup and data reduction details are as described in Chapter 3. The following is a brief description of observations of W3 (H_2O).

4.3.1 NOEMA observations

Observations of W3 (H_2O) at 1.37 mm were made between October 2014 and March 2016 in the A-, B-, and D-array configurations of NOEMA in track-sharing mode with W3 IRS4. The compact D-array observations were made with six antennas while seven antennas were used for the more extended A- and B-array observations. The phase center for the observations of W3 (H_2O) is α(J2000) = $02^h\ 27^m\ 03\overset{s}{.}87$, δ(J2000) = 61° 52′ 24.5″. A summary of the observations can be found in Table 4.1. As we are interested in achieving the highest possible angular resolution, we CLEANed the cubes using the CLARK algorithm (Clark 1980) with a uniform weighting (robust parameter of 0.1) yielding a synthesized beam size of $0.43'' \times 0.32''$, PA=86°, and an RMS noise of 3.2 mJy beam^{-1} for the continuum emission using the combined set of observations in the A-, B-, and D-array configurations (hereafter ABD). We also imaged the data from the A- and B-array configurations together (hereafter AB), as well as the A-array only, for

[1]The luminosity and spectral type calculations are described in detail in Section 4.5.3.

which the synthesized beam sizes and RMS noise values are summarized in Table 4.2.

Table 4.2: Details of CLEANed images.

	Continuum	
Configuration	Synthesized Beam (″×″, PA)	RMS Noise (mJy beam^{-1})
ABD	0.43″ × 0.32″, PA=86°	3.2
AB	0.41″ × 0.30″, PA=86°	2.6
A	0.39″ × 0.28″, PA=88°	2.5
	Line (Narrow-band)	
Configuration	Synthesized Beam (″×″, PA)	Average RMS Noise (mJy beam^{-1} km s^{-1})
ABD	0.42″ × 0.31″, PA=87°	11.2
AB	0.38″ × 0.28″, PA=87°	8.6
A	0.36″ × 0.26″, PA=88°	8.0

4.3.2 30-m observations

Observations of W3 (H_2O) with the IRAM 30-m telescope were obtained on 13 March 2015 centered on the same position as the phase center of the interferometric observations. We used the Eight MIxer Receiver (EMIR) covering the range 213 – 236 GHz, reaching a spectral resolution of 0.3 km s^{-1}. In this work, we have merged the NOEMA observations of ^{13}CO with the single-dish observations using the *MAPPING* software and CLEANed the merged cube with the Steer-Dewdney-Ito (SDI) method (Steer et al. 1984) in order to recover more of the extended features to study molecular outflows. Further details of the IRAM 30-m observations and data reduction as well as the merging process can be found in Mottram et al. (in prep). The resulting merged image has an angular resolution of 1.14″ × 0.92″, PA=49°, and an RMS noise of 8.4 mJy beam^{-1} km s^{-1}. We also make use of our single-dish ^{13}CO data which have been reduced and converted to brightness temperatures for a detailed outflow analysis presented in Section 4.4.3.

4.4 Observational results

In the following, we present our detailed analysis for W3 (H_2O), and when applicable, we also showcase our observational results for W3 (OH). Our analysis mainly uses the continuum and CH_3CN spectral line emission. Maps of the other lines are shown in Appendix A.1.

4.4.1 Continuum emission

Figure 4.1 shows the 1.37 mm (219 GHz) continuum emission map of W3 (H_2O) and W3 (OH) in the ABD configuration. At this wavelength, the continuum emission in our field of view is

dominated in W3 (OH) by free-free emission, while the emission in W3 (H_2O) is due to dust (Wyrowski et al. 1999). In the following, we focus on the fragmentation and kinematics of the younger region, W3 (H_2O).

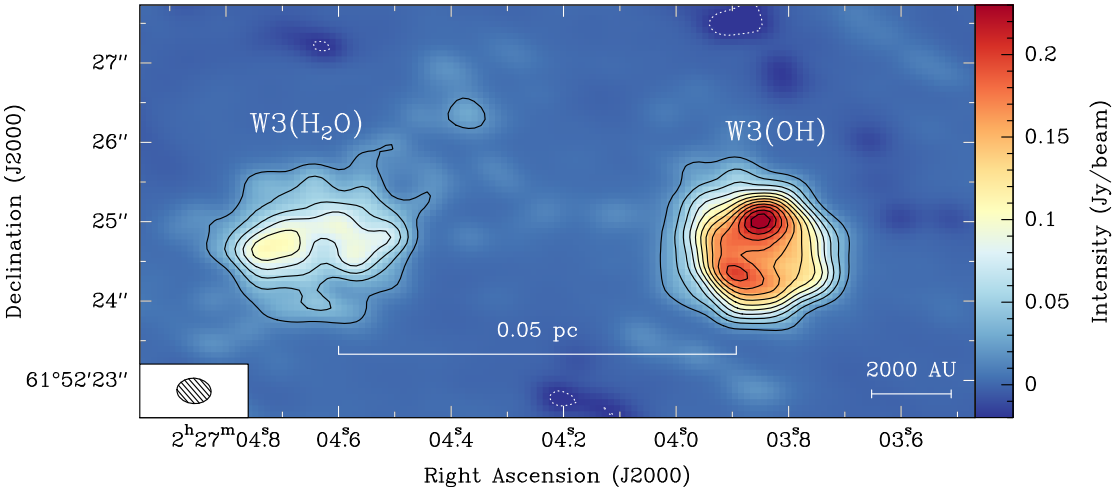

Figure 4.1: NOEMA 1.37 mm (219 GHz) continuum image toward W3 (H_2O) and W3 (OH) in the ABD configuration. The solid contours start at 6σ and increase in steps of 6σ (1σ = 3.2 mJy beam^{-1}). The dotted contours show the same negative levels. A scale-bar and the synthesized beam (0.43″ × 0.32″, PA=86°) are shown in the bottom.

Figure 4.2 shows a comparison of the continuum emission maps of W3 (H_2O) obtained by imaging the ABD, AB, and A-array only observations. The integrated flux within the 6σ contours is 1220 mJy, 656 mJy, and 364 mJy for ABD, AB, and A-array images, respectively. The fragmentation of W3 (H_2O) into two cores, separated by ~2300 au, is best seen in the AB image at 700 au scales. The two cores are labeled W3 (H_2O) E and W3 (H_2O) W, and their peak continuum positions are depicted by stars in Fig. 4.2, marking the positions of embedded (proto)stars. The peak position of W3 (H_2O) E is α(J2000) = 02^h 27^m 04^s.73, δ(J2000) = 61° 52′ 24.66″, and that of W3 (H_2O) W is α(J2000) = 02^h 27^m 04^s.57, δ(J2000) = 61° 52′ 24.59″. The approximate separation boundary between W3 (H_2O) E and W is marked with a vertical dashed line. The integrated flux within 6σ contours and the separation boundary are 377 mJy and 279 mJy for W3 (H_2O) E and W3 (H_2O) W, respectively. Furthermore, there exists an additional emission peak to the northwest of W3 (H_2O) at an offset of −1.6″, 1.6″(α(J2000) = 02^h 27^m 04^s.37, δ(J2000) = 61° 52′ 26.35″) which is best seen in the ABD image as it has the best sensitivity. This is most likely a site for the formation of lower mass stars.

Radiative transfer models by Chen et al. (2006) for W3 (H_2O) in the 1.4 mm wavelength regime show that the averaged dust optical depth is less than 0.09, therefore, we assume the thermal dust emission to be optically thin in our observations. The positions of continuum peaks A and C from Wyrowski et al. (1999) coincide well with the continuum peaks W3 (H_2O) E and W3 (H_2O) W in our observations to within a synthesized beam (see Fig. 4.2). Wyrowski et al. had attributed the third peak in their observations in between the other two core to an interplay of high column density and low temperatures in the central region and concluded W3 (H_2O) to be harbouring two cores at the positions of continuum peaks A and C. Our doubly-peaked continuum image in AB, with a better spatial resolution than that of Wyrowski et al. (1999) by a

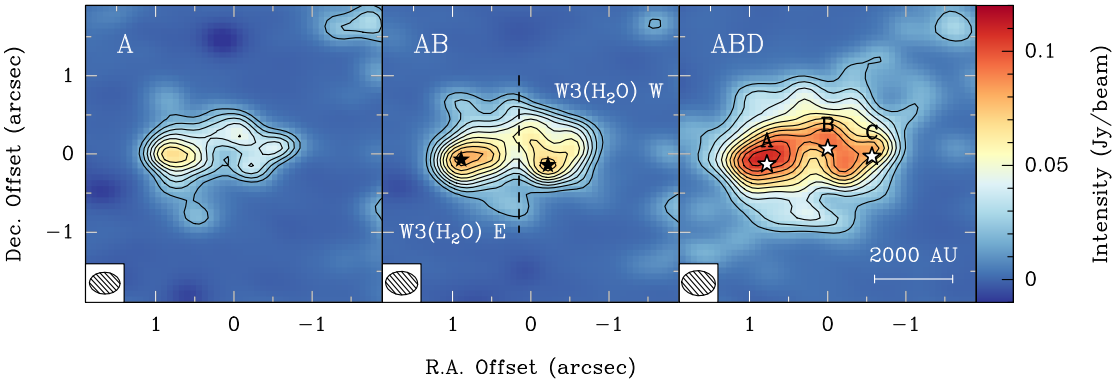

Figure 4.2: 1.37 mm continuum image toward W3 (H_2O) observed with the A (*left*), AB (*center*), and ABD (*right*) configurations of NOEMA. The solid contours start at 6σ and increase in steps of 3σ (see Table 4.2). Synthesized beams are shown in the bottom left corners of each panel, along with a scale bar in the bottom right of the right-hand panel. The black stars in the middle panel correspond to the positions of the continuum peaks, marking the locations of the two individual cores, W3 (H_2O) W and W3 (H_2O) E, with the dashed line as the approximate separation boundary. The white stars in the right panel correspond to the positions of the continuum peaks A, B, and C from Wyrowski et al. (1999). The offset zero position is the phase center of the observations: α(J2000) = $02^h\ 27^m\ 03\overset{s}{.}87$, δ(J2000) = 61° 52′ 24.5″.

factor of 3.3, supports this interpretation. Furthermore, peak B coincides well with the northeast extension of W3 (H_2O) W in our observations, best seen in the middle panel of Fig. 4.2.

4.4.2 Line emission

W3 (H_2O) is one of the most chemically-rich sources in our sample (see Fig. 3.3) with detections of sulfur-bearing species such as ^{33}SO and $^{34}SO_2$, complex species such as $HCOOCH_3$, and vibrationally excited lines of HC_3N, among many others. Fig. 4.3 shows integrated intensity (zeroth moment) and intensity-weighted peak velocity (first moment) maps of CH_3CN ($12_3 - 11_3$) for W3 (H_2O) and W3 (OH). The zeroth moment map confirms the fragmentation of W3 (H_2O) into two cores. The moment maps of most lines covered by the narrowband receiver (see Table 3.3 and Fig. 3.4) are presented in Appendix A.1. All moment maps have been created inside regions where the S/N ratio is greater than 5σ. The integrated intensity maps of most tracers for W3 (H_2O) also show two peaks coincident with the locations of W3 (H_2O) E and W3 (H_2O) W. While the continuum emission is stronger for W3 (H_2O) E, some dense gas tracers (e.g. CH_3CN, HC_3N) show stronger line emission towards W3 (H_2O) W.

The bottom panels in Fig. 4.3 show the intensity-weighted peak velocity (first moment) map of the region in CH_3CN ($12_3 - 11_3$). We chose to do our kinematic analyses on this transition as it is the strongest unblended line in the methyl cyanide (CH_3CN) *K*-ladder. There is a clear velocity gradient in the east-west direction across W3 (H_2O), and in the NW-SE direction across W3 (OH). The systemic velocities of both clumps are determined by averaging the spectra of CH_3CN ($12_3 - 11_3$) over a $4'' \times 4''$ area centered on each source and fitting a Gaussian line to the resulting averaged spectrum. In this way, W3 (H_2O) and W3 (OH) have average velocities of –49.1 and –45.0 km s^{-1}, respectively.

The velocity gradient across W3 (H_2O) is detected in most of the high spectral resolution

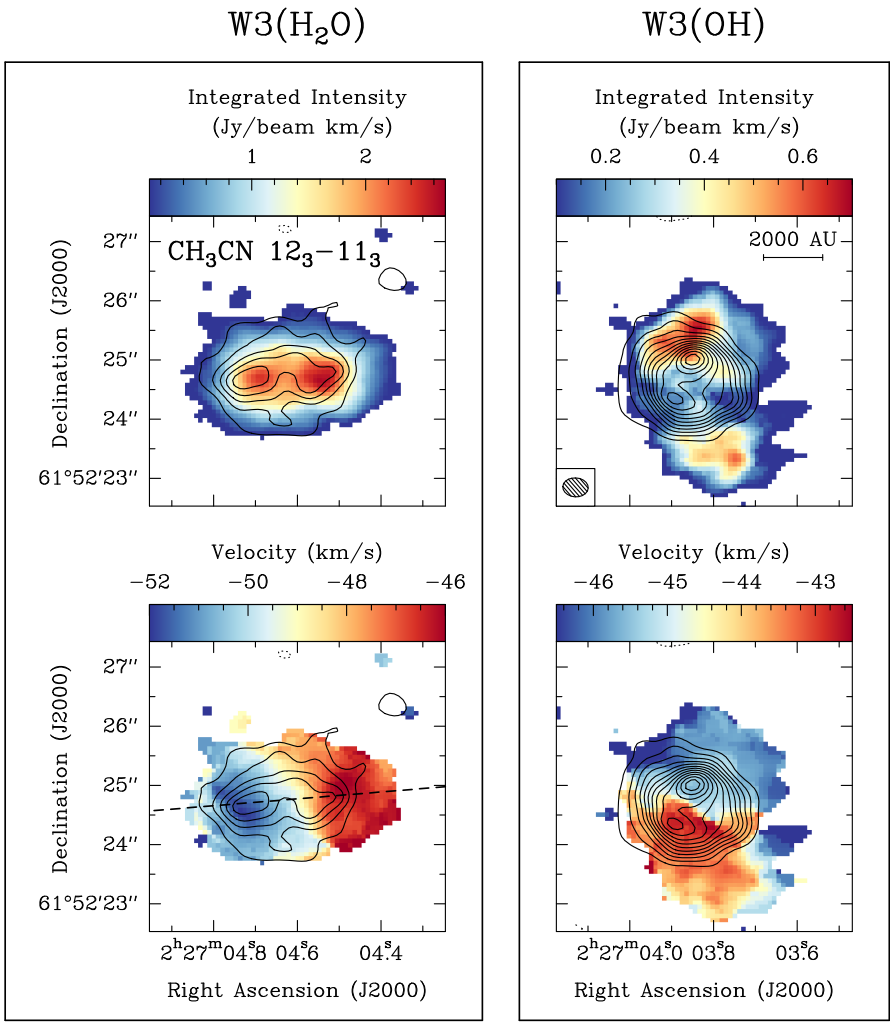

Figure 4.3: *Top*: Integrated intensity (zeroth moment) map of CH_3CN (12_3 – 11_3) for W3 (H_2O) (*left*) and W3 (OH) (*right*) in the ABD configuration. *Bottom:* Intensity-weighted peak velocity (first moment) map of CH_3CN (12_3 – 11_3) for W3 (H_2O) (*left*) and W3 (OH) (*right*) in the ABD configuration. The dashed line corresponds to the cut made for the PV plot of W3 (H_2O) presented in Fig. 4.6. The solid contours correspond to the 1.37 mm continuum, starting at 6σ and increasing in steps of 6σ (1σ = 3.2 mJy beam^{-1}). The dotted contours correspond to the same negative levels. A scale-bar and the synthesized beam (0.43″×0.32″, PA=86°) are shown in the top right panel.

lines in our survey (see Fig. A.2 in Appendix A.1) and spans ~6000 au in size, corresponding to an amplitude of 170 km s^{-1} pc^{-1}. The velocity gradient resolved in W3 (OH) has an amplitude of ~100 km s^{-1} pc^{-1} and is roughly perpendicular to the motion of the ionized gas in the east-west direction as traced by the H92α line in observations of Keto et al. (1995), and is perpendicular to the direction of the "champagne flow" observed to the northeast at radio frequencies (Keto et al. 1995; Wilner et al. 1999). Hence, in W3 (OH) we seem to be witnessing the large-scale motion of the remnant molecular gas. The interpretation of line emission for W3 (OH) is complex, because most of the continuum emission at 1.37 mm is due to free-free emission which affects the appearance of molecular lines. In practice, free-free emission at 1.3 mm reduces the molecular line emission which is reflected by the reduced integrated line emission towards the

peaks of W3 (OH). As this is beyond the scope of this work, we refrain from further analysis of W3 (OH).

4.4.3 Outflow structure

In Fig. 4.4 we show integrated intensity (zeroth moment) maps of outflow-tracing molecules (^{12}CO and ^{13}CO) for the redshifted and blueshifted gas. The minimum intensity below which a pixel is not considered in the creation of the moment maps is based on 5σ RMS noise level in emission-free channels. The single-dish CO (2–1) map (see top left panel of Fig. 4.4) shows the existence of a bipolar outflow in the overall vicinity of W3 (H_2O) but also encompassing W3 (OH), in approximately northeast-southwest direction. The ^{13}CO (2–1) single-dish map (see top right panel of Fig. 4.4) shows less extended emission than the ^{12}CO as the ^{13}C isotopologue is a factor of ~76 less abundant (Henkel et al. 1982), and the map highlights the general northeast-southwest direction of the outflow even better.

The integrated intensity map of ^{12}CO from SMA interferometric data of Zapata et al. (2011) allows for the detection of two bipolar outflows (see bottom left panel of Fig. 4.4). The outflow emanating from W3 (H_2O) E has its blueshifted side to the southwest and its redshifted lobe to the northeast, while, the second outflow emanating from W3 (H_2O) W has its blueshifted side extending to the northeast with its redshifted side to the southwest (Zapata et al. 2011). The difference between the position angles of the two outflows (in the plane of the sky) is 25°. Furthermore, the resulting zeroth moment map of ^{13}CO emission from our combined NOEMA and 30-m single-dish observations, presented in the bottom right panel of Fig. 4.4, confirms the findings of Zapata et al. (2011) with regards to the directions and origin of the redshifted outflow lobe from W3 (H_2O) W and the origins of the blueshifted outflow lobe from W3 (H_2O) E. However, we miss much of the emission that is detected in the ^{12}CO SMA interferometric data, mainly due to the lower abundance of the ^{13}C isotopologue, and thus its lower sensitivity to the outflowing gas. The same coloured arrows obtained from Zapata et al. are redrawn in a zoom panel inside the bottom-right panel of this figure, highlighting that the two outflows are in fact emanating from different positions.

In Fig. 4.5, we show how the cm emission aligns with the mm continuum emission. The directions of bipolar molecular outflows emanating from the cores are shown by red and blue arrows, and the positions of water masers shown by yellow triangles. The elongated radio source centered on W3 (H_2O) E has a spectral index of –0.6 and is a source of synchrotron emission, best described by a jet-like model due to its morphology (Reid et al. 1995; Wilner et al. 1999). The radio source centered on W3 (H_2O) W, however, has a rising spectral index, possibly due to a circumstellar wind being ionized by an embedded (proto)stellar source at this position. Furthermore, the discrepancy between the direction of the synchrotron jet-like object and the molecular outflow could be due to the existence of multiple objects in this core, unresolved by our observations. Interestingly, it has been shown that synchrotron radiation can be produced not only via jets, but also through the acceleration of relativistic electrons in the interaction of disk material with a stellar wind (Shchekinov & Sobolev 2004), providing an alternative explanation for the maser and cm emission.

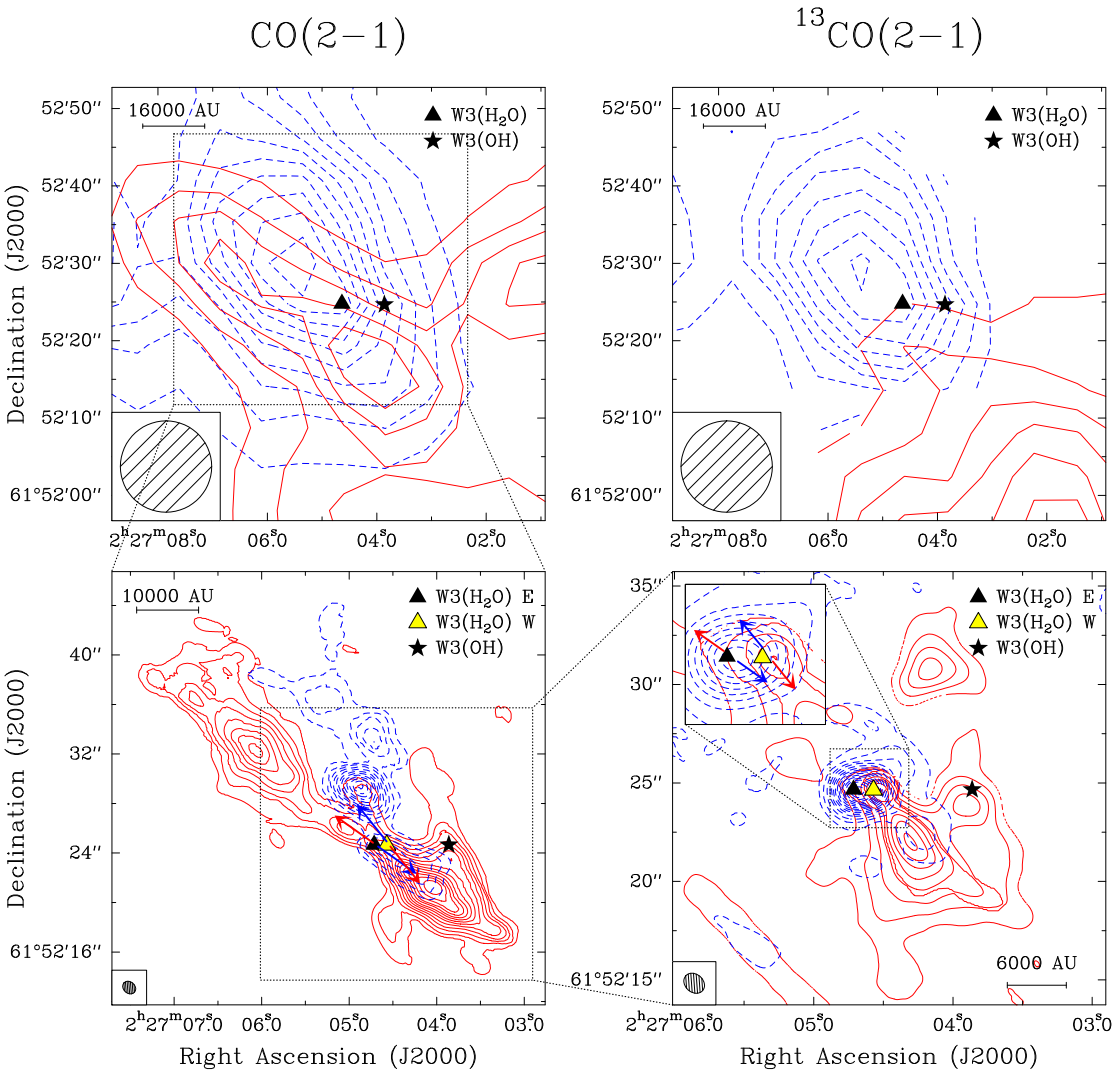

Figure 4.4: *Top left:* Intensity map of CO (2–1) emission from IRAM 30-m integrated over the velocity range of −40 to −20 km s^{-1} for the redshifted and −80 to −55 km s^{-1} for the blueshifted gas. Contours start at 5σ and increase in steps of 5σ (1σ = 1.9 K km s^{-1}). *Top right:* Intensity map of ^{13}CO (2–1) emission from IRAM 30-m integrated over the velocity range of −40 to −20 km s^{-1} for the redshifted and −80 to −55 km s^{-1} for the blueshifted gas. Contours start at 3σ and increase in steps of 2σ (1σ = 0.42 K km s^{-1}). *Bottom left:* Intensity map of CO (2–1) emission obtained by Zapata et al. (2011) with the SMA integrated over the velocity range of −45 to −25 for the redshifted and −75 to −55 for the blueshifted gas. Contours start at 5σ and increase in steps of 5σ (1σ = 1.1 mJy beam^{-1} km s^{-1}). The blue and red arrows highlight the positions and directions of the CO outflows emanating from each source. *Bottom right:* Intensity map of ^{13}CO (2–1) emission from IRAM 30-m merged with NOEMA observations integrated over the velocity range of −41 to −30 for the redshifted and −70 to −53 for the blueshifted gas. Contours start at 3σ and increase in steps of 3σ (1σ = 0.03 mJy beam^{-1} km s^{-1} for redshifted and 0.17 mJy beam^{-1} km s^{-1} for blueshifted sides). The zoom panel in the top left corner highlights the launching positions of each outflow, with the red and blue arrows showing the directions of the two bipolar outflows from Zapata et al. (2011). The RMS noise used in drawing the contours of the integrated intensity maps have been determined by first creating the maps without any constraints on the minimum emission level (threshold of 0) and calculating the noise in an emission-free part of the resulting map.

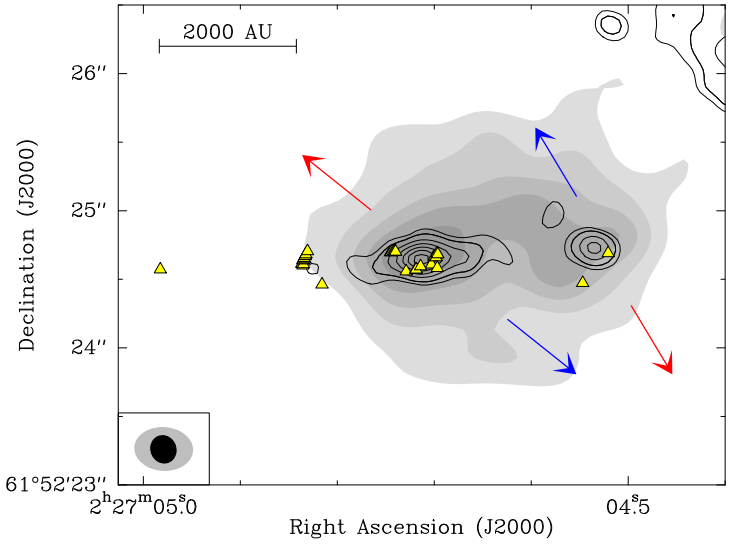

Figure 4.5: NOEMA 1.37 mm (219 GHz) continuum image toward W3 (H_2O) in grey with levels starting at 6σ and increasing in steps of 6σ. The black contours correspond to the cm emission from Wilner et al. (1999). The positions of H_2O masers obtained from Hachisuka et al. (2006) are plotted as yellow triangles. The blue and red arrows show the directions of bipolar molecular outflows from Zapata et al. (2011) (see Fig. 4.4). The synthesized beam size of the cm emission ($0.21'' \times 0.19''$, PA=68°) is shown in black in the bottom left corner. The synthesized beam size of our mm continuum image is shown in grey in the bottom left corner.

4.5 Analysis and discussion

4.5.1 Dense gas kinematics

The kinematics of W3 (H_2O) can be further analyzed by looking at position–velocity (PV) diagrams for various transitions of dense gas and potentially disk-tracing molecules such as CH_3CN and $HCOOCH_3$ (e.g. Beuther et al. 2005). In the following, we divide our focus between the large-scale kinematics of the entire W3 (H_2O) region where we put forward arguments for the observed velocity gradients in CH_3CN and $HCOOCH_3$ being due to rotation instead of infall (Section 4.5.1), and the small-scale kinematics of the two separate cores within W3 (H_2O) (Section 4.5.1). Although the alignment of the elongated radio emission with the water masers can be described by an outflow model oriented in the east-west direction, the detection of two molecular outflows emanating from the positions of the two continuum peaks, roughly perpendicular to the observed velocity gradient in CH_3CN at large scale and perpendicular to the observed velocity gradients on smaller scales (see Section 4.5.1), make it unlikely that the motions in CH_3CN would be due to expansion or outflow. Furthermore, CH_3CN and $HCOOCH_3$ line profiles do not show the broad components typically seen in emission from expanding gas, and such species are nevertheless too complex to exist in an ionized jet. We therefore conclude that the observed velocity gradient is most likely to be due to rotation, which we will assume for the remainder of this chapter.

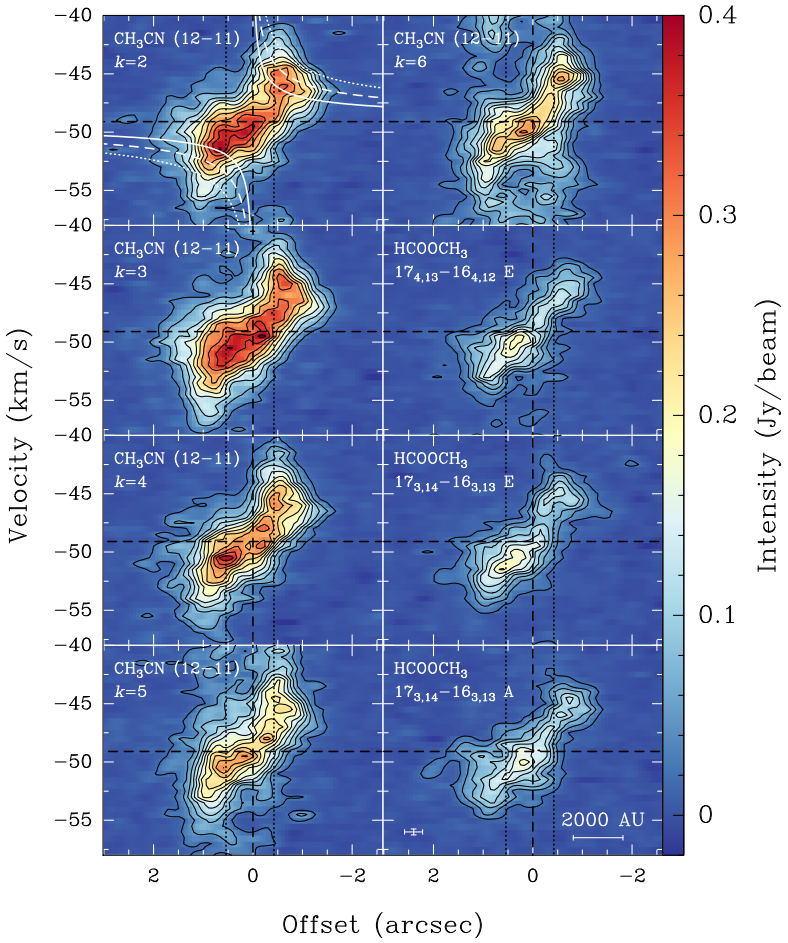

Figure 4.6: Position–velocity plots of W3 (H_2O) for a cut in the direction of rotation as depicted by a dashed line in the bottom left panel of Fig. 4.3 for various species and transitions in the ABD configuration. The vertical dashed lines correspond to the center of the cut. The vertical dotted lines correspond to the positions of continuum peaks corresponding to W3 (H_2O) E and W3 (H_2O) W. The horizontal dashed lines correspond to the LSR velocity of W3 (H_2O). The black contours start at 4σ and increase in steps of 6σ. The white solid, dashed, and dotted lines in the top left panel correspond to the region within which emission is expected if the gas is in a disk in Keplerian rotation about a 10, 25, 50 $M_\odot$ star, respectively. The white curves are not fits to the rotation curve, but are drawn to guide the eye. A scale-bar and a cross that corresponds to the spatial and spectral resolutions are shown in the bottom right panel.

Large-scale

The PV plots of CH_3CN and $HCOOCH_3$ for W3 (H_2O) are shown in Fig. 4.6 for a cut in the direction of the velocity gradient going through the continuum peaks (dashed line in bottom left panel of Fig. 4.3) obtained from the NOEMA observations. White curves in the top left panel correspond to gas in Keplerian rotation with $V_{\rm rot} \propto R^{-1/2}$, about a 10, 25, and 50 $M_\odot$ central object. These white curves are not fits to the PV diagram, but are merely drawn to guide the eye. It is clear that the gas is not in Keplerian rotation; however, higher velocity gas is observed closer to the center of W3 (H_2O) which can be a signpost for differential rotation.

Ohashi et al. (1997a) created models for comparison to their interferometric data of the low-mass protostar L1527, using a thin disk with 2000 au extent configured edge-on and present

PV diagrams for cases with various degrees of infall and rotation. In the case of infall-only motions, their PV plots are axisymmetric with two peaks offset symmetrically in the velocity axis. With the addition of rotation, the peaks become blueshifted and redshifted away from the central positions such that in the case of a pure Keplerian rotation and in the absence of infall one would recover the classical butterfly-shaped rotation curve. Comparing our PV plots to the Ohashi et al. (1997a) scenarios, much of the emission that one would expect in the cases including infall motions would have to appear in the top-left and bottom-right quadrants of our plots, while we observe minimal contributions there. Therefore, we do not detect infall motions in our interferometric data, probably because the infalling envelope is too diffuse and filtered out. Furthermore, models by Tobin et al. (2012) for spherical rotating collapse and filamentary rotating collapse showed similar results to that of Ohashi et al. (1997a), confirming that the absence of infall results in the lack of emission in those quadrants and not the projection or source morphology. Moreover, the PV plots of $HCOOCH_3$, which is a less abundant species than CH_3CN, are more representative of rigid-body-like rotation.

Chen et al. (2006) generated a binary model with radiative transfer post-processing of methyl cyanide for each source within W3 (H_2O), showing that the high-velocity deviations from solid body rotation in their PV plots could be a result of two spatially unresolved cores (on similar scales to our observations) with a small radial velocity difference. The detection of a smooth velocity gradient in all tracers across W3 (H_2O) E and W suggests that the observed angular velocity difference cannot be solely due to binary motion of the cores, but that there also exists a large-scale toroidal structure encompassing and rotating about the two resolved cores. Such circumbinary toroidal structures have indeed been observed previously at lower angular resolutions in other sources (e.g. Beltrán et al. 2005; Beuther et al. 2007b).

Small-scale

Although we see a smooth velocity gradient in CH_3CN across the entire W3 (H_2O) structure, the existence of (at least) two cores within it as presented by our continuum results, and two collimated outflows requires further analysis. Imaging the data in the most extended configuration and therefore reaching our highest resolution, we can filter out the large-scale envelope to analyse the kinematics of gas around each of the cores. Figure 4.7 shows the first moment map of CH_3CN ($12_3 - 11_3$) for the cores to the east and west using the A-array observations exclusively. The maps have been scaled and masked to highlight the velocity structure of each core. The mean line of sight velocity difference between the two main cores, W3 (H_2O) W and E, is a few km s^{-1}. Velocity differences of a few km s^{-1} are observed across each core, approximately perpendicular to the directions of the bipolar molecular outflows emanating from each core (Zapata et al. 2011). This indicates that the small-scale gradients across each individual core are most likely due to rotation. The two line of sight velocity gradients are on the order of ~1000 km s^{-1} pc^{-1}, depending on the choice for the extent of the gradient, much faster than the rotational motion of 170 km s^{-1} pc^{-1} for the whole of W3 (H_2O) from the ABD data. Furthermore, the directions of the velocity gradients observed for each core are slightly inclined with respect to the overall east-west motion of the gas on larger scales (Fig. 4.3), suggesting that the general rotation seen around the two cores may be inherited from the large-scale rotation. Meanwhile, the direction

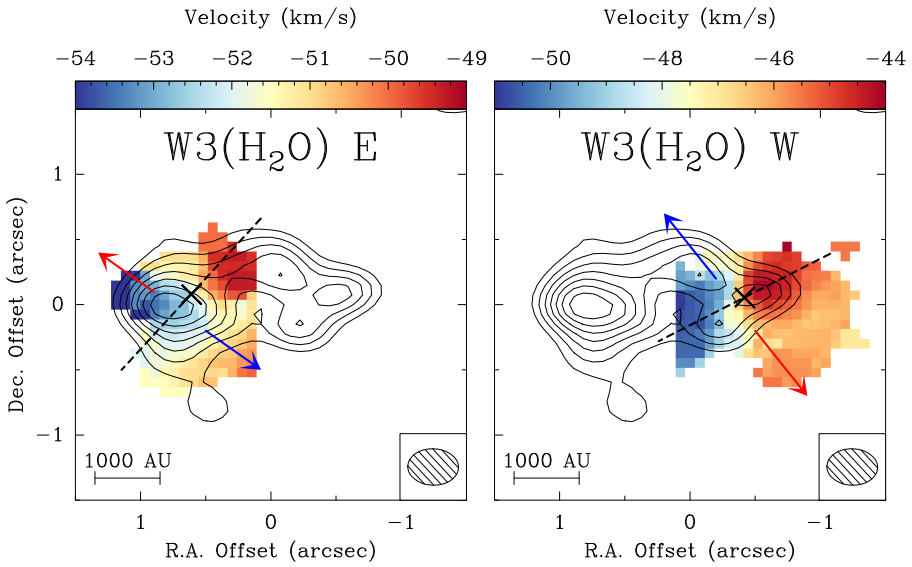

Figure 4.7: Intensity-weighted peak velocity (first moment) map of CH_3CN ($12_3 - 11_3$) using only the A-array observations and masked out to show contributions from W3 (H_2O) E (*left*) and W3 (H_2O) W (*right*). The solid contours correspond to the 1.37 mm continuum in the A-array only observations and start at 6σ and increase in steps of 3σ (1σ = 2.5 mJy beam^{-1}). The dashed lines correspond to the cuts made for the PV plots (Fig. 4.8). The blue and red arrows show the directions of bipolar molecular outflows (Fig. 4.4). A scale-bar and the synthesized beam ($0.39'' \times 0.28''$, PA=88°) are shown in the bottom. Note the different velocity ranges for the two cores.

of the blueshifted (redshifted) outflow emanating from W3 (H_2O) W is almost in the opposite direction of the blueshifted (redshifted) outflow ejected from W3 (H_2O) E. This implies that the inclination angles of the two rotating structures with respect to the plane of the sky are likely different.

Figure 4.8 shows PV diagrams for W3 (H_2O) E (left) and W3 (H_2O) W (right) corresponding to cuts in the directions of rotation as depicted by dashed lines in Fig. 4.7. Based on the PV plots, the LSR velocities of W3 (H_2O) E and W3 (H_2O) W are estimated to be –51 km s^{-1} and –47 km s^{-1}, respectively. White curves correspond to gas in Keplerian rotation about a 5, 10, and 15 $M_\odot$ centrally-dominated object. As on larger scales, these PV diagrams do not show the symmetric 4-quadrant shape expected if the velocity gradients were due to infall.

The PV plot for W3 (H_2O) W contains contributions from W3 (H_2O) E due to the angle and extent of the cut, hence there exists added emission in quadrants toward positive offset, making it difficult to infer rotational signatures pertaining to the blueshifted emission of W3 (H_2O) W. The redshifted rotational signatures seen in the quadrants toward negative offsets however show signatures of increased gas velocities closer to the center of the core. Such a trend in the PV plot implies differential rotation of material, possibly within a disk-like object.

PV plots for W3 (H_2O) E have a lower S/N ratio than W3 (H_2O) W as line emission is typically weaker for this fragment despite its 1.37 mm dust continuum peak being stronger. The linearity of the rotation curves in CH_3CN does not reveal Keplerian signatures but is more consistent with rigid-body-like rotation. In order to increase the S/N ratio, we stacked the PV plots of CH_3CN ($12_K - 11_K$) $K = 2 - 5$ and show this stacked PV plot in the bottom-

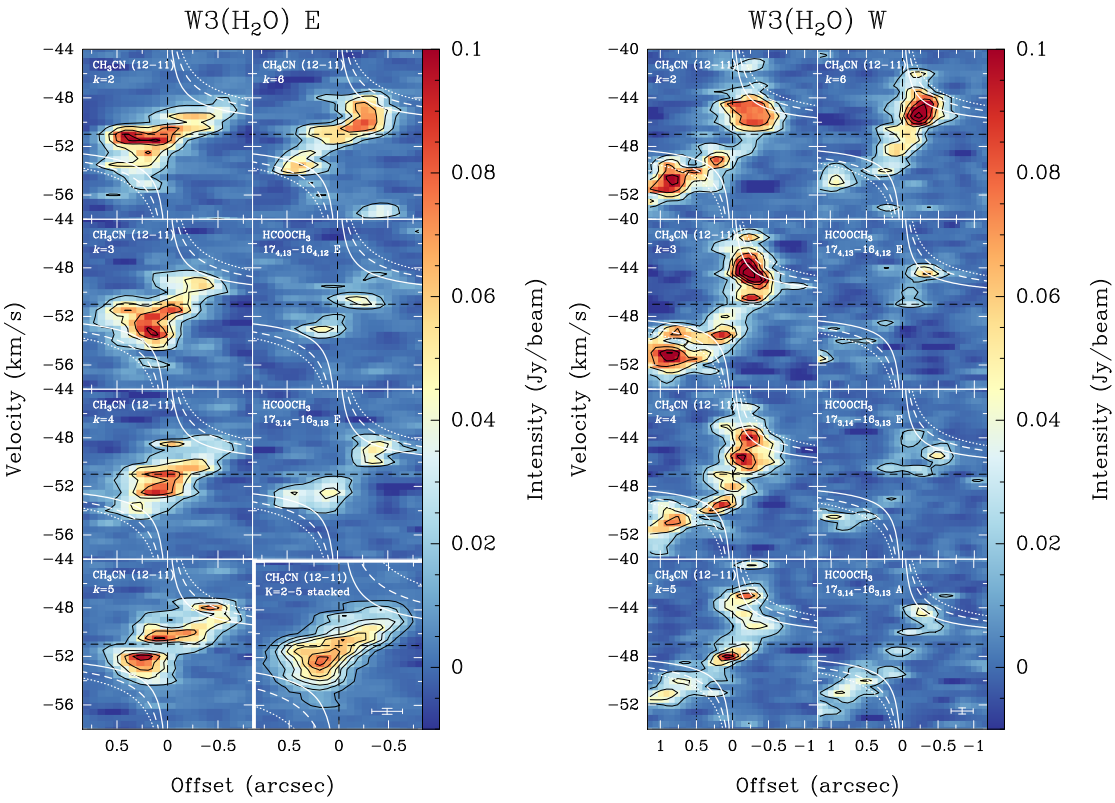

Figure 4.8: Position–velocity plots along a cut in the direction of rotation as depicted by dashed lines in Fig. 4.7 for fragment to the east (*left*) and to the west (*right*). The black contours start at 4σ and increase in steps of 6σ. The white solid, dashed, and dotted lines correspond to the region within which emission is expected if the gas is in a disk in Keplerian rotation about a 5, 10, 15 $M_\odot$ star, respectively. The crosses in the bottom right corners correspond to the spatial and spectral resolutions. Regions to the left of the dotted vertical line in the right figure contain contributions from W3 (H_2O) E.

right panel of Fig. 4.8 for W3 (H_2O) E. Stacking is a reasonable strategy as the variation in average linewidths of these transitions around this core is below our spectral resolution; therefore, assuming these lines to be probing the same surface is valid. In the stacked image, the 4σ contour reveals a high-velocity feature close to the center of the core toward positive offsets. As this feature has an extent on the order of our spatial resolution, it is unclear whether the rotation observed for W3 (H_2O) E is due to a disk-like object, an unresolved binary (or multiple) system, or a combination of the two.

4.5.2 Temperature distribution

As a symmetric top molecule, CH_3CN is an excellent thermometer of hot molecular gas (e.g. Loren & Mundy 1984; Zhang et al. 1998) since its relative populations in different K-levels are dominated by collisions. Our high spectral-resolution observations of CH_3CN covers its $J = 12 - 11$, $K = 0 - 6$ transitions and some of their isotopologues which have upper energy levels in the range 70–325 K with 0.5 km s^{-1} spectral resolution (see Table 3.3).

We made use of the eXtended *CASA* Line Analysis Software Suite (*XCLASS* Möller et al. 2017) to model the observed spectra under the assumption of LTE which is typically valid

for CH_3CN in such high-density environments (see Section 2.3 for the details of the modelling technique). In Fig. 4.9, we present our results of pixel-by-pixel *XCLASS* modelling of $CH_3CN\,(12_K - 11_K)\,K = 4-6$, including $CH_3{}^{13}CN\,(12_K - 11_K)\,K = 0-3$, in AB configuration which produces rotational temperature, column density, peak velocity, and linewidth maps for CH_3CN. The column density map is doubly peaked, similar to the continuum emission, although the column density peaks are slightly offset to the northwest by a synthesized beam. This offset is consistent with the offset found between the continuum peaks and the integrated intensity maps of $CH_3CN\,(12_3 - 11_3)$ (see Fig. 4.3) and most high-density tracers (see Fig. A.1 in Appendix A.1). The median CH_3CN column density is 1.4×10^{15} cm^{-2}. The velocity gradient derived in this way is consistent with the large-scale east-west velocity gradient observed in the first moment map of CH_3CN, confirming that our modelling strategy captures this accurately, regardless of its origin. The linewidths are also larger by a few km s^{-1} for W3 (H_2O) W, also seen in the second moment maps. The median rotational temperature of W3 (H_2O) is ~165 K and the temperature structure does not follow any particular pattern within either core. Two high-temperature features can be seen which may be associated with regions carved out by the molecular outflows allowing a deeper look into the cores, or regions that may have been additionally heated by the outflow. Nevertheless, the compactness of these features, which are on the same order as the size of our synthesized beam, along with decreased S/N ratio at the edges of the map prevent us from making firm conclusions in this regard.

4.5.3 Mass estimates

The combined bolometric luminosity of W3 (H_2O) and W3 (OH), determined from fitting the SED from the near-IR to sub-mm, is $8.3 \times 10^4\,L_\odot$ (Mottram et al. 2011). The contribution from OH can be estimated by first calculating the corresponding flux of ionizing photons (see, e.g. Appendix B.2 of Sánchez-Monge 2011, for more details) using:

$$\left(\frac{Q_0}{\text{photons s}^{-1}}\right) = 8.852 \times 10^{40} \left(\frac{F_\nu}{\text{Jy}}\right)\left(\frac{\nu}{\text{GHz}}\right)^{0.1}\left(\frac{T_\text{e}}{\text{K}}\right)^{0.35}\left(\frac{d}{\text{pc}}\right)^2, \tag{4.1}$$

where F_ν is the flux density of the free-free radio continuum emission at frequency ν, T_e is the electron temperature and d is the distance. The observed integrated radio flux at 15 GHz for W3 (OH) is 2.53 Jy (Kurtz et al. 1994), and assuming a typical electron temperature of 10^4 K, this results in a value of Q_0 = 1.2×10^{48} photons s^{-1}. Interpolating from Table 1 of Davies et al. (2011) and the relationships between spectral type and photospheric temperature from Martins et al. (2005) and Boehm-Vitense (1981) for O and B stars respectively, this ionizing photon flux approximately corresponds to an O8.5 main-sequence star, with $M \approx 20\,M_\odot$ and $L \approx 4.4 \times 10^4\,L_\odot$. This leaves a total bolometric luminosity of $3.9 \times 10^4\,L_\odot$ which we assume to be evenly distributed between the two cores within W3 (H_2O), $1.95 \times 10^4\,L_\odot$ each, which using the same tables would correspond to two 15 $M_\odot$ stars of spectral type B0.

The above estimates are based on Davies et al. (2011) for zero-age main sequence (ZAMS) stars. High-mass protostars growing by accretion resemble ZAMS stars in terms of their luminosities and temperatures when core nuclear burning dominates other sources of luminosity such as accretion and envelope burning. When this occurs depends primarily on when the pro-

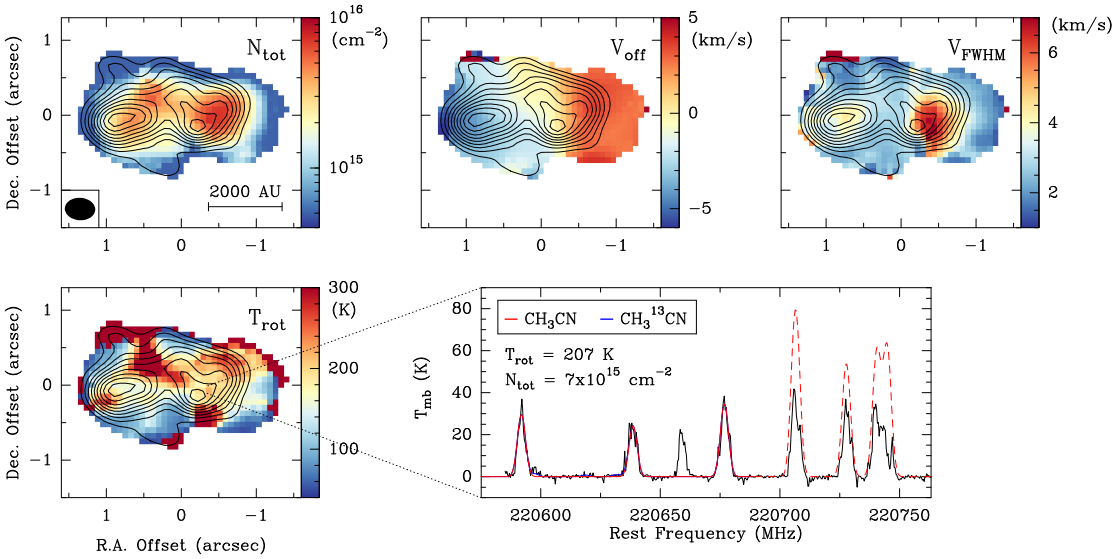

Figure 4.9: Column density (*top left*), velocity offset (*top middle*), full width at half maximum linewidth (*top right*), and rotational temperature (*bottom left*) maps obtained by fitting $CH_3CN\,(12_K - 11_K)\,K = 4 - 6$ and $CH_3{}^{13}CN\,(12_K - 11_K)\,K = 0 - 3$ lines simultaneously with *XCLASS*. The black contours correspond to the continuum image in the AB configuration, start at 6σ and increase in steps of 3σ (see Table 4.2). *Bottom right:* observed spectrum of a given pixel drawn in black and overlaid with the resulting fit for $CH_3CN\,(12_K - 11_K)\,K = 4 - 6$ in red and the marginally detected $CH_3{}^{13}CN\,(12_K - 11_K)\,K = 0 - 3$ in blue. The dashed red line corresponds to the predicted fit for the CH_3CN lines that were not used in the fitting process (see explanation in Sect. 2.3). The bright line detected between $K = 4$ and 5 components is identified as C_2H_5CN. The corresponding fit parameters are provided in the panel. Regions outside of the most extended combination of 6σ contours of integrated intensity of CH_3CN lines are masked out.

tostar gains sufficient mass but also on the accretion rate. Stellar structure calculations suggest this occurs at 5 to 10 $M_\odot$ for accretion rates of 10^{-5} to 10^{-4} $M_\odot$ yr^{-1}, respectively (Norberg & Maeder 2000; Behrend & Maeder 2001; Keto & Wood 2006). The mass estimates further assume that all the emitted energy has been produced within the (proto)stars, ignoring contributions from episodic accretion to the luminosity. Therefore, the 15 $M_\odot$ estimates can be taken as upper limits, in agreement with calculations of Chen et al. (2006) who find a minimum binary mass of 22 $M_\odot$ for the protostars within W3 (H_2O). Furthermore, assuming the gas to be in gravito-centrifugal rotation around the two individual cores, our PV plots (see Fig. 4.8) suggest the range of $5 - 15$ $M_\odot$ to be a reasonable estimate for the protostellar masses.

As dust is typically optically thin in the 1.3 mm wavelength regime and proven to be for this region in particular (Chen et al. 2006), we use the prescription by Hildebrand (1983) to convert the flux density, F_ν, of the continuum observations to a mass. In the form presented by Schuller et al. (2009),

$$M = \frac{d^2\, F_\nu\, R}{B_\nu(T_D)\,\kappa_\nu}, \tag{4.2}$$

where R is the gas-to-dust mass ratio, $B_\nu(T_D)$ is the Planck function at a dust temperature of T_D, and κ_ν is the dust absorption coefficient. We adopt a gas-to-dust mass ratio of $R = 150$ (Draine 2011) and a value of $\kappa_\nu = 0.9$ cm^2 g^{-1} for the dust absorption coefficient from Ossenkopf &

Henning (1994), corresponding to thin ice mantles after 10^5 years of coagulation at a density of 10^6 cm^{-3}.

High-mass cores such as the ones we are studying typically have densities high enough to thermalize the methyl cyanide lines. To check this, using the spontaneous decay rate of CH_3CN ($12_4 - 11_4$) obtained from the LAMDA database[2], 7.65×10^{-4} s^{-1}, and the collision rate of 2.05×10^{-10} cm^3 s^{-1} with H_2 at 140 K (Green 1986), we calculate the simplified 2-level critical density of this line to be $n_{\rm crit} \approx 3.7 \times 10^6$ cm^{-3}. The effective density, once the radiation field is taken into account, is typically an order of magnitude lower (Evans 1999; Shirley 2015). Following Schuller et al. (2009), the H_2 column density is calculated via

$$N_{\rm H_2} = \frac{S_\nu R}{B_\nu(T_D)\,\theta_B\,\kappa_\nu\,\mu\,m_{\rm H}}, \tag{4.3}$$

where S_ν is the peak intensity, θ_B is the beam solid angle, μ is the mean molecular weight assumed to be equal to 2.8, and $m_{\rm H}$ is the mass of the hydrogen atom. At a temperature of 140 K and using our continuum intensity of a given position near the center, we can estimate the H_2 column density to be 4.5×10^{24} cm^{-2}. This can be converted to a volume density of $n_{\rm H_2} > 7 \times 10^7$ cm^{-3}, assuming the extent of the third dimension to be at maximum the plane-of-sky size of the clump (~4000 au). Therefore, since the density of molecular hydrogen is much higher than the critical density of the lines, the LTE assumption is valid and the rotational temperature map of CH_3CN obtained from our modelling can be assumed to be tracing the gas kinetic temperature.

Using Eq. 4.2, our continuum map with its unit converted to Jy pixel^{-1} and the temperature map obtained from *XCLASS*, assuming dust and gas temperatures are coupled, we obtain a pixel-by-pixel mass density map shown in Fig. 4.10. Summing over the pixels in our mass density map in the ABD observations, the total mass for W3 (H_2O) is calculated to be ~26.8 $M_\odot$, with 15.4 $M_\odot$ contributed from the core to the east, and 11.4 $M_\odot$ from the core to the west. Similarly, using the AB observations, we obtain a total mass of ~11.4 $M_\odot$ for W3 (H_2O), with a core mass of 6.7 $M_\odot$ and 4.7 $M_\odot$ from the cores to the east and west, respectively. The effect of spatial filtering of the interferometer is clear in these mass estimates as the exclusion of the D-array data removes more than half of the mass.

Comparing our NOEMA observations to SCUBA-2 850 μm single-dish observations, about 25% of the flux is filtered out by the interferometer in our ABD observations (assuming a $\nu^{-3.5}$ frequency-relation, Beuther et al. 2018), implying that our core mass estimates of 15.4 and 11.4 $M_\odot$ are lower limits, but nevertheless reasonable. Masses estimated in this manner have contributions from the cores and the disk-like structures and not from any embedded (proto)stars.

4.5.4 Toomre stability

For a differentially rotating disk, the shear force and gas pressure can provide added stability against gravitational collapse. This idea was originally introduced by Safronov (1960) and further quantified by Toomre (1964) for a disk of stars, and has since been used in various applications ranging from planet formation to galaxy dynamics. We investigate the stability of the rotating structures in W3 (H_2O), assuming that they are disks in gravito-centrifugal equilibrium, against

[2] http://home.strw.leidenuniv.nl/~moldata/

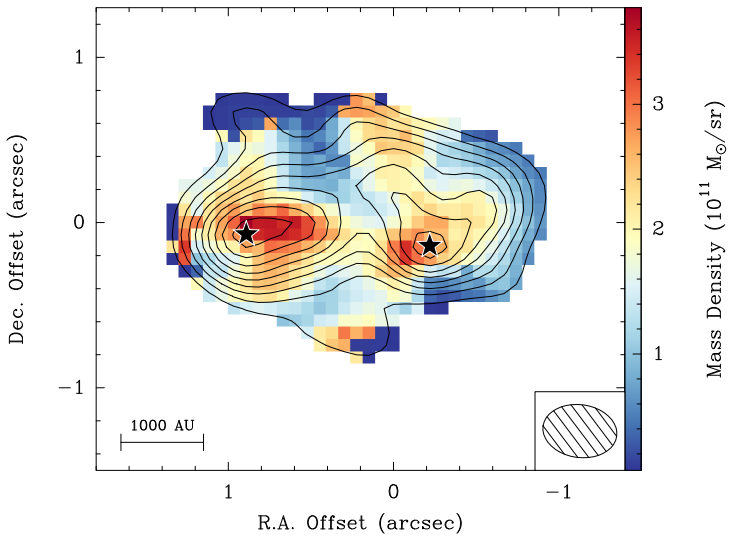

Figure 4.10: Mass density map obtained using the temperature and continuum maps in Eq. 4.2. The solid contours correspond to our continuum observations in the AB configuration, starting at 6σ and increasing in steps of 3σ (1σ = 2.5 mJy beam^{-1}). Each of the peak continuum positions, as depicted by stars, is expected to host at least one 10 $M_\odot$ (proto)star or more lower mass sources.

axisymmetric instabilities using the Toomre Q parameter,

$$Q = \frac{c_s\,\Omega}{\pi G\,\Sigma}, \tag{4.4}$$

where c_s is the sound speed, and Ω is the epicyclic frequency of the disk which is equivalent to its angular velocity. The surface density of the disk, Σ, is calculated by multiplying the column density (Eq. 4.3) by the mean molecular weight and mass of the hydrogen atom ($\mu m_{\rm H}$) to convert the number column density to a mass surface density. A thin disk becomes unstable against axisymmetric gravitational instabilities if $Q < 1$.

Having obtained a temperature map representative of the kinetic temperature, we are able to calculate the Toomre Q parameter pixel-by-pixel. In particular, the temperature is used in the calculation of $B_\nu(T_D)$ and the sound speed,

$$c_s = \sqrt{\frac{\gamma k_{\rm B} T}{\mu m_{\rm H}}}, \tag{4.5}$$

where γ is the adiabatic index with a value of $5/3$.

We assume two 10 $M_\odot$ (proto)stellar objects to be present, one at the position of each of the two continuum peaks (see AB image in Fig. 4.2). The angular velocity maps are created by adding up mass within concentric circles starting at the position of each core and going outwards. In this way, we incorporate the mass of the rotating structures, calculated via Eq. 4.2, and the mass of the central objects. The angular velocity of a disk in gravito-centrifugal equilibrium at a radius r is

$$\Omega(r) = \sqrt{\frac{G(M_* + M_{\rm disk}(r))}{r^3}}, \tag{4.6}$$

where the mass of the central object, M_*, is 10 $M_\odot$, and $M_{\rm disk}(r)$ is the gas mass enclosed within

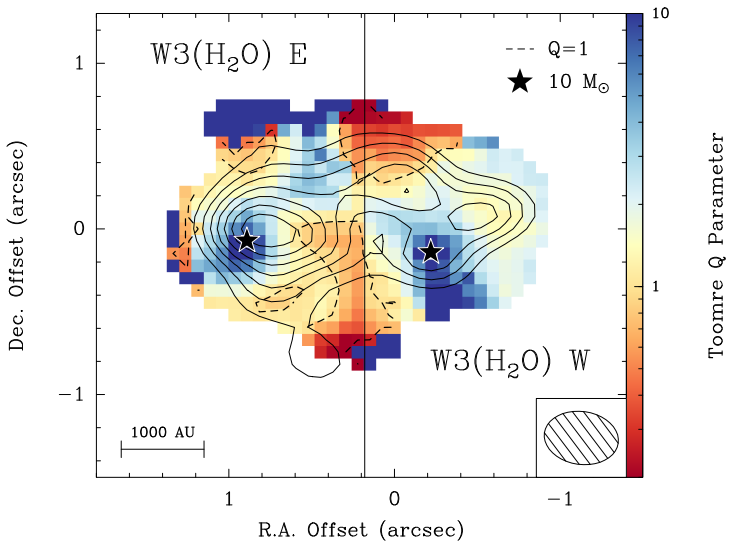

Figure 4.11: Toomre Q map obtained by assuming two disk-like structures in gravito-centrifugal rotation about the positions of peak continuum emission as depicted by the two stars, each with a mass of 10 $M_\odot$. The Toomre Q calculations and the positions of (proto)stars are based on the AB-array data (see Fig. 4.2) with regions outside of the 6σ mm continuum emission masked out. Solid contours correspond to our continuum data in the most extended (A-array) configuration, starting at 6σ and increasing in steps of 3σ (1σ = 2.5 mJy beam^{-1}). The solid vertical line corresponds to the stitching boundary. The dashed lines correspond to $Q = 1$.

r. Given the radii involved, this means that in practice, most parts of the maps are dominated by $M_{\rm disk}$ rather than M_*.

In Fig. 4.11 we present our Toomre Q map of W3 (H_2O), which is created by stitching together the Toomre Q maps of the two individual cores. The stitching boundary is shown by a solid vertical line and the positions of the two central objects corresponding to our continuum peaks in the AB image (see Fig. 4.2) are depicted by stars. While the Toomre Q calculations were performed on the AB-array data, we have drawn the continuum contours from the A-array only observations. The boundary where $Q = 1$ is shown by a dashed line.

The most significant factor stabilizing the disk against Toomre instability is the high gas temperatures and the fast differential rotation of material closest to the (proto)star, therefore, we find the highest Toomre Q values closest to the presumed locations of the (proto)stars depicted by stars in Fig. 4.11 as expected. We find low Toomre Q values at the periphery of W3 (H_2O) E and W, suggesting that both rotating structures are only marginally stable against axisymmetric instabilities. Moreover, W3 (H_2O) W shows low Toomre Q values at the positions of additional continuum peaks in the highest resolution A-array data (solid contours in Fig. 4.11), suggesting further fragmentation at these positions may be possible. As the dimensions of the observed continuum peaks are smaller than the size of our synthesized beam, the validity of this hypothesis needs to be confirmed with higher resolution observations (at 345 GHz) to be taken with NOEMA.

A Toomre stability analysis done by Chen et al. (2016) for the high-mass protostar IRAS 20126+4104 showed that the massive disk around that protostar is hot and stable to fragmentation, with Toomre $Q > 2.8$ at all radii. Hydrodynamic simulations of collapsing protostellar

cores by Klassen et al. (2016) find massive accretion disks which evolve to become asymmetrically Toomre-unstable, creating large spiral arms with an increased rate of accretion of material onto the central object. They find that the self-gravity of these spiral arm segments is lower than the tidal forces from the star, causing the spiral arms in their simulations to remain stable against collapse. However, they find that the Toomre conditions combined with the cooling of the disk (Gammie 2001) would potentially yield the formation of a binary companion. Similarly, simulations by Kuiper et al. (2011) see such spiral arms in a massive disk, and simulations by Krumholz et al. (2009) and more recently Meyer et al. (2017, 2018) see disk fragmentation on even smaller spatial scales, on the order of hundreds of au. Therefore, disk fragmentation scenarios in the high-mass regime are valid from a theoretical stand-point.

Uncertainties:

- Among the assumptions that go into this Toomre analysis is the thin-disk approximation. According to Gammie (2001), the critical value of Q for an isothermal disk of finite thickness should be 0.676 (as derived from Goldreich & Lynden-Bell 1965). Even with such a lower critical value, the rotating structures around each core would still show signs of instability in their outskirts. To get an estimate on the importance of disk thickness, following Gammie (2001), the instability condition for a disk with scale height, $H \simeq c_s/\Omega$, can be written as

$$M_{\rm disk} \gtrsim \frac{H}{r} M_*. \tag{4.7}$$

  Using our temperature and angular velocity maps, we create a map of the H/r ratio. In this way, we calculate an average value of $H/r \approx 0.3$. Assuming the mass of each (proto)star is roughly 10 $M_\odot$, we calculate that for the candidate disks to be unstable against gravitational collapse, the mass of the candidate disk must be $M_{\rm disk} \gtrsim 3\ M_\odot$. Since the mass estimates for the cores obtained from the continuum maps using Eq. 4.2 are 15 and 11 $M_\odot$, the masses are large enough to result in the rotating structures being Toomre-unstable. Therefore, the thickness of the candidate disks does not affect the general interpretation of our results.

- The angular velocity maps used in the calculation of the Toomre Q map have been created assuming a face-on geometry for the candidate disks. If the objects are inclined, we would be overestimating the surface density of the candidate disks and the line of sight angular velocities. Since these two parameters have the opposite effect on the Toomre Q value (see Eq. 4.4), our results are still reasonable.

- W3 (H_2O) E may harbour multiple (proto)stars within it (see Section 4.5.1) such that the possibility of rotational contributions from multi-body rotation would require a different prescription for the epicyclic frequency than what we have assumed.

- The estimation of 10 $M_\odot$ for the central (proto)stars have been deduced from our own and previous mass estimations (see Section 4.5.3), as well as examining the emission in the PV plots with Keplerian curves that are just 'grazing' the emission. The latter method

has the caveat that the observed PV plot is the result of the convolution with the instrumental beam and the line width. Therefore, the real emission is less extended in space and velocity than what we observe and as a result we may be overestimating the mass of the (proto)stars. Performing our Toomre calculations but with the assumption of 5 $M_\odot$ (proto)stars, we obtain median Toomre Q values of 1.3 as compared to a value of 1.7 in the 10 $M_\odot$ calculations. Therefore, lower protostellar masses would lead to the decrease in the Toomre Q value, and thus larger unstable regions, making the disk fragmentation scenario even more plausible. On the other hand, as the mass estimates using the bolometric luminosities suggest the central (proto)stellar masses to be in the 15 $M_\odot$ regime, the median Toomre Q value would be 2.0, with unstable regions still present in the outskirts. The Toomre Q maps created assuming two 5 and 15 $M_\odot$ (proto) stars at the position of the continuum peaks can be found in Appendix A.2. The change of ±5 $M_\odot$ does not strongly affect the Toomre Q maps because we add the mass of the candidate disks, estimated from the continuum emission to be 15 and 11 $M_\odot$, in rings (see Eq. 4.6) and they dominate over an addition or subtraction of 5 $M_\odot$, especially in the outermost regions. This, together with the root dependence on mass lead to uncertainties in M_* to only have a small effect on the Toomre Q results.

The uncertainties outlined here served as motivation for the work that will be presented in Chapter 5, where we will show that the effect of inclination and uncertainties in (proto)stellar mass estimates do not strongly affect the Toomre stability analysis presented here.

4.5.5 Cooling

As outlined in Sect. 1.3.3 of the Introduction, fragments formed via disk fragmentation will only survive if they can rapidly and sufficiently cool. Following the prescription of Klassen et al. (2016),

$$t_{\rm cooling} = \frac{E_z}{F_{\rm grey}}, \tag{4.8}$$

where E_z is the column internal energy integrated in the z-direction (along the axis of rotation), and $F_{\rm grey}$ is the radiative flux away from the disk adopting a greybody approximation. The internal energy of an ideal gas is calculated via

$$E_{int} = c_v \rho T, \tag{4.9}$$

where ρ is the volume density and c_v is the specific heat capacity defined as

$$c_v = \frac{N_A k_B}{M_u(\gamma - 1)}, \tag{4.10}$$

with N_A as Avogadro's number and M_u the molar mass. By replacing the volume density with the surface density, the column internal energy is then

$$E_z = \frac{N_A k_B \Sigma T}{3 M_u(\gamma - 1)}. \tag{4.11}$$

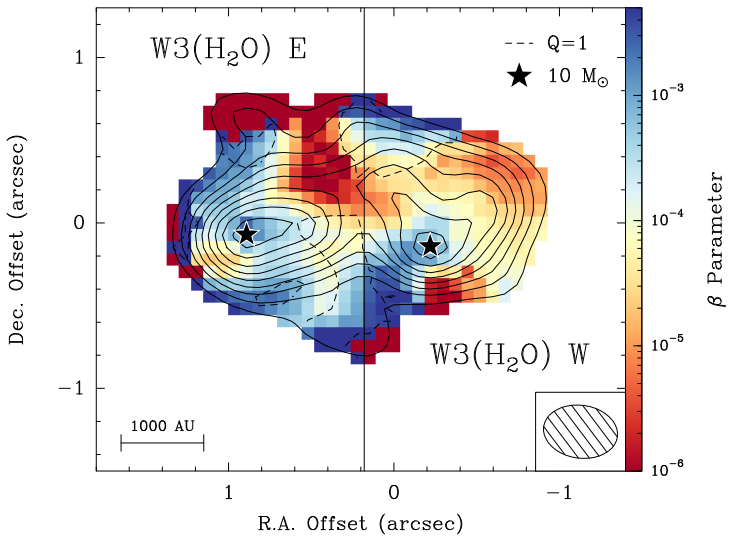

Figure 4.12: Map of β cooling parameter obtained by assuming two disk-like structures in gravito-centrifugal rotation about the positions of peak continuum emission as depicted by stars. The solid contours correspond to our continuum data in the most extended configuration, starting at 6σ and increasing in steps of 3σ (1σ = 2.5 mJy beam^{-1}). The solid vertical line corresponds to the stitching boundary. The dashed line corresponds to Toomre $Q = 1$. Regions outside of the 6σ mm continuum emission contour in the AB configuration are masked out.

Knowing the cooling time, which is on the order of months, and the rotation rate at each pixel, we construct a map for the local β cooling parameter ($\beta = \Omega\, t_{\rm cooling}$). Fig. 4.12 shows the β map for the two disks presumed in gravito-centrifugal equilibrium about the positions of peak continuum emission as depicted by stars. The median β value is 1.8×10^{-4}, and the maximum value found in the outskirts is on the order of 10^{-2}, which is much lower than the critical values of 1–5. This finding is consistent with that of Klassen et al. (2016) and Meyer et al. (2018) who also find $\beta \ll 1$ in their simulation of collapsing protostellar cores with a mass of 100 $M_\odot$ at later times. The rotating bodies within W3 (H_2O) are therefore able to cool rapidly and any local collapse induced by the gravitational instabilities in the disks will lead to fragmentation. Rapid cooling in this context means that the cooling timescale is comparable to the local dynamical timescale.

4.6 Summary and conclusions

We have performed a case-study for one of the sources in the CORE survey, the prototypical hot core W3 (H_2O). With the aim of studying the fragmentation and kinematic properties of W3 (H_2O), the following is a summary of our findings:

- At an angular resolution of ~0.35″ (~700 au at 2 kpc), W3 (H_2O) fragments into two cores, which we refer to as W3 (H_2O) E and W3 (H_2O) W, separated by ~2300 au, as seen in both line and thermal dust continuum emission.
- Based on the integrated dust continuum emission, W3 (H_2O) has a total mass of ~26.8 $M_\odot$, with 15.4 $M_\odot$ contributed from W3 (H_2O) E, and 11.4 $M_\odot$ from W3 (H_2O) W.

- On large scales, there exists a clear velocity gradient in the east-west direction across W3 (H_2O), spanning ~6000 au, attributed to a combination of circumbinary and circumstellar motions. On smaller scales, velocity gradients of a few km s^{-1} are observed across each of the cores, perpendicular to the directions of two bipolar molecular outflows, one emanating from each core, as traced by ^{12}CO and ^{13}CO. The direction of motion of the gas around the individual cores deviates little from the overall larger-scale rotation of W3 (H_2O), suggesting that these motions, which we interpret as rotation, seen around the cores may be inherited from the large-scale rotation.

- The kinematics of the rotating structure about W3 (H_2O) W shows differential rotation of material about a (proto)star as deduced from the redshifted part of its PV plot, suggesting that the rotating structure may be a disk-like object. The radio source with a rising spectrum at this position can be attributed to a circumstellar jet or wind ionized by the embedded (proto)star at this position.

- The PV plots of the rotating structure about W3 (H_2O) E is inconclusive on whether the observed rotation is due to a disk-like rotating object, an unresolved binary (or multiple) system, or a combination of both.

- We fit the emission of CH_3CN $(12_K - 11_K)$ $K = 4 - 6$ and $CH_3{}^{13}CN$ $(12_K - 11_K)$ $K = 0 - 3$ with *XCLASS* and produce temperature, column density, peak velocity, and velocity dispersion maps. On average, the entire structure is hot (~165 K) with no particular temperature structure. The column density map of CH_3CN is doubly peaked, similar to the continuum and line emission maps, with a median column density of $\sim 1.4\times10^{15}$ cm^{-2}. Close to the center of the cores, the H_2 column density is estimated to be $\sim 5\times10^{24}$ cm^{-2}.

- We investigate the axis-symmetric stability of the two rotating structures using the Toomre criterion. Our Toomre Q map shows low values in the outskirts of both rotating structures, suggesting that they are unstable to fragmentation. Some regions with low Toomre Q values in the vicinity of W3 (H_2O) W coincide with unresolved thermal dust continuum peaks (in our highest resolution observations), hinting at the possibility of further fragmentation in this core.

- The Toomre-unstable regions within W3 (H_2O) E and W3 (H_2O) W are able to cool rapidly and any local collapse induced by the gravitational instabilities will lead to further fragmentation.

In this work, we showcased our in-depth analysis for the kinematics and stability of the rotating structures within W3 (H_2O). We showed that high-mass cores can be prone to fragmentation induced by gravitational instabilities at ~1000 au scales, and core fragmentation at larger scales. Therefore, different modes of fragmentation contribute to the final stellar mass distribution of a given region. The question still remains, how universal are these findings for the high-mass star formation process? To this end, we aim to benchmark our methods using hydrodynamic simulations in the following chapter and extend our analysis to the full CORE sample in Chapter 6.

CHAPTER 5

Linking Simulations and Observations

Based on Ahmadi et al. (2019)
accepted for publication in *Astronomy & Astrophysics* (in press)

5.1 Motivation

As we obtain the observational capabilities to resolve high-mass protostellar disks, it is important to create frameworks with which to study their properties. Synthetic observations play a crucial role in this effort as they not only allow meaningful predictions to be made from theoretical models, but they also provide valid interpretations for observations (for a review, see Haworth et al. 2018). To date, only a few works have created synthetic observations from radiation-hydrodynamic simulations of high-mass star formation with the aim of providing predictions for long-baseline interferometry (Krumholz et al. 2007; Harries et al. 2017; Meyer et al. 2018). Due to the computational cost of running numerical simulations and radiative transfer models for a wide range of parameters, such studies have not been very comprehensive. Jankovic et al. (2019) were able to explore a larger parameter space by adopting a semi-analytical treatment of the density, temperature, and velocity fields with prescriptions for molecular freeze-out and thermal dissociation. Their synthetic dust continuum and molecular line observations probe different disk masses, distances, inclinations, thermal structures, dust distributions, and number and orientation of spirals and fragments.

In the following work, we report on our study of the kinematics and stability of high-mass protostellar disks in detail; we created synthetic observations for the highest resolution 3D radiation-hydrodynamic simulations that lead to the fragmentation of a massive disk. In particular, we studied the effect of inclination and spatial resolution on the derived disk and protostellar properties. To investigate the effects of spatial resolution, we assumed a close distance of 800 pc and a more typical distance of 2 kpc, and created synthetic observations in the millimetre regime for ALMA at long baselines reaching very high resolutions (~80 mas) and for NOEMA with six antennas covering much shorter baselines currently providing the highest resolutions possible (~0.3″) in the northern sky. In this way, we were able to study the properties of high-mass protostellar disks when they are resolved, and we studied unresolved disks

which resemble toroidal-like structures often seen in observations of intermediate- to high-mass stars. The motivation for this work arrived in part because we aim to study the stability of the candidate disks and characterize their properties for a large sample of disk candidates within the CORE survey, presented later in Chapter 6. It is therefore paramount to understand the observational limitations in detail and benchmark our methods. From the analysis of synthetic observations, not only do we learn about the observational limitations but we will also be able to use the observations to their full potential and gain higher confidence in the conclusions.

The chapter is organized as follows. Sect. 5.2 outlines the details of the simulations. The radiative transfer modelling scheme is summarized in Sect. 5.3. In Sect. 5.4 we describe how the synthetic observations for ALMA and NOEMA were created. In Sect. 5.5 we summarize our analysis and results, divided into subsections describing the continuum (Sect. 5.5.1) and gas kinematics (Sect. 5.5.2), temperature distribution (Sect. 5.5.3), mass estimates from dust and position–velocity (PV) diagrams (Sect. 5.5.4), and the Toomre stability of the disks (Sect. 5.5.5). A summary of the work and main conclusions can be found in Sect. 5.6.

5.2 Simulations[1]

The numerical simulation starts from a collapsing reservoir of dusty gas and follows the evolution of the system including the formation and evolution of a central massive protostar and the formation and fragmentation of its surrounding accretion disk. A theoretical investigation of this simulation (plus a convergence study) will be presented in Oliva et al. (in prep.) and covers an analysis of the disk's stability against non-axially symmetric features such as spiral arms; an analysis of its fragmentation probability; and a determination of the fragment statistics, their masses, and orbital parameters. For the purpose of the synthetic observations presented here, we summarize in the following the physics covered in the simulation, the limitations of the model, the physical initial conditions, and the numerical grid setup, highlighting the uniqueness of the extremely high spatial resolution of the disk fragmentation simulation. We refer to Kuiper et al. (2011), Meyer et al. (2017), and Meyer et al. (2018) for previous 3D studies of disk evolution around high-mass protostars that use the same numerical framework.

For the hydrodynamic evolution, we utilize version 4.1. of the open source code *Pluto* (Mignone et al. 2007; Mignone et al. 2012). Self-gravity of the gas is included via the *Haumea* module (Kuiper et al. 2010; Kuiper et al. 2011). Stellar irradiation and disk cooling are modelled using the hybrid radiation transport module *Makemake* (Kuiper et al. 2010; Kuiper & Klessen 2013), updated to a so-called two-temperature scheme (Commerçon et al. 2011). The first application of this scheme is presented in Kuiper & Hosokawa (2018) and Bhandare et al. (2018). The evolution of the central protostar follows the tracks outlined by Hosokawa & Omukai (2009). Details on the numerical implementation and coupling to the hydrodynamics are given in Kuiper et al. (2010) and Kuiper & Yorke (2013).

The simulation focusses on the formation, evolution, and fragmentation of the circumstellar accretion disk. In order to be able to achieve the required high spatial resolution (discussed in detail below), we have to neglect other potential feedback effects from the forming protostar.

[1]Disclaimer: The numerical simulation and its radiative transfer post-processing presented in this chapter were conducted by Rolf Kuiper.

First, radiation forces are not taken into account. Because we analyse a snapshot of the simulation in which the central protostar has reached 10 $M_{\odot}$, radiation forces are indeed much lower than gravity and centrifugal forces. Second, photoionization feedback and the formation of an HII region is not taken into account. Again, these physics take place at a later evolutionary stage than considered here, namely after the contraction of the central protostar to the zero age main sequence, when it starts to emit copious radiation in the extreme UV (EUV) regime. With respect to feedback of radiation and pressure and photoionization, we refer to Kuiper & Hosokawa (2018). Third, no feedback by protostellar outflows is taken into account in this simulation unlike in our previous feedback studies (Kuiper et al. 2015; Kuiper et al. 2016). The injection of a fast outflow would reduce the numerical timestep per main iteration due to the CFL condition (Courant et al. 1967) of the explicitly solved hydrodynamics. This would make the simulation computationally too expensive, and modelling the entire disk fragmentation phase would become infeasible. From a physical point of view, the outflow itself only marginally impacts the disk physics by lowering the optical depth in the bipolar outflow cavity. The most severe limitation of the current disk fragmentation model is the negligence of large-scale magnetic fields pervading the initial collapsing mass reservoir. Although we have previously used the same numerical framework to model the collapse of magnetized high-mass star-forming regions (Kölligan & Kuiper 2018), the effect of magnetic fields are neglected here. The collapse of a magnetized mass reservoir would not only lead to the launching of fast collimated jets and wide-angle outflows, but would also impact the morphology and dynamics, especially of the innermost disk structure via additional magnetic pressure and angular momentum transport. The final impact of magnetic fields on disk fragmentation will have to be investigated in future studies.

The initial mass reservoir of the simulation is described by a spherically symmetric mass density profile $\rho(r) \propto r^{-1.5}$ and an axially symmetric rotation profile $\Omega(R) \propto R^{-0.75}$, where r and R denote the spherical and cylindrical radii, respectively. The outer radius of the reservoir is set to 0.1 pc and its total mass to 200 $\mathrm{M}_{\odot}$. The corresponding free-fall time is $t_{\mathrm{ff}} \approx 37$ kyr. The ratio of rotational energy to gravitational energy of the initial mass reservoir is set to 5%, corresponding to an angular rotation frequency normalized to a value of roughly 10^{-10} Hz at $R = 10$ au. The temperature of the gas and dust is initially set to 10 K.

The uniqueness of this simulation is based on its extremely high spatial resolution of the forming accretion disk and its fragments. The gravito-radiation-hydrodynamical evolution of the system is computed on a numerical grid in spherical coordinates. In order to achieve a high dynamic range, we refined the grid cells in the radial direction towards the inner disk rim and in the polar direction towards the disk midplane. The refinement was done such that the grid cells in the disk midplane (at $\theta = 90°$) have the same extent in the radial, the polar, and the azimuthal direction ($\Delta r = r\Delta\theta = r\Delta\phi$). The radial extent of the inner sink cell is 30 au. The outer radius of the computational domain is 0.1 pc. In the polar direction, the grid extends from the upper to the lower polar axis ($0° \leq \theta \leq 180°$). In the azimuthal direction, the grid covers the full angle range as well ($0° \leq \phi \leq 360°$). The number of grid cells in the radial, the polar, and the azimuthal directions are $268 \times 81 \times 256$, respectively. This grid configuration results in

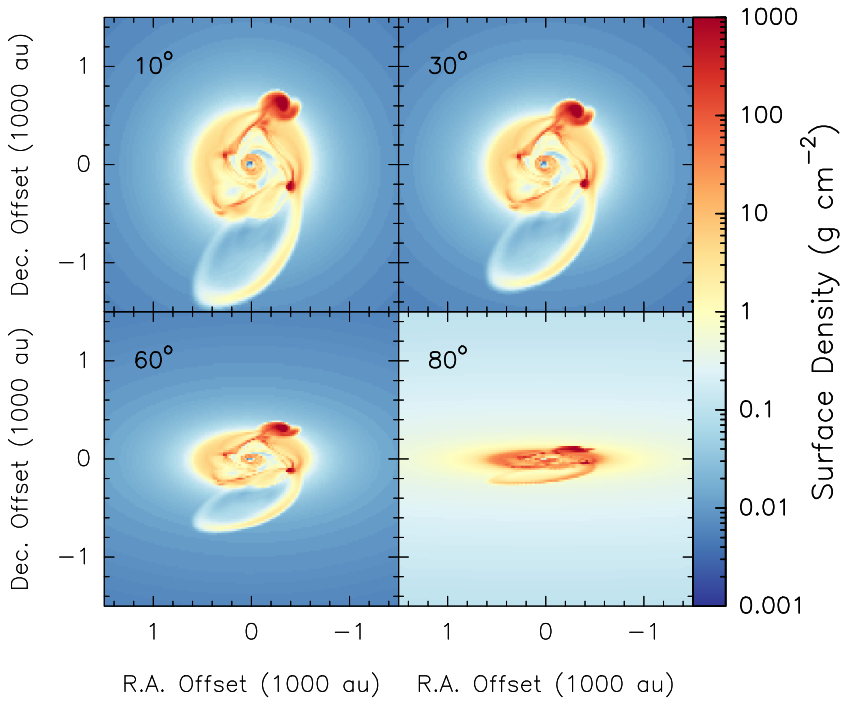

Figure 5.1: Disk surface density maps extracted from the numerical simulation at a snapshot of 12 kyr, inclined to 10°, 30°, 60°, and 80°, as denoted in the panels.

a spatial resolution of the disk's midplane layer as function of distance to the host star r of

$$\Delta x(r) \approx 0.025 \text{ au} \times r/(1 \text{ au}). \tag{5.1}$$

Hence, at the inner rim of the computational domain at 30 au, the disk is resolved down to 0.75 au. We analysed the disk structure at 12 kyr after the onset of collapse when the disk had grown to ≈ 1000 au (see Fig. 5.1). At this outer disk edge, the disk is resolved down to 25 au. In conclusion, the circumstellar disk (defined as gas with densities higher than 10^{-16} g cm^{-3}) is represented by more than a million grid cells in total. Both important physical length scales associated with disk evolution, namely the disk's pressure scale height H (which is related to disk cooling) and the disk's Jeans length $\lambda_{\rm J}$ (which is related to the fragmentation process of the disk) are resolved. In comparison, to achieve the same dynamic range on a Cartesian grid with adaptive-mesh-refinement or nested levels, 15 levels of refinement would be required. This is calculated as follows: to resolve the entire computational domain with $L_{\rm box} = 2 \times 0.1$ pc down to a minimum spatial resolution of dx $= 0.75$ au requires $2^n = L_{\rm box}/{\rm dx}$, so that the levels of refinement $n \sim 15.7$.

In addition to the high spatial resolution, another important and unique feature of this simulation is that no subgrid models such as sink particles are used to represent fragments in the disk. A strongly self-gravitating subregion of the disk can undergo local collapse, and fragmentation barriers such as the required disk cooling and disk shear timescale are self-consistently taken into account because the model solves for the hydrodynamics, radiation transport, and self-gravity, while resolving the pressure scale height and Jeans length. The high spatial resolution of the grid even allows us to resolve the hydrostatic physics of the forming first Larson cores, at least in the

inner parts of the disk where fragmentation occurs first; fragments, which are expelled from the disk towards larger radii ($r > 1000$ au) are not resolved as first Larson cores anymore. Those first Larson cores, where self-gravity is in balance with internal thermal pressure, further interact with the large-scale accretion disk in which they are embedded. They accrete gas and dust from their own smaller-scale accretion disks (discussed later in Sect. 5.5.2). The fragments migrate due to angular momentum exchange with the disk via gravitational torques, and sometimes merge, losing parts of their outer atmospheres back into the disk phase. Some fragments even get fully disrupted, for example in the case of interactions with a spiral arm.

From this simulation, we take a snapshot at 12 kyr after the onset of collapse, when the host star has grown to 10 $M_\odot$. While at this snapshot the protostar would be classified as a B-type star, the setup of the simulation is valid for the formation of a more massive O-type star as it will continue to accrete through the disk and the migration of the fragments, which induces episodic accretion onto the central protostar. Therefore, we expect this snapshot to also be representative of a slightly later evolutionary phase in which the protostar will be classified as an O-type star. In the simulations of Meyer et al. (2018), which follow a similar numerical setup to ours and reach stellar masses as high as 35 $M_\odot$, the effects of stellar irradiation and the initial angular velocity distribution are tested. In all cases the disk forms spiral arms that fragment due to gravitational instabilities, as in the simulation analysed in this work. What the change in the initial angular velocity distribution affects is the disk size and the temporal evolution of the disk-to-star mass ratio, but the fact that the disk would eventually fragment remains unchanged. Similarly, the adoption of a steeper density distribution, as done in some other works (e.g. $\rho(r) \propto r^{-2}$ in Kuiper & Yorke 2013 and Kuiper & Hosokawa 2018), would make the disk initially more stable as more mass is concentrated in the centre rather than distributed in the envelope/disk, and this lower disk-to-star mass ratio would make the disk more Toomre-stable initially, but not enough to hinder spiral arm formation and ultimately the fragmentation of the disk (Kuiper et al. 2011). Therefore, the initial conditions we have chosen for this simulation are reasonable for the formation of massive protostar(s) and the study of disk fragmentation.

Figure 5.1 shows the surface density map extracted from the numerical simulations and inclined to 10°, 30°, 60°, and 80°, where 0° denotes a face-on view of the circumstellar disk and 90° denotes an edge-on view. To extract the surface density map, we have made use of the pressure scale height

$$H(R) \approx \frac{R\, c_s}{v_{\mathrm{KSG}}}, \tag{5.2}$$

where c_s is the sound speed and v_{KSG} the Keplerian velocity taking into account the central host mass as well as the disk mass interior to that radius R. The surface density is then calculated via

$$\Sigma(x, y) \approx \rho(x, y)\, H(R), \tag{5.3}$$

where $\rho(x, y)$ is the gas mass density of the midplane. Since the calculation of the pressure scale height is only meaningful inside the disk region, the high column densities seen in the outskirts of the maps which are especially visible in the 80° inclined map are not valid. The fragmented accretion disk of the snapshot at 12 kyr is further analysed by radiative transfer post-processing, as described in the following section.

5.3 Radiative transfer post-processing

The simulation snapshot under investigation consists of a central protostar with 10 $M_\odot$, a radius of $\approx$ 9 $R_\odot$, and an effective surface temperature of 17 700 K, surrounded by a fragmented accretion disk of $\approx$ 2000 au in diameter, harbouring spiral arms and a number of first Larson cores. We used the open source software *RADMC-3D* (Dullemond 2012) to create synthetic dust continuum observations at 1.3 mm and molecular line emission for the $12_K - 11_K, K = 0-8$ rotational transitions of CH_3CN. We present the generated models in subsequent sections, and in the following paragraph we summarize the parameters used in *RADMC-3D*.

Gas and dust densities, temperatures, and gas velocity are extracted from the hydrodynamics simulation snapshot. Gas and dust temperatures are assumed to be in equilibrium, as was done for the radiation-hydrodynamics simulation. Dust opacities are from Laor & Draine (1993), used also for the continuum radiation transport in the hydrodynamics simulation. The CH_3CN abundance (with respect to H_2) is set to 10^{-10} for temperatures $\leq$90 K, 5×10^{-9} for temperatures >90 K, and 10^{-8} for temperatures >100 K based on Collings et al. (2004) and Gerner et al. (2014). The spectral width of the ray-tracer is set to $\pm$247.8 km s^{-1} around the central frequency of the non-Doppler-shifted line profile. The spectral resolution is set to 1400 frequency bins. The spatial resolution is 400×400 pixels for a region of the inner 8400 au $\times$ 8400 au around the protostar. The inclination-dependent output of this radiative transfer post-processing task, mimicking an observation by a perfect telescope, is further processed to generate synthetic observational data cubes. Details are given in the following section.

5.4 Synthetic observations

We shift the inclined post-processed snapshot of the model simulations at 12 kyr in both dust continuum and lines to two different distances of 800 and 2000 pc by dividing the fluxes by a factor of distance squared and adjusting the pixel resolution accordingly. The generation of the synthetic observations for ALMA and NOEMA are described in detail in the following subsections.

5.4.1 ALMA

To create synthetic ALMA observations, we use the ALMA simulator task *simalma* within the Common Astronomy Software Applications (*CASA*) software package[2] to create visibility files. The model simulations adjusted to the desired distance and in units of jansky per pixel are used as the 'sky model'. The location of the sky model is set to a generic position in the southern sky, with the coordinates of the centre of the map at α(J2000) = 24^h 00^m 00^s, δ(J2000) = -35^d 00^h 00^s. The observed sky frequency is set to 220.679 GHz with the widths of the channels for the line cubes set to 260.3 MHz (~0.35 km s^{-1}). We use a combination of two ALMA Cycle 5 configurations, 5–6 and 5–9, to reach a desired angular resolution of ~0.08″. The configuration files containing the information about the distribution of the antennas were obtained within *CASA* (version 5.1.2-4) and were labelled 'alma.cycle5.6.cfg' and 'alma.cycle5.9.cfg' for configurations 5–6 and

[2] http://casa.nrao.edu/

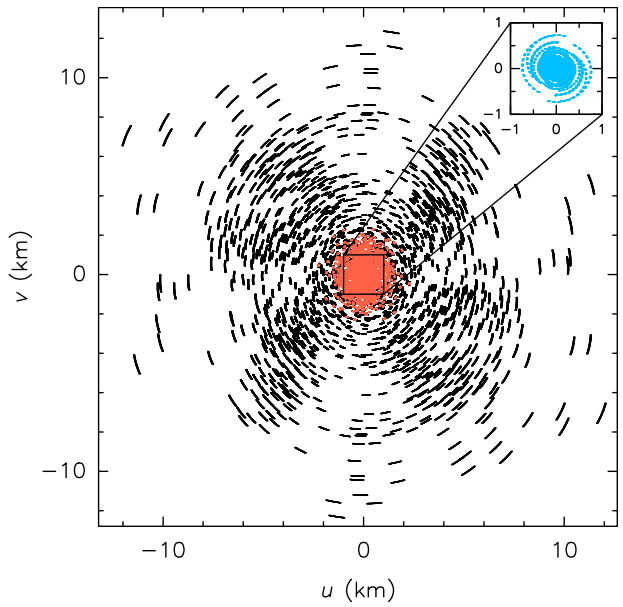

Figure 5.2: The *uv*-coverage of simulated ALMA observations in configuration 5–9 (in black) and configuration 5–6 (in red). The *uv*-coverage of simulated NOEMA observations in the ABD configuration is shown in the zoom box to the top right (in blue).

5–9, respectively. In Cycle 5, ALMA made use of 43 antennas in the 12m arrays. The *uv*-coverage of the ALMA array in configuration 5–6 has baselines in the range of 15 m to 2.5 km, and in configuration 5–9 covers a range of 375 m to 13.9 km. We set the integration time of the synthetic observations to 30-second intervals for a total time of 18 minutes in configuration 5–6 and 35 minutes in configuration 5–9. Figure 5.2 shows the *uv*-coverage of the synthetic observations. Thermal noise was automatically added to the observations assuming precipitable water vapour of 0.5 mm.

The images were generated in *CASA* using the *clean* task with the *högbom* algorithm (Högbom 1974) and a natural weighting. Considering the large number of channels in the data cubes (1400), we clean the line cubes using a circular mask spanning the extent of the input sky model to make the imaging process run faster. The images at 800 and 2000 pc have synthesized beam sizes of 0.09″× 0.06″, PA=88° and 0.07″× 0.06″, PA=90°, respectively. The reason for the slight increase in the size of the beam for the images at 800 pc is due to the more prominent contribution of side-lobe noise at 800 pc as the source is observed to be more extended. The synthesized beam sizes and RMS noise values for both continuum and line observations are summarized in Table 5.1.

5.4.2 NOEMA

For the synthetic NOEMA observations, we use the *uv_fmodel* task in the *GILDAS*[3] software package developed by IRAM and Observatoire de Grenoble. To this end, we created a *uv* table from the input sky model by providing a *uv* table that specifies the desired sampling of the antennas in the *uv*-plane. In order to make direct comparisons to our NOEMA large program, CORE, we used the *uv*-coverage of our NOEMA observations in the A, B, and D arrays for

[3]http://www.iram.fr/IRAMFR/GILDAS

Table 5.1: Details of synthetic observations.

	Distance (pc)	synthesized beam (″×″, PA)	Resolution (au)	$\sigma_{\rm cont}$ [a] (mJy beam^{-1})	$\sigma_{\rm line}$ [b] (mJy beam^{-1})
ALMA	800	0.09″× 0.06″, 88°	60	0.25	0.17
	2000	0.07″× 0.06″, 90°	130	0.06	0.04
NOEMA	800	0.44″× 0.34″, 44°	312	0.60	1.08
	2000	0.44″× 0.34″, 44°	780	0.54	0.78

Note: Values are averages for 10°, 30°, 60°, and 80° inclinations.

[a)] The RMS noise in an emission-free region.

[b)] The RMS noise in an emission-free region in the channel that has the peak of emission for CH_3CN ($12_4 - 11_4$), therefore the unit is per 0.35 km s^{-1} channel.

source W3 (H_2O) presented in Chapter 4 (Ahmadi et al. 2018). Six 15 metre antennas were used at the time of the observations of W3 (H_2O), with baselines extending the range of 19 to 760 m. The upper right panel of Fig. 5.2 shows the *uv*-coverage of the synthetic NOEMA observations. The integration time of the synthetic observations were made in 20-minute intervals for a total time of ~11 hours spread among the three different arrays. The details of the observing sequence is described in detail in Ahmadi et al. (2018). To achieve the highest possible angular resolution, we cleaned the synthetic visibilities using the *MAPPING* program of the *GILDAS* package with the *clark* algorithm (Clark 1980) and a uniform weighting (robust parameter of 0.1). The images have synthesized beam sizes of 0.44″× 0.34″, PA=44°. The synthesized beam sizes and RMS noise values for both continuum and line observations are summarized in Table 5.1.

5.5 Analysis and results

In the following, we present the continuum maps, and study the kinematics, physical conditions, and stability of the disks. We refer to the numerical simulations as 'model simulations' and the synthetic ALMA and NOEMA observations accordingly.

5.5.1 Continuum maps

Figure 5.3 shows the 1.3 mm dust continuum models of the simulations at distances of 800 and 2000 pc at four different inclinations (10°, 30°, 60°, and 80°) and the corresponding synthetic ALMA and NOEMA observations. The synthesized beam sizes, linear resolutions, and RMS noise values are summarized in Table 5.1. At this snapshot, after about 12 kyr of evolution, the fragmented accretion disk spans an extent of ~1000 au in dust continuum with four fragments seen on scales of ≤500 au, which are actively accreting material from their own smaller accretion disks (described in detail in the following section). Overdense regions connecting the fragments are a result of gravitational instabilities in the disk which had initially formed spiral arms and resulted in the creation of the fragments. The disk at this stage is still highly dynamic, with the fragments rotating about the central protostar, migrating inwards, and encountering orbital

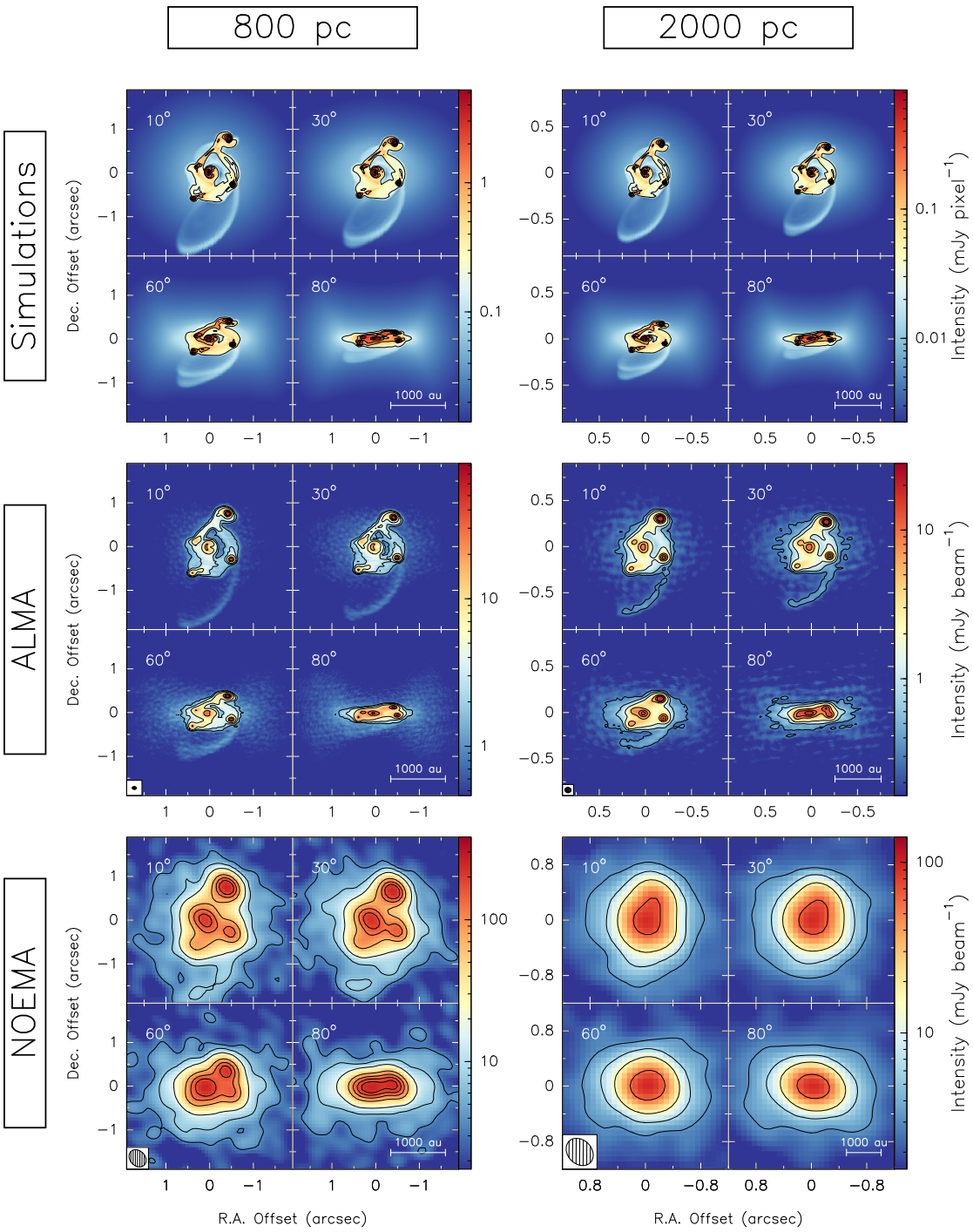

Figure 5.3: 1.37 mm continuum images of the model simulations *(top row)*, synthetic ALMA observations *(middle row)*, and synthetic NOEMA observations *(bottom row)*, shifted to a distance of 800 pc (*left column*) and 2000 pc (*right column*). Each panel contains four sub-panels corresponding to the image inclined by 10° *(top left)*, 30° *(top right)*, 60° *(bottom left)*, and 80° *(bottom right)*. The contours for the model simulations are drawn at 1, 5, 9, 20, 40, and 60% of the peak of the emission. The two outermost contours for the synthetic observations correspond to the 6σ and 12σ levels, the rest start at 30σ and increase in steps of 80σ (see Table 5.1 for the noise values). The synthesized beam is shown in the bottom left corner and a scale bar in the bottom right corner of each set of synthetic observations. The intensity scale is different in each panel.

interactions and mass transfer with each other. The centre, where the protostar is actively accreting material from the disk and envelope, has a half doughnut shape as a result of the boundary conditions of the numerical simulations. The central sink has a radius of 30 au; the region within the sink is not included in the computation domain. As a result, the strongest continuum peak is the fragment found to the north-west of the protostar. The arc of material seen in the lower part of the disk shows the ejection of some material from the system. The halo seen around the disk corresponds to the envelope, which is much less dense than the disk.

The synthetic ALMA observations at 800 pc, corresponding to a linear resolution of 60 au, resolve all fragments at all inclinations. The RMS noise of the continuum ALMA images at 800 au is higher than the case of the ALMA images at 2000 au as the extended nature of the structure results in more prominent side-lobe noise. Therefore, although the arc of material being ejected in the bottom is visible, it is not detected with 6σ or higher certainty. On the contrary, the synthetic ALMA observations at 2000 pc have lower side-lobe noise and therefore detect this arc with 6σ confidence. At this distance, with a linear resolution of 130 au, ALMA is able to detect all fragments, but just barely detects the closest one to the protostar, and detangling the fragments at an inclination of 80° becomes difficult. This disparity in the nature of the noise and the more prominent contribution of side-lobe noise at 800 pc is the reason why the synthesized beam at 800 pc has a slightly larger size than at 2000 pc.

The synthetic NOEMA observations at 800 pc, corresponding to a linear resolution of ~300 au, are able to resolve all the fragments at 10° and 30° inclinations, while only three are resolved at 60° inclination, and two at a near edge-on view of 80° inclination. At 2000 pc, corresponding to a linear resolution of ~800 au, only one structure is resolved regardless of the inclination. However, the structure has an elongated shape in the direction of the brightest fragment in the north-west, hinting at the possibility of unresolved fragmentation. At both distances the disk is seen to have a larger extent due to beam smearing. The angular resolution of NOEMA is expected to improve by roughly a factor of two with the expected baseline extension in the coming years. With the upgraded NOEMA, our synthetic NOEMA observations at 2000 pc will roughly resemble the presented observations at 800 pc.

5.5.2 Kinematics

In the following, we study the kinematics of the disk through moment analysis and PV diagrams.

Moment maps

We create moment maps of CH_3CN $(12_4 - 11_4)$ to study the disk kinematics in more detail. For the model simulations, we add arbitrary Gaussian noise to the cubes and create the moment maps with constraints on the minimum emission level set at 6σ. While there is no need to add noise to the model simulations, it makes for a cleaner presentation of the data and easier comparison with maps of the synthetic observations, and allows for the automation of the procedures with the observations. For the synthetic observations, due to the non-Gaussian nature of noise and the large contribution of side-lobe noise in the imaged cubes, we take a higher threshold of 18σ to constrain our study of the kinematics to the disk region. The range of velocities over which

the moment maps have been integrated is the same for the model simulations and the synthetic observations.

Figure 5.4 shows the integrated intensity (zeroth moment) map of of CH_3CN ($12_4 - 11_4$) for the model and synthetic observations, with continuum contour overlays. The distribution of CH_3CN gas is found to be extended by a few hundred astronomical units beyond the compact dust emission, with the peaks of gas emission coinciding with dust emission peaks as expected. This extension of gas is due to the contribution of the envelope. The envelope itself is rotating and infalling onto a ring-like structure at the location of the centrifugal barrier which can best be seen in the zeroth moment maps of the 10° and 30° inclined cubes (further discussed in Sect. 5.5.2). The arc of ejected material in the bottom is also seen in the integrated intensity maps and is clearly recovered in some of the synthetic observations. The distribution of gas in the synthetic NOEMA observations at 2000 pc are more symmetrically distributed than the dust emission, which has an elongated shape. This occurs because the fraction of gas that is being accreted onto each of the fragments is completely washed out by the large beam, and therefore the main contribution left is the larger scale disk component that is feeding the protostar at the centre. Similarly, in the synthetic NOEMA observations at 800 pc the peak of the integrated intensity map is at the centre, whereas the dust continuum peaks at the location of the fragment to the north-west. This is because the innermost 30 au around the accreting protostar is not included in the computation domain, due to the existence of the sink particle, and is therefore not bright in the continuum observations.

Figure 5.5 shows the intensity-weighted peak velocity (first moment) map of CH_3CN ($12_4 - 11_4$) for the numerical simulations and synthetic observations, with continuum contour overlays. The velocity gradient seen at 10° inclinations mainly show the contribution from the infalling and rotating envelope with the edges of the envelope shell clearly visible as it has the highest velocity offset from the LSR velocity. As the structure gets more inclined, the disk contribution becomes more clearly visible with larger velocity variation seen between the red-shifted and blue-shifted gas. The synthetic observations are able to recover the kinematics of the gas well, with the envelope and disk contributions becoming heavily blended in the poorly resolved NOEMA observations making the amplitude of the velocity gradient smaller. The Yin-Yang appearance of the first moment map is due to the fragments accreting some of the infalling gas that would have otherwise accreted onto the central protostar had the fragments not existed. This can be seen more clearly in Fig. 5.6, which shows zoom panels of the first moment map of CH_3CN ($12_4 - 11_4$) on the positions of the fragments for the model simulations at 800 pc and inclined by 60°. The line of sight velocity gradient across the central protostar is in the east–west direction and has the largest amplitude as the accretion rate is highest onto the central protostar. The rotation axis of small accretion disks surrounding each of the fragments is not necessarily inherited from the east–west rotational motion of the large-scale disk, but is set according to local dynamics. In the more inclined views towards edge-on, the Yin-Yang effect is less prominent than in the more face-on views as the fragments and their small disks are seen in one plane and start to obscure each other.

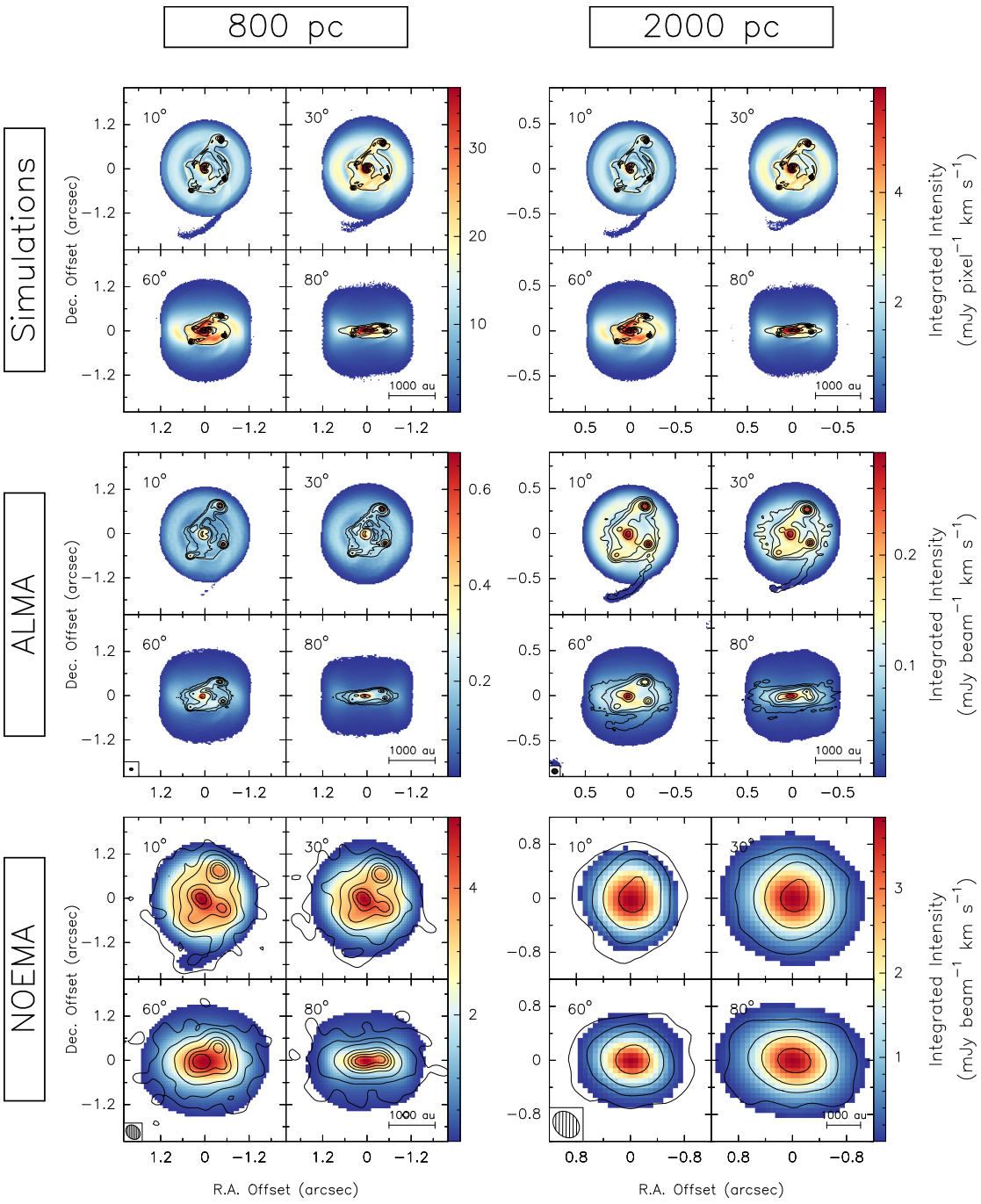

Figure 5.4: Integrated intensity (zeroth moment) maps of CH_3CN ($12_4 - 11_4$) for the model simulations *(top row)*, synthetic ALMA observations *(middle row)*, and synthetic NOEMA observations *(bottom row)*, shifted to a distance of 800 pc (*left column*) and 2000 pc (*right column*). Each panel contains four sub-panels corresponding to the image inclined by 10° *(top left)*, 30° *(top right)*, 60° *(bottom left)*, and 80° *(bottom right)*. The contours correspond to 1.37 mm continuum as shown in Fig. 5.3. The synthesized beams is shown in the bottom left corner and a scale bar in the bottom right corner of each set of synthetic observations. The scale is different in each panel.

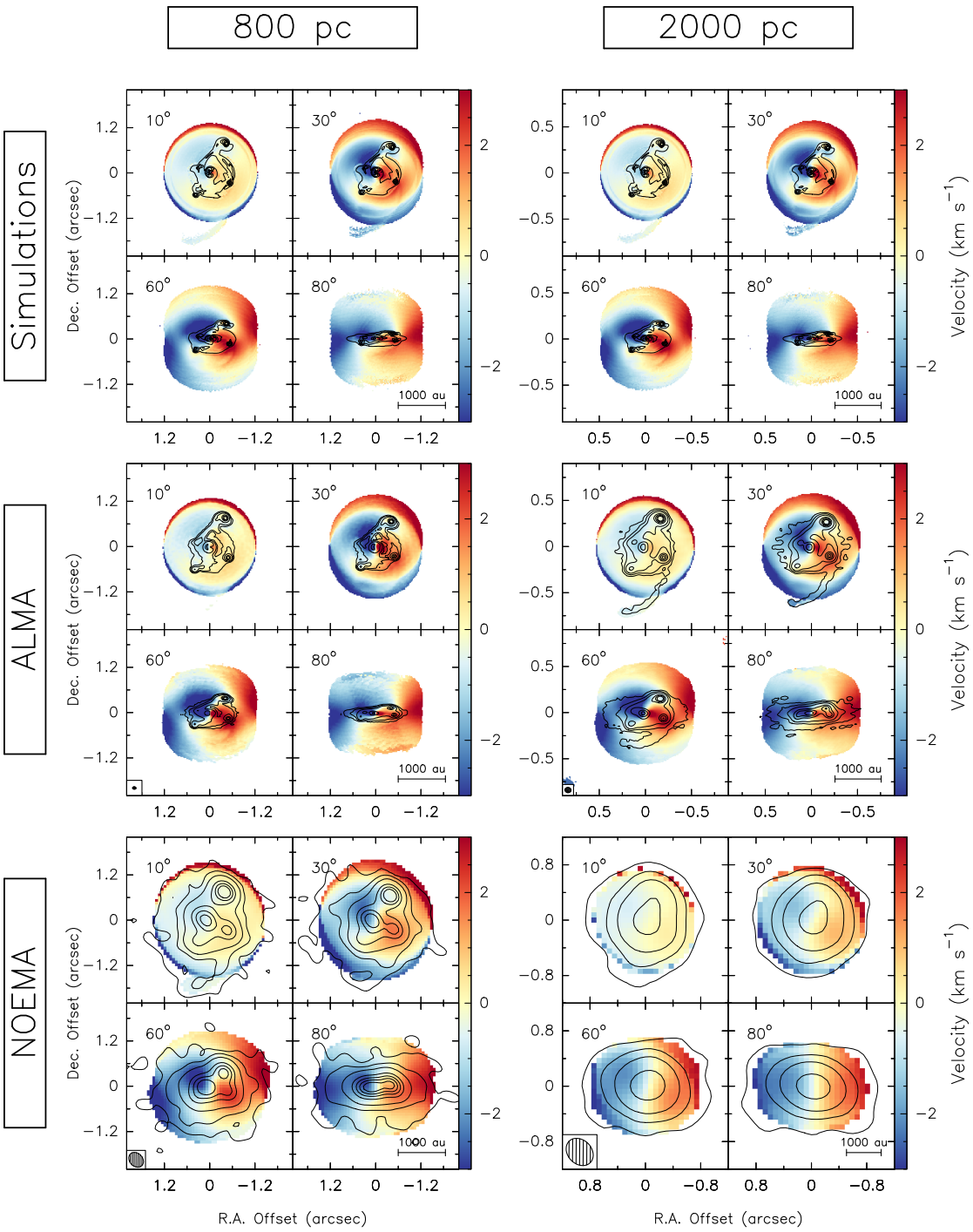

Figure 5.5: Intensity-weighted peak velocity (first moment) maps of CH_3CN ($12_4 - 11_4$) for the model simulations *(top row)*, synthetic ALMA observations *(middle row)*, and synthetic NOEMA observations *(bottom row)*, shifted to a distance of 800 pc (*left column*) and 2000 pc (*right column*). Each panel contains four sub-panels corresponding to the image inclined by 10° *(top left)*, 30° *(top right)*, 60° *(bottom left)*, and 80° *(bottom right)*. The contours correspond to 1.37 mm continuum as shown in Fig. 5.3. The synthesized beam is shown in the bottom left corner and a scale bar in the bottom right corner of each set of synthetic observations.

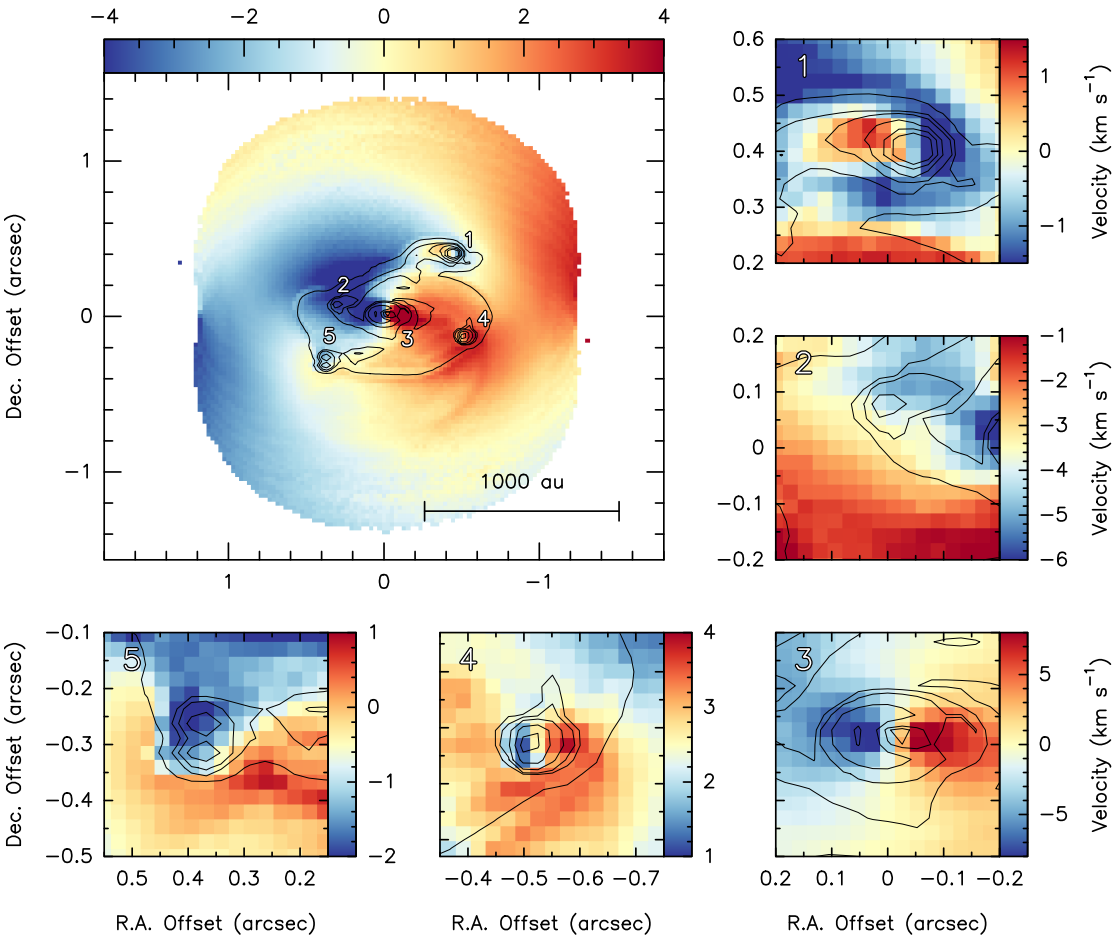

Figure 5.6: Intensity-weighted peak velocity (first moment) map of $CH_3CN\,(12_4 - 11_4)$ for the model simulations at an inclination of 60° and shifted to a distance of 800 pc *(top left)*. The surrounding panels show zoomed views of the kinematics of each fragment as marked by the numbers in the main panel. The contours correspond to the 1.37 mm continuum shown in Fig. 5.3.

Position--velocity diagrams

To study the kinematics in more detail, we created PV plots for a cut in the east–west direction, perpendicular to the direction of the rotation axis. Figure 5.7 shows the PV plots of $CH_3CN\,(12_4 - 11_4)$ for the model simulations and synthetic observation. The PV plots of the model simulations show the effect of inclination clearly in that the inner disk contribution ($r < 250$ au) is not strong in the more face-on views. As the source is more inclined towards edge-on, the disk component becomes prominent, with high-velocity contributions seen very close to the central protostar. The inner disk is in clear differential rotation with a Keplerian profile $v(r) = \sqrt{GM/r}$ about a central object with a mass of ~10 $M_\odot$, as depicted by the green curve. The contribution seen at $r > 250$ au corresponds to the region where the rotating envelope is falling onto the inner disk, which has a lower radial velocity than the infall velocity of the envelope. In recent years this transition has been observed around low-mass protostars (e.g. Sakai et al. 2014; Oya et al. 2016; Lee et al. 2017; Alves et al. 2017). These studies have found that at this position, accretion shocks lead to local heating, causing a change in the chemistry

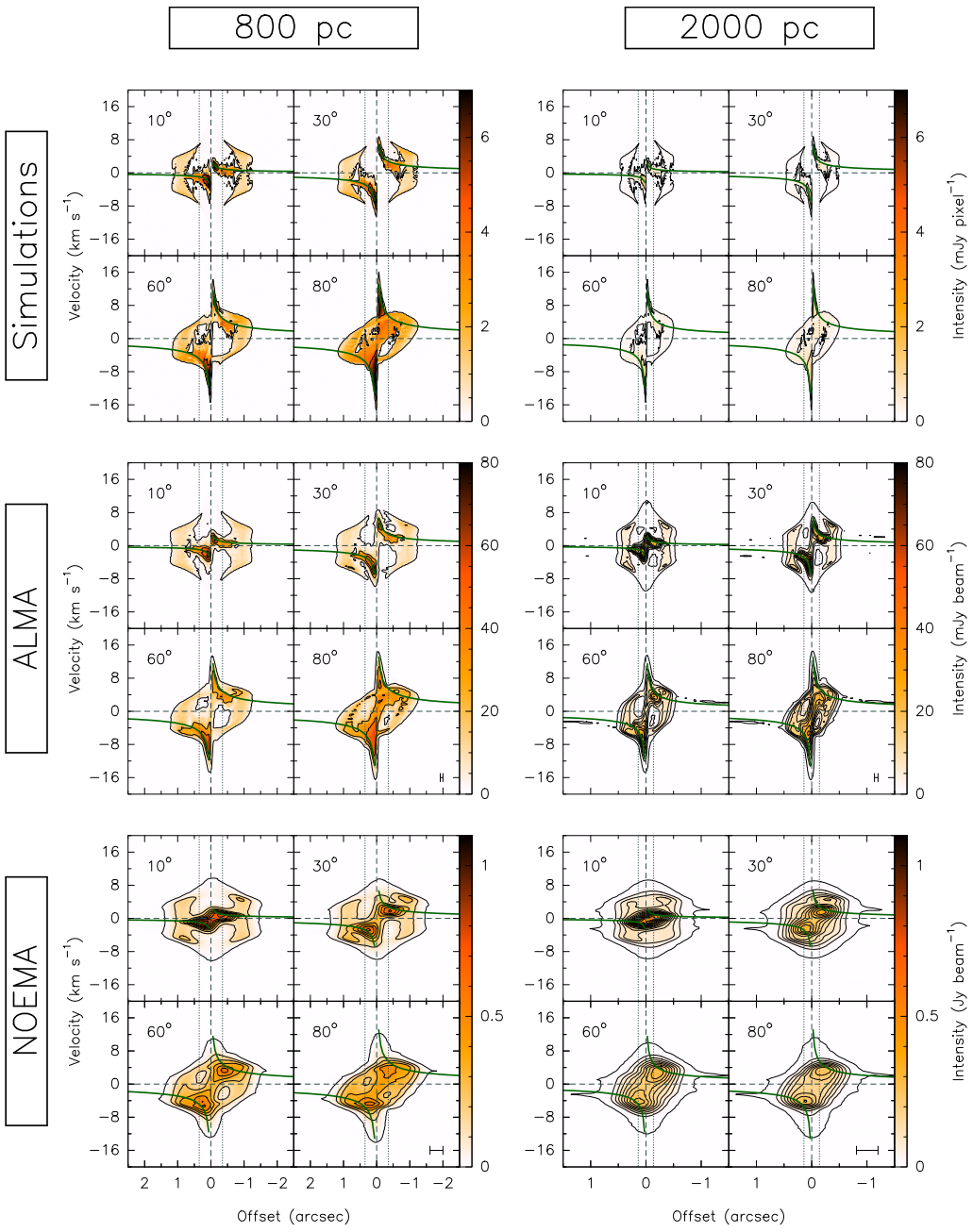

Figure 5.7: Position–velocity plots of $CH_3CN\,(12_4 - 11_4)$ for a cut in the east–west direction across the model simulations *(top row)*, synthetic ALMA observations *(middle row)*, and synthetic NOEMA observations *(bottom row)*, shifted to a distance of 800 pc (*left column*) and 2000 pc (*right column*). Each panel contains four sub-panels corresponding to the image inclined by 10° *(top left)*, 30° *(top right)*, 60° *(bottom left)*, and 80° *(bottom right)*. The three outermost black contours correspond to the 6, 12, and 18σ levels. The remaining black contours increase in steps of 150σ. The green curves correspond to the region within which emission is expected if the gas is in a disk in Keplerian rotation about a 10 $M_\odot$ star. The colour scale is the same for each row to show the effect of loss of emission with increasing distance. The vertical and horizontal dashed lines correspond to the position of the protostar and zero LSR velocity. The vertical dotted lines correspond to the radii at which the centrifugal barrier is seen (±250 au). The position resolution is shown as a scale bar in the bottom right corner of each set of synthetic observations. The velocity resolution is 0.35 km s^{-1}.

as material is liberated off the ice mantles to the gas phase. Furthermore, evidence for the centrifugal barrier around a high-mass protostellar envelope has recently been reported by Csengeri et al. (2018). This transition region is estimated to be an order of magnitude closer to the central protostar in the low-mass regime (e.g. 30–50 au for IRAS 16293–2422 Source B; Oya et al. 2018) than in the reported high-mass case (300–800 au; Csengeri et al. 2018). Our estimate of the centrifugal barrier located at r ~250 au is in agreement with the lower end of the estimates from the observations of Csengeri et al. (2018).

The sharpness of this discontinuity feature seen in the PV plots is a function of resolution and inclination angle. It can be seen in the NOEMA observations at 2000 au that the 'kink' seen in the other PV plots as a result of this transition is completely smoothed out. Furthermore, the velocity profile of the infalling rotating envelope would look different depending on the offset between the line of sight and the source position, as depicted in Figure 3b of Sakai et al. (2014), which can have an effect on the sharpness of this discontinuity. The PV plots presented in this work have been made for a cut that goes through the protostar as we have knowledge of the precise location of the protostar.

The PV plots of the synthetic ALMA observations resemble the PV plots of the model simulations, but smoothed in the position direction. The high-velocity components are still clearly detected in the more inclined cases, but the spreading of emission would mean that the Keplerian curve corresponding to rotation of matter about a ~10 $M_\odot$ star does not perfectly fit anymore, especially in the 2000 pc case. As we move to the synthetic NOEMA observations and the emission gets even more smeared in the position direction, the high-velocity components seen in the more inclined views become hard to detect and the Keplerian curve does not fit the observations well. This is best seen in the synthetic NOEMA observations at 2000 pc where the inner disk and envelope contributions are completely blended and the resulting PV plots more closely resemble rigid-body rotation than differential rotation, similar to many observational data sets in the last decade at comparable resolutions.

As temperature is expected to be higher in regions of the disk closer to the protostar, we would expect line transitions that require higher excitation energies to be present in regions closer to the star. One signpost of differential rotation in observations is often seen in the steepening of the slope of the emission in the PV diagrams for the higher excited lines, such that a transition that is tracing the innermost regions of the disk would have higher velocities at smaller radii than the transitions that trace the entire disk region. This has been observed in the case of higher K transitions of CH_3CN (Johnston et al. 2015), or vibrationally excited CH_3CN transitions (Cesaroni et al. 2017). Comparing the PV plots of CH_3CN $(12_2 - 11_2)$ to CH_3CN $(12_4 - 11_4)$ and CH_3CN $(12_6 - 11_6)$, we do not see this steepening of the slope with higher K levels because all lines trace regions with similar optical depths and therefore probe similar regions.

5.5.3 Temperature distribution

To gain a better understanding of the disk structure, we calculated the rotational temperature and column density of the dense-gas tracer CH_3CN under the assumption of LTE. To do so, we used the eXtended *CASA* Line Analysis Software Suite (*XCLASS*[4], Möller et al. 2017) software

[4]https://xclass.astro.uni-koeln.de

in *CASA*. In Fig. 5.8 we show the resulting rotational temperature maps obtained from pixel-by-pixel *XCLASS* modelling of CH_3CN $(12_K - 11_K)$ $K = 4 - 6$ for the synthetic observations. The recipe is as outlined in Appendix B of Ahmadi et al. (2018) where we discuss the reasoning behind not including the lower K-ladder transitions in the fitting routine. In these runs, we also allowed the size of the source to be a fitting parameter rather than fixing it to a value larger than the beam. This strategy was tested and it yields smoother temperature maps. For each synthetic observation, we calculated the RMS noise in the emission-free region in the channel that has the peak of emission for CH_3CN $(12_4 - 11_4)$, and only fit pixels with signal higher than six times this noise. We note that the spectra at the positions where the envelope is directly falling onto the disk are triply peaked corresponding to red- and blue-shifted infall from the envelope onto the disk with a third component corresponding to the rotational motion of the disk itself. This is particularly prominent in the views closer to face-on. Since performing a three-component fit to the entire map was not feasible, we smoothed the velocity resolution by a factor of eight, reaching a spectral resolution of 2.8 km s^{-1}, to blend all three components of the lines enough to perform a one-component fit to the spectrally smoothed data cubes.

Figure 5.8 shows the resulting rotational temperature maps for the synthetic observations. Under the LTE assumption, the rotational temperature of CH_3CN can be accepted as the kinetic temperature of the gas. The median gas temperatures obtained from the synthetic observations at each inclination are listed in Table 5.2. On average, temperature decreases as the system becomes more inclined, which is expected as the observed column densities are higher in the more inclined views. In addition, the arc of material being ejected from the system seen at the bottom of the disk has a higher temperature than its surroundings. For comparison, the face-on view of the disk mid-plane temperature from the model simulations is presented in Fig. 5.9 on the same logarithmic scale. Mid-plane temperatures at the location of fragments can reach values higher than 1000 K, but on average the median temperature for the inner disk ($r < 400$ au) is 177 K, about 50 K warmer than the outer envelope (400 au $< r <$ 800 au), which has a median temperature of 128 K. In Table 5.2 we also list median temperature values calculated for the regions within 12σ dust continuum contours (the second outermost contours in Fig. 5.8), which more closely correspond to the disk. On average, and as expected, the temperatures are higher in the disk than in the outer envelope. Moreover, the temperature decreases as angular resolution worsens when the disk structure is no longer recovered. Interestingly, the temperature distributions for the synthetic NOEMA observations at 2000 pc at 10° and 30° inclinations are elongated in the same direction as the continuum, while this elongation feature is not seen in the respective zeroth moment maps of CH_3CN $(12_4 - 11_4)$ (bottom right panel of Fig. 5.4).

5.5.4 Mass estimates

At the snapshot of the numerical simulations under investigation, the protostar has gained a mass of ~10 $M_\odot$. In the following, we describe the different techniques often used in observations for determining core and protostellar masses.

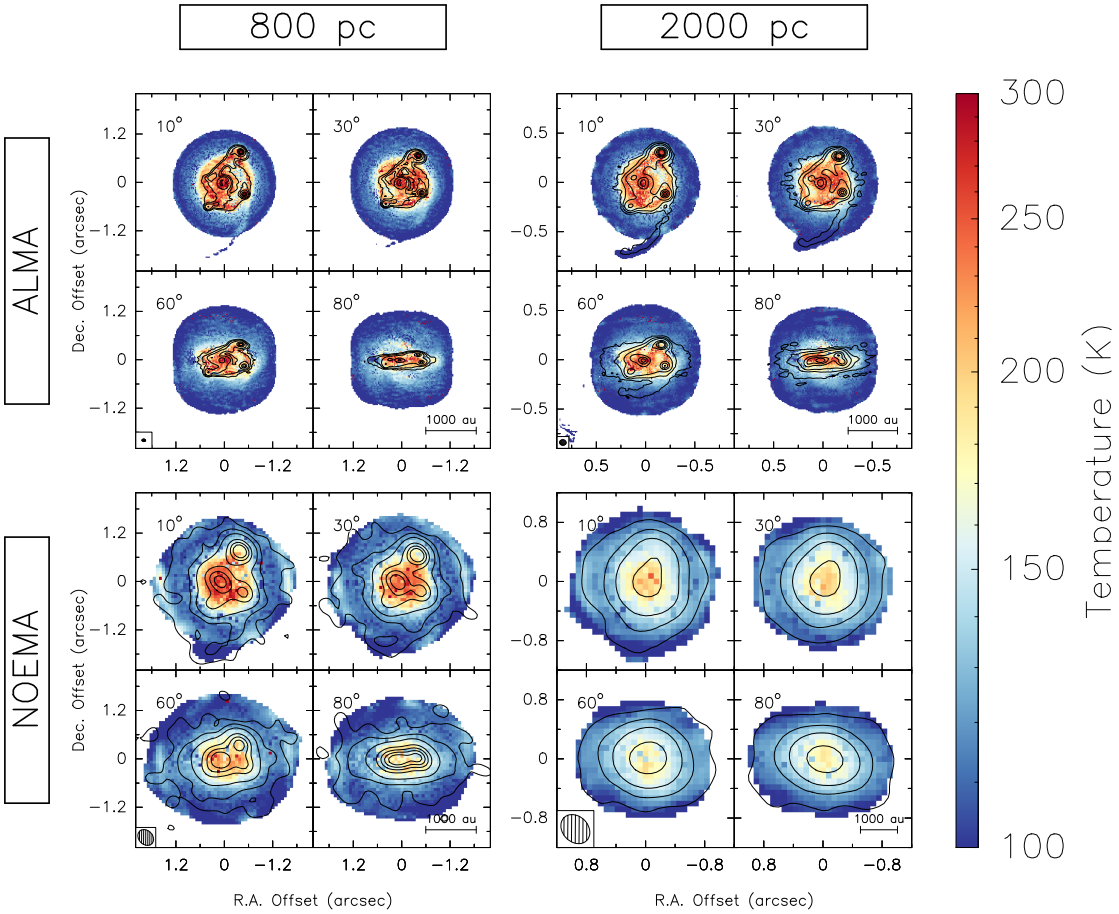

Figure 5.8: Rotational temperature maps of synthetic ALMA observations *(top row)* and synthetic NOEMA observations *(bottom row)*, shifted to a distance of 800 pc (*left column*) and 2000 pc (*right column*), obtained by fitting CH_3CN $(12_K - 11_K)$ $K = 4 - 6$ lines simultaneously with *XCLASS*. Each panel contains four sub-panels corresponding to the image inclined by 10° *(top left)*, 30° *(top right)*, 60° *(bottom left)*, and 80° *(bottom right)*. The synthesized beam is shown in the bottom left corner of each set of synthetic observations. The contours correspond to the 1.37 mm continuum shown in Fig. 5.3. The scale used in the plots is for ease of comparison to the 'true' disk mid-plane temperature shown in Fig. 5.9.

Masses from dust emission

Because dust opacity decreases with increasing wavelength, thermal emission of dust at longer wavelengths in the Rayleigh-Jeans limit can trace large column densities and provide estimates for the dust mass if the dust emissivity is known (Hildebrand 1983). Assuming optically thin dust emission at 1.3 mm, for a gas-to-dust mass ratio R and a dust absorption coefficient κ_ν, we can convert the flux density F_ν of the continuum observations to a mass value via

$$M = \frac{d^2 F_\nu R}{B_\nu(T_D)\,\kappa_\nu}, \tag{5.4}$$

where d is the distance to the source and $B_\nu(T_D)$ is the Planck function, which at the wavelengths under investigation follows the Rayleigh-Jeans law and is linearly dependent on the dust temperature T_D. We adopt a value of 150 for the gas-to-dust mass ratio (Draine 2011) and

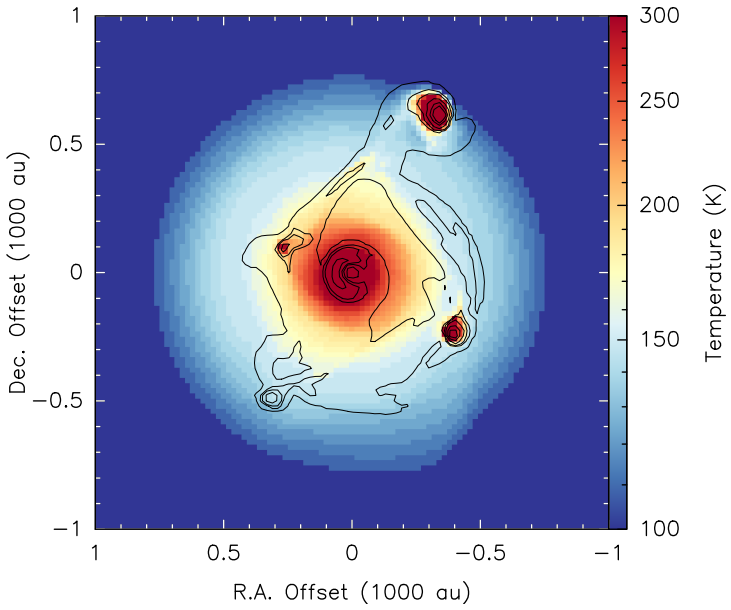

Figure 5.9: Face-on view of the disk mid-plane temperature from the model simulations. The contours correspond to the continuum image and are drawn at 1, 5, 9, 20, 40, and 60% of the peak of the emission. The scale used in the figure is for ease of comparison to the synthetic observations shown in Fig. 5.8. Temperatures at the locations of the fragments get as high as 1000 K.

$\kappa_\nu = 0.9$ cm^2 g^{-1} corresponding to thin ice mantles after 10^5 years of coagulation at a density of 10^6 cm^{-3} (Ossenkopf & Henning 1994). We assume the kinetic temperature of the gas, derived from the radiative transfer modelling of CH_3CN $(12_K - 11_K)$ $K = 4 - 6$ (see Sect. 5.5.3) to be coupled to the dust temperature. Therefore, we use the temperature maps presented in Fig. 5.8 together with the continuum maps shown in Fig. 5.3 to create mass maps. Summing over all pixels, we then obtain a total mass for each synthetic observation, summarized in Table 5.2. The values are on average between 2.5–3.5 $M_\odot$. For comparison, the total mass within the inner 8400 × 8400 au box for the model simulations is ~14 $M_\odot$ calculated in the same manner by using the face-on continuum map and the mid-plane temperature shown in Fig. 5.9, which accounts for the total gas mass in this area. The bulk of the remaining mass is on larger scales and is not included in our analysis. Therefore, the mass estimates from the synthetic observations recover roughly 20% of the total mass calculated from the model simulations and the bulk of the flux is filtered out by the interferometer.

Considering only the synthetic ALMA observations, the mass estimates at 2000 pc are on average smaller than at 800 pc, by roughly 10%. Since the average temperature distribution does not vary significantly between the two cases, we would expect the mass estimate to also be consistent. This small excess of mass corresponds to the contribution from the halo of material found outside of the 6σ continuum contours in the middle panels of Fig. 5.3. Since the continuum maps at 800 pc are noisier than at 2000 pc (see Table 5.1) the mass estimates at 800 pc are higher than at 2000 pc. Conversely, the mass estimates at 2000 pc for the synthetic NOEMA observations are roughly 20% higher than at 800 pc. While the average temperature is not significantly different in the two cases (see Table 5.2), the distribution of temperatures

Table 5.2: Summary of temperatures, masses, and Q values for the synthetic observations.

Interferometer	Distance (pc)	Inclination (degrees)	$T_{\mathrm{median}}{}^{a}$ (K)	$T_{\mathrm{median,\,12}\sigma}{}^{b}$ (K)	$M_{\mathrm{gas}}{}^{c}$ ($M_\odot$)	Q_{median}
ALMA	800	10	115	228	2.9	2.6
	800	30	112	213	3.2	2.3
	800	60	110	204	3.3	1.5
	800	80	110	202	2.8	0.5
ALMA	2000	10	112	214	2.9	3.5
	2000	30	111	211	3.0	3.1
	2000	60	108	187	3.0	2.0
	2000	80	108	173	2.5	0.7
NOEMA	800	10	121	153	2.6	5.2
	800	30	118	145	2.7	4.7
	800	60	115	142	2.6	3.1
	800	80	114	139	2.4	1.0
NOEMA	2000	10	125	148	3.5	3.6
	2000	30	125	146	3.4	3.4
	2000	60	123	143	3.3	2.0
	2000	80	119	143	2.9	0.5

[a)] Median temperature, calculated from the maps presented in Fig. 5.8.
[b)] Median temperature within 12σ dust continuum (second outermost) contours as presented in Fig. 5.8.
[c)] Gas mass is calculated from the dust emission using Eq. 5.4.

in the innermost regions where the bulk of continuum emission is concentrated is significantly cooler in the 2000 pc case than at 800 pc (see bottom row of Fig. 5.8), resulting in a higher mass estimate at the greater distance.

Protostellar masses from PV plots

Protostellar masses are often estimated from fitting Keplerian profiles with $v(r) = \sqrt{GM/r}$ to PV diagrams. In Fig. 5.7 we show the PV plots for the model simulations and synthetic observations for a cut along the east–west direction going through the centre of the sink particle where the protostar is located. While the green curves correspond to the region within which emission is expected if the gas is in a disk in Keplerian rotation about a 10 $M_\odot$ star, they do not represents fits to the PV plots. In order to estimate protostellar masses from these PV plots, we use the *KeplerFit* package[5] (described in Bosco et al. 2019), which uses the method presented in Seifried et al. (2016). The method first identifies the two quadrants of the PV plot that contain most of the emission and then, starting from the positions closest to the protostar and moving outwards, it determines the highest velocity at which the signal becomes higher than a given

[5]Developed by Felix Bosco, available at https://github.com/felixbosco/KeplerFit.

threshold. This then determines the boundary which these authors call the 'upper edge' of the PV plot which is then fit with a Keplerian profile to determine the enclosed mass. This method has proven to yield more accurate mass estimates than fitting the pixels with the maximum intensity for each radius or for each velocity channel (Seifried et al. 2016).

It can clearly be seen from the PV plots shown in Fig. 5.7 that the rotating and infalling envelope (regions outside the vertical dashed lines) shows different kinematic signatures than the inner disk, as discussed in Sect. 5.5.2. More specifically, there is a discontinuity in the resolved PV plots as a result of the infalling and rotating envelope having a higher infall velocity than the inner disk. Therefore, fits to the inner regions would be expected to yield lower mass estimates than to the outer envelope, which at a given position has higher velocities. For this reason we fit the inner and outer part of the disk separately and compare the results to the case where the entire PV diagram is fitted. An example is shown in Fig. 5.10 for the model simulations at 800 pc. We always fit the 6σ outer edge for a range of radii and always exclude in the fitting the regions closest to the protostar where the velocity decreases with decreasing distance to the protostar as a result of finite resolution (see Appendix A.3.2 of Bosco et al. 2019). The resulting mass estimates from fitting the inner, outer, and entire PV curves for the model simulations and synthetic observations are presented in Fig. 5.11. Knowing that the central protostar has gained a mass of ~10 $M_\odot$ and that the disk mass is ~8 $M_\odot$ at this snapshot of the simulation, we can test the accuracy of estimating the enclosed masses using this method in each scenario. We first focus on the general findings.

As rotational velocity is expected to scale with inclination angle i by a factor of $\sin(i)$, the mass estimates are expected to scale by a factor of $\sin^2(i)$. Therefore, it is expected that fitting the kinematics of the more inclined disks would result in higher mass estimates than their less inclined counterparts (grey curves in Fig. 5.11). While this general trend is seen in our fitting results, we find that the fitted masses are on average higher than the theoretical expectation, similar to the findings of Seifried et al. (2016). For example, we would expect the enclosed mass estimate at 30° to be 0.25 times lower than the true value of 18 $M_\odot$ at 90° inclination; however, the mass estimate from the fitting the inner region of the model simulation is higher than the expected 4.5 $M_\odot$ by 35%. Seifried et al. (2016) attribute this increase to the existence of considerable radial motions, which in the more inclined views noticeably contributes to the line of sight velocities. It is worth noting that while the 10 $M_\odot$ protostar is located at the centre of the computational domain at zero offset in the PV diagrams, the disk which contains roughly 8 $M_\odot$ spans a range of radii, such that the mass-velocity relation is $v(r) = \sqrt{G(M_* + M_{\rm disk}(r)/r}$. Therefore, the enclosed mass is not exactly 18 $M_\odot$ at all radii and the true theoretical curve lies somewhere between the solid and dashed lines in Fig. 5.11. Interestingly, the fits to the inner disk of the model simulations inclined to 60° and 80° provide mass estimates in this range.

For the model simulations where we fit the PV curves of the model simulations and the ALMA observations at 800 pc, the protostellar mass estimates obtained from fitting the inner disk regions are, as expected, smaller than the estimates from fitting the outer or entire regions, and provide estimates closer to the expected values. For these cases, fits to the entire region yield masses that are less than the mass estimates obtained from fitting the outer regions. In these cases, fits to the outer regions overestimate the masses because the component that is fitted is

mainly the envelope within which more mass is contained and which does not necessarily have a Keplerian rotation profile.

For all observations, the method overestimates the mass, even when fitting the inner disk regions. The mass is much more overestimated for disks with lower inclinations (i.e. views closer to face-on). The fact that we generally overestimate the masses especially at lower inclinations can be seen as favourable since without knowing the inclination in most observations, the mass estimate obtained from fitting the PV diagram is typically adopted as the protostellar mass without any corrections for inclination. Therefore, it is somewhat reassuring that fits to the entire region for the model simulations and all ALMA observations, which properly resolve the disk, are quite close to the expected enclosed mass of ~18 $M_\odot$ at all inclinations.

As resolution worsens, in the case of the synthetic ALMA observations at 2000 pc and synthetic NOEMA observations at both distances, the fits to the outer regions provide the lowest mass estimates, which are also closer to the expected value. For the ALMA observations, the variations in the mass estimates from fits to different regions are not as significant as for the NOEMA observations at 800 and 2000 pc, where the fits to the inner regions can yield masses that are larger than the fits to the outer regions by almost a factor of 2 and 4, respectively.

While the Seifried et al. (2016) method of fitting the outer edge of the PV diagram used to determine the enclosed mass is the most accurate method currently used, we find that fitting the entire PV diagram of poorly resolved observations yields masses that are highly overestimated.

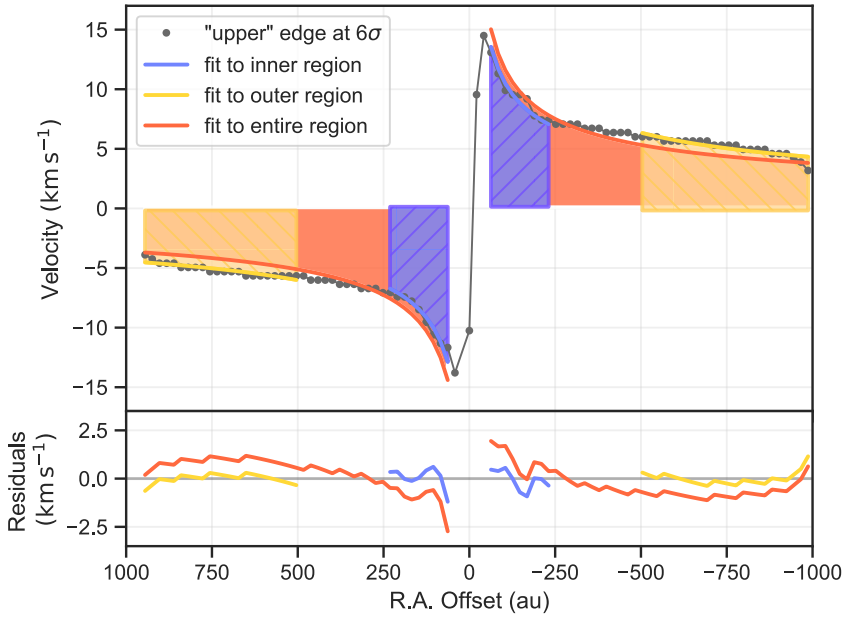

Figure 5.10: Example of the Keplerian fitting approach based on Seifried et al. (2016) to the 6σ outer edge of the PV plot of CH_3CN ($12_4 - 11_4$) for the model simulation inclined to 60° at a distance of 800 pc in order to determine the protostellar mass. The fits to the inner, outer, and entire regions yield protostellar mass estimates of 12.4, 21.4, and 15.4 $M_\odot$, respectively. The inner region traces the disk that follows a Keplerian rotation curve better than the outer region, which has contributions from the rotating and infalling envelope. The bottom panel shows the residuals. The protostar has a mass of ~10 $M_\odot$ while the disk has a mass of ~8 $M_\odot$.

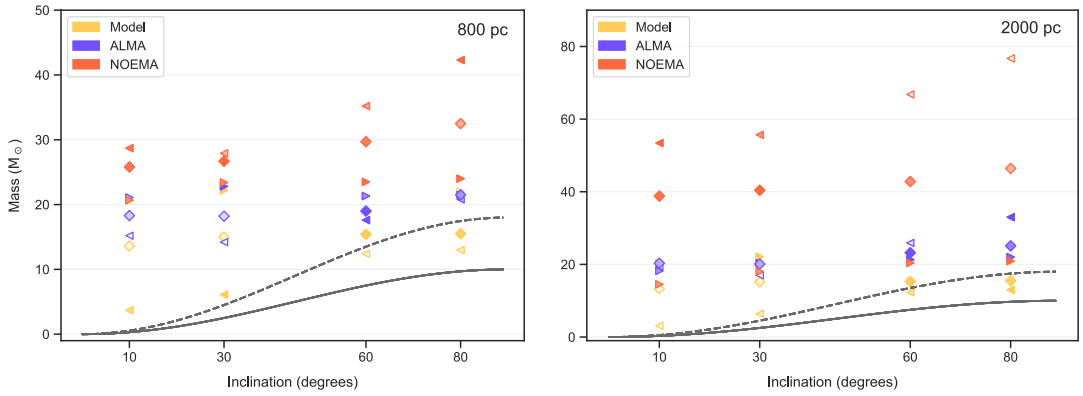

Figure 5.11: Mass estimates from fitting the 6σ edges of the PV diagrams of CH_3CN $(12_4–11_4)$ shown in Fig. 5.7 using the method introduced by Seifried et al. (2016) for the model simulations *(yellow)*, ALMA *(purple)*, and NOEMA observations *(orange)* at 800 pc *(left)* and 2000 pc *(right)*. The triangles pointing to the left and right correspond to fits to the inner and outer regions, respectively. The diamonds correspond to fits to the entire PV curves. The transparency of the markers correspond to the χ^2 value of the fit, weighted by the χ^2 value of the best-fit curve for a given region. The more opaque the marker, the better the fit. The solid and dashed grey curves correspond to the true estimate for the mass of the protostar (10 $M_\odot$), and the mass of the protostar + disk (18 $M_\odot$), respectively, corrected by $\sin^2(i)$ for each inclination i.

This is expected as the emission is smeared over a larger area with the envelope and disk components completely blended, resulting in the PV diagrams not having a Keplerian shape (see bottom row of Fig. 5.7). In these cases, we find that fitting the outer regions of the PV diagram (in our cases, regions beyond 1600 au) provides better estimates for the protostellar mass. The same analysis was done for the PV plots of CH_3CN $(12_K - 11_K)$, $K = 3, 5, 6$ lines, and the variations in the mass estimates were marginal compared with those presented in Fig 5.11 for the $K = 4$ transition. The only noticeable difference was that the mass estimates obtained from fitting the PV diagrams of the $K = 3$ transition were slightly higher than those obtained from the other lines as this transition is more easily excited than the others and the emission is hence distributed over a larger area.

5.5.5 Toomre stability

As mentioned in the Introduction, the Toomre Q parameter can be used to study the stability of a disk against gravitational collapse (Toomre 1964). The stabilising force of gas pressure is included in the expression of Q (Eq. 1.4) via the sound speed,

$$c_s = \sqrt{\frac{\gamma k_B T}{\mu m_H}}, \tag{5.5}$$

where γ is the adiabatic index with a value of $7/5$ for diatomic gas, k_B is the Boltzmann constant, μ is the mean molecular weight with a value of 2.8, and m_H is the mass of the hydrogen atom. Furthermore, we account for the stabilising force of shear by assuming the disk is in Keplerian-

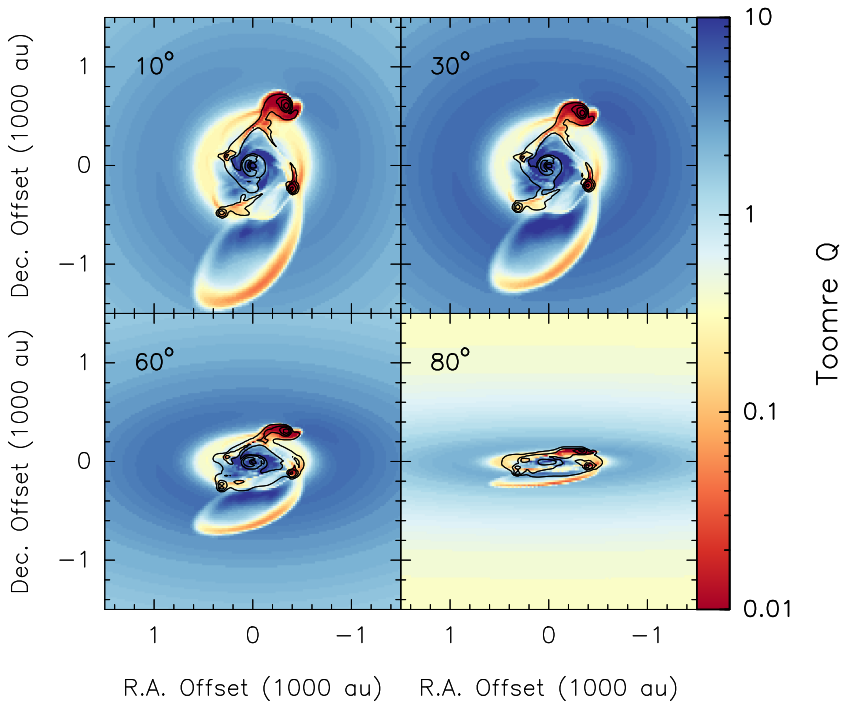

Figure 5.12: The 'true' Q map obtained from the model simulations inclined by 10° *(top left)*, 30° *(top right)*, 60° *(bottom left)*, and 80° *(bottom right)*. The contours correspond to 1.37 mm continuum as shown in Fig. 5.3. Q values less than 1 correspond to regions unstable against gravitational collapse.

like rotation such that the angular velocity of the disk at a given radius r would be

$$\Omega(r) = \sqrt{\frac{G\,M}{r^3}}. \tag{5.6}$$

In Fig. 5.12 we show the 'true' Q map obtained from the model simulations. As expected, we see low Q values at the positions of the fragments since these regions have already collapsed to form protostars; we also see low Q values in a ring coincident with the edge of the disk. Since the mid-plane temperature decreases smoothly towards the edges of the disk (see Fig. 5.9), we would expect a decrease in the Q parameter in the outskirts of the disk, but the existence of low Q values in a ring-like structure is due to enhanced disk surface density in a ring of material in this region (see Fig. 5.1). It is important to note that the Toomre analysis is meaningless outside of the disk region; therefore, the transition from stable (high Q) on envelope scales to unstable (low Q) at larger radii in the outskirts of the maps has no physical meaning. This transition is best seen in the view closest to edge-on in Fig. 5.12 at a declination offset of about ±800 au.

In the following, we estimate the distribution of Q for the synthetic observations and start the analysis by adopting the known protostellar mass at this snapshot and correcting the angular velocities for the known inclinations. The effects of not correcting the velocities properly and uncertainties in mass estimates are further discussed in Sections 5.5.5 and 5.5.5, respectively. We assume that the LTE assumption is valid in such a high-density environment, and use the rotational temperature of CH_3CN modelled in Sect. 5.5.3 as representative of the kinetic temperature of the gas. To account for the self-gravity of the disk, we include the mass of the disk

within a given radius ($M_{\rm disk}(r)$) to the mass of the protostar M_* assumed to be 10 $M_\odot$. The angular velocity is further corrected to account for the inclination of the disk such that

$$\Omega(r_{\rm proj}) = \sqrt{\frac{G\,(M_* + M_{\rm disk}(r_{\rm proj}))}{r_{\rm proj}^3}}. \tag{5.7}$$

In particular, the radius at each pixel in a face-on disk is calculated as $r = \sqrt{\Delta x^2 + \Delta y^2}$, where Δx is the distance from the protostar in right ascension and Δy is the distance from the protostar in declination. Since we do not rotate the structure, but only incline it about the x-axis, the projected radius is $r_{\rm proj} = \sqrt{\Delta x^2 + \Delta y^2 \cos^2(i)}$.

The mass of the disk is calculated as discussed in Sect. 5.5.4 from the continuum emission maps by summing up the mass contained within each projected radius using the aperture photometry tools of the *photutils* package (Bradley et al. 2016) within the *astropy* package (Astropy Collaboration et al. 2013) in Python. Furthermore, the beam-averaged surface density of the disk is calculated via

$$\Sigma = \frac{S_\nu R}{B_\nu(T_D)\,\Omega_B\,\kappa_\nu}, \tag{5.8}$$

where S_ν is the peak intensity and Ω_B is the beam solid angle.

In Fig. 5.13, we show the Q maps for the synthetic observations. Again, as expected, we find low Q values below the critical value of 1 at the positions of the fragments in the synthetic observations which resolve them. This is attributed to the enhanced surface density at the positions of the fragments that have already collapsed to form stars. We also find low Q values (~1–2) in the arms connecting the fragments, as well as the arc of material to the south being expelled from the system. The arms connecting the fragments can be locations where further disk fragmentation can take place. The extremely low Q values above and below where the continuum contours are drawn in the view closest to edge-on (80°) are a result of low angular velocities at these positions since the disk only extends a small distance in declination. The gas contribution at these locations comes from the rotating and infalling envelope, and the Toomre analysis is actually not applicable for this envelope medium.

The ring of low Q values seen in the model simulations (see Fig. 5.12) is not seen in the Toomre maps of the synthetic observations. Since the produced dust continuum images are essentially a convolution of the temperature with the density, the radial decrease in temperature in the outskirts (see Fig. 5.9) where the ring exists in the density (see Fig. 5.1) results in this component not being prominent in the final continuum images (see Fig. 5.3). Therefore, because we use the continuum maps to calculate the surface density of the disks in the Toomre equation, this component is also non-existent. Interestingly, we find high Q values in a ring just outside of the lowest continuum contours, best seen in the synthetic ALMA observations inclined 10° and 30°. This is a result of high gas temperatures in these regions, due to shock heating of gas falling from the rotating envelope onto the disk.

The synthetic NOEMA observations at 800 pc still show low Q values at the positions of the fragments, but the low values expected to be seen in the arms connecting the fragments are absent because the temperature distribution is uniform in the inner regions (see bottom left panel of Fig. 5.8). Most interestingly, although the synthetic NOEMA observations at 2000 pc do not

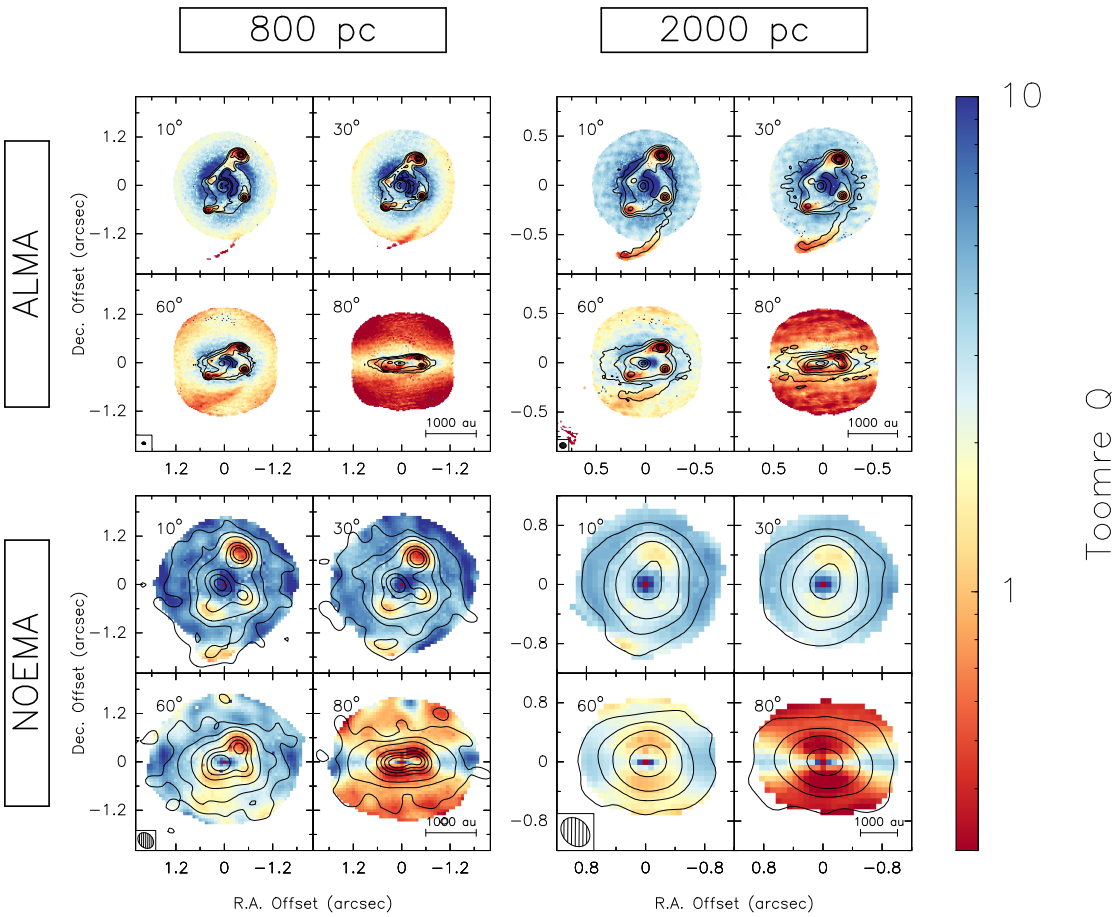

Figure 5.13: Toomre Q maps of synthetic ALMA observations *(top row)* and synthetic NOEMA observations *(bottom row)*, shifted to a distance of 800 pc (*left column*) and 2000 pc (*right column*). Each panel contains four sub-panels corresponding to the image inclined by 10° *(top left)*, 30° *(top right)*, 60° *(bottom left)*, and 80° *(bottom right)*. In each case, the disk is assumed to be in Keplerian rotation about a 10 $M_\odot$ star at the centre. The angular velocities have been corrected for the inclination (see text). The contours correspond to the 1.37 mm continuum shown in Fig. 5.3. The synthesized beam is shown in the bottom left corner and a scale bar in the bottom right corner of each set of synthetic observations. Q values of less than 1 correspond to regions unstable against gravitational collapse.

resolve the individual fragments, we find low Q values ~2 in the outskirts of the disk. This is a result of the structure having a non-circular elongated shape in the direction of the brightest fragment in the north-west in both the continuum and temperature distributions.

The critical value of Q is often taken to be 1 in theoretical calculations, and lowers to ~0.7 for an isothermal disk of finite thickness (Goldreich & Lynden-Bell 1965; Gammie 2001). Considering that our modelling of the level populations of the CH_3CN K-ladder provides gas temperatures that may probe layers above the disk mid-plane, we assume that regions where Q is less than ~2 are unstable against gravitational collapse. The median Q values are listed in Table 5.2 and follow a trend opposite to that of the mass estimates; the Toomre parameter is inversely proportional to the surface density of the disk, which is calculated in a manner similar to that used for the mass estimates but without the distance dependence.

At first glance we see that, on average, the Q parameter gets lower with increasing inclina-

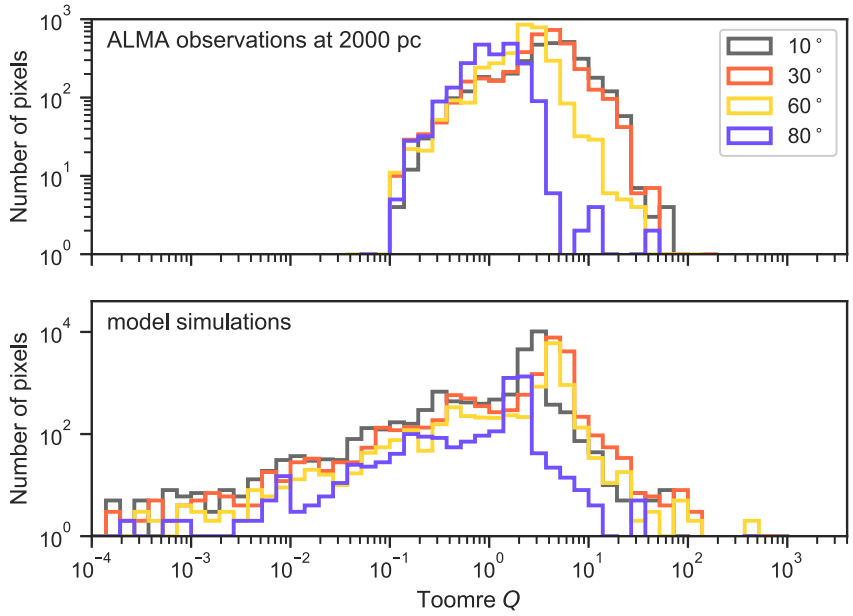

Figure 5.14: *Top:* Histogram of Q values for synthetic ALMA observations at 2000 pc (see top right panel of Fig. 5.13), including only pixels that lie within 6σ continuum contours to show the Q distribution mostly associated with the disk rather than the envelope. *Bottom:* Histogram of Q values for model simulations (see Fig. 5.12), including only pixels within a radius of 1600 au.

tion. This is naively expected as in the edge-on views one looks through a larger column. To investigate the effect of inclination further in the resolved observations, the histogram of Q values for synthetic ALMA observations at 2000 pc is shown as an example in the top panels of Fig. 5.14. We attempt to remove as much of the contribution as possible from the envelope by only plotting the histogram of Q values for the pixels that lie within 6σ continuum contours, which are the outermost contours drawn on the maps in Fig. 5.13. The Q distributions in these inner regions do not vary much for the 10°, 30°, and 60° views, but still a large portion of the contribution for the 80° inclined map comes from the envelope since the disk contribution is just a narrow region spanning a few pixels in declination. The angular velocities in the envelope for the case closest to edge-on are low and therefore result in low Q values there. For comparison, in the bottom panel of Fig. 5.14 we show the histogram of Q values for the inclined models where only pixels within a radius of 1600 au are included in order to exclude the meaningless contribution from the larger scale cloud. While the distribution is broader, as there are more pixels with low Q values for each fragment, the findings remain the same.

Inclination of the angular velocity field

In true observations, we seldom have information about the inclination of the source. Sometimes the outflow geometry can help, but high-mass stars form in highly clustered environments, and with the outflow angles widening with time (Beuther & Shepherd 2005) there is a very good chance that outflows emanating from different sources may overlap, making the deduction of an inclination angle for the disk difficult. To check how the lack of knowledge about the inclination

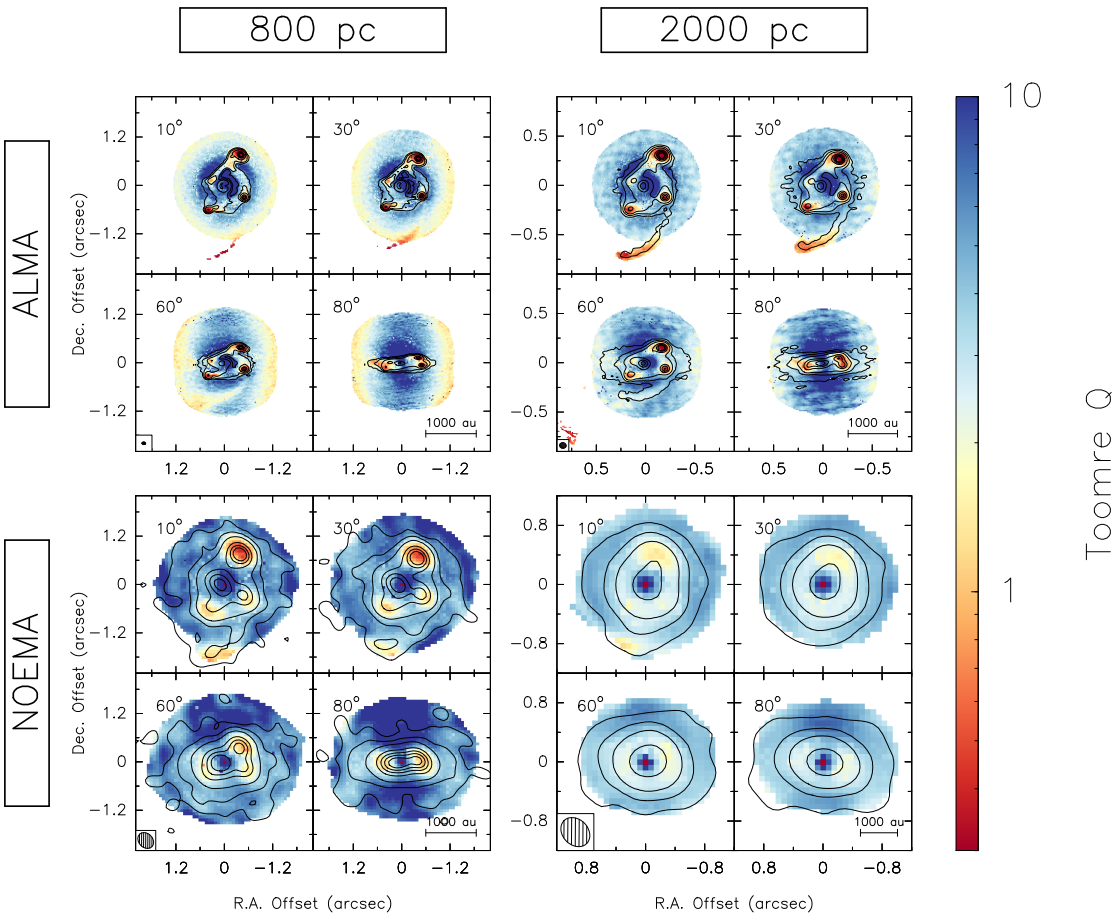

Figure 5.15: Same as Fig. 5.13, but assuming the inclination of the object is not known, and therefore with the velocities not corrected to the actual rotation velocities.

of the disk would affect our analysis, we produced an angular velocity map where at each pixel $r = \sqrt{\Delta x^2 + \Delta y^2}$, which essentially means we assume the angular velocity at each position is what it would be if the disk was edge-on in that direction.

Figure 5.15 shows the Q maps for the synthetic observations without the inclination correction. In the resolved ALMA observations at both distances and NOEMA observations at 800 pc, we still find low Q values, as expected, at the positions of the fragments, but the higher inclined views show higher Q values at the locations of the fragments than in the inclination-corrected cases, precisely because the angular velocities at a given point above and below the zero declination line are higher in the uncorrected maps. Interestingly, in the synthetic NOEMA observations at 2000 pc where the fragments are not resolved, we still see the low Q values in the outskirts of the structure. Therefore, the conclusion from the corrected case still holds that we are able to predict fragmentation of the disk without actually resolving the fragments.

Uncertainties in the mass of the central object

In our Toomre analysis, we have assumed the mass of the protostar at the centre to be 10 $M_\odot$ as we have access to this information. In Sect. 5.5.4 we outlined how the mass of the central object is often estimated from the kinematics of the disk, and explained that with loss of resolution, the shape of the rotation curve of the disk changes from differential to a more rigid-body ap-

pearance. Therefore, fitting Keplerian curves to the PV plots of poorly resolved structures would overestimate the mass of the central object. Since the mass of the protostar has a square root dependence in the expression of Q (Eq. 1.4), overestimating the protostellar mass by a factor of 4 would yield Q values that are on average higher by a factor of two, making the disks seem more stable.

5.6 Summary and conclusions

In this work, we have presented synthetic ALMA and NOEMA observations for a high-resolution 3D radiation-hydrodynamic simulation of a high-mass protostellar disk that fragments into a highly dynamic system. At the snapshot of the simulation at 12 kyr, the system comprises a central protostar and four companion fragments on scales ≤500 au, all accreting material from the infalling and rotating envelope that feeds the disk that is in Keplerian rotation. Smaller accretion disks are formed around each of the fragments, through which some of the large-scale disk and envelope material is accreted onto the fragments. The aim of the investigation has been to study the effect of inclination and spatial resolution in recovering disk structure and to study the stability of the disk in order to predict disk fragmentation and better understand recent and future high-resolution observations. The following is a summary of our findings:

- Synthetic ALMA observation at 800 pc are able to detect all fragments at all inclinations in both continuum and line emission at 1.3 mm. At 2000 pc, the ALMA observations at 80° inclination cannot resolve the closest fragment to the protostar. The NOEMA observations at 800 pc can resolve all fragments at 10° and 30° inclinations, but not all at higher inclinations. At 2000 pc, NOEMA observations only show a single structure that looks slightly elongated towards the brightest fragment.

- In the zeroth moment maps of CH_3CN (12–11) rotational transitions, the peak of emission is at the position of the protostar. For the ALMA observations at both 800 and 2000 pc, we are able to detect the rotating envelope that is infalling onto a ring-like structure at the position of the centrifugal barrier. The effect is best seen in the 10° and 30° inclined views.

- In the first moment maps of CH_3CN (12–11) rotational transitions the disk contribution is best seen in the higher inclined views, as expected. There are small accretion disks around each fragment feeding them part of the disk material; this leads to the large-scale velocity field of the disk having a Yin-Yang shape. Envelope and disk contributions are heavily blended in the poorly resolved case of NOEMA observations at 2000 pc (linear resolutions ~800 au) where the emission is also smeared over a larger distance, making the amplitude of the observed velocity gradient smaller.

- PV diagrams of CH_3CN (12–11) rotational transitions for a cut through the disk perpendicular to its rotation axis show the differential (Keplerian) rotation of material best in the close to edge-on view. At a radius of ~250 au a discontinuity is seen, corresponding to the position of the centrifugal barrier because the infalling envelope has a higher infalling

velocity than the radial velocity of the disk. As the entire structure becomes less resolved in the NOEMA observations, the high-velocity components of the disk become washed out and blended with the envelope component, making the PV diagrams resemble rigid-body rotation.

- We fit the emission of CH_3CN $(12_K - 11_K)$ $K = 4 - 6$ with *XCLASS* to obtain rotational temperature maps for the disks. On average we find temperatures in the range of 100–300 K, decreasing as the system becomes more inclined. The envelope is roughly a factor of 2 cooler than the disk. In the poorly resolved NOEMA observations, the envelope and inner disk contributions become blended and the difference between the temperature of the inner and outer regions is not as apparent as in the resolved cases.

- Assuming gas and dust temperatures are coupled, mass estimates from dust for the synthetic observations account for roughly 20% of the mass calculated from the model simulations for the inner 8400 × 8400 au, and the rest is filtered out by the interferometers.

- We make use of the method presented in Seifried et al. (2016) to fit the PV plots with Keplerian models to obtain protostellar mass estimates. Since there is a discontinuity in the 6σ outer edge of the PV plots as a result of material falling from the envelope onto the disk, we fit the inner disk and outer envelope regions separately. In the case of well-resolved disks with Keplerian profiles, we find the fits to the inner regions the most accurate and the fits to the entire PV curves adequate for estimating enclosed masses. For poorly resolved disks, the fits to the outer regions of the PV diagrams yield much more accurate mass estimates as opposed to fits to the entire region which overestimate the mass. The factor by which the mass is overestimated depends on how poorly the disk is resolved.

- Studying the Toomre stability of the disks, we find low Q values below the critical value for stability against gravitational collapse at the positions of the fragments and in the arms connecting the fragments for the resolved synthetic ALMA observations. For the synthetic NOEMA observations at 800 pc (linear resolutions ~300 au), low Q values are seen at the locations of the fragments, but the unstable region in the disk is no longer seen since the temperature structure is uniformly warm for the inner disk. For the NOEMA observations at 2000 pc (linear resolutions ~800 au) where only one structure is resolved, we find low Q values in the outskirts of the disk. This is an important result as it implies that despite the lack of ability in resolving any of the fragments, we are able to predict that the disk is unstable and fragmenting.

- Assuming that the inclination of the disk is not known, recalculating the Q maps using Keplerian velocities of an edge-on disk to all radial directions for all inclinations provide slightly higher values for the Q parameter, but the conclusions from the previous point still hold. This is reassuring as disk inclinations are difficult to establish.

In this chapter, we showcased the potential and limitations of studying disks in high-mass star formation with current (millimetre) interferometers. We benchmarked a method for study-

ing the stability of such disks, showing that even with poorly resolved observations it is possible to predict whether a disk is prone to fragmentation.

CHAPTER 6

Kinematics and Stability of the CORE Sample

Based on Ahmadi et al.
to be submitted to *Astronomy & Astrophysics*

6.1 Motivation

As higher resolution observations are becoming more accessible, thus allowing structures to be resolved on scales <1000 au, it is important to determine whether disks around intermediate to high-mass stars (OB-type) are ubiquitous and if so, to characterize their properties. What is the typical extent of these disks? Are they in differential rotation similar to their low-mass counterparts and if so, over what range of radii? Is there any scale where a core stops fragmenting? At what scales do we see the fragmentation of disks? Are close binary/multiple systems an outcome of disk fragmentation as suggested by, for example, Meyer et al. (2018)? If so, stability analyses of these high-mass rotating cores and disks are needed to shed light on fragmentation at disk scales. These questions can only be answered with a statistical approach for a large sample of high-mass star-forming regions. To this end, we have observed a sample of 20 high-mass YSOs ($L > 10^4\ L_\odot$) at the highest possible resolution (0.4″, ~1000 au) in the northern sky with the NOEMA interferometer and the IRAM 30-m telescope. The observational setup and data reduction details were presented in Chapter 3. I will outline our findings on the kinematics and stability of the best disk candidates within the CORE survey. The chapter is organized as follows. We begin with a brief description of the large-scale environment in Sect. 6.2 and then turn our focus onto the dense gas distribution and kinematics in Sect. 6.3. To confirm the position angles of the disk candidates, in Sect. 6.4 we examine the outflow directions. The temperature distribution is presented in Sect. 6.5 with estimates for gas and protostellar masses given in Sect. 6.6. We analyse the candidacy of the sources as disks in Sect. 6.7 by studying their lifetimes and specific angular momenta. Finally, in Sect. 6.8 we outline our findings on the stability of the disk candidates and summarize our conclusions in Sect. 6.9.

6.2 Large-scale structure

While the focus of this work is on the kinematics on small disk scales, it is useful to begin with a brief overview of the larger scale environment. The following is a summary of the structure of the target regions in both dust continuum and lines.

6.2.1 Core fragmentation

We detect strong millimetre continuum emission from all sources within the CORE survey, mainly associated with cold dust (see Table 3.1 for source positions and properties). Figure 6.1 shows the continuum observations, with all sources shown on the same linear scale in order to make comparing them possible. A diversity of fragmentation level among the sources can be seen, with some regions harbouring as many as 20 cores (e.g. IRAS21078), while others remain singular (e.g. AFGL2591). In an attempt to understand this diversity, we performed a minimum-spanning-tree analysis and found the separation between the cores to be on the order of the thermal Jeans length or smaller (Beuther et al. 2018). This analysis indicated that either the initial density structure or magnetic fields are most likely responsible for setting the fragmentation diversity we see on these scales. Because the smallest separation between the cores were often found to be at our resolution limit, it is expected that further fragmentation can be found on even smaller scales. Since the resolution we probe with NOEMA, at thousands of au, is the scale at which disk-like structures are expected to exist in high-mass star forming regions (see review by Beltrán & de Wit 2016), this chapter focuses on the role of disk fragmentation further contributing to the fragmentation diversity we see in high-mass star-forming regions (see Chapter 1 for a description of core versus disk fragmentation).

6.2.2 Kinematics

Since our spectral setup covers a wide range of transitions at high spectral resolution (see Table 1.1 for a list of bright lines covered in the Narrowband receiver), we make use of the easily excited transitions of low-density tracers such as H_2CO and CH_3OH to probe the distribution of gas on large scales. Figure 6.2 shows the intensity-weighted peak velocity (zeroth moment) maps of $H_2CO(3_{0,3} - 2_{0,2})$ for the entire sample. We detect gas with velocities varying on the order of a few km s^{-1} in each field. For some sources which have filamentary-like structure (e.g. IRAS23033 or W3IRS4), there exists a velocity gradient along the filament, consistent with flows of material along the filament onto the hot cores (IRAS23033: Bosco et al. 2019; W3IRS4: Mottram et al. subm.). In these cases, there exist separate velocity gradients at the edge of the filament where hot cores reside with different position angles and amplitudes than the large flow along the filament. This finding is consistent with the filamentary paradigm of star formation (see reviews by André et al. 2014 and Motte et al. 2018; also Fig. 1.2 in the Introduction). Whether the large-scale velocity structure observed for other sources correspond to infall, expansion, or rotation motions is not a focus of this work but one we will return to at the end of this thesis in Chapter 8.

Although we attempted to observe regions at the same evolutionary stage (i.e. the HMPO phase), the CORE sample does inevitably span a range in age, as high-mass star formation

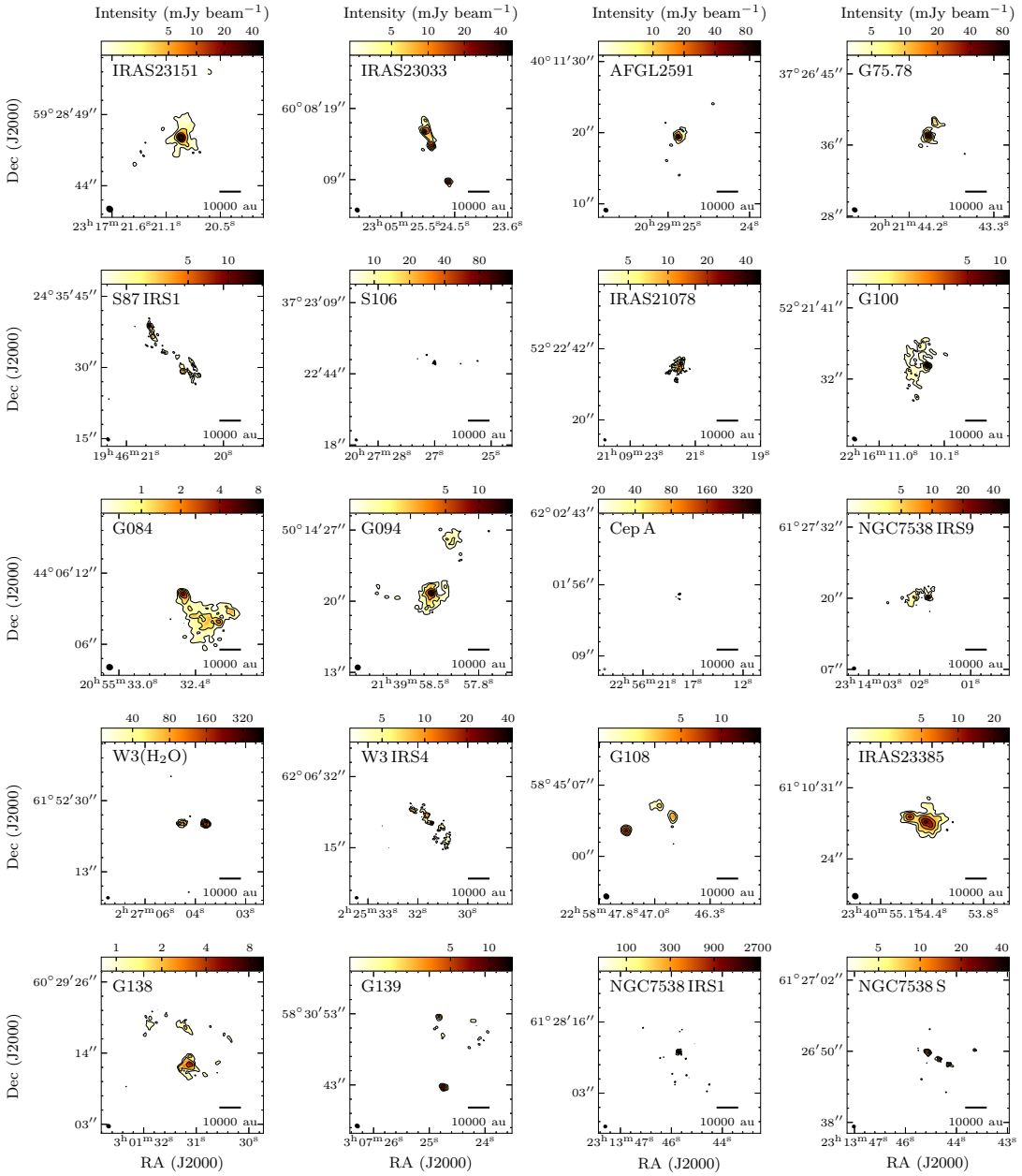

Figure 6.1: NOEMA 1.37 mm continuum maps of the CORE sample. The contours start at 5, 10, and 20σ, increasing in steps of 15σ, with the exception of IRAS23151, NGC7538 IRS1, NGC7538 IRS9 and AFGL2591 for which the contours start at 5, 15, and 40σ, increasing in steps of 25σ (see Table 6.1 for σ values). The synthesized beam is shown in the bottom left corner and a scale bar in the bottom right corners of each panel.

occurs on much shorter timescales compared to the formation of low-mass stars. This is evident because some YSOs show a rich hot core chemistry (e.g. AFGL2591, G75.78, Cep A HW2, and W3 (H_2O)), while others are weaker in line emission (e.g. S87 IRS1, S106, G108, G138, G139). For two of these weak sources, namely S106 and S139, we barely detect any $H_2CO(3_{0,3} - 2_{0,2})$ emission at the position of the cores (see Fig. 6.2). Furthermore, there is no correlation between the richness in lines and the infrared (IR) brightness of the sources (see Table 3.1), where the threshold between IR-bright and -dark is defined according to Motte et al. (2007) based on

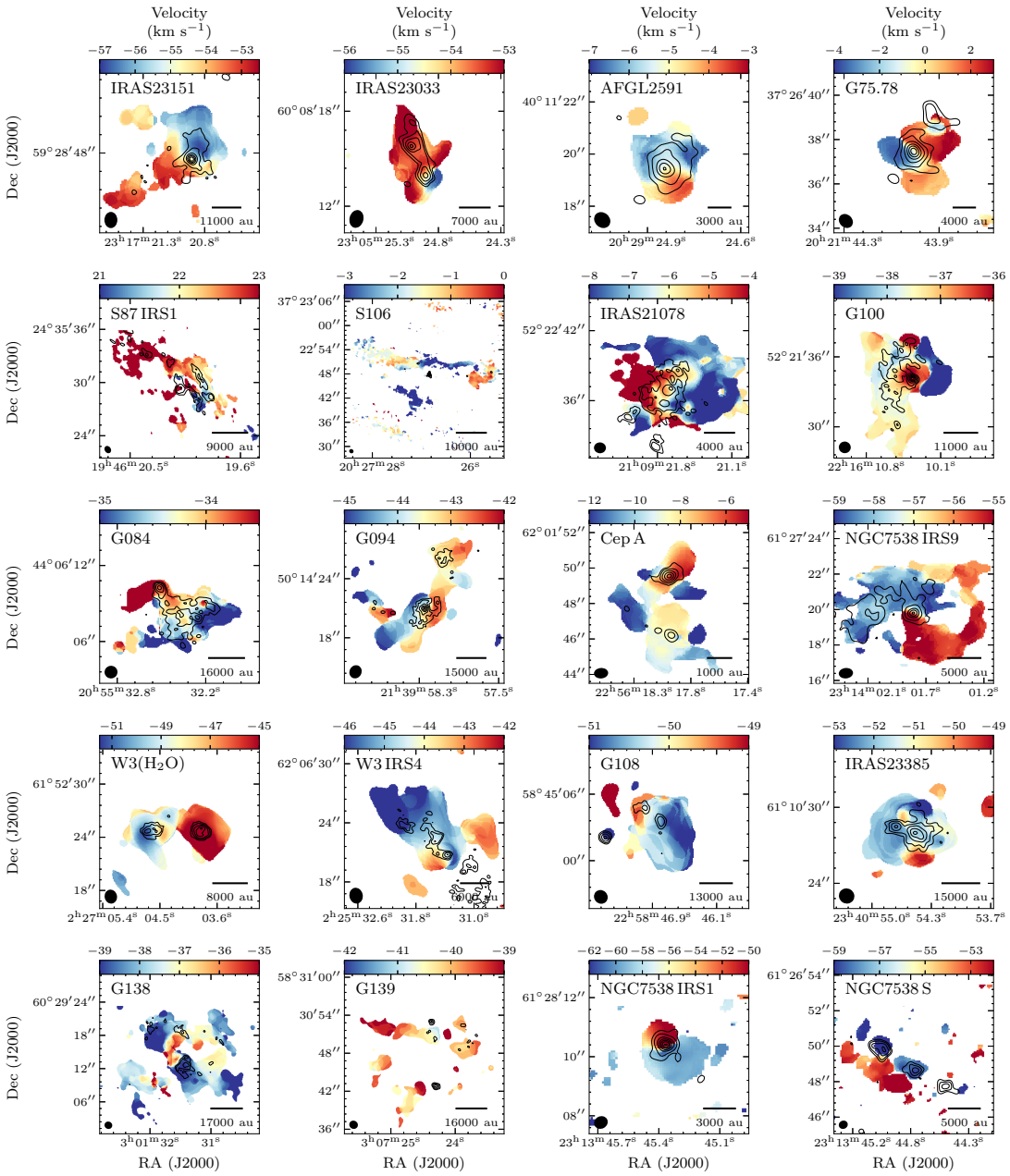

Figure 6.2: Intensity-weighted peak velocity (first moment) maps of $H_2CO(3_{0,3} - 2_{0,2})$ showing the large-scale kinematics of the full CORE sample. The contours correspond to the continuum maps imaged with uniform weighting as presented in Beuther et al. (2018) starting at 5, 10, and 20σ, increasing in steps of 15σ, with the exception of IRAS23151, NGC7538 IRS1, NGC7538 IRS9 and AFGL2591 for which the contours start at 5, 15, and 40σ, increasing in steps of 25σ (see Table 6.1 for σ values). The synthesized beam is shown in the bottom left corner and a scale bar in the bottom right corner of each panel. When displayed in Adobe Acrobat, it is possible to switch to the first moment map of $CH_3OH(4 - 3)$ and back to the first moment map of $H_2CO(3_{0,3} - 2_{0,2})$ for comparison.

cores in the Cygnus X star-forming region at a distance $D = 1.7$ kpc, such that if a core with a luminosity of 1000 $L_\odot$ has 21 μm flux ($S_{21\mu m}$) below 10 Jy it would be categorized as IR quiet. Therefore regions with $S_{21\mu m} < 10\,\mathrm{Jy}\left(\frac{1.7\,\mathrm{kpc}}{D}\right)^2\left(\frac{L}{1000\,L_\odot}\right)$ are classified as IR-dark. The fact

that some of the most chemically-rich sources in our survey are IR-dark points to their young deeply embedded nature, during which they are already capable of producing a rich chemistry and driving powerful outflows.

We further find a number of stages in the evolutionary sequence of high-mass star formation within some of the targeted fields, hinting at the importance of the environment on triggering star formation. For example, in the case of W3IRS4, we find two cold cores along a filamentary structure with a hot core situated at the junction of the filament with an expanding UCH II region known as W3C and seen as a circular structure to the southwest with almost no H_2CO emission. While there may exist H_2CO emission at this position that is filtered out by the interferometer, we can compare this source to another UCH II region in the CORE sample, W3(OH) which is at the same distance and has a similar mass sensitivity to W3IRS4. W3(OH) is the western-most feature seen in the maps labeled as W3 (H_2O), around which we detect extended H_2CO emission, unlike W3C. This difference can in part be attributed to the fact that W3C is probably at a later evolutionary stage than W3(OH) as its larger extent suggests, hence warmer conditions have already destroyed many of the species that would often be found during an earlier evolutionary phase.

6.3 Dense gas kinematics

We make use of CH_3CN $(12_K - 11_K)$ transitions to study the dense gas kinematics of the full sample, just as we did for the case study presented in Chapter 4 and the synthetic observations shown in Chapter 5. Initially, we imaged the CH_3CN cubes for the entire sample with a uniform weighting (robust 0.1 in *GILDAS* lingo) to reach the highest possible angular resolution. For sources for which CH_3CN was either not detected or only one or two of the lowest K transitions were detected, we re-imaged the data cubes with weightings that help in recovering more extended emission (higher robust parameter closer to natural weightings). The sources for which up-weighting the compact configuration helped in recovering some CH_3CN emission were IRAS23033, IRAS23385, G100, and G084. Even with such a strategy, we did not have proper detections of CH_3CN for 5 of the 20 core sources: S87 IRS1, S106, G108, G138, and G139. Interestingly, all of these objects are IR-bright confirming our hypothesis that these sources are likely at a slightly older evolutionary phase whereby the warmer environment has already destroyed the species. These five sources were therefore omitted from our search for circumstellar disks.

In Fig. 6.3 we show the intensity-weighted peak velocity (first moment) maps of CH_3CN $(12_3 - 11_3)$ for the remaining 15 sources in the CORE sample for which we detect this transition. The details of image weighting parameters and the associated beam sizes as well as the ranges over which the emission is integrated for the creation of the moment maps are listed in Table 6.1. The corresponding zeroth and first moment maps can be found in Appendix B.1. The threshold used for creating the moment maps is set to 6σ where sigma is estimated as the RMS noise in an emission-free area in the channel that contains the peak of CH_3CN $(12_4 - 11_4)$ transition, also listed in Table 6.1. We detect velocity gradients across almost all 15 cores with magnitudes of a few km s^{-1}, depicted by black dotted lines in the panels, spanning a physical

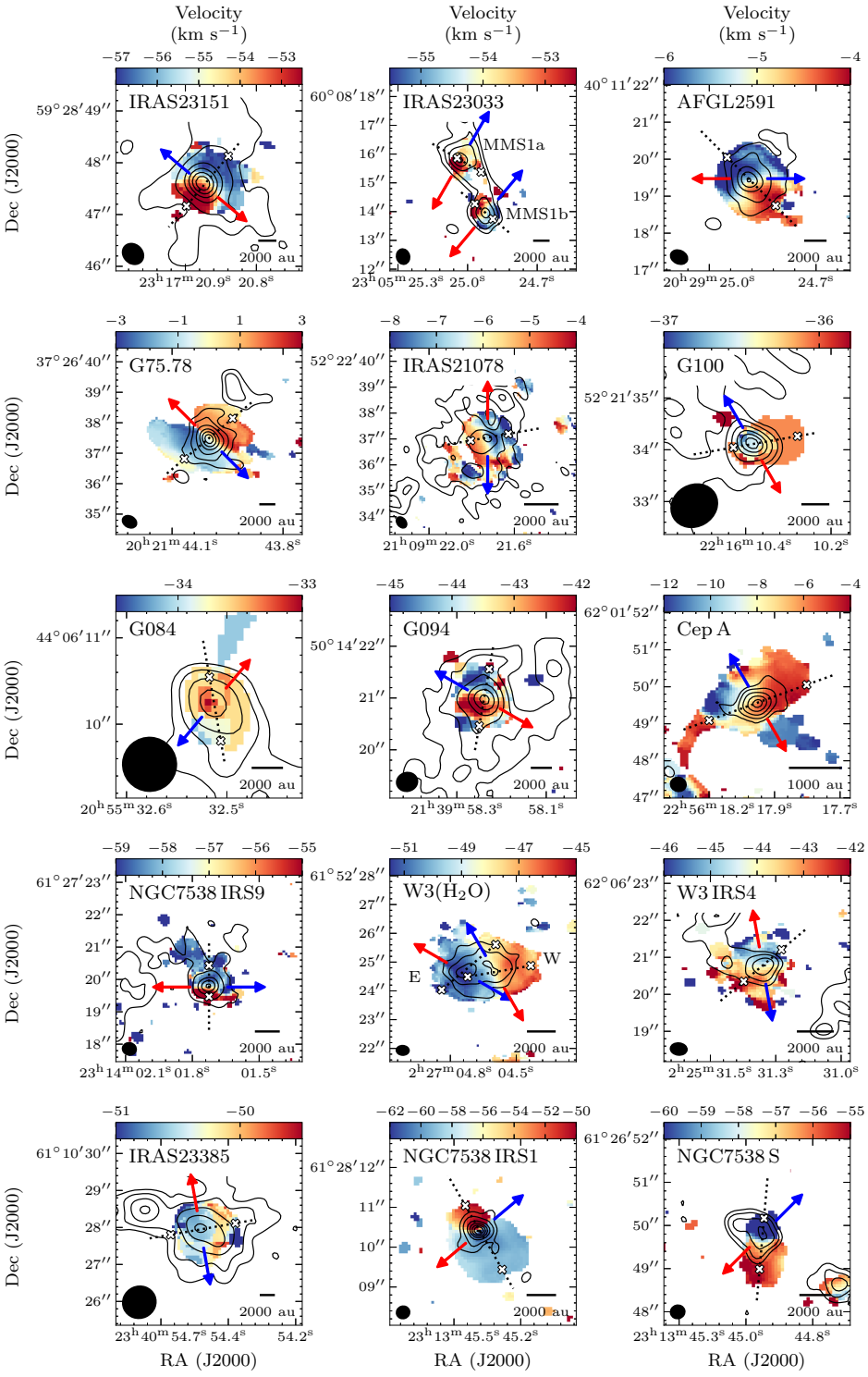

Figure 6.3: Intensity-weighted peak velocity (first moment) maps of CH_3CN ($12_3 - 11_3$) showing the dense gas kinematics for 15 of the 20 sources in the CORE survey. The contours correspond to the 1.37 mm continuum as described in Fig. 6.2. The synthesized beam is shown in the bottom left corner and a scale bar in the bottom right corner of each panel. The blue and red arrows correspond to the estimated directions of bipolar blueshifted and redshifted molecular outflows, respectively. The dotted lines indicate the position of the strongest velocity gradient tracing the disk, i.e. perpendicular to the rotation axis. The edges of the assumed disk extent are marked with an ×. When displayed in Adobe Acrobat, it is possible to switch to the decomposed velocity map and back to the first moment map for comparison.

projected distance of 2000–8000 au. The bulk of the emission for most sources is covered by many beams, allowing us to properly resolve these objects, with the exception of the sources for which we degraded the resolution in order to detect CH_3CN. In these cases, the extent of the emission is only one or two beams across. For two of these sources in particular (G084 and G100), the velocity gradients in the first moment maps do not seem convincing. This is partially a result of inherent downfall and sensitivity of intensity-weighted first moment maps to noise in the spectrum and any asymmetries in the line profile (see Teague & Foreman-Mackey 2018 for a short overview). We have fitted Gaussian profiles to the spectra of all sources using the *Spectral-Cube* tool within the *PySpecKit* package in Python (Ginsburg & Mirocha 2011; Ginsburg et al. 2019) in order to overcome this issue and be able to detect the velocity field beyond the 6σ threshold used in the creation of moment maps which can often mask more than needed. In the decomposed velocity maps we detect emission that is slightly more extended in all directions for all sources, and for the two sources under question here, the velocity gradients become clearer than in the first moment maps, albeit not so strong, with amplitudes below 1 km s^{-1}, making them not the best disk candidates.

The velocity gradients observed using the dense gas tracer CH_3CN are consistent and coherent with the motion of more diffuse gas on larger scales as traced by H_2CO (see Fig. 6.2). Furthermore, IRAS23033 consists of two sub-cores, MMS1a and MMS1b, both of which have some detection of CH_3CN with MMS1b being the brighter of the two and located at the edge of the filamentary structure with gas flowing along the filament onto this core (Bosco et al. 2019). Similarly, W3 (H_2O) consists of two sub-cores, E and W corresponding to the eastern and western cores, respectively, approximately 2000 au apart (Ahmadi et al. 2018). Therefore, we have detections of CH_3CN with velocity gradients across almost all of them for 17 cores in total. The position angles of the velocity gradients are listed in Table 6.1, defined with respect to the east-west axis and counterclockwise.

In Fig. 6.4 we show the position velocity maps of CH_3CN ($12_3 - 11_3$) along cuts across the strongest velocity gradients as depicted by dotted lines in Fig. 6.3. The yellow curves correspond to Keplerian rotation profiles with $v(r) = \sqrt{GM/r}$ for enclosed masses listed in Table 6.3 (described further in Sect. 6.6.2). It is clear that in many of the sources the PV diagrams do not resemble differential rotational motion of the gas well, but rather mimic rigid-body-like rotation ($v(r) \propto r$). Furthermore, the existence of excess emission in the two quadrants opposite where the rotational motions of the disk are expected correspond to the presence of infalling material from the envelope (e.g. see models of Ohashi et al. 1997a and Tobin et al. 2012). While weak (or lack of) differential rotation could be an indicator that these rotating objects may not be disks, we have shown through synthetic observations in Chapter 5 that in fact PV diagrams of poorly resolved disks do often mimic rigid-body-like rotation with excess infall contributions in opposite quadrants as the disk and envelope material become blended. Therefore, the use of PV diagrams to rule out the existence of disks is a challenging task.

From the PV plots, we see that some sources like AFGL2591, G75.78, IRAS21078, W3 (H_2O) E and and NGC7538 IRS1 are better disk candidates than others as some gas is found at high-velocities close to the central object at zero offset, with lower velocity gas further out. The PV plot of Cep A HW2 is particularly interesting, as it has a very extended nature, with

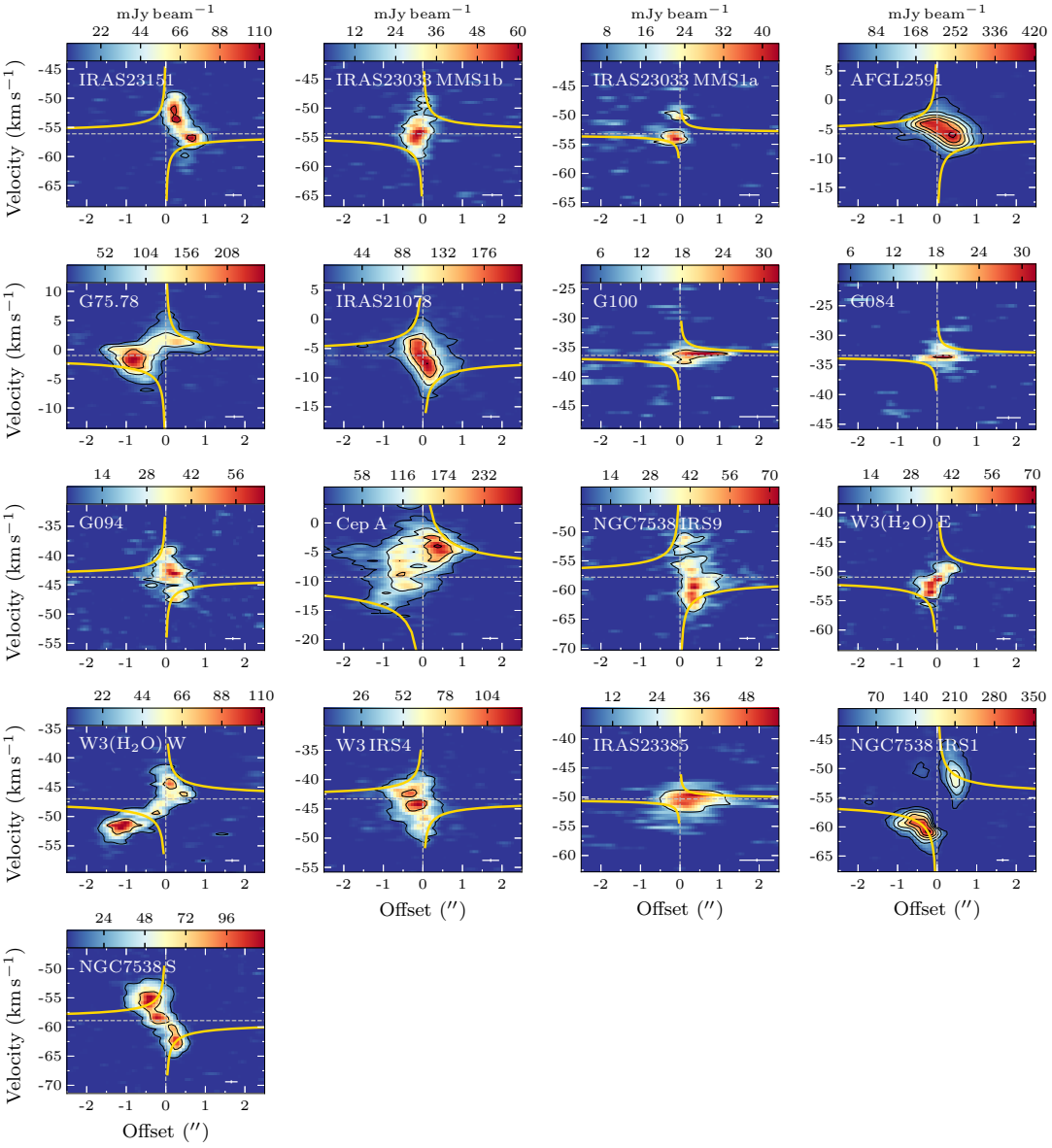

Figure 6.4: Position–velocity (PV) plots of CH_3CN ($12_3 - 11_3$) along cuts in the direction of rotation as depicted by dotted lines in Fig. 6.3. The width of the cut is the size of a synthesized beam to increase the S/N ratio. The PV plots of W3 (H_2O) E and W3 (H_2O) W make use of the A-array only observations in order to gain more resolution and detangle the two cores from the circumbinary material. PV plots for all other sources make use of the full dataset observed in the CORE survey. The contours correspond to the 6σ level increasing in steps of 24σ. Yellow lines show the Keplerian rotation curves for enclosed masses listed in Table 6.3 for each source. The crosses in the bottom right corners correspond to the spatial and spectral resolutions.

a significant amount of emission present in the top-left quadrant associated with infall motions. In fact, using the 3D velocity field of 6.7 GHz CH_3OH masers, Sanna et al. (2017) show that the velocity field in Cep A HW2 is dominated by an infall component from a radius of 900 au (~1.3″) down to 300 au (~0.4″) where a rotational component associated with an accretion disk becomes dominant.

6.4 Molecular outflows

We make use of outflow tracing molecules, mainly the $(2-1)$ transition of CO (from our single-dish IRAM 30-m observations) and its ^{13}CO isotopologue (from our single-dish, NOEMA, and merged observations), to infer the directions of molecular outflows being driven by these YSOs. In Appendix B.2 we show the intensity maps of the blue and redshifted gas with respect to the systemic velocity of the source by integrating over the blue and red wings of the emission for these transitions as well as for C^{18}O $(2-1)$ and SO (6_5-5_4). Since the interferometer filters out most of such extended emission, we mostly make use of the IRAM 30-m data with a field of view of 1.5′ by 1.5′ (and half-power beam width of ~11″ at this frequency) to infer the structure of these large-scale flows, however, the interferometer and in particular the combination of the interferometric with single-dish observations for ^{13}CO$(2-1)$ are particularly useful in detangling the ejection points of the expected outflows especially in cores which have substructure as multiple outflows may exist being driven by other (sometimes lower mass) objects (e.g. the case of W3 (H_2O) presented in Fig. 4.4 of Chapter 4).

In all 17 cores, we detect extended high-velocity CO $(2-1)$ emission in the vicinity of the most luminous source in the field, while not all sources have clear extended high-velocity ^{13}CO$(2-1)$ emission (e.g. NGC7538 S or IRAS21078). In many of the sources, we detect clear bipolar molecular outflows (e.g. IRAS23151, AFGL2591, G084, G094, Cep A, W3 (H_2O)) while the case is more complex for others. As an example, for NGC7538 IRS1, our data suggest a bipolar outflow in the NW-SE direction confirmed by molecular outflows from other works (e.g. Keto 1991; Davis et al. 1998; Beuther et al. 2013), while an ionized jet in the N-S direction has been detected by others (e.g. Gaume et al. 1995; Sandell et al. 2009; Moscadelli & Goddi 2014; Goddi et al. 2015). In fact this ambiguity can be attributed to the fact that further fragmentation has been reported within this source by higher resolution observations of Beuther et al. (2017a) in the centimeter regime, made more complex by the fact that the central source is already ionizing a hypercompact H II region. In fact, NGC7538 IRS1 is the only source within the CORE survey for which we detect the molecular line transitions in absorption against the strong continuum background at the peak position of the continuum emission spanning an area roughly the size of the synthesized beam. Furthermore, for sources which are in complex environments such as IRAS23033 and W3IRS4, establishing an exact direction for the molecular outflow(s) is difficult. For IRAS23033, we adopt the directions of outflows determined by Bosco et al. (2019) who performed a detailed analysis of this region using the same CORE data. Similarly, for W3IRS4, Mottram et al. (subm.) provided an in-depth study of this region using the CORE data. Considering there exist infrared K_s band data (Bik et al. 2012) and 4.5 μm *Spitzer* IRAC continuum images that show emission extending from W3IRS4 to the north, with the 4.5 μm emission possibly associated with shocked H_2 emission (see, e.g. Cyganowski et al. 2008), Mottram et al. (subm.) adopted an outflow direction roughly in the N/NW-S/SE direction, which is roughly what we settle on here as well.

The estimated directions of blueshifted and redshifted molecular outflows are shown on Fig. 6.3 as blue and red arrows, respectively. Interestingly in almost all cases, the velocity gradients seen in CH_3CN (12_3-11_3) are perpendicular to the direction of the molecular outflows,

simplifying the explanation for the velocity gradients probed by dense gas tracers to being associated with rotation motions, therefore making these objects excellent disk candidates. The exceptions to this finding are W3IRS4 and possibly IRAS23033 MMS1a for which the velocity fields in CH_3CN seem to trace the outflows, and G084 and G100 which have very weak velocity gradients.

6.5 Temperature distribution

We make use of the *XCLASS* software within *CASA* to fit pixel-by-pixel the spectra of $CH_3CN\,(12_K - 11_K)\,K = 0 - 6$, including $CH_3{}^{13}CN\,(12_K - 11_K)\,K = 0 - 3$, under the assumption of LTE, which is valid in such dense environments. The recipe is as outlined in Sect. 2.3 of Chapter 2. In summary, the user provides initial guesses and sets allowed ranges for a set of parameters (column density, rotational temperature, line velocity, linewidth, and source size) for which the software solves the radiation transfer equation and through a minimization routine modifies these parameters until the best fit is found to the spectrum. The software then creates maps for each of the fitted parameters. For each source, we set the expected observed isotopic ratio according to its galactocentric distance, $D_{\rm GC}$, based on estimates of Wilson & Rood (1994): $^{12}C/^{13}C = (7.5 \pm 1.9)D_{\rm GC} + (7.6 \pm 12.9)$. Furthermore, we only fitted pixels above 6σ detection limit (σ values and isotopic ratios are listed in Table 6.1).

In Fig. 6.5, we show the rotational temperature maps. Assuming the lines are thermalized, rotational temperature can be directly taken as the kinetic temperature of the gas in these dense regions. Median temperature values are listed in Table 6.2 and are on average between 100–200 K. Because the parameters, in particular column density and temperature, have a dependency on each other, it is useful to have a look at the maps of CH_3CN column density, line velocity, linewidth, and source size when analysing the spatial distribution of gas temperatures (see Appendix B.3). In the following, we aim to summarize some of the trends we find for the physical conditions probed by CH_3CN.

In the case of a true disk, temperature and column density are expected to decrease with increasing radius. While for some of the sources in our sample we do see such a behaviour (e.g. AFGL 2591, W3 (H_2O) E, W3 (H_2O) W, Cep A), the distribution of temperature is often not as smooth and symmetric as one would expect. Associating substructure in the temperature maps with underlying substructure in the disk is not straight forward. In fact, we have shown in Chapter 5 (Ahmadi et al. 2019) that temperature is overestimated in regions of the disk with non-Gaussian line shapes as well as multi-component line profiles to which we only fit one component. Such multi-component line profiles are in fact expected as we start to resolve the infalling material from the envelope onto the disk, which results in gas motions at various velocities along the line of sight depending on the inclination of the object. Furthermore, another caveat of the *XCLASS* modelling scheme is the fact that it does not account for density and temperature gradients along the line of sight.

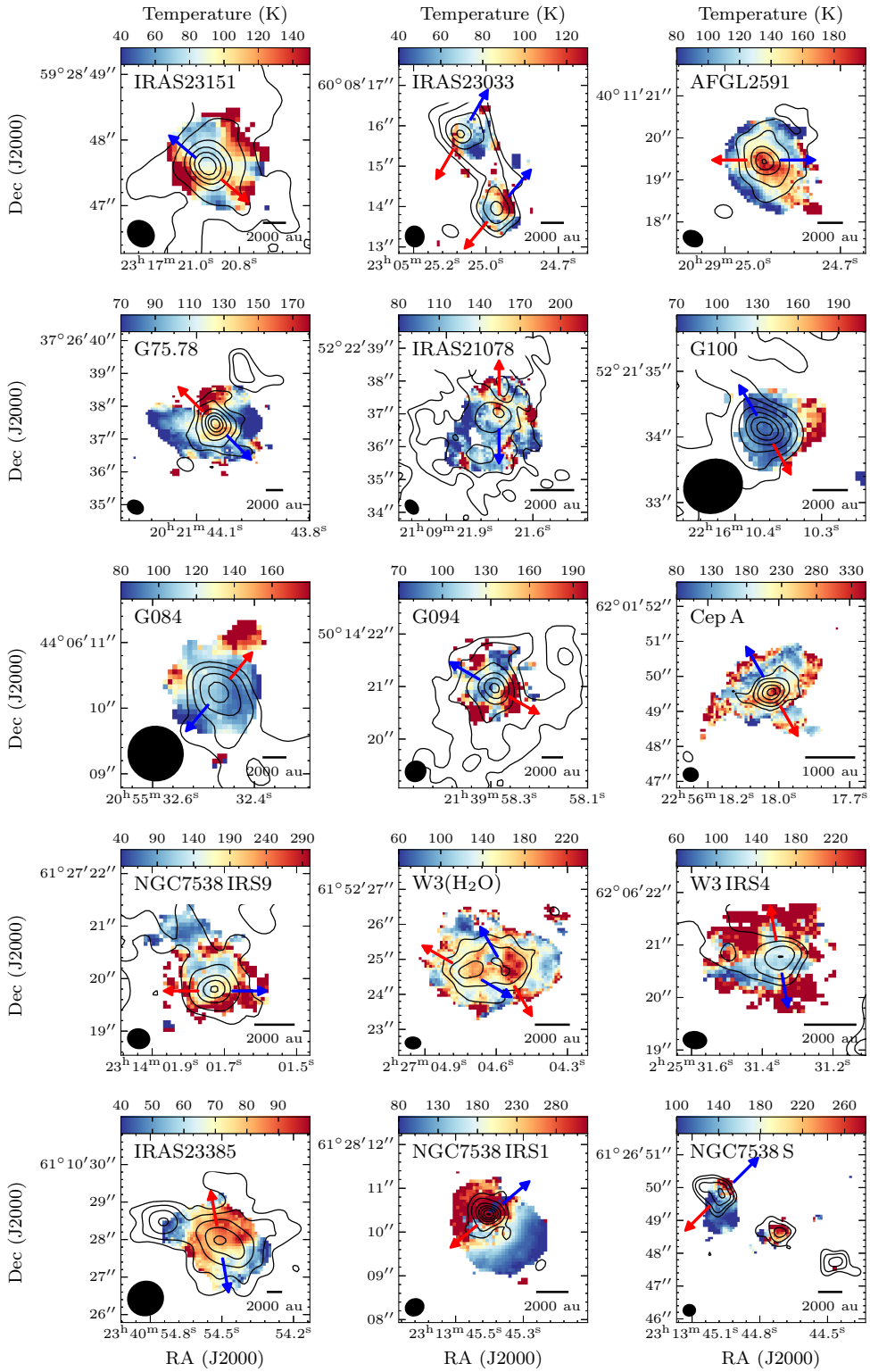

Figure 6.5: Rotational temperature maps obtained by fitting CH_3CN (12_K-11_K) $K=0-6$ and $CH_3{}^{13}CN$ (12_K-11_K) $K=0-3$ lines with *XCLASS*. The contours correspond to the 1.37 mm continuum as described in Fig. 6.2. The synthesized beam is shown in the bottom left corner and a scale bar in the bottom right corner of each panel. The blue and red arrows correspond to the estimated directions of bipolar blueshifted and redshifted molecular outflows, respectively.

Table 6.1: Observational parameters for the disk candidates within the CORE survey.

Source	Weighting	Beam ($''\times''$, PA)	Res.[a] (au)	$\sigma_{\rm cont}$[b] (mJy beam^{-1})	$\sigma_{\rm line}$[c] (mJy beam^{-1})	Disk PA (°)	$R_{\rm blue}$ (au)	$R_{\rm red}$ (au)	Extent (au)	$v_{\rm LSR}$[d] (km s^{-1})	Moment Range (km s^{-1})	$\frac{^{12}C}{^{13}C}$
IRAS23151	robust 0.1	0.42×0.35, 47°	1280	0.19	3.60	50	4210	2940	7150	−53.1	$-64 \rightarrow -48$	93
IRAS23033 MMS1a	robust 1	0.49×0.43, 9°	1980	0.46	3.86	150	1030	1810	2840	−53.0	$-59 \rightarrow -48$	81
IRAS23033 MMS1b	robust 1	0.49×0.43, 9°	1980	0.46	3.86	140	520	1300	1820	−54.4	$-59 \rightarrow -48$	81
AFGL2591	robust 0.1	0.45×0.34, -115°	1310	0.60	5.91	135	2680	3400	6080	−5.6	$-11 \rightarrow 0$	68
G75.78	robust 0.1	0.45×0.34, 59°	1510	0.60	5.19	40	3920	3920	7840	0.2	$-7 \rightarrow 5$	67
IRAS21078	robust 0.1	0.45×0.31, 39°	570	0.60	4.04	10	1220	990	2210	−7.0	$-15 \rightarrow 2$	69
G100	natural	0.90×0.79, 115°	2950	0.08	3.89	10	1360	3270	4630	−36.5	$-43 \rightarrow -33$	78
G084	robust 5	0.82×0.81, 70°	4500	0.10	4.21	10	2470	1650	4120	−33.4	$-43 \rightarrow -30$	77
G094	robust 0.1	0.38×0.36, -48°	1480	0.14	3.92	80	2900	2540	5440	−42.9	$-52 \rightarrow -35$	80
Cep A	robust 0.1	0.40×0.36, 77°	270	4.00	6.94	20	980	980	1960	−5.6	$-17 \rightarrow 2$	70
NGC7538 IRS9	robust 0.1	0.40×0.35, 78°	1020	0.30	4.27	90	1725	770	2495	−56.9	$-68 \rightarrow -47$	77
W3(H_2O) E	robust 0.1	0.42×0.30, 87°	720	4.50	6.81	40	1930	2970	4900	−51.6	$-57 \rightarrow -39$	79
W3(H_2O) W	robust 0.1	0.42×0.30, 87°	720	4.50	6.81	10	1930	2520	4450	−48.7	$-57 \rightarrow -39$	79
W3 IRS4	robust 0.1	0.43×0.30, 84°	730	0.60	4.31	40	1330	1330	2620	−44.0	$-54 \rightarrow -36$	79
IRAS23385	robust 5	0.93×0.88, 113°	4440	0.25	5.02	10	3980	4700	8680	−50.6	$-57 \rightarrow -43$	90
Pilot study												
NGC7538 IRS1	robust 0.1	0.41×0.36, 118°	1030	10.0	3.88	120	2980	1990	4970	−56.3	$-66 \rightarrow -45$	78
NGC7538 S	robust 0.1	0.31×0.29, 104°	800	0.60	3.12	85	990	2190	3180	−61.4	$-66 \rightarrow -50$	78

Note: Images are from a combination of configurations A, B, and D arrays of NOEMA with the exception of pilot sources which lack D-array observations.

[a)] Average linear resolution, using distances from Table 3.1.

[b)] RMS noise in the continuum maps imaged with a robust 0.1 (uniform) weighting from Beuther et al. (2018). The corresponding values for S87 IRS1, S106, G108, G138, and G139 are 0.23, 1.25, 0.25, 0.16, and 0.17 mJy beam^{-1}, respectively.

[c)] RMS noise in the emission-free region in the channel that has the peak of emission for CH_3CN ($12_4 - 11_4$), therefore the unit is per 0.5 km s^{-1} channel.

[d)] Peak velocity of CH_3CN ($12_3 - 11_3$) at the position of the continuum peak.

Interestingly, for some of the sources we find the outskirts to be warmer than the inner regions (e.g. IRAS23151, W3IRS4, NGC7538IRS9). These regions have been legitimately modelled by *XCLASS* and are not results of fitting noisy spectra as we have masked out the regions below 6σ (although the spectra are noisier in the outskirts than inside the cores). For these sources, it is helpful to simultaneously look at the maps of other parameters (Figs. B.9–B.12). These outer hot components are almost always associated with large linewidths, consistent with our decomposed maps of linewidth which are able to cover more extended emission than the second moment maps. Interestingly, in many cases the hot component associated with broad linewidths are found in the ejection direction of the outflows. This hints at the possibility that these regions have been carved out by the molecular outflows allowing a deeper look into the cores, and/or are regions that may have been additionally heated by the outflows and associated shocks. This touches on an important point about high-mass star formation, that such bipolar outflows which form early may be critical in creating 'holes' through which intense radiation pressure is able to escape, allowing the accretion of mass onto their disks. The case of W3 (H_2O) is perhaps the most impressive, with G75.78 and G084 as other examples. (see the large linewidths and positions of outflows in Fig. B.11). Similarly, since establishing the direction of the outflows for W3IRS4 is difficult, supposedly spanning a cone of ~30° in the N/NW-S/SE direction with near- to mid-IR emission detected to the N/NW (Mottram et al. subm.), the extended warm component detected in the outskirts of this hot core is much more extended than in the other cases. The existence of this warm component is further justified considering the fact that this hot core is situated in an extremely dynamic environment, being fed with gas from an extended filament while being pinched on the other side by the UCH II region W3C.

6.6 Mass estimates

In the following section, we summarize our efforts in determining the mass of the (proto)stars and the gas surrounding them.

6.6.1 Gas mass

Assuming optically thin dust emission at 1.3 mm and a gas-to-dust mass ratio R of 150 (Draine 2011), we can convert the flux density F_ν of the continuum observations to a mass via

$$M = \frac{d^2 F_\nu R}{B_\nu(T_D)\,\kappa_\nu}, \tag{6.1}$$

where d is the distance to the source and $\kappa_\nu = 0.9\,\mathrm{cm^2\,g^{-1}}$ the dust absorption coefficient of thin ice mantles after 10^5 years of coagulation at a density of 10^6 $\mathrm{cm^{-3}}$ (Ossenkopf & Henning 1994). $B_\nu(T_D)$ is the Planck function, which at the wavelength under investigation follows the Rayleigh-Jeans law and is linearly dependent on the dust temperature T_D. We assume that gas and dust are in equilibrium and use the temperature maps presented in the previous section (Fig. 6.5) and the continuum maps shown in Fig. 6.1 to create maps of gas mass for each core. The only source with significant free-free contribution in the millimetre is NGC7538 IRS1 (Beuther et al. 2017a) which we subtracted from the millimetre continuum observations and used this corrected

Table 6.2: Gas mass estimates.

Source	F_ν [a] (mJy)	$T_{\rm median}$ (K)	$M_{\rm gas}(T_{\rm median})$ ($M_\odot$)	$M_{\rm gas}$ ($M_\odot$)
IRAS23151	55	100	9.9	10.7
IRAS23033 MMS 1a	57	72	5.6	6.2
IRAS23033 MMS 1b	47	84	3.9	3.9
AFGL2591	156	132	7.1	6.2
G75.78	123	103	9.6	8.1
IRAS21078	301	120	3.2	3.3
G100	10	91	0.9	0.9
G084	9	107	1.5	1.6
G094	27	132	2.8	3.0
Cep A	457	212	0.6	0.5
NGC7538 IRS9	59	173	1.3	1.3
W3(H_2O) E	669	149	9.9	9.4
W3(H_2O) W	544	149	8.1	7.0
W3 IRS4	59	221	0.6	0.9
IRAS23385	96	72	18.3	19.1
Pilot study				
NGC7538 IRS1	1820	172	42.9	19.5
NGC7538 S	67	119	2.3	1.8

[a] Continuum flux density for regions surrounding each core where CH_3CN is detected (see text for details).

map in the remainder of this work. Summing over all pixels with continuum emission above 6σ gives a final mass value for each core, listed in Table 6.2. As is common in the field to use one temperature value rather than produce temperature maps, for example if good thermometers were not observed, we also list gas mass estimates calculated using the median temperature values. For this calculation, the flux density is calculated by converting the units of each map from Jy beam^{-1} to Jy pixel^{-1}, masking out the continuum emission below 6σ as well as regions that do not have any detection for CH_3CN, and summing over the remaining pixels. For each of the two cores in IRAS 23033 the emission is integrated over a circular region encompassing each of the MMS1 sources. For W3 (H_2O) E and W, we simply define a vertical boundary in between the two cores similar to what we presented in Chapter 4 (Ahmadi et al. 2018). It is reassuring that gas mass estimates calculated using median temperatures are in almost all cases very close to the estimates that use the full temperature maps. The only exception is NGC7538 IRS1 which is the brightest continuum source in the sample. This large difference is because gas temperatures are warm (> 200 K) where the bulk of continuum emission is found, while regions outside of the continuum emission are colder lowering the value of the median temperature resulting in a higher mass estimate.

6.6.2 Protostellar mass

To determine protostellar masses, we fit Keplerian curves to 6σ edges of emission in the PV diagrams shown in Fig. 6.4 (the outermost contours) using the *KeplerFit*[1] package in *Python*. This method was first introduced by Seifried et al. (2016) who showed that fitting the edge of emission in PV diagrams provides a more accurate estimate for the enclosed mass than other methods. We benchmarked this method for our purposes in Chapter 5 where we showed that depending on how resolved disk/envelope systems are, fits to either the inner or outer parts of the PV diagrams may provide more accurate protostellar mass estimates. We further showed that fitting the PV plots of poorly resolved disk/envelope systems result in masses that are overestimated because emission is stretched over a larger area and high-velocity components of a disk that typically span small radii close to the central object are beam-smeared to lower velocities. For this reason, often velocities have a constant value at regions closest to the central object and have to be masked in order to obtain better fits to the PV curves.

Using the *KeperFit* code, we fit the 6σ edges of emission in the PV diagrams of $CH_3CN\,(12_K - 11_K)\,K = 3 - 5$ as they are not blended by other lines. We also create and fit PV plots of $CH_3CN\,(12_K - 11_K)\,K = 3 - 5$ transitions stacked together, which is particularly useful in sources for which the emission of individual CH_3CN transitions is weak. In Table 6.3 we present the mass estimates corresponding to the best fitted PV diagrams, where the goodness of the fit is determined according to its χ^2 value and confirmed by eye. The quality eye check is important as some fits may only have one or two data points to which any curve can be fitted. In such cases we chose the next best fitted curve that contained more data points. The Keplerian curves corresponding to the best mass estimates are shown as solid yellow lines on the PV diagrams shown in Fig. 6.4. The inner radii which were masked as well as LSR velocities estimated from the fitting routine are also listed in Table 6.3.

For G084, none of the CH_3CN transitions were adequate as their emission for this source is weak with only a few beams resolving the structure. In this case, we fitted other dense gas tracers such as OCS, HC_3N, C_2H_5N and $HCOOCH_3$ and chose the next best fitted curve, in this case OCS. The same was done for NGC7538 IRS1, but for a different reason. The PV plot of this source shows the emission of CH_3CN to be very extended in position such that the best fitted PV curves yield masses that are extremely large and unrealistic considering the luminosity of the region. Observations of thermal CH_3OH in the centimeter regime have shown that this source harbours two disk-like structures embedded within the same rotating circumbinary envelope Beuther et al. (2017a), therefore, fitting the PV diagrams of CH_3CN which also likely traces this envelope is not valid. For this reason, the PV diagrams of the rarer molecule C_2H_5CN resulted in better fits. On the other hand for the circumbinary envelope encompassing W3 (H_2O) E and W, we were able to detangle the gas contributions from each of the two cores by using only the observations from the most extended configuration (A-array) of NOEMA (Ahmadi et al. 2018, Chapter 4). In fact, the emission in the bottom-left quadrant of the PV plot for W3 (H_2O) W corresponds to W3 (H_2O) E, therefore the expected Keplerian curve corresponding to a mass of 10 $M_\odot$ shown as a yellow line properly fits the contribution from W3 (H_2O) W in the top-right quadrant. Similarly, NGC7538 S likely harbours multiple protostars as the continuum

[1]Developed by Felix Bosco, available at https://github.com/felixbosco/KeplerFit.

Table 6.3: Summary of results from fitting the PV diagrams using the Seifried et al. (2016) method.

Source	$R_{\rm masked}$ (au)	$M_{\rm PV}$ ($M_\odot$)	$v_{\rm LSR}$ (km s^{-1})	Best Fitted Transition
IRAS23151	1100	15	−56.1	$CH_3CN\,(12_3 - 11_3)$
IRAS23033 MMS 1a	400	2	−52.8	$CH_3CN\,(12_2 - 11_2)$
IRAS23033 MMS 1b	700	13	−54.0	$CH_3CN\,(12_2 - 11_2)$
AFGL2591	1000	16	−5.0	$CH_3CN\,(12_4 - 11_4)$
G75.78	2000	19	−0.4	$CH_3CN\,(12_5 - 11_5)$
IRAS21078	300	11	−6.3	$CH_3CN\,(12_5 - 11_5)$
G100	100	4	−36.6	$CH_3CN\,(12_2 - 11_2)$
G084	200	4	−35.0	$OCS\,(18 - 17)$
G094	1000	12	−45.5	$CH_3CN\,(12_{345} - 11_{345})$ stacked
Cep A	500	20	−8.6	$CH_3CN\,(12_4 - 11_4)$
NGC7538 IRS9	200	18	−54.8	$CH_3CN\,(12_2 - 11_2)$
W3(H_2O) E	(...)	10	−51.0	$CH_3CN\,(12 - 11)^*$
W3(H_2O) W	(...)	10	−47.0	$CH_3CN\,(12 - 11)^*$
W3 IRS4	800	8	−44.2	$CH_3CN\,(12_4 - 11_4)$
IRAS23385	200	2	−50.3	$CH_3CN\,(12_3 - 11_3)$
Pilot study				
NGC7538 IRS1	900	23	−53.4	$C_2H_5CN(25_{22,4} - 24_{22,3})$
NGC7538 S	1400	10	−54.7	$CH_3CN\,(12_2 - 11_2)$

* Based on A-array observations presented in Ahmadi et al. (2018) (Chapter 4).

emission has an elongated shape as well as the fact that $CH_3CN\,(12_3 - 11_3)$ has multiple peaks along this elongation (see Fig. B.1). Therefore, for this source, only one side of the PV plot was fitted. Finally, it is important to note that the sources for which low masses were estimated (IRAS23033 MMS1a, G100, G084, IRAS23385) do not necessarily harbour protostars with such low masses, but rather that the CH_3CN emission is not very extended, perhaps because the source may be more evolved.

6.7 Disk candidacy

In the following section, we present two methods to determine whether the sources under investigation are good disk candidates.

6.7.1 Timescales

Following Cesaroni et al. (2006), Beltrán et al. (2011) defined the term 'toroids' for rotating structures surrounding the most massive stars that span thousands of au with masses of several 10 $M_\odot$, much greater than the mass of the central protostar(s). These objects are thought to be

transient, feeding a central cluster of forming stars, each surrounded by their own centrifugally-supported disk on smaller scales. They are analogous to rotating infalling envelopes around forming low-mass stars. Beltrán et al. (2011) studied the stability of rotating structures around O- and B-type stars by plotting the ratio of free-fall timescale to the rotational period at the outer radius, $t_{\rm ff}/t_{\rm rot}$, versus $M_{\rm gas}$. The free-fall timescale represents the time it takes the gas to collapse under its own gravity. The rotational period at the outer radius is the time it takes the rotating structure to re-adjust its internal structure and stabilize after accreting new material. Simplifying the equations given in Sánchez-Monge et al. (2014), we calculated the rotational period via

$$\begin{aligned} t_{\rm rot} &= \frac{2\,\pi\,R}{v_{\rm rot}} \\ &= 29.8\left(\frac{R}{\rm au}\right)\left(\frac{v_{\rm rot}}{\rm km\ s^{-1}}\right)^{-1}\ {\rm yr}, \end{aligned} \tag{6.2}$$

where $v_{\rm rot}$ is the rotational velocity at the outer radius, R. Moreover, the free-fall timescale is calculated according to

$$\begin{aligned} t_{\rm ff} &= \sqrt{\frac{3\,\pi}{32\,G\,\rho}} \\ &= 0.195\left(\frac{M_{\rm gas}}{M_\odot}\right)^{-0.5}\left(\frac{R}{\rm au}\right)^{1.5}\ {\rm yr}. \end{aligned} \tag{6.3}$$

Because the rotating structures traced by CH_3CN are not always symmetrically distributed on the position of the continuum peak, we calculate the rotational period and free-fall timescale for the redshifted and blueshifted sides of the rotating structures separately. We estimate the radii of the blueshifted and redshifted sides ($R_{\rm blue}$ and $R_{\rm red}$) as the distance from the continuum peak to the edge of the CH_3CN emission along the strongest velocity gradient (dotted lines on Fig. 6.3). We manually set the positions of $R_{\rm blue}$ and $R_{\rm red}$ if the velocity field appears to have a turnover close to the edge of the emitting region (e.g. blueshifted side of Cep A) or if the cores are blended (e.g. blueshifted side of W3 (H_2O) W). The positions of $R_{\rm blue}$ and $R_{\rm red}$ are marked by an $\times$ in Fig. 6.3. $v_{\rm rot}$ is estimated by subtracting the peak velocity at these positions from the LSR velocity measured at the continuum peak position (listed in Table 6.1).

In Fig. 6.6, we show the plot of $t_{\rm ff}/t_{\rm rot}$ versus $M_{\rm gas}$ for the redshifted and blueshifted sides of the 17 cores under investigation. The black dashed line corresponds to the theoretical curve corresponding to $t_{\rm ff}/t_{\rm rot}$ for a disk of mass $M_{\rm gas}$ rotating about a star with mass $M_* = 10\ M_\odot$. This is obtained by substituting $v_{\rm rot} = \sqrt{G(M_{\rm gas}+M_*)/R}$ in the above equations such that

$$\frac{t_{\rm ff}}{t_{\rm rot}} = \sqrt{\frac{M_{\rm gas}+M_*}{32\,M_{\rm gas}}}. \tag{6.4}$$

In a review by Beltrán & de Wit (2016), the authors created the $t_{\rm ff}/t_{\rm rot}$ versus $M_{\rm gas}$ plot for the largest sample of intermediate and high-mass protostars from the literature and confirmed the findings of Beltrán et al. (2011), that disks and toroids are kinematically and dynamically different structures, populating different regimes in this plot. Toroids contain more gas mass

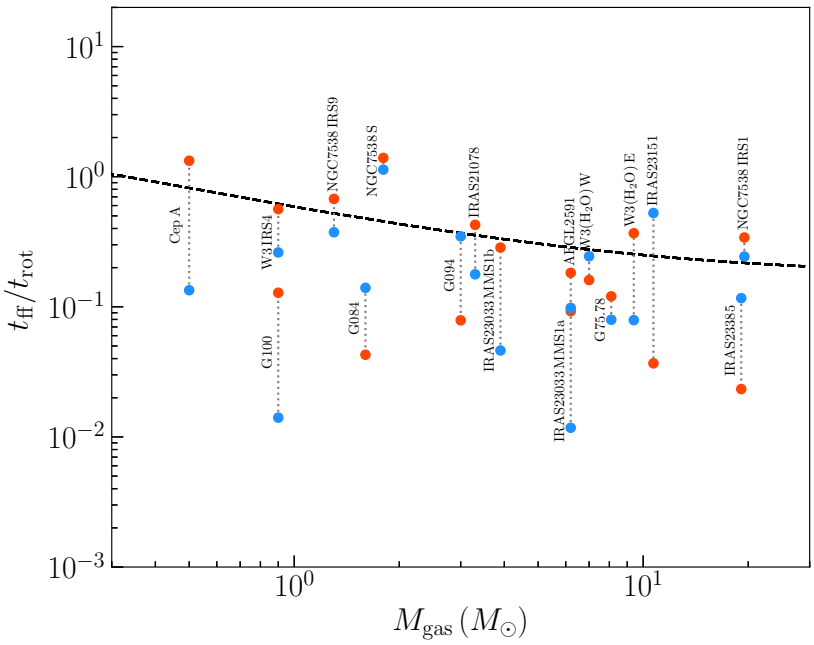

Figure 6.6: Ratio of free-fall to rotational timescale as a function of disk gas mass, showing most of the sources with CH_3CN velocity gradients are rotationally supported. The blue and red dots correspond to the values calculated based on the rotational velocities at the edges of the disks on the blueshifted and redshifted sides, as depicted by crosses in Fig. 6.3 and listed in Table 6.1. The black dashed line corresponds to theoretical curve corresponding to $t_{\rm ff}/t_{\rm rot}$ for a disk of mass $M_{\rm gas}$ rotating about a star with mass $M_* = 10\ M_\odot$ (see Eq. 6.4).

and are less rotationally supported with lower $t_{\rm ff}/t_{\rm rot}$, while for centrifugally supported disks in Keplerian rotation the infalling material has enough time to settle onto the disk, therefore the rotational timescale is shorter and the $t_{\rm ff}/t_{\rm rot}$ is higher. Comparing Fig. 6.6 to Fig. 14 of Beltrán & de Wit (2016), all of our sources lie in the regime corresponding to true disks. Interestingly, the sources which have lower $t_{\rm ff}/t_{\rm rot}$ ratios are those which we had already identified as poor disk candidates (e.g. G100, G084, IRAS23033 MMS1a).

6.7.2 Specific angular momentum

For a molecular cloud to form a star, it must lose many orders of magnitude in specific angular momentum (j). Various mechanisms at a multitude of scales can contribute to this loss (and transport) of angular momentum (e.g. disks, jets, outflows, winds, magnetic fields). It has been shown that on dense core scales (0.1 pc), the local specific angular momentum (i.e. the product of $v_{\rm rot}$ and r) scales as $r^{1.6}$ (Goodman et al. 1993), down to a scale of about ~6000 au where the specific angular momentum is conserved until disk scales (~100 au). Ohashi et al. (1997b) was first to measure a constant j value of ~ 10^{-3} km s^{-1} pc for this intermediate regime and attribute it to protostellar envelopes that are dynamically collapsing. Below ~100 au, Keplerian rotation dominates allowing material to move inward and angular momentum outward. A review by Belloche (2013) compiles most of the relevant observations from literature on this topic and presents the correlation of the specific angular momentum with radius from disk to core scales in their Fig. 8. In a recent work, Pineda et al. (2019) calculated the specific angular momentum

radial profiles toward two Class 0 objects and a hydrostatic core candidate in Perseus and found a power-law relation with $j \propto r^{1.8}$ from 800–10000 au. These authors concluded that because the power-law index is between that of solidbody rotation ($j \propto r^2$) and pure turbulence ($j \propto r^{1.5}$), the influence of the dense core's initial level of turbulence is still present even down to 1000 au, inherited from the turbulent parental molecular cloud.

Since the above findings are based on observational evidence from low-mass star-forming regions, it is important to calculate the specific angular momenta for our sources for comparison. In an effort to determine whether the rotational signatures that we have observed are more in agreement with core rotation, conservation of angular momentum, or differential rotation of a disk-like object, we calculate the specific angular momenta as a function of radius following the prescription in Belloche (2013). The rotational kinetic energy of a rotating object with mass M and radius r is $E_{\rm rot} = \frac{1}{2} I \Omega^2$, where Ω is the angular velocity and $I = \frac{2}{3} M r^2 \left(\frac{3-\alpha}{5-\alpha}\right)$ is the moment of inertia. The value of α is determined based on the power law density profile of the object such that $\rho \propto r^{-\alpha}$. Assuming $\alpha = 1.5$, the angular momentum is then $J = I\Omega$ with the specific angular momentum

$$j = \frac{J}{M} = \frac{2}{7} \Omega r^2. \tag{6.5}$$

The angular velocity is calculated by subtracting the LSR velocity, defined to be the velocity at the position of the continuum peak (see Table 6.1), from the centroid velocity $v_{\rm cen}$, at each position and dividing by the radius at that position with a sin i correction factor included for the inclination i:

$$\Omega = \frac{|v_{\rm cen} - v_{\rm LSR}|}{r \sin(i)}. \tag{6.6}$$

Putting together Eq. 6.5 and Eq. 6.6, we can calculate the specific angular momentum as a function of radius for each of the sources in the sample, such that

$$j_{\rm obs}(r) \sin(i) = \frac{2}{7} |v_{\rm cen} - v_{\rm LSR}| \, r. \tag{6.7}$$

Simulations and synthetic observations

In order to better understand the observational findings, we first analyse the expected specific angular momentum profiles for the numerical simulations presented in Ahmadi et al. (2019) (Chapter 5) to study the effects of inclination and angular resolution on j. The 3D radiation-hydrodynamic simulation under investigation follows the collapse of a massive core with 200 $M_\odot$ in gas and dust, which results in the formation and fragmentation of a massive disc. At this snapshot, the star has gained 10 $M_\odot$, being fed from a fragmented disk with a mass of 8 $M_\odot$. It is important to note that the simulation presented here does not include magnetic fields, which are an important ingredient for disk formation, and that an initial axially symmetric rotation profile $\Omega(r) \propto r^{-0.75}$ was adopted.

We calculate the observed specific angular momentum according to Eq. 6.7 using the first moment maps of CH_3CN $(12_3 - 11_3)$ at 10°, 30°, 60°, and 80°, along a cut in the E-W direction for the redshifted and blueshifted sides of the disk (see Fig. 5.5). Figure 6.7 shows the local specific angular momentum radial profiles for the simulations at the different inclinations as well as for a set of synthetic observations each with successively worse resolution. Similar to the

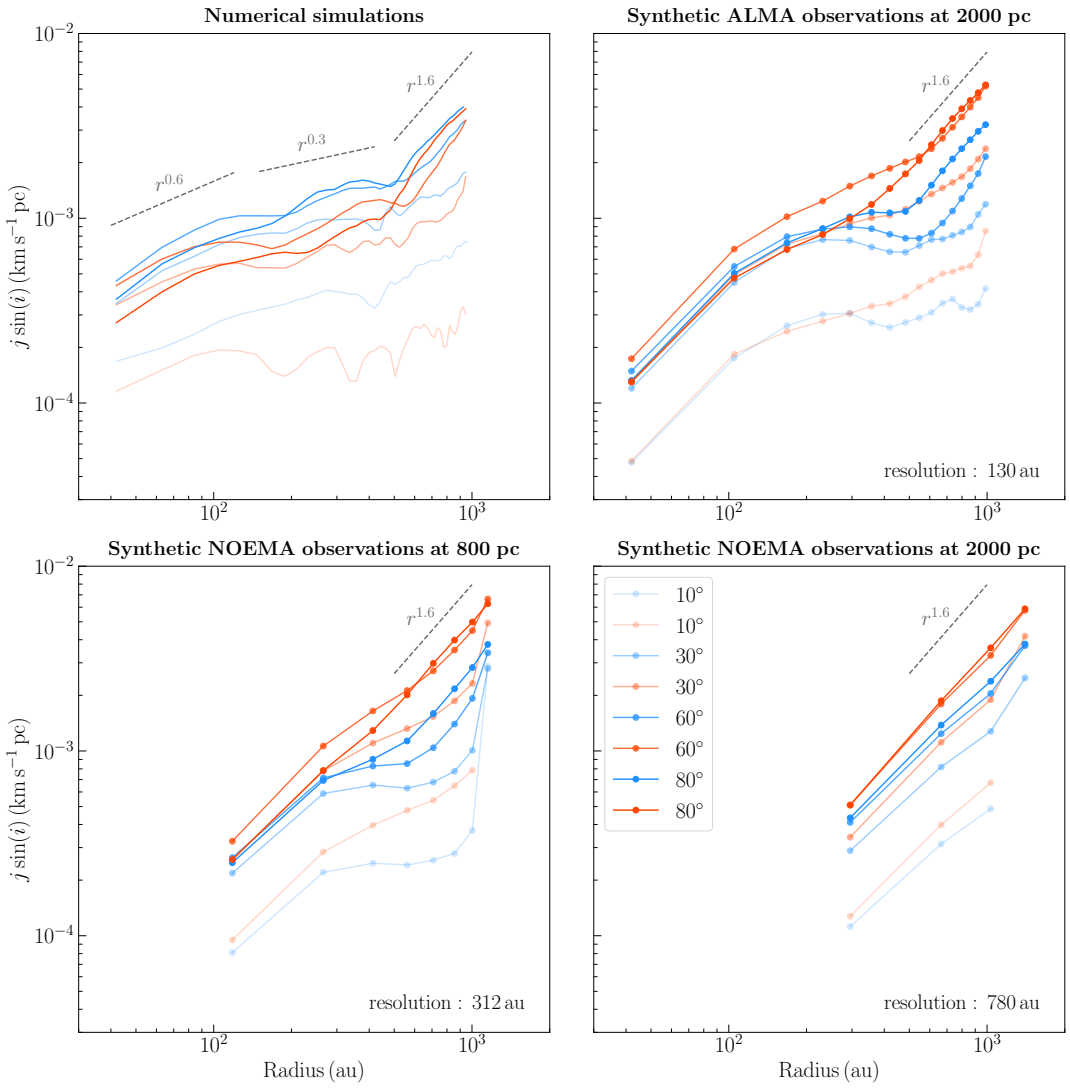

Figure 6.7: Specific angular momentum radial profiles for a high-resolution numerical simulation of a high-mass core having formed a massive disk that is feeding the central protostar, inclined to 10°, 30°, 60°, and 80° *(top left)*, their synthetic ALMA observations at 2000 pc *(top right)*, and synthetic NOEMA observations at 800 pc *(bottom left)* and 2000 pc *(bottom right)* (see Chapter 5). The blue and red colours correspond to the blueshifted and redshifted sides, respectively, and the hues correspond to the different inclinations. The distance between each neighbouring point is a half beam spacing.

observational findings for low-mass star formation, we find three distinct regimes in the j radial profile. The inner disk region ($r < 200$ au) actively accreting material onto the central protostar with $j \propto r^{0.6}$, an intermediate region where j is quite flat but not exactly constant, and the region beyond 700 au which is rather consistent with the $j \propto r^{1.6}$ relation that had been found for the rotation of dense cores. The intermediate regime has a significant amount of substructure as four fragments reside in this range of radii at this snapshot, being fed part of the disk material.The discontinuity at ~700 au roughly corresponds to the position at which the rotating core/envelope begins to dynamically collapse. The exact values for the minimum least-squared power-law fits to the various lines in this plot can be found in Appendix B.4. j has purposefully not been

corrected for the known inclination and we find that the simulation with more of a face-on view has almost an order of magnitude lower specific angular momentum with flatter radial profiles.

As resolution worsens, the substructure in the j radial profile becomes smoother with the power-law relations for the different regimes becoming more continuous and not as clear to disentangle. The specific angular momentum of the blueshifted side seems to have a more pronounced kink than the redshifted side, best visible in the synthetic observations at 800 pc. This is due to the existence of a fragment at this position, accreting some of the disk material and complicating its angular momentum at this position. At the scale of synthetic NOEMA observations at 2 kpc, the envelope and disk components become completely blended, with only one power-law relation seen across all scales, with $j \propto r^{1.6}$. Interestingly, there still exists a small shallowing of the slope (a kink) in the j profiles.

CORE observations

The observed specific angular momentum for the CORE sample were calculated according to Eq. 6.7 using the decomposed velocity maps of $CH_3CN\,(12_3 - 11_3)$ for each source along the cut with the strongest velocity gradient (dotted lines on Fig. 6.3) for the redshifted and blueshifted sides separately, and the resulting radial profiles are presented in Fig. 6.8 as circular data points with their errors, propagated from the error in velocity from the Gaussian decomposition, shown as regions with filled colours. The upward and downward pointing triangles correspond to the same procedure but performed for a cut with a position angle that is respectively 10° larger and smaller than the position angle of the cut with the strongest velocity gradient. The distance between two data points corresponds to half-beam spacing to ensure the data points are independent of each other, and the specific angular momenta plotted are averaged over a synthesized beam. Only the sources for which we had at least 5 data points (i.e. more than 2 beams) for either the redshifted or blueshifted sides are shown. Therefore, this criteria excludes IRAS23033 MMS1a, G084, G100, IRAS23385, and NGC7538 IRS9.

We can compare the angular momentum of each source with some estimate for the maximum value above which the core becomes gravitationally unbound. Because neither the rotation nor the density profile is expected to be uniform, we follow the approach in Zhang et al. (2018), assuming the structure is flattened with its mass growing linearly with radius (see Mestel disk: Mestel 1963). The maximum specific angular momentum can be written as

$$j_{\max}(r) = \frac{1}{2}\sqrt{G\,M(r)\,r}, \tag{6.8}$$

where $M(r)$ is the mass interior to r and is equal to $M_* + M_{\rm gas}(r)$. For the protostellar masses, we used the estimates from fitting the PV diagrams of dense gas tracers (see Sect. 6.6.2) unless other detailed studies of the sources using our data provided better estimates (see Table 6.5). We used the gas mass maps created using Eq. 6.1 and the temperature maps obtained from our radiative transfer modelling with *XCLASS* to calculate $M(r)$. The maximum specific angular momenta are overplotted on Fig. 6.8 with black lines, and the grey shaded areas surrounding the black curves correspond to the estimate for $j_{\max}$ with $M_* \pm 5\ M_\odot$. The maximum radius for which we calculate j shown in blue and red data points corresponds to the extent of the blueshifted

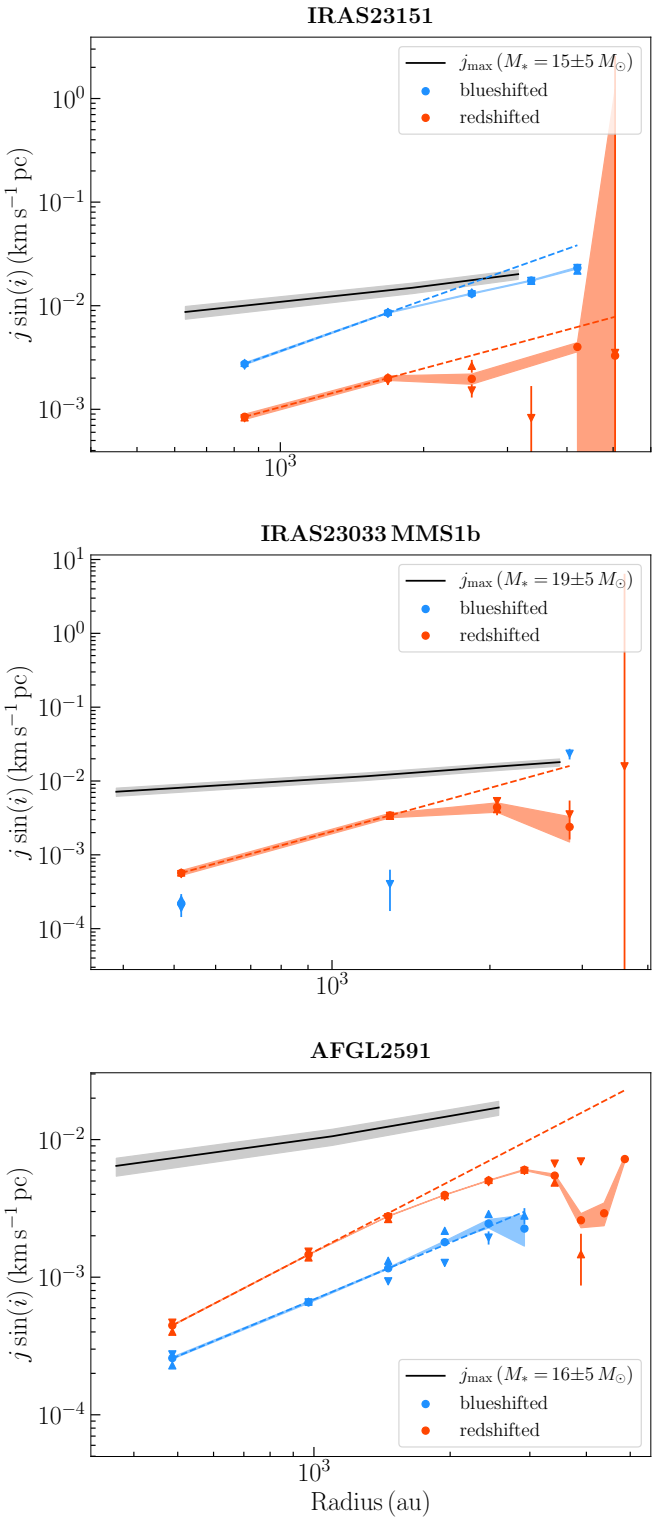

Figure 6.8: Specific angular momentum radial profiles calculated using Eq. 6.7 along the cut with the strongest velocity gradient (dotted lines in Fig. 6.4) *(circles)*, a cut with position angle $+10°$ *(triangles pointing up)*, and a cut with position angle $-10°$ *(triangles pointing down)* with respect to the strongest velocity gradient, for the redshifted and blueshifted sides of the emission. The blue and red filled regions show the error in j for the circles. The blue and red dashed lines show least-squared power-law fits to the first two datapoints and extrapolated to larger radii. The black curve shows the maximum specific angular momentum calculated using Eq. 6.8 for M_* listed in the subpanels with the grey region corresponding to $M_* \pm 5\ M_\odot$.

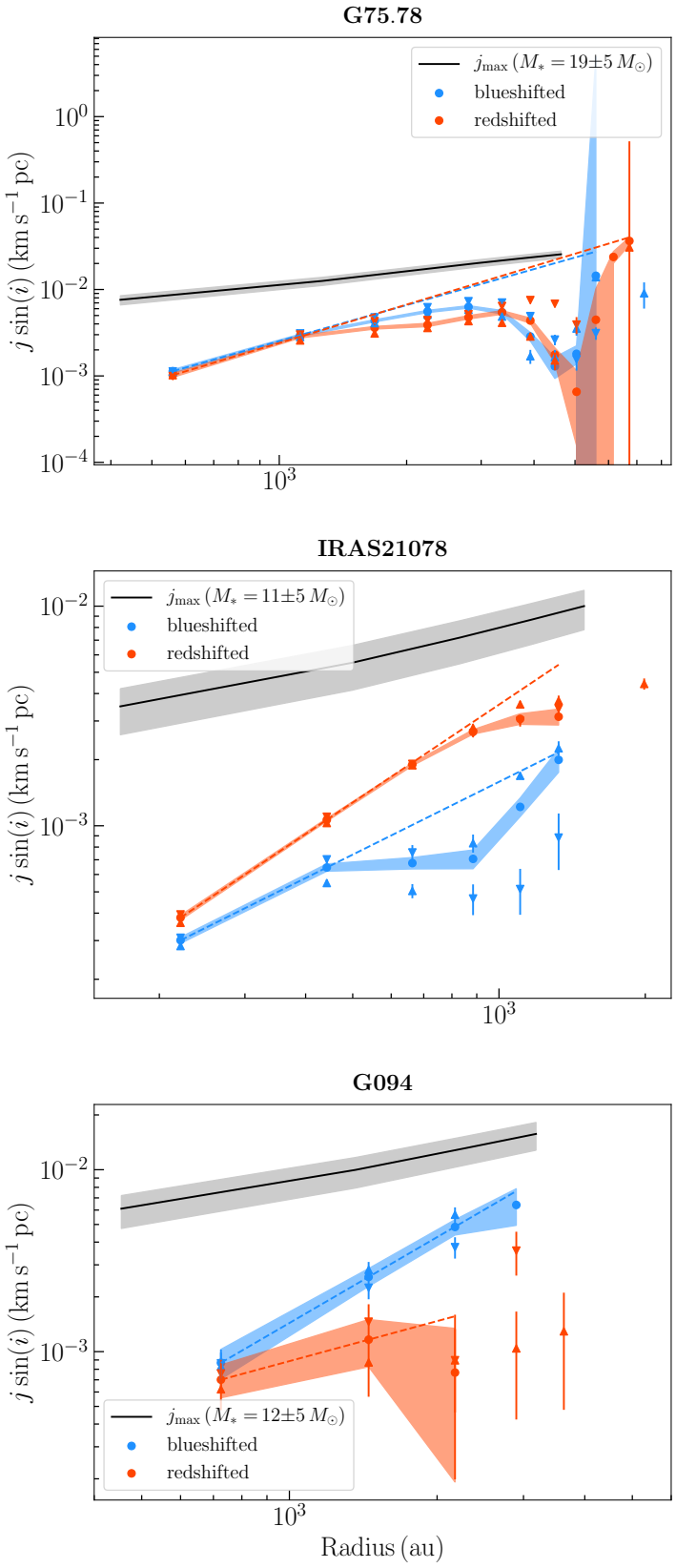

Figure 6.8: Continued.

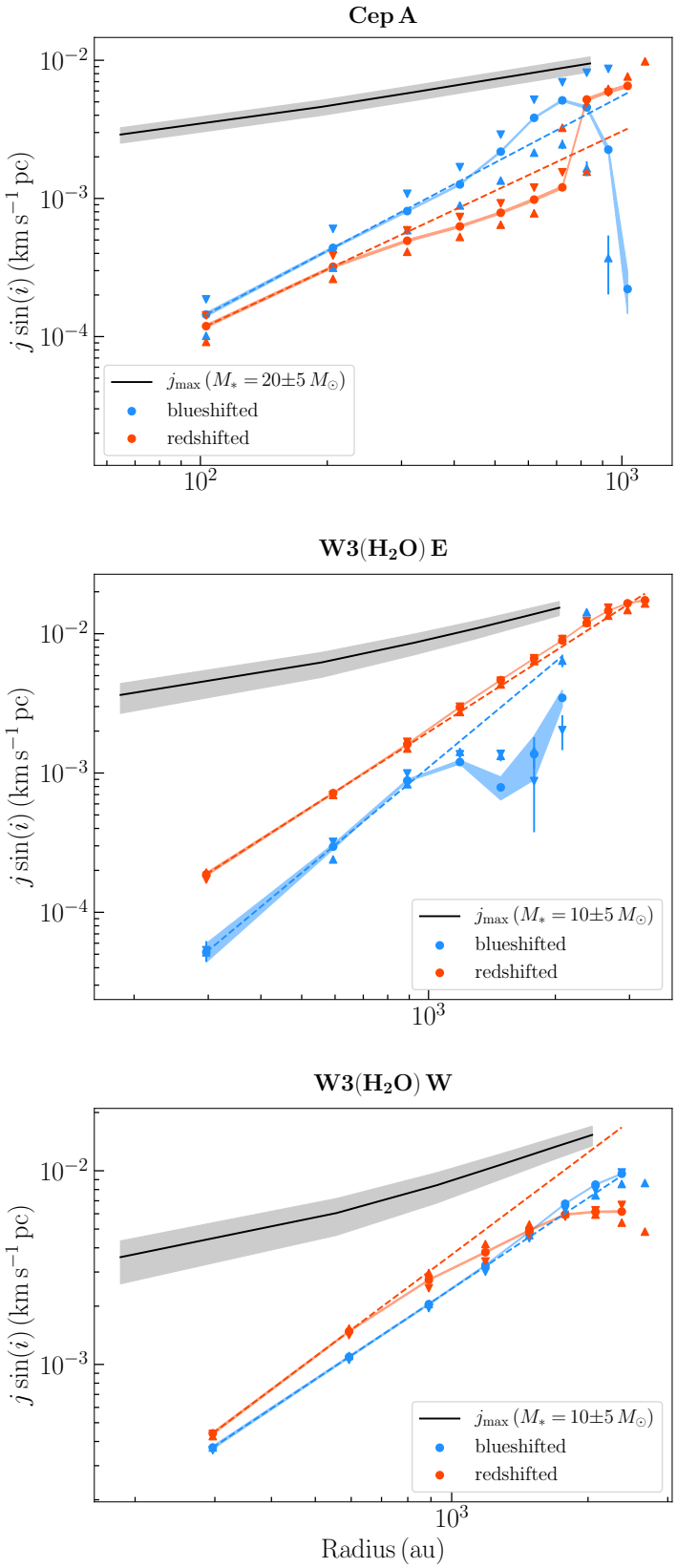

Figure 6.8: Continued.

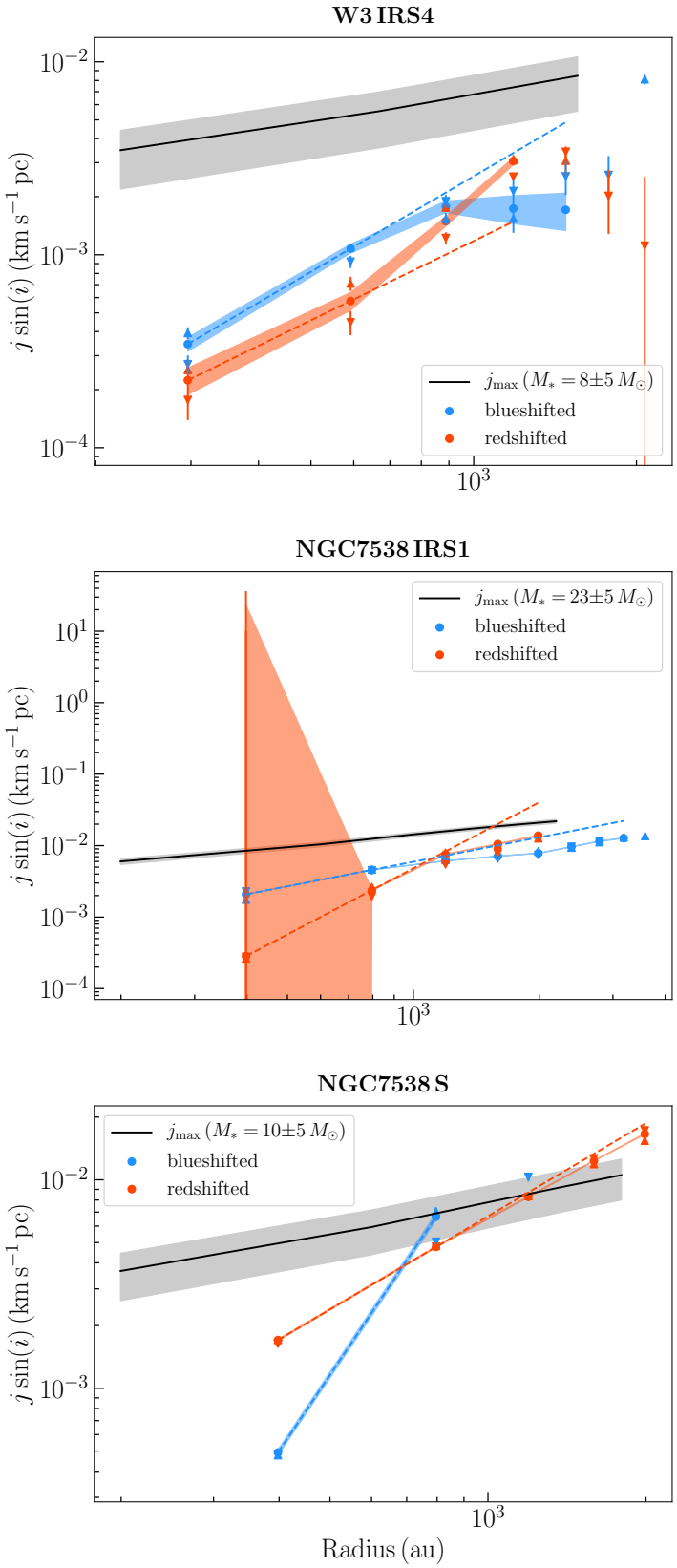

Figure 6.8: Continued.

Table 6.4: Fit parameters to the specific angular momentum radial profiles shown in Fig. 6.8.

Source	$a_{\rm blue}$	$a_{\rm red}$	$b_{\rm blue}$	$b_{\rm red}$
IRAS23151	1.6	1.2	−2.4	−3.0
IRAS23033 MMS 1b	(...)	2.0	(...)	−2.7
AFGL2591	1.4	1.7	−3.2	−2.8
G75.78	1.4	1.5	−2.6	−2.6
IRAS21078	1.1	1.5	−2.8	−2.4
G094	1.6	0.7	−2.8	−3.1
Cep A	1.6	1.4	−2.3	−2.5
W3(H_2O) E	2.5	1.9	−3.0	−2.7
W3(H_2O) W	1.6	1.7	−2.6	−2.4
W3 IRS4	1.6	1.4	−2.6	−2.9
Pilot study				
NGC7538 IRS1	1.1	3.1	−2.2	−2.3
NGC7538 S	3.8	1.5	−1.8	−2.2

Note: The heading parameters a and b satisfy the following relation: $j\sin(i) = 10^b\,(\frac{r}{1000\ \rm au})^a$, for the blueshifted and redshifted sides. Line profiles corresponding to these parameters are drawn as dashed lines on Fig. 6.8.

and redshifted gas emission (depicted with × markers on Fig. 6.3), while the extent of the black curves corresponding to $j_{\rm max}$ mark the edge of the continuum emission at 6σ. Comparing this curve with the observed j radial profiles, we see that almost all cores are gravitationally bound as they lie below $j_{\rm max}$ with the exception of NGC7538 S which has an elongated shape in both the continuum and CH_3CN towards the redshifted side - a sign that further fragmentation has taken place.

From the specific angular momentum radial profiles we see that all sources span a range in j of 1–2 orders of magnitude, on average around $\sim 10^{-3}$ km s^{-1} pc, and exhibit a shallowing of their power-law slopes. The dashed lines in Fig. 6.8 correspond to least-squared power-law fits to the first two datapoints and extrapolated to larger radii to clearly show this behaviour. The power-law slopes and intercepts corresponding to these dashed lines are listed in Table 6.4. For some sources the decrease in j towards conservation of angular momentum is more subtle (e.g. IRAS23151, IRAS23033 MMS1b, G094, NGC7538 S) than other sources (e.g. G75.78 and Cep A). For AFGL2591 and G75.78 the decrease in j is followed by a sharp increase as a result of the complex velocity structures in the outskirt of these objects (see Fig. 6.3), perhaps as a result of material flowing from larger scales. The redshifted side of W3 (H_2O) E and the blueshifted side of W3 (H_2O) W are contaminated by the emission from each other and have a similar shape, while the blueshifted side of W3 (H_2O) E and the redshifted side of W3 (H_2O) W which actually correspond to the edges of these rotating structures show the decrease in j better.

If the decrease in j is in fact as a result of the transition between a Keplerian disk and the

collapse of the envelope for which the angular momentum is conserved (i.e. j is constant), one could put a limit on the size of the inner disk that is actively accreting onto the protostar. We refrain from calculating exact numbers for each source due to the uncertainties in such an estimate and our coarse resolution, but note that for most of the sources this transition is seen around 1000 – 2000 au. The only exceptions are Cep A and IRAS21078 which are the closest sources in the sample and hence resolved the best, for which this transition is seen around 300–400 au, and 500–700 au, respectively. With this, we are confident that most of these objects are excellent disk candidates and in the following section study the stability of these rotating structures.

6.8 Toomre stability

We determine the stability of the disk candidates against axisymmetric gravitational collapse using the Toomre Q parameter,

$$Q = \frac{c_s \, \Omega}{\pi \, G \, \Sigma}. \tag{6.9}$$

The Toomre equation determines the balance between the stabilising force of pressure (through the sound speed, c_s) and shear forces (through the angular velocity, Ω) against the force of gravitaty (through the disk surface density, Σ). For a disk that is sufficiently massive, the self-gravity of the disk could cause it to fragment. The Toomre Q parameter quantifies this scenario such that if $Q < 1$, the disk is prone to fragmentation.

The sound speed is calculated using the temperature maps obtained from our radiative transfer modelling of CH_3CN lines with *XCLASS*, presented in Sect. 6.5, such that

$$c_s = \sqrt{\frac{\gamma k_\mathrm{B} T}{\mu m_\mathrm{H}}}, \tag{6.10}$$

where γ is the adiabatic index with a value of $7/5$ for diatomic gas, k_B is the Boltzmann constant, μ is the mean molecular weight with a value of 2.8, and m_H is the mass of the hydrogen atom. Using the obtained temperature maps and assuming gas and dust temperatures are coupled, the surface density of the disk is calculated according to

$$\Sigma = \frac{S_\nu \, R}{B_\nu(T_D) \, \Omega_B \, \kappa_\nu}, \tag{6.11}$$

where S_ν is the peak intensity and Ω_B is the beam solid angle. Furthermore, assuming the disk is in gravito-centrifugal equilibrium following a Keplerian rotation profile, the angular velocity at a given radius is

$$\Omega(r) = \sqrt{\frac{G(M_* + M_\mathrm{disk}(r))}{r^3}}, \tag{6.12}$$

where M_* is the protostellar mass and $M_\mathrm{disk}(r)$ is the gas mass interior to r calculated from the continuum maps (see Sect. 6.6.1). Protostellar masses were estimated from fitting the PV diagrams of CH_3CN transitions and other dense gas tracers as discussed in Sect. 6.6.2. For sources which were studied in more depth using the same CORE data (IRAS23033: Bosco et al. 2019; IRAS23385: Cesaroni et al. 2019), we adopted the same mass estimates reported by these authors. We compared the protostellar mass estimates from fitting the PV diagrams, M_PV,

against masses derived from the source luminosities $M_{\rm lum}$ (see Table 3.1) using the spectral type-temperature calibration of Crowther (2005). Since the reported luminosities are from multi-wavelength SED fitting of lower resolution observations (see Mottram et al. 2011), estimates for $M_{\rm lum}$ are upper limits, especially in sources with multiple cores detected (e.g. IRAS23033 or W3 (H_2O)). For all sources, our mass estimates from fitting the PV diagrams were lower than this upper mass limit. An overview of mass estimates using various techniques as well as the established protostellar masses are presented in Table 6.5.

Assuming the protostar is positioned at the location of the continuum peak, we calculate the Toomre Q parameter for each disk candidate, accounting for the self-gravity of the disk by including the enclosed gas mass at each radius. The resulting Q maps are presented in Fig. 6.9 for the 17 disk candidates in the CORE survey. Regions outside of the 6σ continuum contours are masked out since the continuum maps are used as input for the calculation of Q. The median Q value for each source is provided in Table 6.5.

The critical value of the Toomre parameter, $Q_{\rm crit}$, which determines the stability of a disk is in theory equal to 1, while effectively it lies somewhere between 1–2 (Kennicutt 1989; Elmegreen 1991, 1994). Considering the uncertainties in our analysis, especially in determining temperatures from radiative transfer modelling of CH_3CN K-ladder (10–20% uncertainty, see Appendix B of Gieser et al. 2019) as well as the fact that the derived temperatures may be probing layers above the disk mid-plane, we assume that regions where $Q \lesssim 2$ are unstable against gravitational collapse. Synthetic NOEMA observations presented in Ahmadi et al. (2018) (Chapter 5) confirmed this limit to be a reasonable threshold. Because the Toomre parameter quantifies local stability in a disk, the median values listed in Table 6.5 should be used with caution as a determining factor for whether a disk is stable against gravitational instabilities. Therefore, we establish whether the candidate disks are stable at the scales resolved by of our observations based on the distribution of Q and include these conclusions in the table as well. A few sources fall in the regime of being borderline Toomre stable depending on the exact threshold used for the critical Q: IRAS23033 MMS1b, G100, and G094. These targets are not the best disk candidates in our sample, especially G100 which has a uniform temperature distribution and a velocity gradient that is not very strong. Moreover, for G084 and G100 with protostellar mass estimates that are too low to categorize them as high-mass YSOs, reproducing the Q maps with masses that are at least 8 $M_\odot$ would increase their Q value by $\sqrt{2}$ pushing them towards stability.

6.8.1 Toomre unstable disks

There exist regions with $Q \lesssim 2$ for most disk candidates, meaning they are unstable against gravitational instabilities and prone to fragmentation. While some candidate disks appear to be Toomre unstable almost entirely (IRAS23151, IRAS23033 MMS1a, AFGL2591, G75.78, W3 (H_2O) E and W, IRAS23385, NGC7838 IRS1), others show signs of instability only in their outskirts (G084, NGC7538 S). For some sources, the low Q values are coincident with the elongation of the continuum, hinting at the existence of underlying substructure. The best examples for such cases are IRAS23033 MMS1a, G084, IRAS23385, and NGC7538 S. In fact, the in-depth analysis of Cesaroni et al. (2019) using the CORE survey data confirms that IRAS23385 is forming a cluster of massive stars. An interesting case worth noting is

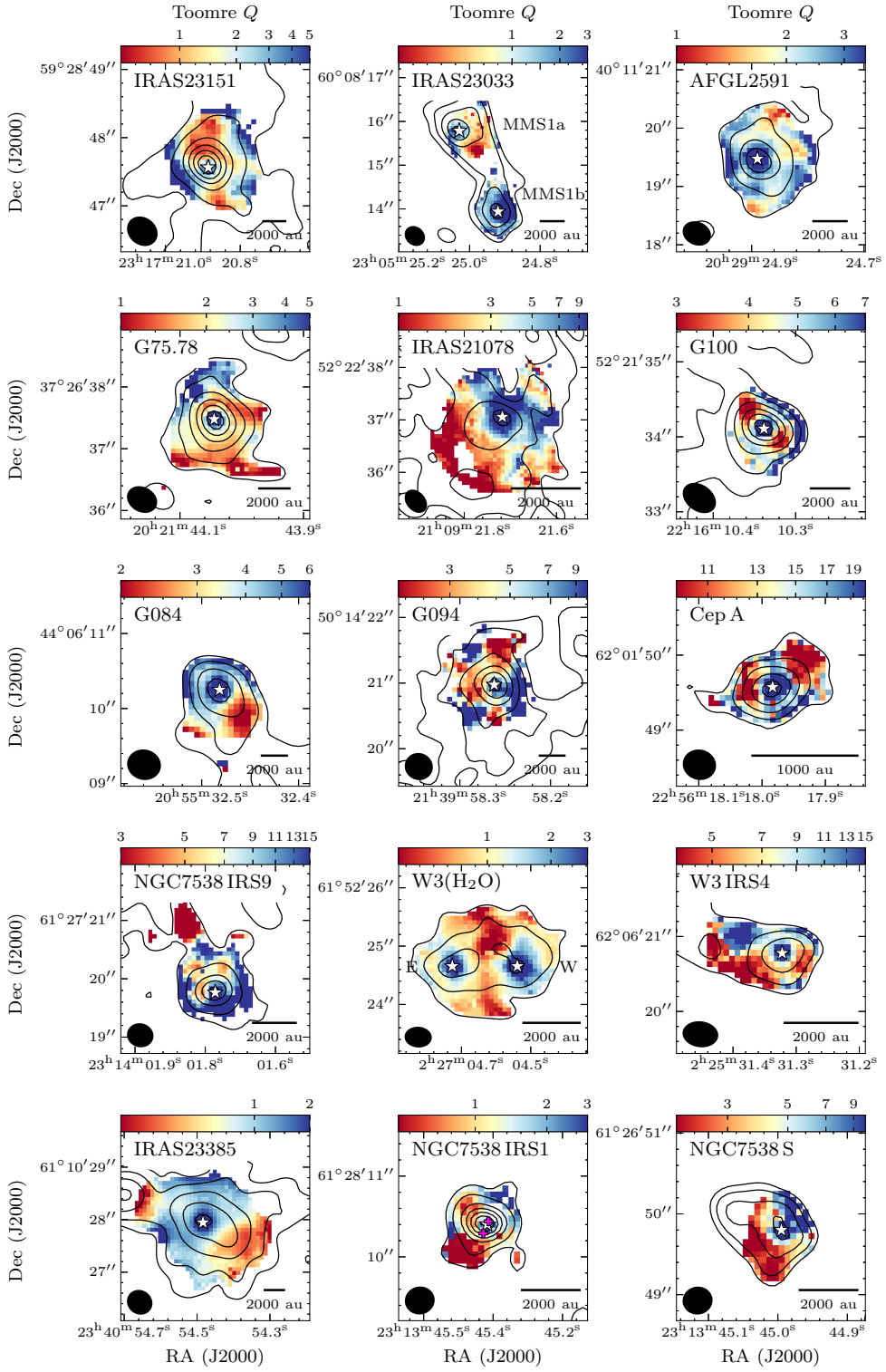

Figure 6.9: Toomre Q maps for 15 of the 20 sources in the CORE survey assuming a protostar is located at the position of the continuum peak as depicted by a star and accounting for the self-gravity of the disk (protostellar and gas mass values are listed in Table 6.5). The contours correspond to the 1.37 mm continuum as described in Fig. 6.2. Regions outside of 6σ continuum contours are masked out. The synthesized beam is shown in the bottom left corner and a scale bar in the bottom right corner of each panel. Fragments detected in NGC7538 IRS1 by higher resolution observations in the centimetre are marked by plus symbols in magenta (Beuther et al. 2017a).

Table 6.5: Overview of mass estimates and Toomre Q results.

Source	$M_{\rm gas}$ ($M_\odot$)	$M_{\rm PV}$ ($M_\odot$)	$M_{\rm lum}$ [a] ($M_\odot$)	M_* ($M_\odot$)	$Q_{\rm median}$	$\left(\frac{H}{r}\right)^{b}_{\rm median}$	Toomre Stable
IRAS23151	10.7	15	24	15	1.8	0.23	no
IRAS23033 MMS 1a	6.2	2	21	5*	0.7	0.23	no
IRAS23033 MMS 1b	3.9	13	21	19*	2.0	0.15	yes/no
AFGL2591	6.2	16	40	16	2.3	0.24	no
G75.78	8.1	19	34	19	2.0	0.25	no
IRAS21078	3.3	11	19	11	2.0	0.25	no
G100	0.9	4	21	4	4.8	0.37	yes/no
G084	1.6	4	19	4	4.0	0.50	no
G094	3.0	12	25	12	4.8	0.31	yes/no
Cep A	0.5	20	21	20	14.2	0.17	yes
NGC7538 IRS9	1.3	18	24	18	9.9	0.28	yes
W3(H_2O) E	9.4	10	33	10†	0.9	0.23	no
W3(H_2O) W	7.0	10	33	10†	1.0	0.24	no
W3 IRS4	0.9	8	28	8	5.9	0.44	yes
IRAS23385	19.1	2	21	9‡	0.9	0.25	no
Pilot study							
NGC7538 IRS1	19.5	23	41	23	1.0	0.19	no
NGC7538 S	2.4	10	21	10	2.2	0.29	no

[a] Luminosity mass extrapolated from Table 1 of Crowther (2005) using luminosities reported in Table 3.1.
[b] Median ratio of disk scale height to radius.
* Based on Bosco et al. (2019) using data from the CORE survey.
† Based on A-array observations presented in Ahmadi et al. (2018) using data from the CORE survey (Chapter 4).
‡ Based on Cesaroni et al. (2019) using data from the CORE survey.

IRAS21078, for which the low Q values are coincident with a secondary source detected in continuum, ~0.5″ to the southeast of the continuum peak. Similarly, other sources for which we know further fragmentation has taken place are NGC7538 IRS1 (Beuther et al. 2017a) and AFGL2591 (Suri et al. in prep). In particular, observations of Beuther et al. (2017a) which resolve the fragmentation in NGC7538 IRS1 using centimetre continuum emission (with 0.055″ resolution, ~150 au) find two HCH II regions with a projected separation of ~430 au (marked by magenta plus symbols in Fig. 6.9). These authors resolve velocity gradients in thermal CH_3OH across each HCH II regions, painting a picture of two disk-like structures embedded within the same rotating circumbinary envelope. 6.7 GHz methanol masers have also been detected consistent with the accretion disk scenario (Moscadelli & Goddi 2014). The position angles of these disks are misaligned with that of the rotating structure we detect by about 30°. This scenario is similar to the synthetic observations of the numerical simulation we presented in Ahmadi et al.

(2019) (Chapter 5) whereby the disk on large scales has a different rotation axis than the inner small-scale disks that have formed around each of the fragments. Whether the large-scale rotating structure is a circumbinary envelope rather than a flattened disk-like structure is difficult to establish especially because our line observations at the location of the protostar(s) are seen in absorption. The large extent of CH_3CN emission in the PV diagrams (see Fig. 6.4) at first glance may hint at the possibility that the structure is not a disk, especially because the mass estimates from fitting the PV diagram are much in excess of the mass estimated from the luminosity. However, as we showed in Ahmadi et al. (2019) (Chapter 5), PV diagrams of poorly resolved disks often have very large sizes resulting in mass estimates that are significantly higher than the true enclosed mass. Due to the small separation between the two embedded disks, it is likely that they formed via disk fragmentation.

6.8.2 Toomre stable disks

The candidate disks that appear to be completely Toomre stable against gravitational instabilities include Cep A HW2, NGC7538 IRS9 and W3 IRS4. Due to the complex nature of the outflows in W3 IRS4 region, it is unclear whether the velocity gradient observed in CH_3CN traces a disk or the outflows, therefore conclusions regarding the stability of W3 IRS4 are conditional on this uncertainty. The stability of Cep A is in part as a result of warmer temperatures across the entire structure as compared with other sources as well as the low gas mass (0.5 $M_\odot$) to stellar mass (20 $M_\odot$) ratio. Therefore, the self-gravity of the disk is not very strong and the disk is warm prohibiting any possible fragments to effectively cool and survive. The Q values for Cep A HW2 are so high that even if we have overestimated the mass of the protostar by a factor of 2 (e.g. due to contamination of the blueshifted emission by a hot core that is located 0.3″away from the main continuum peak (Jiménez-Serra et al. 2009)), the disk would still appear stable at the scales probed by our observations.

6.8.3 General trends

In Fig. 6.10 we plot the median Q values listed in Table 6.5 versus the ratio of disk to stellar mass, coloured according to the luminosity of the region. We find that more luminous YSOs have disks that are more massive and as a result more prone to fragmentation. As explained in the previous section, since Toomre stability is a measure for the *local* stability of the disk against axisymmetric gravitational instabilities, simply using $Q_{\rm crit} = 1$ to determine the stability of these disks from this plot of median Q values is incorrect. Based on the analysis presented above by looking at the distribution of Q for each individual case, disks with masses that exceed the stellar mass by $\sim 20-30\%$ are subject to fragmentation through gravitational instabilities. The inverse relationship between Q and $M_{\rm gas}/M_*$ is as a result of a tight anti-correlation between Q and $M_{\rm gas}$ and less so due to a correlation between Q and M_* (see Fig. 6.11). Numerical simulations of Kratter et al. (2010) find that the maximum disk mass before disk fragmentation occurs is on the same order as the stellar mass, while a review on the subject by Kratter & Lodato (2016) provides a value of $M_{\rm disk}/M_* \geq 0.1$ for gravitational instabilities to become important. Therefore our observations confirm that disk fragmentation must be prevalent in high-mass star formation. Whether the fragments survive as companions to the central protostar depends largely on

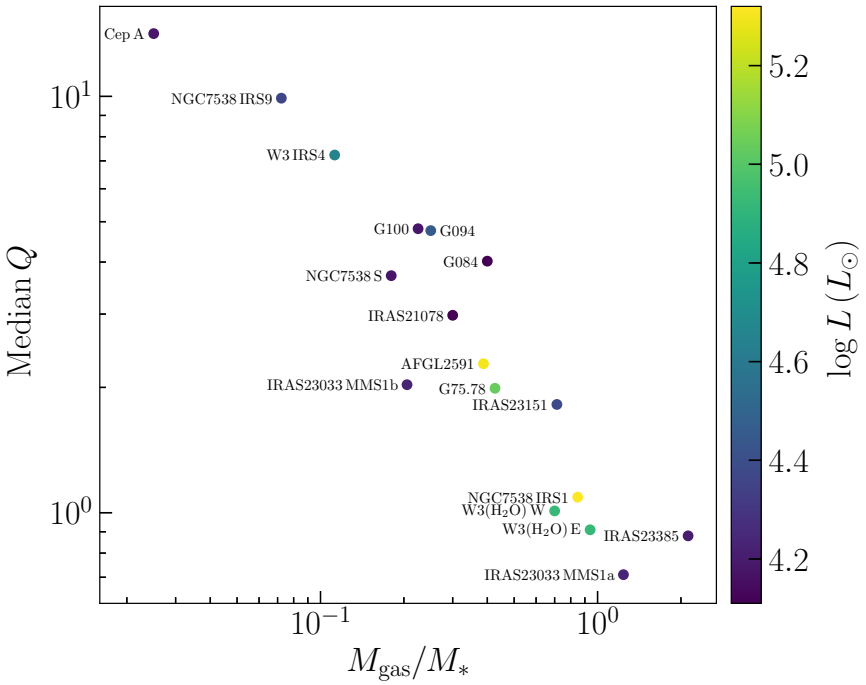

Figure 6.10: Median Q plotted against gas to stellar mass ratio for 17 candidate disks within the CORE survey, coloured according to the luminosity of the regions within which they reside.

whether they can cool fast enough. The cooling time has been confirmed to be short enough relative to the orbital period both numerically (Klassen et al. 2016) and observationally (Ahmadi et al. 2018) (Chapter 4) such that fragments that are beyond ~50 au of the central protostar should be rapidly cooling (see review by Kratter & Lodato 2016). This is an important finding as nearly all high-mass stars are found in binary or multiple systems (Sana et al. 2014).

It is important to note that we have neglected the effect of magnetic fields as we do not have information about the magnetic field strengths in our sources. Theoretically, one can incorporate the Alfvén velocity in the Toomre equation in order to determine the magnetic Q parameter, $Q_{\rm mag}$ (Kim & Ostriker 2001). In their numerical collapse simulations of strongly magnetized and turbulent molecular cloud cores, Seifried et al. (2013) compare Q measurements with $Q_{\rm mag}$. The find that $Q_{\rm mag}$ rises above the value of Q, confirming that disk fragmentation is suppressed by the presence of magnetic fields as magnetic pressure provides added support against collapse. However, fragmentation in a magnetized environment can still proceed through other mechanisms (e.g. high amplitude fluctuations in the core initially, ambipolar diffusion and fragmentation during the second collapse; see e.g. Hennebelle & Teyssier 2008). Therefore, without information about the magnetic field strengths in the CORE sources, it is not trivial to estimate to what extent that may affect our conclusions.

6.8.4 Disk thickness

One of the main assumptions for the Toomre analysis is the thin-disk approximation, such that $Q_{\rm crit}$ for an isothermal disk of finite thickness is lower ~0.7 (Goldreich & Lynden-Bell 1965). This is because the thicker a disk, the more diluted its self-gravity becomes. To get an estimate for

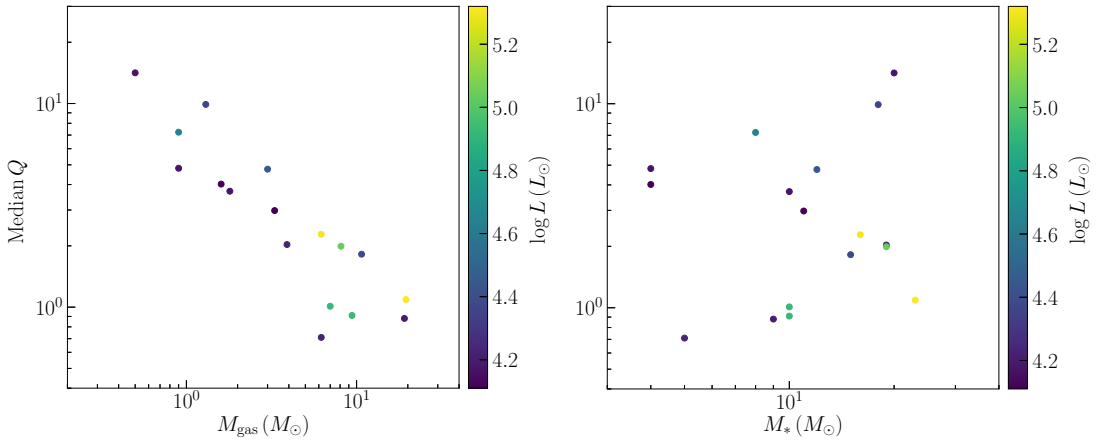

Figure 6.11: Median Q plotted against gas mass (*left*) and stellar mass (*right*) for 17 candidate disks within the CORE survey, coloured according to the luminosity of the regions within which they reside.

the importance of disk thickness, Gammie (2001) derived an additional stability criterion taking into account the disk scale height, $H \simeq c_s/\Omega$, such that a disk is unstable against gravitational instabilities if

$$M_{\rm disk} \gtrsim \frac{H}{r} M_*. \tag{6.13}$$

Using Eqs. 6.10 and 6.12, we create maps of H/r ratio and report the median H/r values in Table 6.5. In Fig. 6.12 we plot $M_{\rm gas}$ for each source coloured by its median Q value, sorted in increasing luminosity from left to right. The grey shaded area corresponds to $M < (H/r)M_*$. Sources that are Toomre unstable with low Q values all have $M_{\rm gas}$ above this threshold, therefore fulfilling the Gammie criterion as well. Similarly, sources which are Toomre stable have $M_{\rm gas}$ that are far below the $(H/r)M_*$ curve, also in agreement with the Gammie criterion. Moreover, sources with Q close to $Q_{\rm crit}$ lie close to the Gammie threshold for stability as well. Note that, again, since we have plotted median values, the edge of the shaded area should not be taken as a strict boundary.

6.9 Summary and conclusions

In this chapter, I presented the gas kinematics and stability properties for a sample of 20 high-mass YSOs observed with the NOEMA interferometer at a resolution of ~0.4″ as part of the CORE survey. While the sample was chosen uniformly to target the early phase of high-mass star formation, there exists a diversity in the age as we find some sources that show a rich hot core chemistry (AFGL2591, G75.78, Cep A, W3 (H_2O)) while others are weak in lines (S87 IRS1, S106, G108, G138, G139). We focused our study on the small-scale dense gas kinematics of the sample and therefore omitted these line poor sources from our analysis. Two of the remaining 15 sources included two hot cores within the field, hence the total number of cores studied increased to 17. The following is a summary of our results:

- Using the K ladder rotational transitions of the dense gas tracer CH_3CN ($12_K - 11_K$), we found velocity gradients across all cores perpendicular to the directions of bipolar molecu-

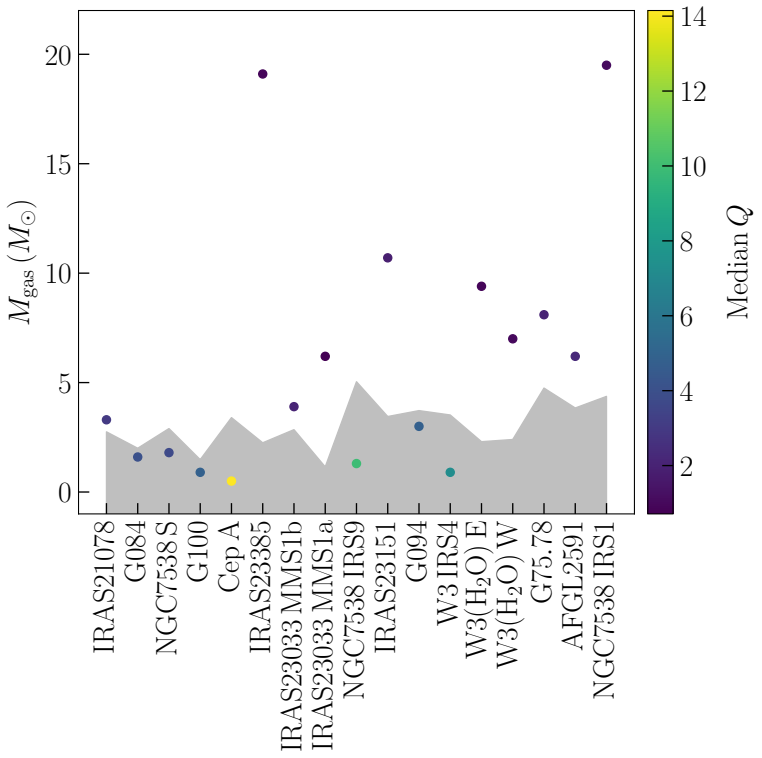

Figure 6.12: Gas masses plotted for each source sorted in increasing luminosity from left to right and coloured according to their median Q value. Regions with mass lower than median $(H/r)M_*$ are shaded in grey.

lar outflows, making them excellent disk candidates. The directions of molecular outflows were determined from a combination of tracers (^{12}CO, ^{13}CO, C^{18}O, and SO), both from single-dish IRAM 30-m observations as well as combined NOEMA and single-dish observations, included in the CORE survey. Determining the outflow directions was sometimes difficult due to the complex and dense nature of the regions with the possibility of hidden lower mass protostars contributing to the outflow emission.

- The rotating structures vary in size from 800 to 8000 au, measured from the extent of $CH_3CN\,(12_3 - 11_3)$ emission across the direction of the strongest velocity gradient.

- The velocity profiles of some sources resemble differential rotation with high-velocity components closest to the central object while other sources mimic rigid-body-like rotation. The latter may be a consequence of lack of spatial resolution. We fitted the 6σ edge of the PV diagram for each source with a Keplerian profile and determined the protostellar mass, typically in the range of 10–20 $M_\odot$.

- Modelling the level population of $CH_3CN\,(12_K - 11_K)\,K = 0 - 6$ lines under LTE conditions using *XCLASS*, we provide temperature maps of the regions. Temperatures are on average warm (70–200 K, depending on the target) with a diversity in distributions. Some are warm in the center, cooler in the outskirts while others are more uniformly at the same temperature. In many cases the ejection points of the outflows coincide with regions of warmer temperature where linewidths are also broader. Therefore, these regions

may have been carved out by the outflows, allowing a deeper look into the cores where temperatures are warmer. This is an important finding as outflows can provide a means by which intense radiation pressure can escape from the system, hence allowing accretion of mass onto the central protostar to continue.

- We calculated the gas mass of the disk-like structures assuming gas and dust temperatures are in equilibrium and optically thin dust emission. Masses range from 1 $M_\odot$ to as high as 20 $M_\odot$, depending on the region.

- From the ratio of free-fall to rotational timescales as a function of gas mass, we established that most sources in this sample are in fact good disk candidates and not transient toroids, with the exception of a few sources which are not resolved with more than a few beams.

- Radial profiles of the specific angular momentum for the best disk candidates show a break at ~1000 au, suggesting that true disks must exist below this scale, while above it we are observing the collapse of a rotating envelope. For the closest sources in our sample which are resolved at better linear resolutions, this limit was estimated at 300–400 au and 500–700 au for Cep A and IRAS21078, respectively.

- Assuming the candidate disks to be in Keplerian rotation about a star with the estimated protostellar mass and accounting for the self-gravity of the disk by including its gas mass, we created maps of the Toomre Q parameter to determine the stability of the candidate disks against axisymmetric gravitational collapse. Most disk candidates are Toomre unstable at the scales probed by our observations. In particular, disks with masses that exceed the stellar mass by ~20–30% are subject to fragmentation through gravitational instabilities, with the most luminous sources having the lowest Q values. The conclusions remain even when accounting for the thickness of the disks. Considering the short cooling timescales in the outskirts of these disks, the fragments will potentially survive as companion objects.

With the analysis presented in this chapter, we discovered that most high-mass YSOs are prone to disk fragmentation early in their formation due to the high disk to stellar mass ratio. This has profound implications for the formation of the most massive stars, as it inhibits the accumulation of mass onto one single high-mass protostar. Considering the fact that almost all high-mass stars are found in binary or multiple systems, disk fragmentation seems to be an important mechanism by which such systems may be formed.

CHAPTER 7

Summary and Conclusions

In this thesis we embarked on a journey in search of disks around high-mass YSOs to determine whether high-mass stars form in a similar manner as low-mass stars - through disk accretion. While a hand-full of individual disk candidates have been found and studied in the past few years, there has been no large observational survey dedicated to this effort. With this goal in mind, the CORE survey has obtained the very high resolution (~0.4″) observations of 20 well-known highly luminous star-forming regions in the northern sky in the 1.37 mm wavelength regime in both line and dust continuum emission using the IRAM NOEMA interferometer and the 30-m telescope. The aim of the project is many-fold, from the fragmentation mode of high-mass star-forming regions, to the kinematic properties of the gas, and the rich chemical diversity of the regions. This thesis is dedicated to the study of the small-scale kinematics of the sample to provide clues to the existence of disks in the early phases of high-mass star formation and to characterize the stability of such structures against fragmentation due to gravitational instabilities.

In Chapter 2, I outlined the mechanisms by which disks around high-mass YSOs can be identified and gave an overview of the observational techniques and data analysis tools currently used in the (sub)-millimetre regime. I introduced the observational setup of the CORE survey in Chapter 3 outlining the data reduction methods used to calibrate and image the interferometric data. As an integral part of the data reduction team, I was responsible for calibrating roughly one quarter of the interferometric data and provided to the team imaged cubes for all 23 lines covered in the highest spectral resolution setup (Narrowband receiver) for all 20 sources.

I began the scientific analysis with a case study presented in Chapter 4 (published in Ahmadi et al. 2018) for one of the most interesting hot cores in our sample: W3 (H_2O). With a linear resolution of 700 au, W3 (H_2O) fragments into two cores (W and E), separated by 2300 au. Using the rotational transitions of the dense gas tracer CH_3CN ($12_K - 11_K$), the two cores are found to be surrounded by a circumbinary rotating envelope. Analysing the observations from the most extended configuration of NOEMA exclusively, we were able to resolve two separate velocity gradients with amplitudes of a few km s^{-1} across each core. These velocity shifts seen in dense gas were found to be perpendicular to the directions of two bipolar outflows, one emanating from each core, making the case for the motion seen in dense gas being due to rotation. Studying the rotation curve of each structure, we found that the kinematics of the rotating structure about W3 (H_2O) W shows signs of differential rotation, possibly in a disk-like object, while the rotational signature around W3 (H_2O) E may be due to a disk-like object, an unresolved binary (or multiple) system, or a combination of both. Modelling the level

populations of various CH_3CN transitions with the radiative transfer code *XCLASS*, we derived a map of gas temperature with a median temperature of ~165 K across W3 (H_2O). The stability of the rotating structures against gravitational instabilities was determined by creating a map of the Toomre Q parameter. The rotating structures appear to be Toomre unstable close to their outer boundaries, with a possibility of further fragmentation in the differentially rotating core, W3 (H_2O) W. Considering the outer regions are rapidly cooling, any potential fragment at these locations could survive as companion objects. Therefore, in W3 (H_2O), we were able to identify two modes of fragmentation at play with core fragmentation on large scales, and indications for disk fragmentation on ~1000 au scales.

In Chapter 5 (published in Ahmadi et al. 2019), I investigated the effects of inclination and spatial resolution on the observable kinematics and stability of disks in high-mass star formation. To do so, a high-resolution 3D radiation-hydrodynamic simulation that leads to the fragmentation of a massive disk was used as the model. Using *RADMC-3D*, we produced 1.3 mm continuum and CH_3CN line cubes at four different inclinations. The model was set to two different distances (800 and 2000 pc), and synthetic observations were created for ALMA at 80 milli-arcsecond resolution and NOEMA at 0.4″. The synthetic ALMA observations at both distances and the synthetic NOEMA observations at 800 pc were able to resolve all fragments and their kinematics well, while the synthetic NOEMA observations at 2000 pc could only resolve a single structure slightly elongated towards the brightest fragment. Keplerian-like rotation was best recovered in views closer to edge-on in the well-resolved synthetic observations, with a transition from envelope to disk clearly seen as a discontinuity in the rotation curves at ~250 au. The PV diagrams of the poorly resolved observations better resemble rigid-body-like rotation rather than differential. As a result, protostellar mass estimates obtained from fitting Keplerian profiles to the rotation curves of poorly resolved observations highly overestimate the true protostellar mass. The degree to which mass is overestimated depends on how poorly the observations are resolved. Employing the same techniques as presented in the case study, we obtained temperature maps with values in the range 100–300 K across the disks. In the resolved synthetic observations, maps of the Toomre Q parameter showed instabilities at the positions of fragments and in the arms connecting them. Perhaps the most important finding from this study is the fact that even in the poorly resolved observations, the disks could be identified as unstable against gravitational instabilities. Therefore, the Toomre analysis can be used as a powerful tool for predicting disk fragmentation even when the resolving power is lacking. These findings are valid regardless of the knowledge about the inclination of the disks.

With the methods for studying the kinematics and stability of disks in high-mass star formation benchmarked in Chapter 5, I expanded the analysis to the full sample of 20 high-mass YSOs in the CORE survey in Chapter 6 (to be submitted to Astronomy & Astrophysics upon submission of this thesis). Five sources were removed from the analysis due to lack of line emission as they may be more evolved, while two regions contained two cores within their field, leaving us with a total of 17 targets to study. We found velocity gradients in dense gas roughly perpendicular to the directions of molecular outflows in almost all regions. Radial profiles of the specific angular momentum along the directions of the strongest velocity gradients revealed that 12 of these objects are excellent disk candidates with indications that true disks may exist at scales

below ~1000 au while above this scale infalling rotating envelopes better fit the observations. Further examination of the free-fall to rotational timescale provided additional support for the disk candidacy of the full sample, and particularly for these remaining 12 sources. Again, by modelling the CH_3CN transitions, we found the candidate disks to be on average warm with a diversity of temperature distributions. In some cases, we found the ejection points of the molecular outflows to be coincident with regions of warmer temperature and larger linewidths. This is an important finding as outflows are thought to provide an outlet for radiation pressure to escape, allowing matter to accrete from the envelopes onto disks. Furthermore, by fitting Keplerian profiles to the rotation curves of the disk candidates we estimated masses for the protostellar objects and created maps of the Toomre Q parameter, taking into account the self-gravity of the disks. Most disk candidates were found to be unstable at the scales probed by our observations. We determined that disk masses that exceed the stellar mass by 20–30% are subject to fragmentation through gravitational instabilities with disks residing in the most luminous regions being the most unstable. Considering the short cooling timescales expected in the outskirts of these disks, such fragments will potentially survive as companion object to the central protostar.

To summarize, in this thesis I showed that rotating structures seem to be ubiquitous in the early phase of high-mass star formation, indicating that high-mass star formation may be a scaled up version of low-mass star formation. I established a robust method for determining the stability of disk-like structures around high-mass YSOs, benchmarked using synthetic observations of numerical simulations and applied this method to the largest sample of disk candidates to-date. I conclude that most high-mass disk candidates appear to be unstable to gravitational instabilities at scales probed by our observations (~0.4″), indicating that disk fragmentation contributes to the final stellar mass distribution of a given region.

CHAPTER 8

Outlook

In this thesis, I characterized the properties of high-mass accretion disks in the context of the formation of the most massive stars using high-resolution observations in the millimitre regime. In the following, I will touch on some of the upcoming major advancements which will help in understanding the formation of high-mass stars.

From clumps to cores

As molecular clouds collapse to form stars, the infalling gas loses many orders of magnitude in specific angular momentum until the formation of protoplanetary disks. Different physical processes at various scales and stages of the star formation process contribute to this loss of angular momentum (see review by Belloche 2013). However, it is still unclear how exactly gas gets accumulated into the centers of the most luminous cores. Moreover, the two main theories of high-mass star formation - the turbulent core scenario (McKee & Tan 2003) and the competitive accretion scenario (Bonnell et al. 2007) - take opposing views on the importance of the cloud-scale environment. One of the unique capabilities of the CORE survey is that it includes observations from both an interferometer and a single-dish telescope for a sample of 20 high-mass YSOs. Combining these two datasets for various tracers which probe the range of densities, temperatures and spatial scales ($\sim 0.35'' - 1'$) involved, we can constrain global collapse motions and link the temperature, kinematic and chemical structure of these sources on small scales to their environment.

Perhaps one of the most impactful observational datasets to-come for the field of high-mass star formation is that of ALMAGAL, an ALMA large-program uniformly observing the largest sample of ~1000 high-mass star forming regions over a wide variety of clump masses, evolutionary stages, and Galactic environments at 1.3 mm. The observational setup is very similar to the CORE survey, observing the same tracers at spatial scales from 0.3″ to 30″. While the CORE survey was able to shed light on the fragmentation diversity that is observed in high-mass star formation (Beuther et al. 2018), the sample did not cover a large number of clumps at the exact same high linear resolution and it focused only on one evolutionary stage. With ALMAGAL, physical processes that influence the fragmentation of cluster forming clumps can be studied as a function of evolutionary stage, revealing the star formation history inside clumps. Furthermore, with the large spatial scales observed, the relationships between cores and their hosting clumps can be better studied. This includes the study of the flow of matter from clumps to cores in order to understand how cores gain their mass, as well as investigating the internal

feedback mechanisms from cores to clumps.

Although the CORE sample was uniformly selected to target the evolutionary stage where disks are expected to exist, we found a diversity in age that reduced the sample size by a quarter with an additional quarter having weak emission in dense tracers. Observing this remaining sample that had a distance range from 700 pc to 5.5 kpc meant that our resolving power spanned a large range in physical scale (300 au to 2000 au). The large sample size of ALMAGAL will allow a statistically significant number of disk candidates to be detected at similar linear resolutions, and to study the exact transition from a rotating infalling envelope to the disk phase in better detail. Considering the fact that 'catching' the disk phase in the fast formation lifetime of high-mass stars is difficult (as shown by the work presented in this thesis as well as that of Cesaroni et al. 2017), ALMAGAL will provide an excellent database from which a statistically significant sample of disk candidates can be selected to observe at higher spatial resolutions with ALMA and other instruments, paving the path to understanding the properties of disks in high-mass star formation.

From cores to disks

In this thesis I showed that it is difficult to find true disks even at 0.3″ resolution. What we typically observe at these scales (> 1000 au) is the transition from a rotating infalling envelope to a disk-like object, therefore, higher angular resolutions are needed to get to the scales where disks exist. As mentioned in the previous section, to detect disks, the selection criteria must be set meticulously. To this end, we have a successful ALMA program (PI: Ahmadi) to observe a homogeneously chosen sample of six high-mass YSOs to detect and characterize their disks. The sample is based on Boley et al. (2013) who observed 24 intermediate- to high-mass YSOs at tens of milli-arcsecond resolution with the Mid-infrared Interferometric Instrument (MIDI) on the VLTI in the N band (8 – 13 μm) and have modelled the visibilities to derive the size, orientation, and elongation of the circumstellar material. The ALMA observations will complement the mid-IR observations at the same angular resolution of 30 milli-arcsecond (~100 au). In this way, we can compare the distribution of warm dust to the cold dust by tracing both the Wien and Rayleigh-Jeans parts of the SED. This sample is in queue for observations under our ongoing guaranteed time observations with the new MATISSE instrument at the VLTI. This successor

Figure 8.1: The Atacama Large Millimeter Array (ALMA) located on the Chajnantor Plateau in Chile. Photo credits: ALMA (ESO/NAOJ/NRAO)

of MIDI covers the 3 – 13 μm range and makes direct image reconstruction in the thermal IR possible. This complementarity with ALMA at the same angular resolution will help connect the different phases of thermal dust and gas emission for this unique sample in order to study disk formation and evolution in the high-mass regime.

With its long awaited launch expected in 2021, the extraordinary impact of the James Webb Space Telescope in the field of star formation cannot go unmentioned. Its unmatched sensitivity will allow the detection of the most deeply embedded sources in the mid-IR. With observations using its mid-IR instrument (MIRI), this part of the SED which is most sensitive to geometries and the presence of disks can allow for the characterization of disk properties. Furthermore, the many atomic and molecular lines, including H_2, will help constrain the physics and chemistry of embedded disks and the associated jets/outflows.

Finally, the expected advancements in numerical simulations are also of importance for developing and constraining models that explain the upcoming observations. Efforts are being made to include self-consistent launching of jets and outflows into the remarkable high-resolution numerical simulations of massive disks. The addition of magnetized mass reservoirs as well as global simulations that form such disks within a turbulent medium will be of importance. Connections between theoretical models and observations through the use of synthetic observations will be invaluable for painting a complete picture of mechanisms at play in high-mass star formation.

Figure 8.2: The Very Large Telescope Interferometer (VLTI) located on Cerro Paranal in Chile. Photo credits: ESO/B. Tafreshi (twanight.org)

APPENDIX A

Supplemental material for Chapter 4

A.1 Moment maps

In this section we present zeroth (Fig. A.1), first (Fig. A.2), and second (Fig. A.3) moment maps of various detected lines in the narrow-band receiver for W3 (H_2O) (top panels) and W3 (OH) (bottom panels) in the combined A-, B-, and D-array observations. All moment maps have been created inside regions where the S/N ratio is greater than 5σ.

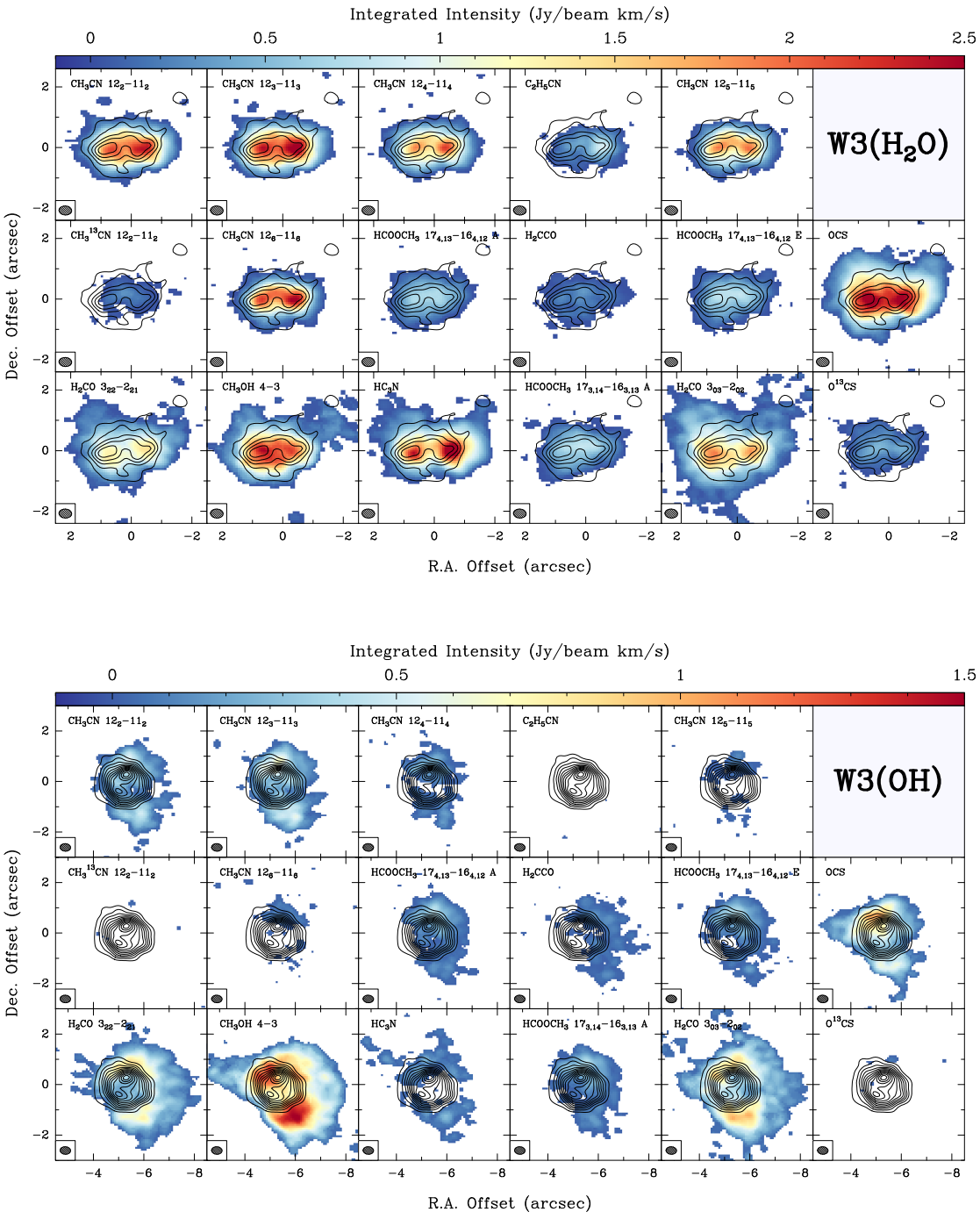

Figure A.1: Integrated intensity (zeroth moment) maps of most important lines covered in the narrow-band receiver for the observations in the ABD configuration for W3 (H_2O) (*top*) and W3 (OH) (*bottom*). The solid contours correspond to the dust continuum and start at and increase by 6σ (1σ = 3.2 mJy beam^{-1}). The size of the synthesized beam is shown in the bottom left of each panel. The map of CH_3CN ($12_5 - 11_5$) may not be accurate because it is blended with other lines.

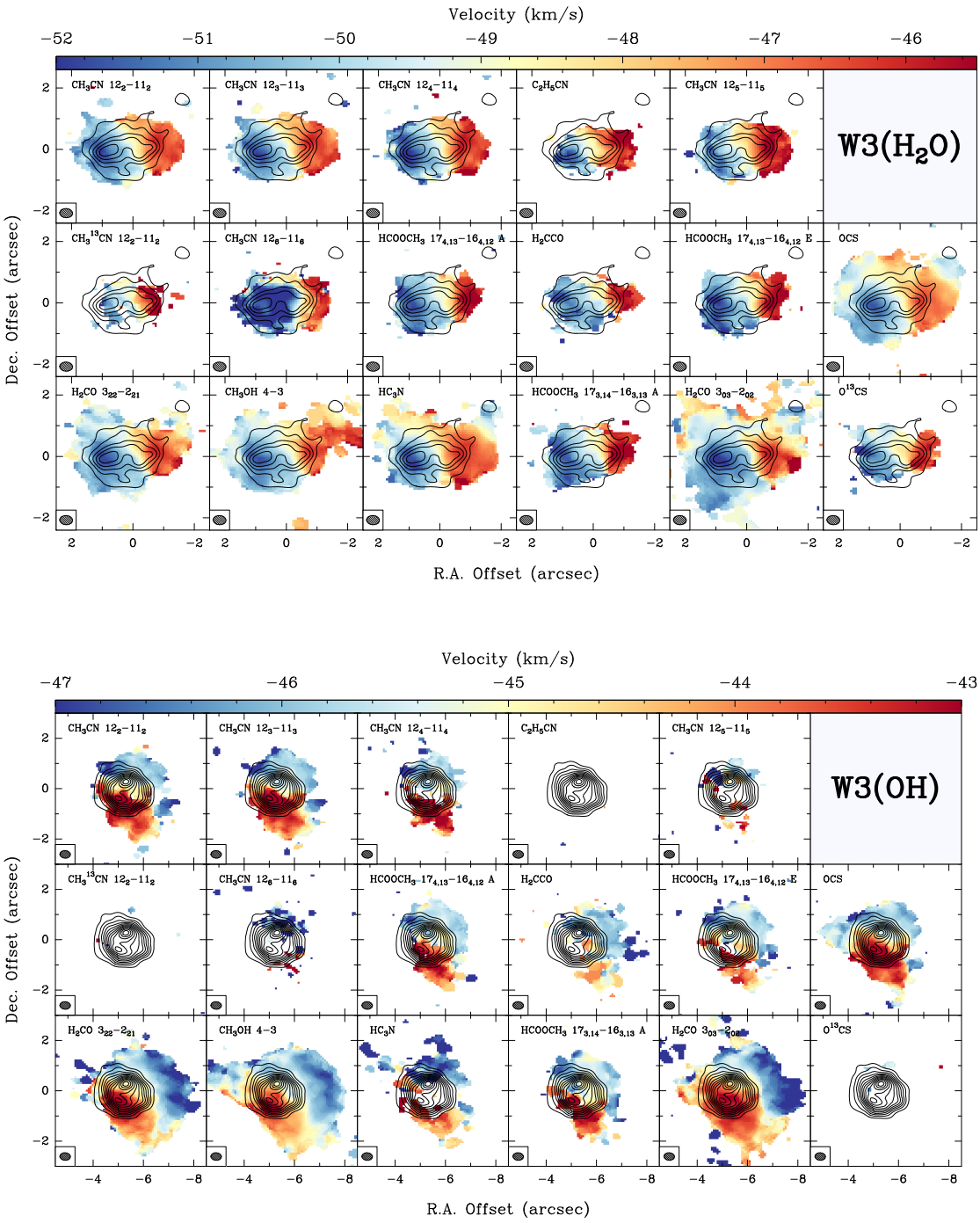

Figure A.2: Intensity-weighted peak velocity (first moment) maps of most important lines covered in the narrow-band receiver for the observations in the ABD configuration for W3 (H_2O) (*top*) and W3 (OH) (*bottom*). The solid contours correspond to the dust continuum and start at and increase by 6σ (1σ = 3.2 mJy beam^{-1}). The size of the synthesized beam is shown in the bottom left of each panel. The map of CH_3CN ($12_5 - 11_5$) may not be accurate because it is blended with other lines.

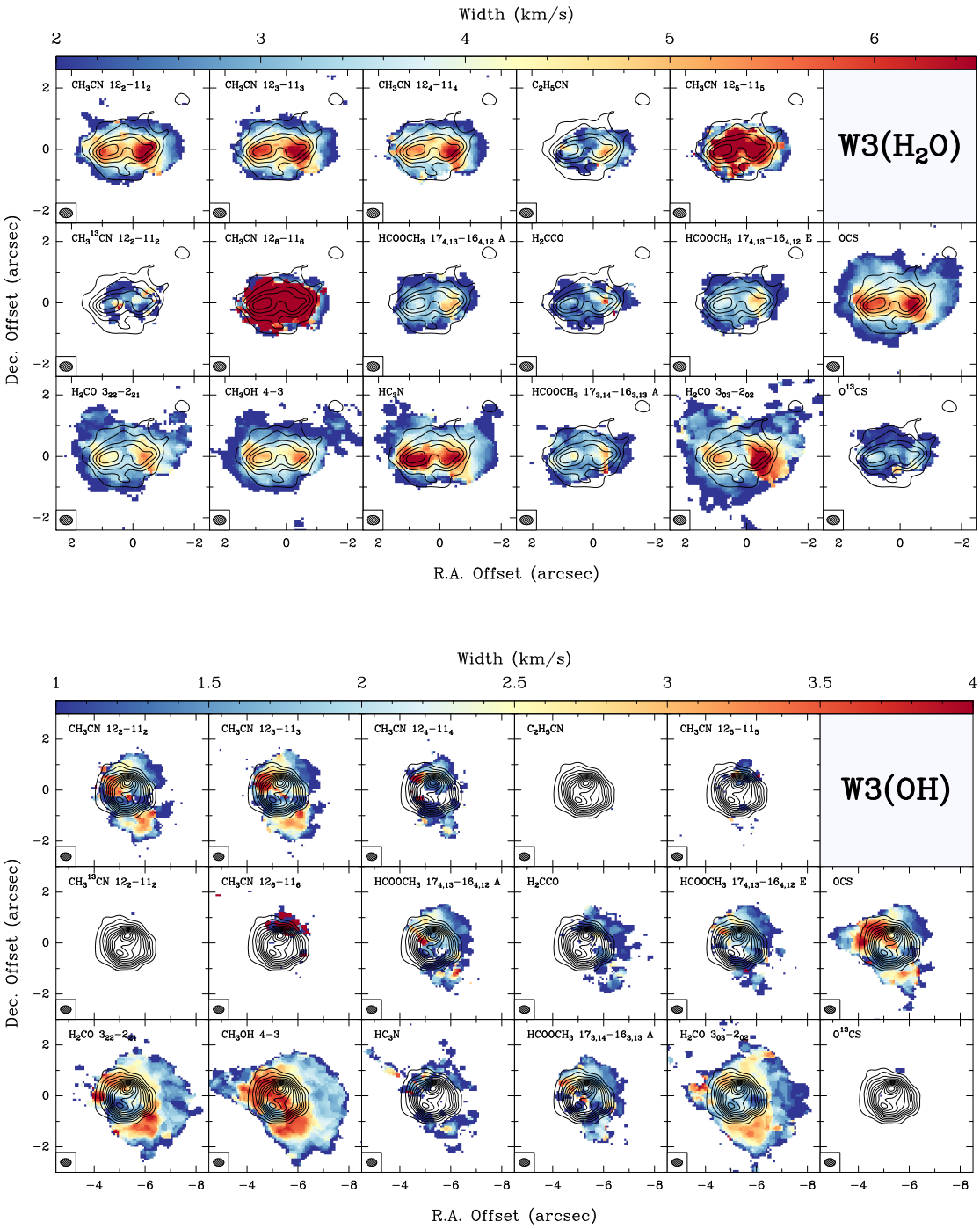

Figure A.3: Intensity-weighted velocity dispersion (second moment) maps of most important lines covered in the narrow-band receiver for the observations in the ABD configuration for W3 (H_2O) (*top*) and W3 (OH) (*bottom*). The solid contours correspond to the dust continuum and start at and increase by 6σ (1σ = 3.2 mJy beam^{-1}). The size of the synthesized beam is shown in the bottom left of each panel. The map of CH_3CN ($12_5 - 11_5$) may not be accurate because it is blended with other lines.

A.2 Toomre Q maps

In Fig. A.4, we present Toomre Q maps created assuming either two 5 $M_\odot$ (proto)stars at the positions of the two continuum peaks (top panel), or two 15 $M_\odot$ (proto)stars (bottom panel).

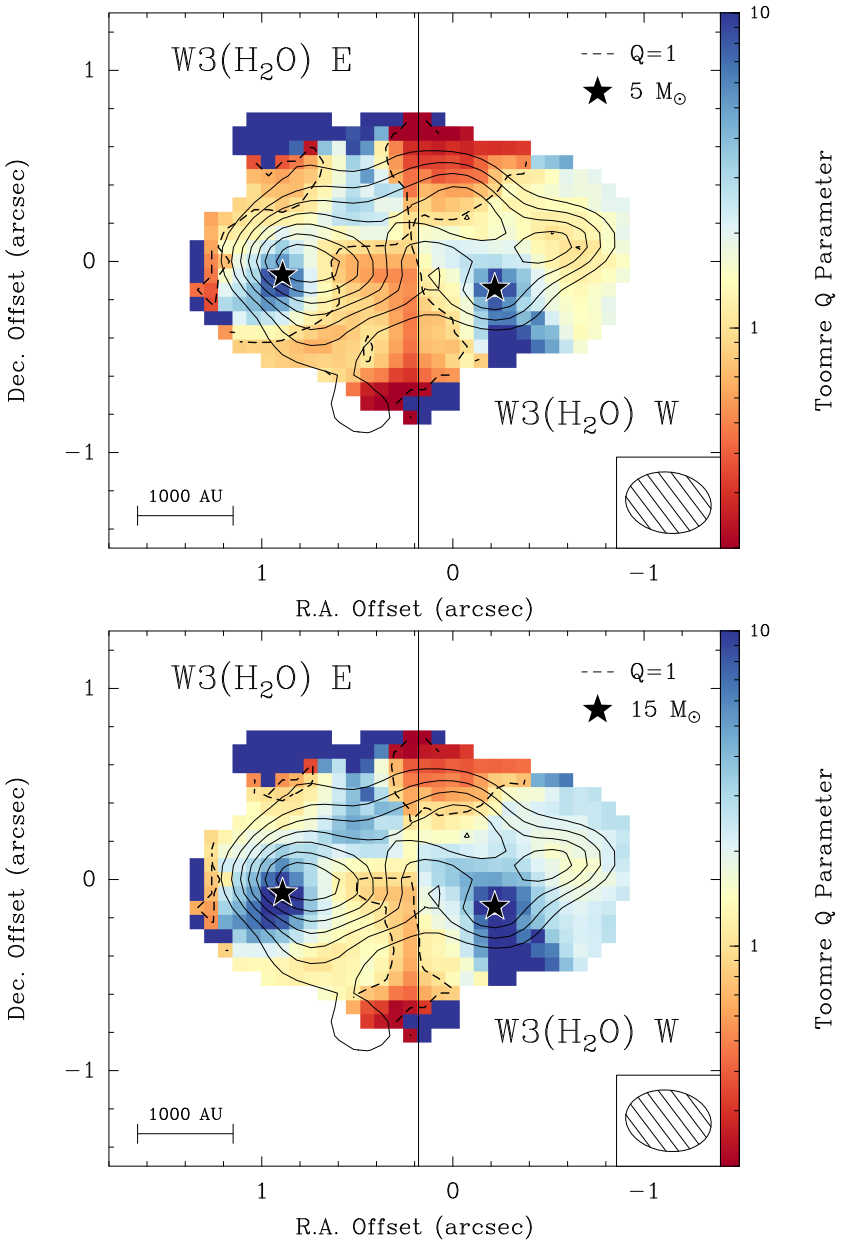

Figure A.4: Toomre Q map obtained by assuming two disks in gravito-centrifugal rotation about two 5 $M_\odot$ (proto)stars (*top*) and two 15 $M_\odot$ (proto)stars (*bottom*) at the positions of peak continuum emission as depicted by the two stars. The solid contours correspond to our continuum data in the most extended configuration, starting at 6σ and increasing in steps of 3σ (1σ = 2.5 mJy beam^{-1}). The solid vertical line corresponds to the stitching boundary. The dashed line corresponds to $Q = 1$. Regions outside of the 6σ mm continuum emission contour in the AB configuration are masked out.

APPENDIX B

Supplemental material for Chapter 6

In this appedix, I present ancillary figures supplementing Chapter 6. In Sect. B.1, I present first and second moment maps of $CH_3CN\,(12_3 - 11_3)$. In Sect. B.2, the distribution of outflow and shock tracing transitions are presented. Further *XCLASS* output maps such as the column density, velocity offset, linewidth, and source size maps are shown in Sect. B.3. Finally, a table of minimum least-squared power-law fit parameters to the specific angular momentum maps of the simulations are summarized in Sect. B.4.

B.1 Moment maps

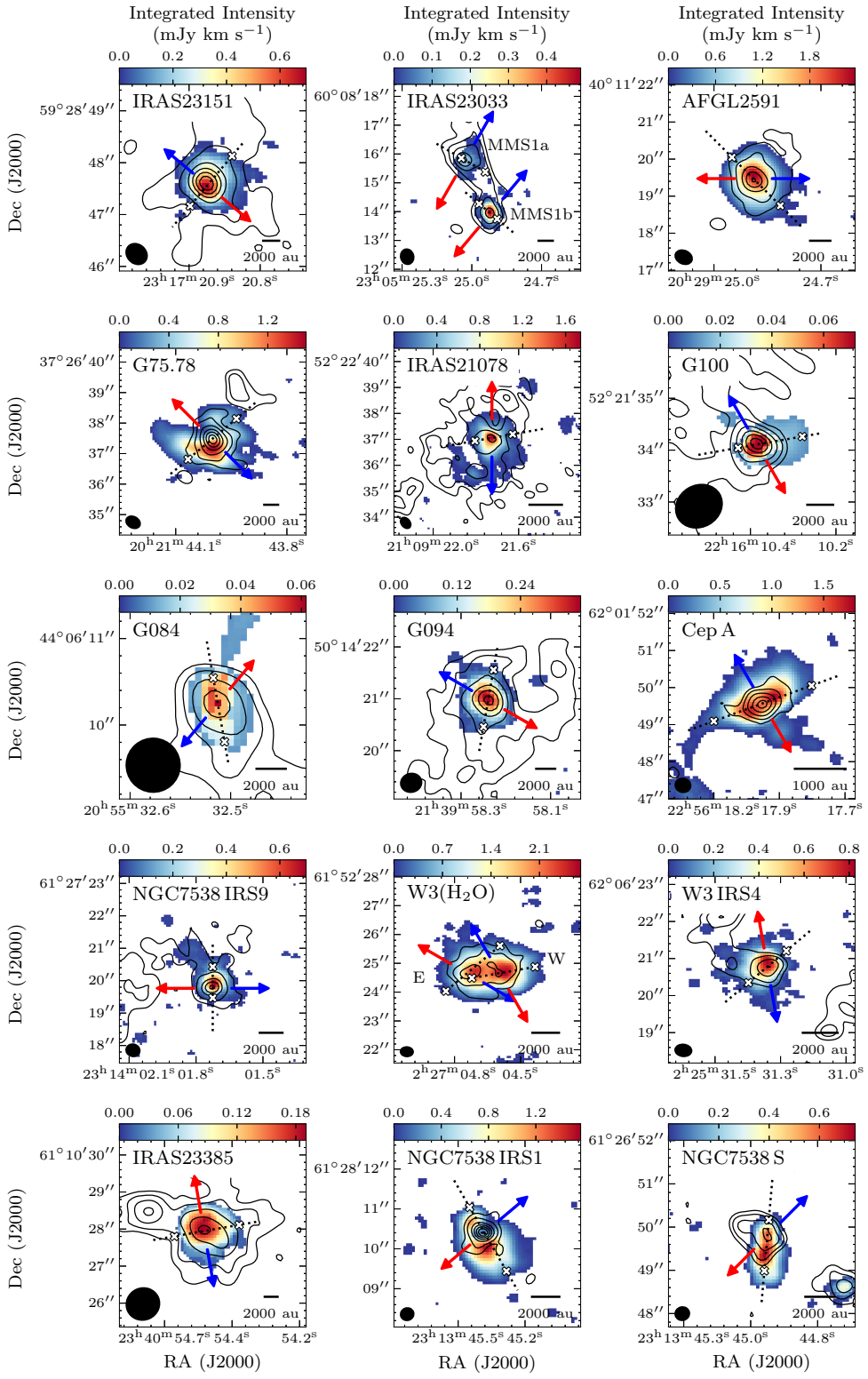

Figure B.1: Integrated intensity (zeroth moment) maps of CH_3CN ($12_3 - 11_3$) showing the dense gas distribution for 15 of the 20 sources in the CORE survey. The contours and features are as described in Fig. 6.3.

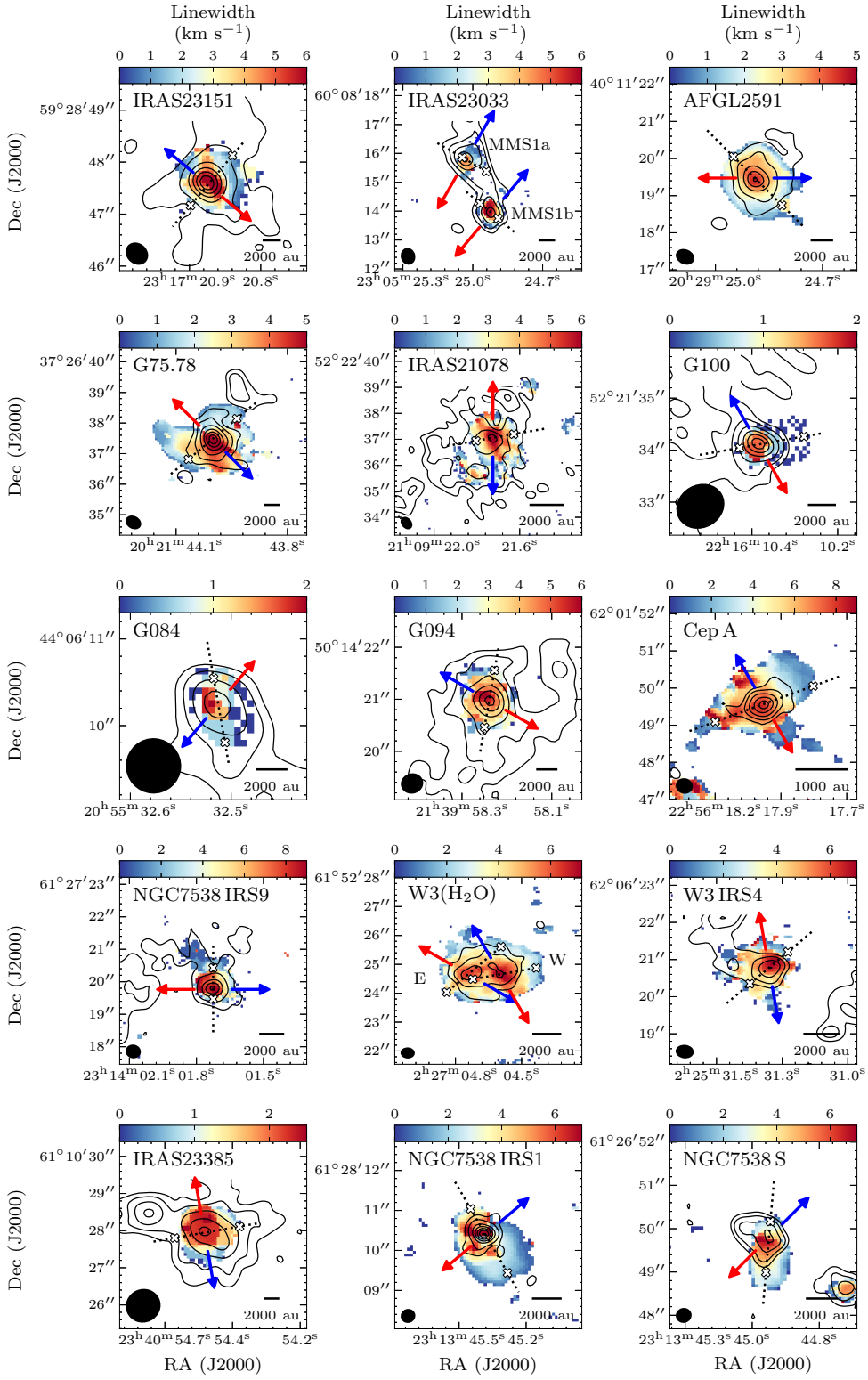

Figure B.2: Intensity-weighted velocity dispersion intensity (second moment) maps of CH_3CN ($12_3 - 11_3$) showing the dense gas kinematics for 15 of the 20 sources in the CORE survey. The contours and features are as described in Fig. 6.3.

B.2 Molecular outflows

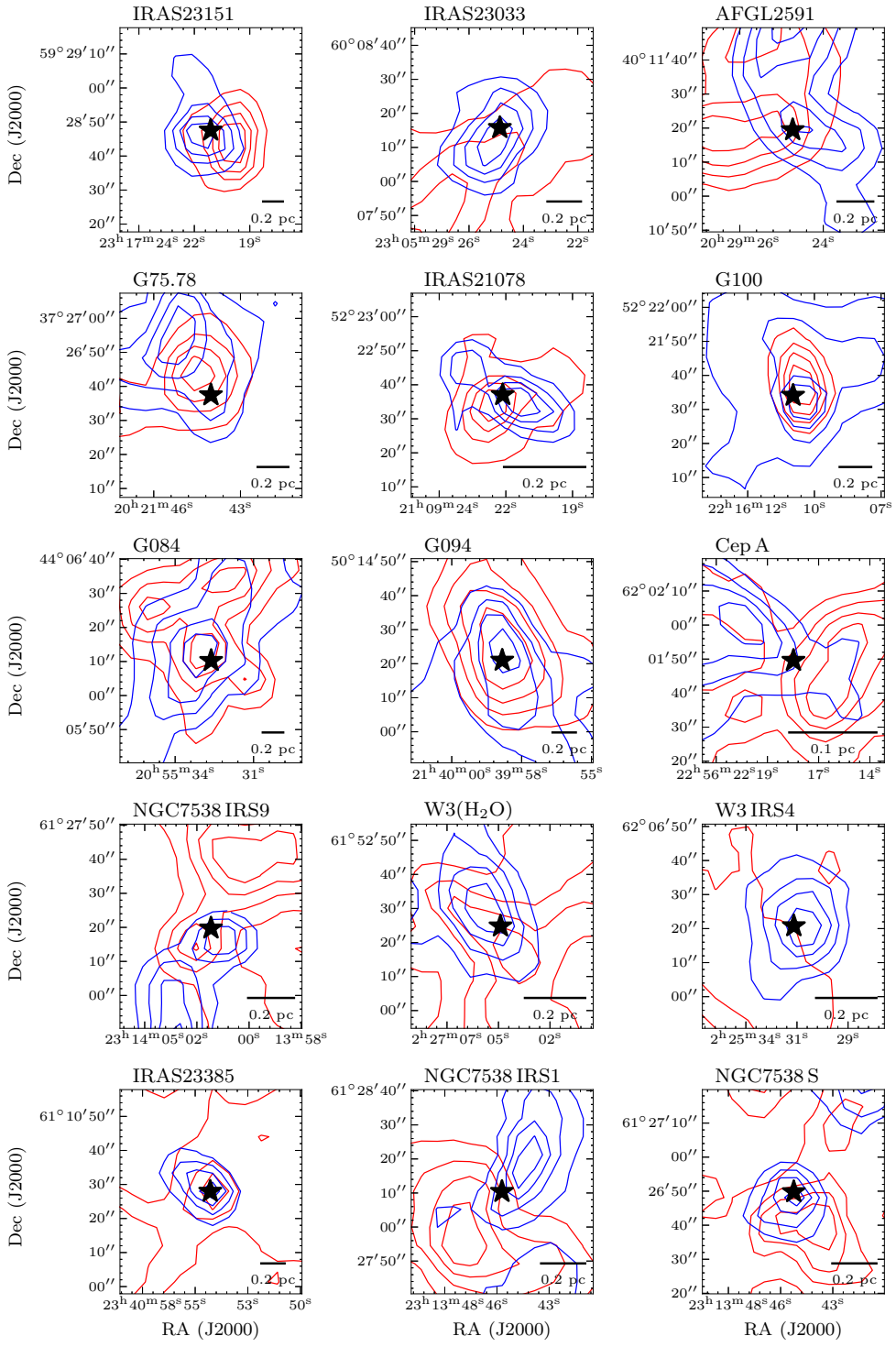

Figure B.3: Intensity maps of CO (2–1) emission from IRAM 30-m telescope integrated over the blue and redshifted wings of emission, showing the outflow structure. The position of the strongest source in the field is depicted by a star. A scale-bar is shown in the bottom right corner of each panel. The field of view of the IRAM 30-m observations is 1.5′ by 1.5′ with a half-power beam width of ∼11″ at this frequency.

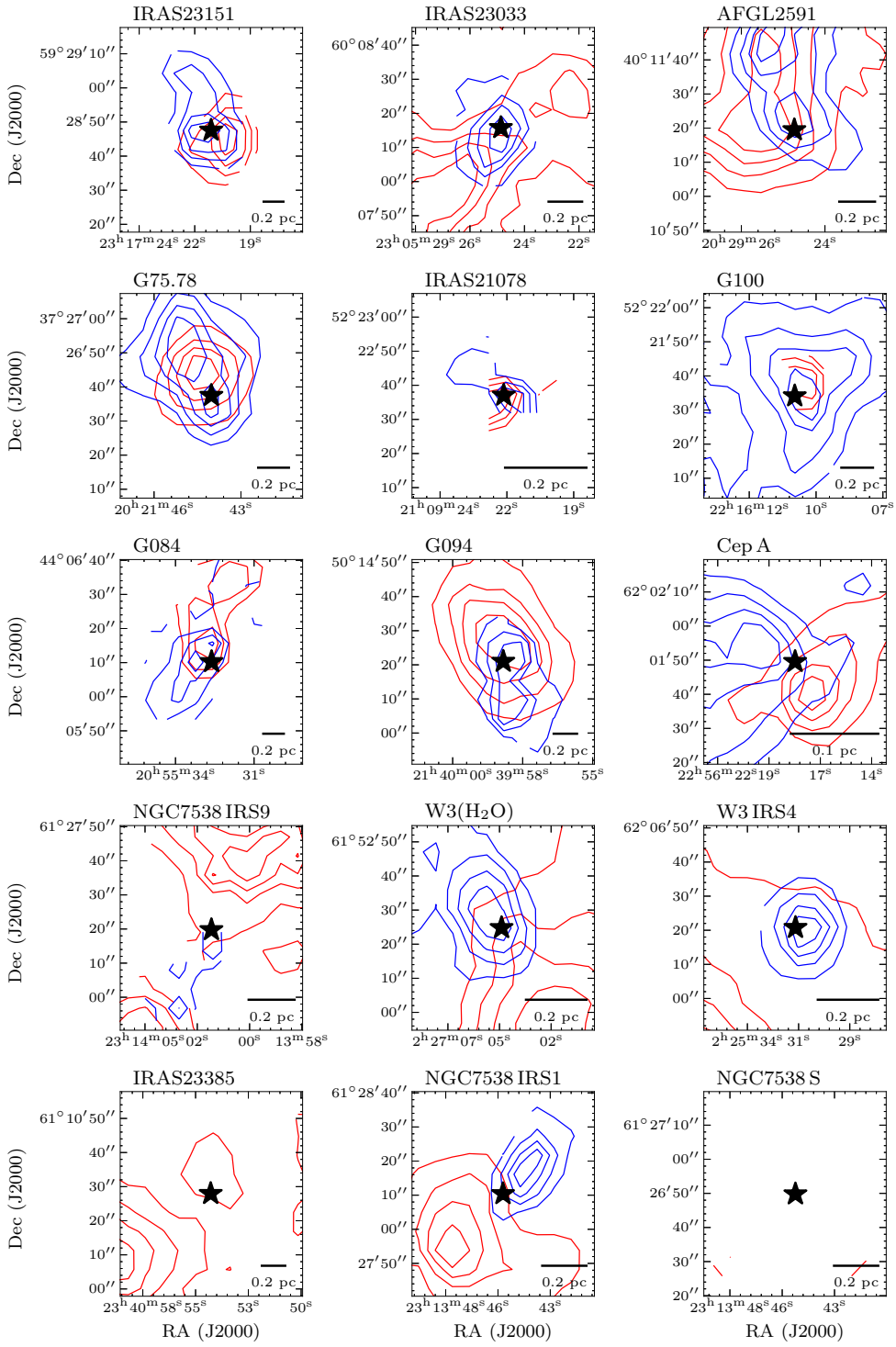

Figure B.4: Intensity maps of ^{13}CO (2 – 1) emission from IRAM 30-m telescope integrated over the blue and redshifted wings of emission, showing the outflow structure. The position of the strongest source in the field is depicted by a star. A scale-bar is shown in the bottom right corner of each panel. The field of view of the IRAM 30-m observations is 1.5′ by 1.5′ with a half-power beam width of ~11″ at this frequency. We did not have the corresponding data for the pilot sources at the time of this work, hence the missing panels.

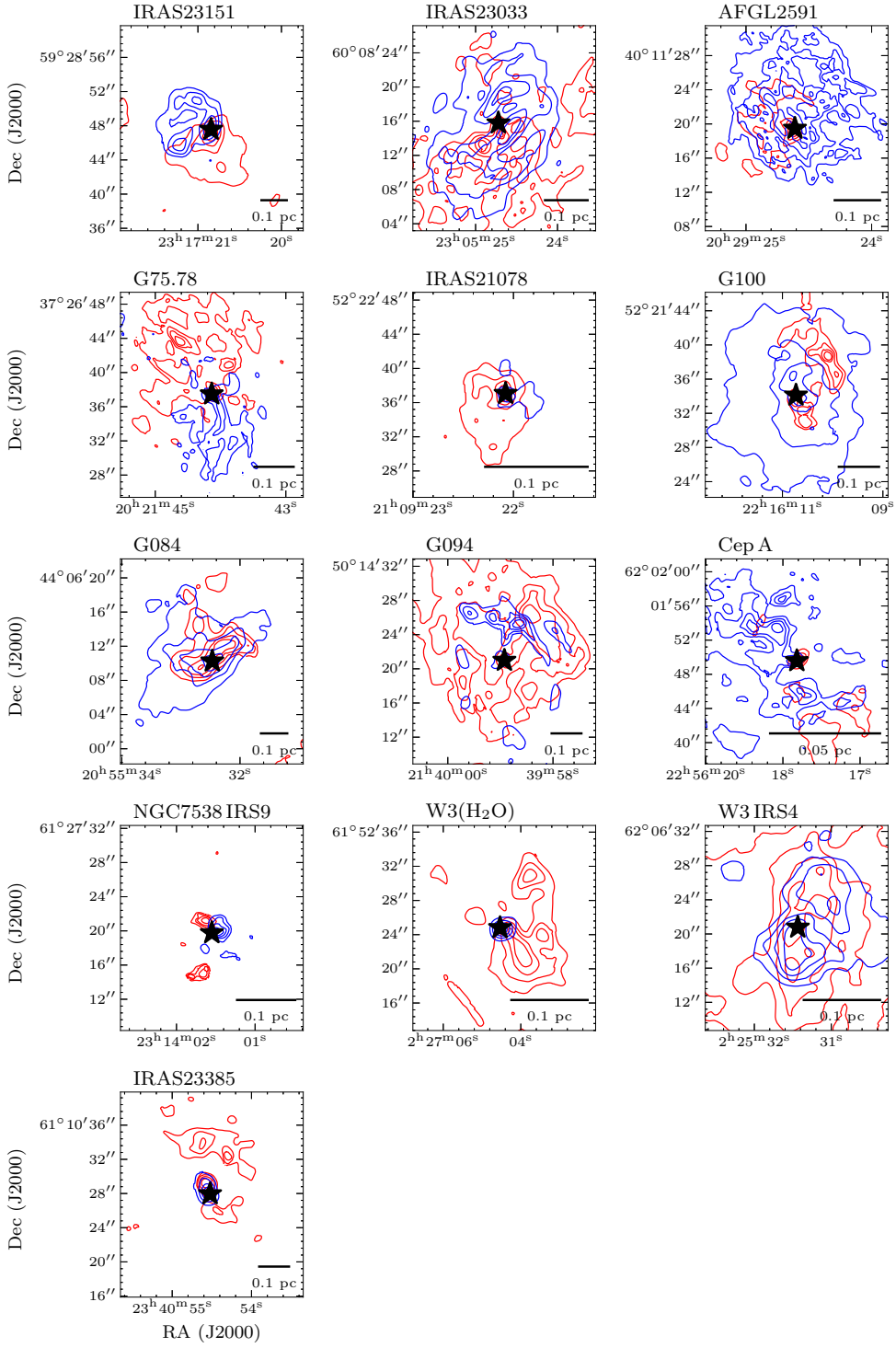

Figure B.5: Intensity maps of ^{13}CO (2 – 1) emission from merged NOEMA and IRAM 30-m data integrated over the blue and redshifted wings of emission, showing the outflow structure. The position of the strongest source in the field is depicted by a star. A scale-bar is shown in the bottom right corner of each panel. The field of view of the IRAM 30-m observations is 1.5′ by 1.5′ with a half-power beam width of ~11″ at this frequency. We did not have the corresponding data for the pilot sources at the time of this work, hence the missing panels.

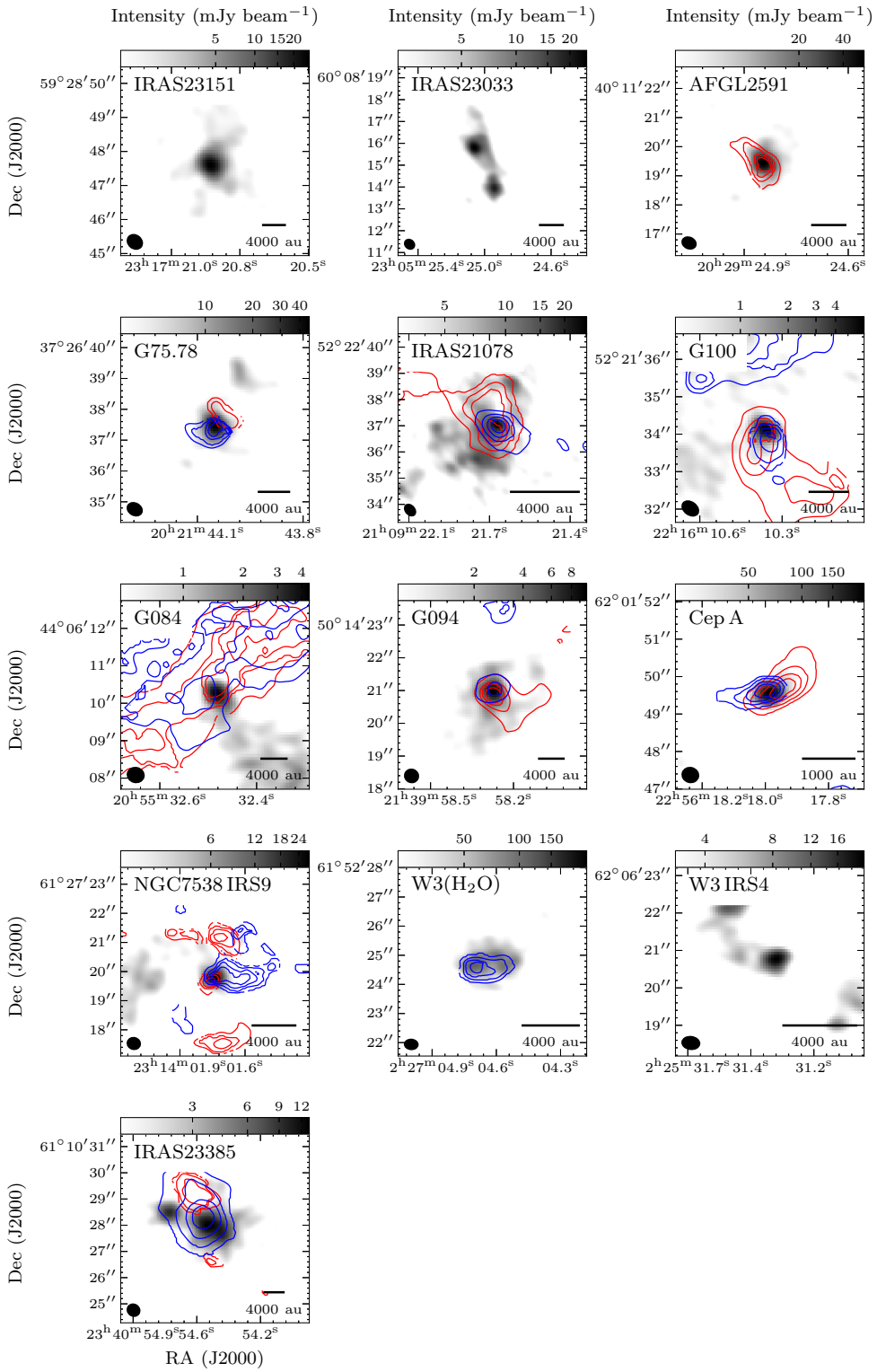

Figure B.6: The greyscale corresponds to the 1.37 mm continuum while the blue and red contours correspond to the NOEMA intensity maps of ^{13}CO (2 – 1) integrated over the blue and redshifted wings of emission, tracing either outflows or disk winds. The position of the strongest source in the field is depicted by a star. A scale-bar is shown in the bottom right corner of each panel. Note that most of the emission is filtered out by the interferometer.

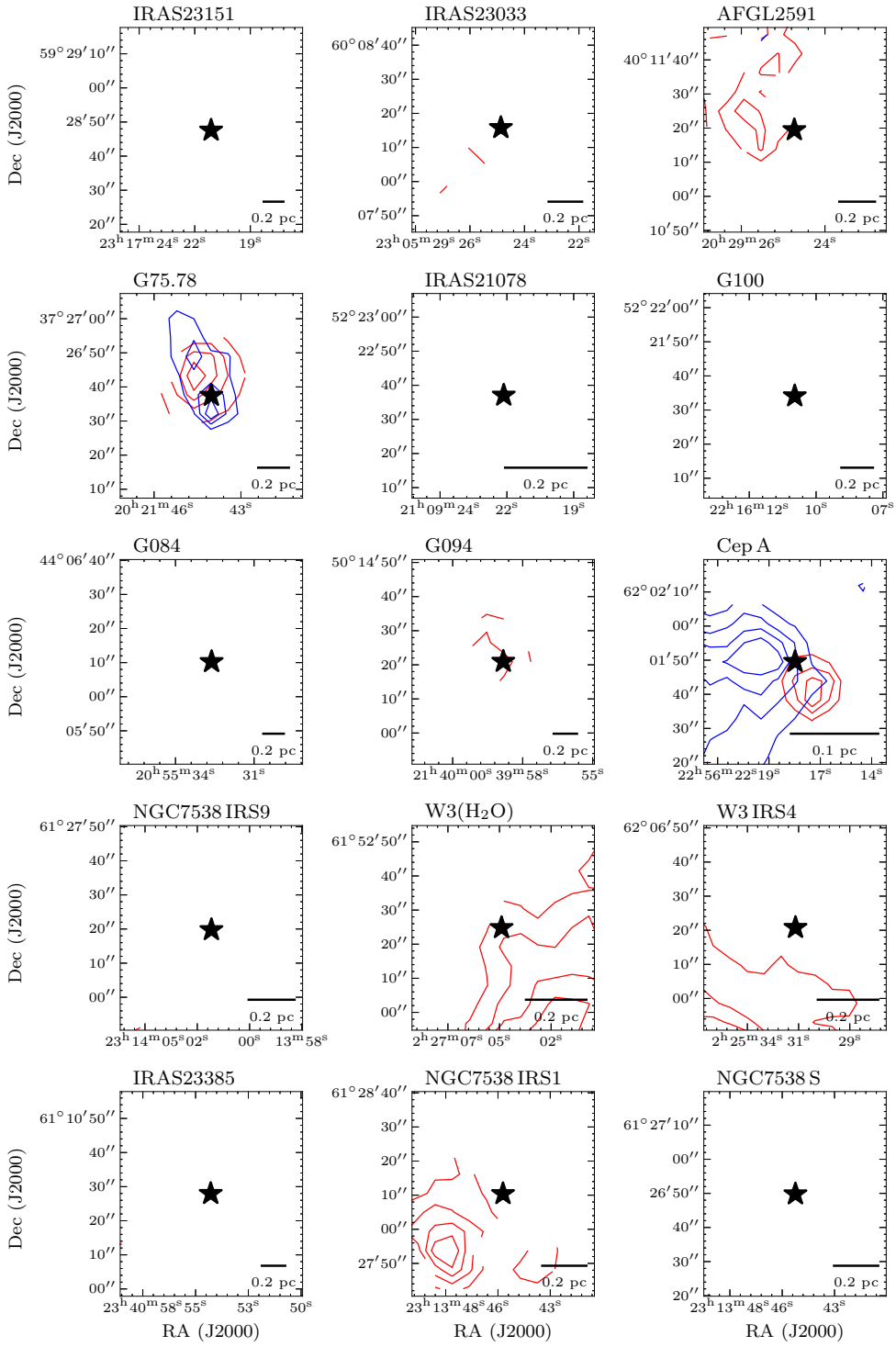

Figure B.7: Intensity maps of $C^{18}O$ (2 – 1) emission from IRAM 30-m telescope integrated over the blue and redshifted wings of emission, showing the outflow structure. The position of the strongest source in the field is depicted by a star. A scale-bar is shown in the bottom right corner of each panel. The field of view of the IRAM 30-m observations is 1.5′ by 1.5′ with a half-power beam width of ~11″ at this frequency. $C^{18}O$ is a good outflow tracer only for the brightest sources, hence the many empty panels.

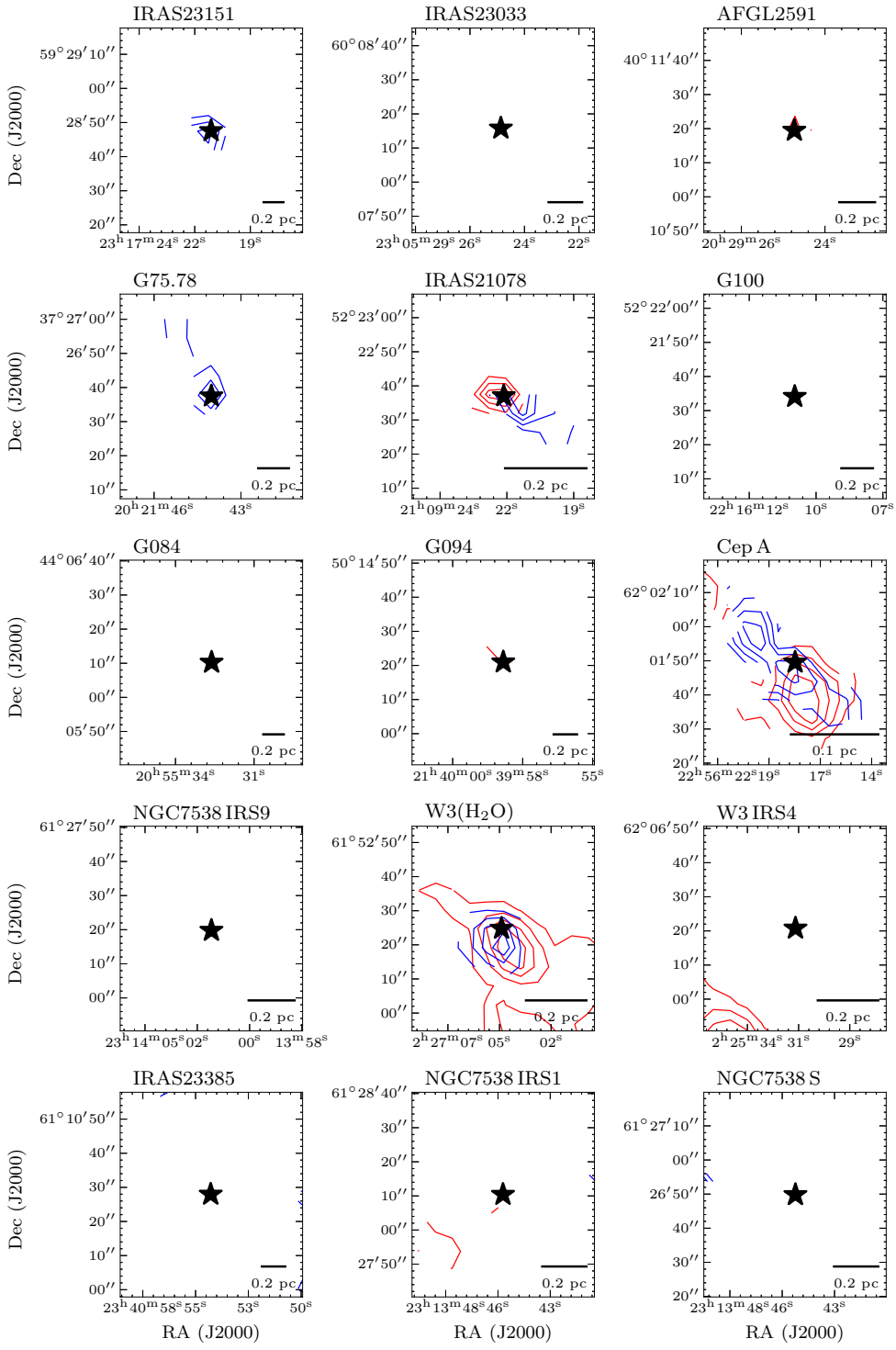

Figure B.8: Intensity maps of SO $(6_5 - 5_4)$ emission from IRAM 30-m telescope integrated over the blue and redshifted wings of emission, showing the outflow structure. The position of the strongest source in the field is depicted by a star. A scale-bar is shown in the bottom right corner of each panel. The field of view of the IRAM 30-m observations is 1.5′ by 1.5′ with a half-power beam width of ~11″ at this frequency.

B.3 XCLASS maps

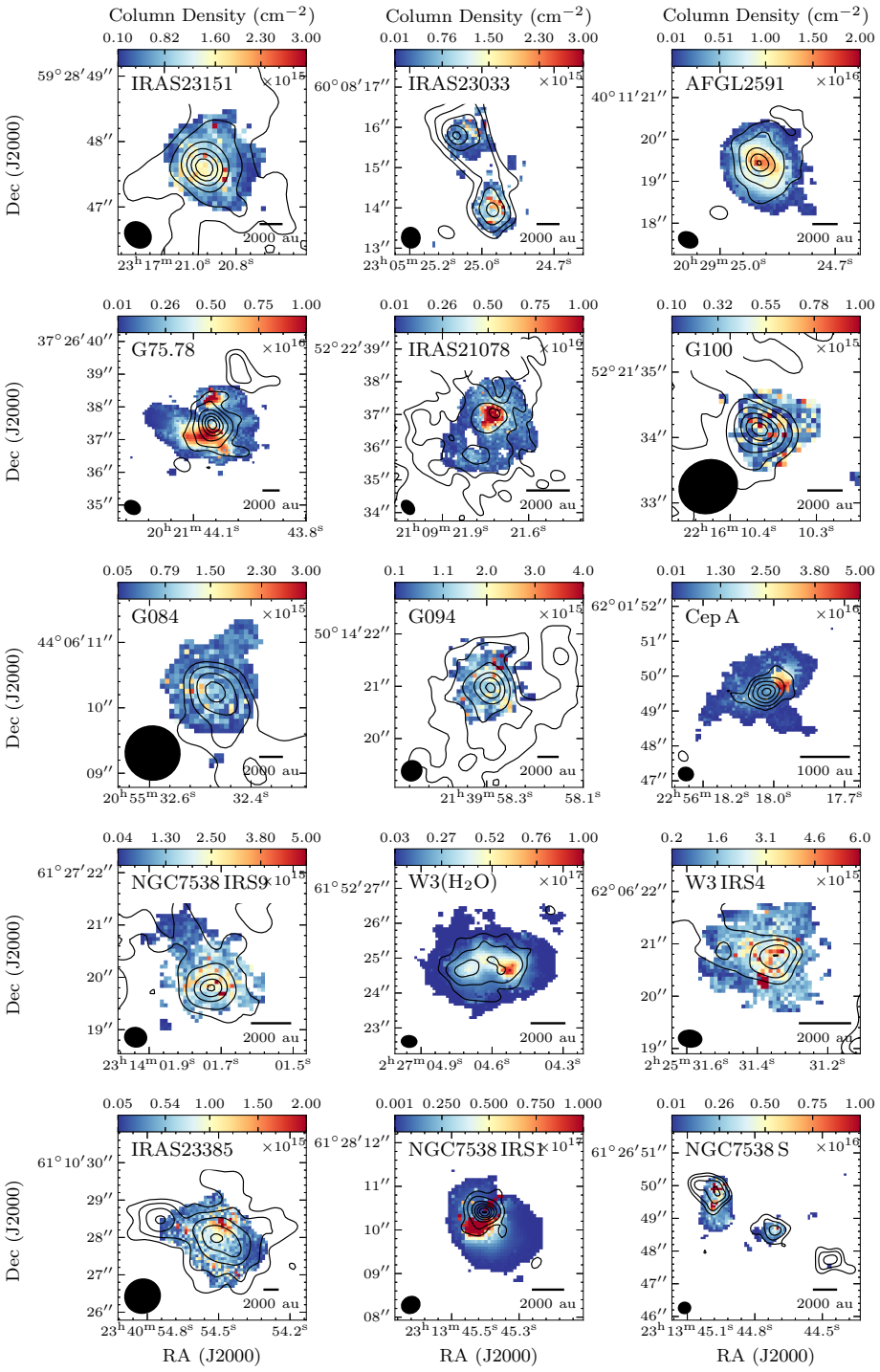

Figure B.9: CH_3CN column density maps obtained by fitting $CH_3CN\,(12_K - 11_K)$ $K = 0-6$ and $CH_3{}^{13}CN\,(12_K - 11_K)$ $K = 0-3$ lines with *XCLASS* for 17 cores in the CORE survey. The contours correspond to the 1.37 mm continuum as described in Fig. 6.2. The synthesized beam is shown in the bottom left corner and a scale bar in the bottom right corner of each panel. The blue and red arrows correspond to the estimated directions of bipolar blueshifted and redshifted molecular outflows, respectively.

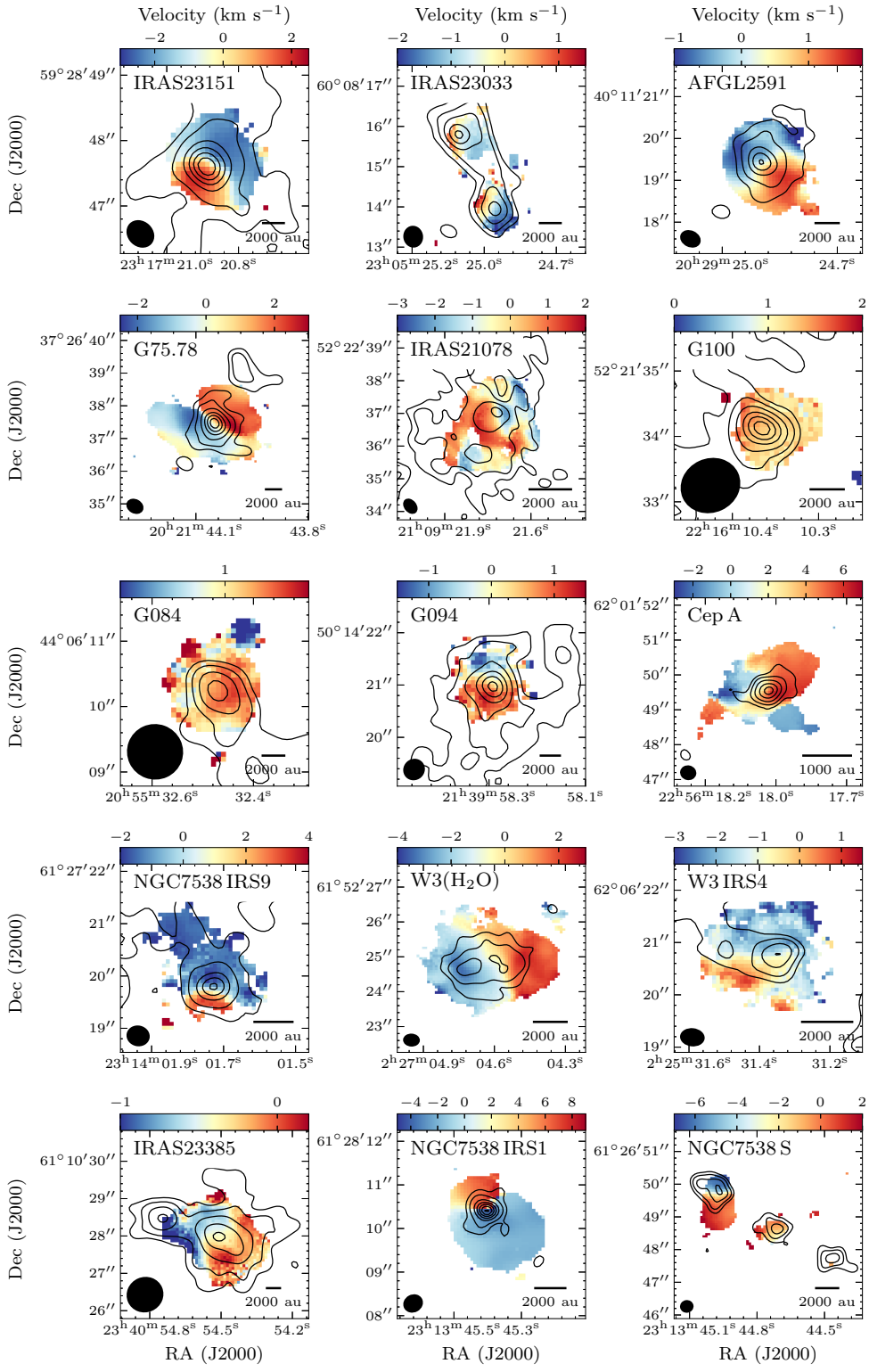

Figure B.10: Maps of offset velocity with respect to the systemic velocity obtained by fitting CH_3CN $(12_K - 11_K)$ $K = 0 - 6$ and $CH_3{}^{13}CN$ $(12_K - 11_K)$ $K = 0 - 3$ lines with *XCLASS* for 17 cores in the CORE survey. The contours correspond to the 1.37 mm continuum as described in Fig. 6.2. The synthesized beam is shown in the bottom left corner and a scale bar in the bottom right corner of each panel. The blue and red arrows correspond to the estimated directions of bipolar blueshifted and redshifted molecular outflows, respectively.

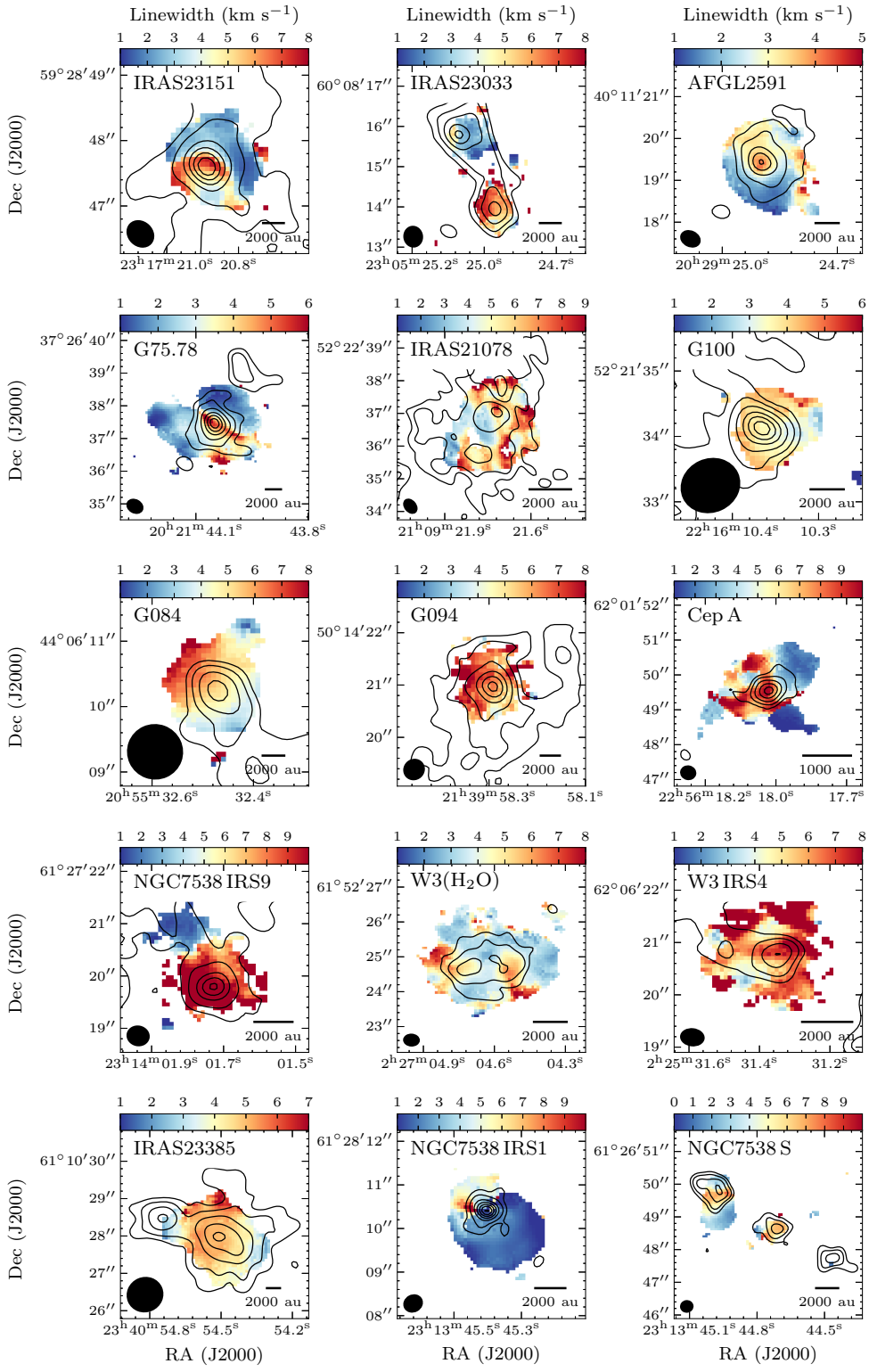

Figure B.11: Maps of linewidth obtained by fitting $CH_3CN\,(12_K - 11_K)\,K = 0 - 6$ and $CH_3{}^{13}CN\,(12_K - 11_K)\,K = 0 - 3$ lines with *XCLASS* for 17 cores in the CORE survey. The contours correspond to the 1.37 mm continuum as described in Fig. 6.2. The synthesized beam is shown in the bottom left corner and a scale bar in the bottom right corner of each panel. The blue and red arrows correspond to the estimated directions of bipolar blueshifted and redshifted molecular outflows, respectively.

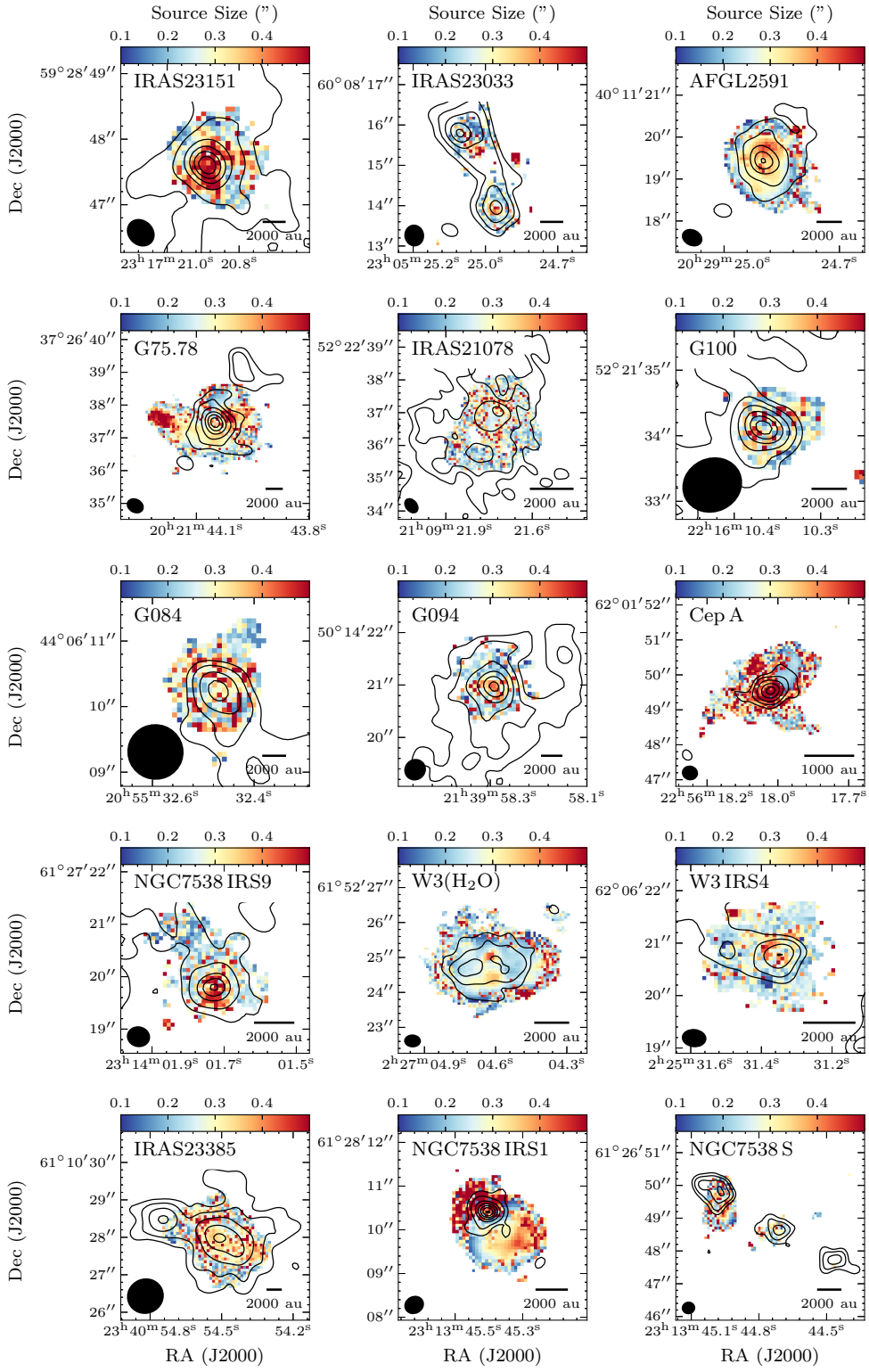

Figure B.12: Maps of source size parameter obtained by fitting CH_3CN $(12_K - 11_K)$ $K = 0-6$ and $CH_3{}^{13}CN$ $(12_K - 11_K)$ $K = 0-3$ lines with *XCLASS* for 17 cores in the CORE survey. The contours correspond to the 1.37 mm continuum as described in Fig. 6.2. The synthesized beam is shown in the bottom left corner and a scale bar in the bottom right corner of each panel. The blue and red arrows correspond to the estimated directions of bipolar blueshifted and redshifted molecular outflows, respectively.

B.4 Specific angular momentum

Table B.1: Fit parameters to different regions of the specific angular momentum radial profiles of the simulations shown in Fig. 6.7.

	Inner ($r < 40$ au)			
Inclination	a_{blue}	a_{red}	b_{blue}	b_{red}
10°	0.56 ± 0.06	0.56 ± 0.06	-3.16 ± 0.06	-3.16 ± 0.06
30°	0.54 ± 0.07	0.54 ± 0.07	-2.71 ± 0.07	-2.71 ± 0.07
60°	0.56 ± 0.09	0.56 ± 0.09	-2.6 ± 0.1	-2.6 ± 0.1
80°	0.75 ± 0.08	0.75 ± 0.08	-2.51 ± 0.08	-2.51 ± 0.08
	Middle (40 au $< r <$ 400 au)			
Inclination	a_{blue}	a_{red}	b_{blue}	b_{red}
10°	0.14 ± 0.05	-0.01 ± 0.08	-3.36 ± 0.03	-3.77 ± 0.05
30°	0.15 ± 0.04	0.26 ± 0.04	-2.96 ± 0.02	-3.04 ± 0.02
60°	0.35 ± 0.03	0.54 ± 0.05	-2.69 ± 0.02	-2.7 ± 0.03
80°	0.52 ± 0.04	0.48 ± 0.03	-2.58 ± 0.02	-2.83 ± 0.02
	Outer ($r >$ 400 au)			
Inclination	a_{blue}	a_{red}	b_{blue}	b_{red}
10°	0.78 ± 0.03	0.6 ± 0.1	-3.12 ± 0.01	-3.53 ± 0.02
30°	0.74 ± 0.05	1.0 ± 0.1	-2.76 ± 0.01	-2.85 ± 0.02
60°	1.30 ± 0.05	1.75 ± 0.09	-2.45 ± 0.01	-2.45 ± 0.01
80°	1.45 ± 0.03	1.75 ± 0.05	-2.34 ± 0.01	-2.34 ± 0.01

Note: The heading parameters a and b satisfy the following relation: $j \sin(i) = 10^b \, (\frac{r}{1000 \text{ au}})^a$, for the blueshifted and redshifted sides.

Acronyms

ALMA	Atacama Large Millimeter Array
CDMS	Cologne Database for Molecular Spectroscopy
ESO	European Southern Observatory
FWHM	full width at half maximum
GMC	giant molecular cloud
HMC	hot molecular core
HMSC	high-mass starless core
HMPO	high-mass protostellar object
IMF	initial mass function
ISM	interstellar medium
IR	infrared
IRAM	Institut de Radioastronomie Millimétrique
ISM	interstellar medium
LSR	local standard of rest
LTE	local thermodynamic equilibrium
MIDI	Mid-infrared Interferometric Instrument
NOEMA	NOrthern Extended Millimeter Array
PMS	pre-main-sequence
PV	position–velocity
RMS	root mean square
SED	spectral energy distribution
S/N	signal-to-noise
UV	ultraviolet
VLA	Karl G. Jansky Very Large Array
VLTI	Very Large Telescope Interferometer
YSO	young stellar object

List of Refereed Publications

Publications as first author

- **Ahmadi, A.**; Beuther, H.; Mottram, J. C.; Bosco, F.; Linz, H.; Henning, Th.; Winters, J. M.; Kuiper, R.; Pudritz, R.; Sánchez-Monge, Á.; Keto, E.; Beltran, M.; Bontemps, S.; Cesaroni, R.; Csengeri, T.; Feng, S.; Galvan-Madrid, R.; Johnston, K. G.; Klaassen, P.; Leurini, S. Longmore, S. N.; Lumsden, S.; Maud, L. T.; Menten, K. M.; Moscadelli, L.; Motte, F.; Palau, A.; Peters, T.; Ragan, S. E.; Schilke, P.; Urquhart, J. S.; Wyrowski, F.; Zinnecker, H. (2018), *Core fragmentation and Toomre stability analysis of W3 (H_2O). A case study of the IRAM NOEMA large program CORE*, Astronomy & Astrophysics 618, A46 (Chapter 4, parts of Chapter 3)

- **Ahmadi, A.**; Kuiper, R.; Beuther, H. (2019) *Disk kinematics and stability in high-mass star formation: Linking simulations and observations*, Astronomy & Astrophysics in press (Chapter 5)

- **Ahmadi, A.**; Beuther, H.; & the CORE Team, *Kinematics and stability of high-mass protostellar disk candidates at subarcsecond resolution. Evidence from the IRAM NOEMA large program CORE*, to be submitted to Astronomy & Astrophysics (Chapter 6)

Publications as contributing author[1]

- Beuther, H.; Mottram, J. C.; **Ahmadi, A.**; Bosco, F.; Linz, H.; Henning, Th.; Klaassen, P.; Winters, J. M.; Maud, L. T.; Kuiper, R.; Semenov, D.; Gieser, C.; Peters, T.; Urquhart, J. S.; Pudritz, R.; Ragan, S. E.; Feng, S.; Keto, E.; Leurini, S.; Cesaroni, R. Beltran, M.; Palau, A.; Sánchez-Monge, Á.; Galvan-Madrid, R.; Zhang, Q.; Schilke, P.; Wyrowski, F.; Johnston, K. G.; Longmore, S. N.; Lumsden, S.; Hoare, M.; Menten, K. M.; Csengeri, T. (2018), *Fragmentation and disk formation during high-mass star formation. IRAM NOEMA (Northern Extended Millimeter Array) large program CORE*, Astronomy & Astrophysics 617, A100 (parts of Chapter 3)

- Bosco, F.; Beuther, H.; **Ahmadi, A.**; Mottram, J. C.; Kuiper, R.; Linz, H.; Maud, L.; Winters, J. M.; Henning, T.; Feng, S.; Peters, T.; Semenov, D.; Klaassen, P. D.; Schilke, P.; Urquhart, J. S.; Beltrán, M. T.; Lumsden, S. L.; Leurini, S.; Moscadelli, L.; Cesaroni, R. Sánchez-Monge, Á.; Palau, A.; Pudritz, R.; Wyrowski, F.; Longmore, S. (2019), *Fragmentation, rotation, and outflows in the high-mass star-forming region IRAS 23033+5951. A*

[1]Only refereed publications during the time of the PhD are included, listed in order of involvement.

case study of the IRAM NOEMA large program CORE, Astronomy & Astrophysics 629, A10

- Cesaroni, R.; Beuther, H.; **Ahmadi, A.**; Beltrán, M. T.; Csengeri, T.; Galván-Madrid, R.; Gieser, C.; Henning, T.; Johnston, K. G.; Klaassen, P. D.; Kuiper, R.; Leurini, S.; Linz, H.; Longmore, S.; Lumsden, S. L.; Maud, L. T.; Moscadelli, L.; Mottram, J. C.; Palau, A.; Peters, T. Pudritz, R. E.; Sánchez-Monge, Á.; Schilke, P.; Semenov, D.; Suri, S.; Urquhart, J. S.; Winters, J. M.; Zhang, Q.; Zinnecker, H. (2019), *IRAS 23385+6053: an embedded massive cluster in the making*, Astronomy & Astrophysics 627, A68

- Gieser, C.; Semenov, D.; Beuther, H.; **Ahmadi, A.**; Mottram, J. C.; Henning, Th.; Beltran, M.; Maud, L. T.; Bosco, F.; Leurini, S.; Peters, T.; Klaassen, P.; Kuiper, R.; Feng, S.; Urquhart, J. S.; Moscadelli, L.; Csengeri, T.; Lumsden, S.; Winters, J. M.; Suri, S. Zhang, Q.; Pudritz, R.; Palau, A.; Menten, K. M.; Galvan-Madrid, R.; Wyrowski, F.; Schilke, P.; Sánchez-Monge, Á.; Linz, H.; Johnston, K. G.; Jiménez-Serra, I.; Longmore, S.; Möller, T. (2019), *Chemical complexity in high-mass star formation: An observational and modeling case study of the AFGL 2591 VLA 3 hot core*, Astronomy & Astrophysics in press

- Beuther, H.; **Ahmadi, A.**; Mottram, J. C.; Linz, H.; Maud, L. T.; Henning, Th.; Kuiper, R.; Walsh, A. J.; Johnston, K. G.; Longmore, S. N. (2019), *High-mass star formation at sub-50 au scales*, Astronomy & Astrophysics 621, A122

- Cesaroni, R.; Sánchez-Monge, Á.; Beltrán, M. T.; Johnston, K. G.; Maud, L. T.; Moscadelli, L.; Mottram, J. C.; **Ahmadi, A.**; Allen, V.; Beuther, H.; Csengeri, T.; Etoka, S.; Fuller, G. A.; Galli, D.; Galván-Madrid, R.; Goddi, C.; Henning, T.; Hoare, M. G.; Klaassen, P. D.; Kuiper, R. Kumar, M. S. N.; Lumsden, S.; Peters, T.; Rivilla, V. M.; Schilke, P.; Testi, L.; van der Tak, F.; Vig, S.; Walmsley, C. M.; Zinnecker, H. (2017), *Chasing discs around O-type (proto)stars: Evidence from ALMA observations*, Astronomy & Astrophysics 602, A59

- Beltrán, M. T.; Cesaroni, R.; Rivilla, V. M.; Sánchez-Monge, Á.; Moscadelli, L.; **Ahmadi, A.**; Allen, V.; Beuther, H.; Etoka, S.; Galli, D.; Galván-Madrid, R.; Goddi, C.; Johnston, K. G.; Klaassen, P. D.; Kölligan, A.; Kuiper, R.; Kumar, M. S. N.; Maud, L. T.; Mottram, J. C.; Peters, T. Schilke, P.; Testi, L.; van der Tak, F.; Walmsley, C. M. (2018), *Accelerating infall and rotational spin-up in the hot molecular core G31.41+0.31*, Astronomy & Astrophysics 615, A141

- Moscadelli, L.; Rivilla, V. M.; Cesaroni, R.; Beltrán, M. T.; Sánchez-Monge, Á.; Schilke, P.; Mottram, J. C.; **Ahmadi, A.**; Allen, V.; Beuther, H.; Csengeri, T.; Etoka, S.; Galli, D.; Goddi, C.; Johnston, K. G.; Klaassen, P. D.; Kuiper, R.; Kumar, M. S. N.; Maud, L. T.; Möller, T. Peters, T.; Van der Tak, F.; Vig, S. (2018), *The feedback of an HC HII region on its parental molecular core. The case of core A1 in the star-forming region G24.78+0.08*, Astronomy & Astrophysics 616, A66

- Maud, L. T.; Cesaroni, R.; Kumar, M. S. N.; van der Tak, F. F. S.; Allen, V.; Hoare, M. G.; Klaassen, P. D.; Harsono, D.; Hogerheijde, M. R.; Sánchez-Monge, Á.; Schilke, P.; **Ahmadi, A.**; Beltrán, M. T.; Beuther, H.; Csengeri, T.; Etoka, S.; Fuller, G.; Galván-Madrid, R.; Goddi, C.; Henning, Th. Johnston, K. G.; Kuiper, R.; Lumsden, S.; Moscadelli, L.; Mottram, J. C.; Peters, T.; Rivilla, V. M.; Testi, L.; Vig, S.; de Wit, W. J.; Zinnecker, H. (2018), *Chasing discs around O-type (proto)stars. ALMA evidence for an SiO disc and disc wind from G17.64+0.16*, Astronomy & Astrophysics 620, A31

- Maud, L. T.; Cesaroni, R.; Kumar, M. S. N.; Rivilla, V. M.; Ginsburg, A.; Klaassen, P. D.; Harsono, D.; Sánchez-Monge, Á.; **Ahmadi, A.**; Allen, V.; Beltrán, M. T.; Beuther, H.; Galván-Madrid, R.; Goddi, C.; Hoare, M. G.; Hogerheijde, M. R.; Johnston, K. G.; Kuiper, R.; Moscadelli, L.; Peters, T. Testi, L.; van der Tak, F. F. S.; de Wit, W. J. (2019), *Substructures in the Keplerian disc around the O-type (proto-)star G17.64+0.16*, Astronomy & Astrophysics 627, L6

Bibliography

Ahmadi, A., Beuther, H., Mottram, J. C., et al. 2018, A&A, 618, A46

Ahmadi, A., Kuiper, R., & Beuther, H. 2019, arXiv e-prints [arXiv:1909.04051]

Alves, F. O., Girart, J. M., Caselli, P., et al. 2017, A&A, 603, L3

Ando, K., Nagayama, T., Omodaka, T., et al. 2011, PASJ, 63, 45

André, P., Di Francesco, J., Ward-Thompson, D., et al. 2014, in Protostars and Planets VI, ed. H. Beuther, R. S. Klessen, C. P. Dullemond, & T. Henning, 27

Andre, P., Ward-Thompson, D., & Barsony, M. 1993, ApJ, 406, 122

Andre, P., Ward-Thompson, D., & Barsony, M. 2000, in Protostars and Planets IV, ed. V. Mannings, A. P. Boss, & S. S. Russell, 59

Astropy Collaboration, Robitaille, T. P., Tollerud, E. J., et al. 2013, A&A, 558, A33

Baehr, H., Klahr, H., & Kratter, K. M. 2017, ApJ, 848, 40

Banerjee, R. & Pudritz, R. E. 2008, in Astronomical Society of the Pacific Conference Series, Vol. 387, Massive Star Formation: Observations Confront Theory, ed. H. Beuther, H. Linz, & T. Henning, 216

Bastian, N., Covey, K. R., & Meyer, M. R. 2010, ARA&A, 48, 339

Behrend, R. & Maeder, A. 2001, A&A, 373, 190

Belloche, A. 2013, in EAS Publications Series, Vol. 62, EAS Publications Series, ed. P. Hennebelle & C. Charbonnel, 25–66

Beltrán, M. T., Cesaroni, R., Neri, R., & Codella, C. 2011, A&A, 525, A151

Beltrán, M. T., Cesaroni, R., Neri, R., et al. 2005, A&A, 435, 901

Beltrán, M. T. & de Wit, W. J. 2016, Astronomy and Astrophysics Review, 24, 6

Bergin, E. A. & Tafalla, M. 2007, ARA&A, 45, 339

Beuther, H., Ahmadi, A., Mottram, J. C., et al. 2019, A&A, 621, A122

Beuther, H., Churchwell, E. B., McKee, C. F., & Tan, J. C. 2007a, in Protostars and Planets V, ed. B. Reipurth, D. Jewitt, & K. Keil, 165

Beuther, H., Linz, H., & Henning, T. 2012, A&A, 543, A88

Beuther, H., Linz, H., & Henning, T. 2013, A&A, 558, A81

Beuther, H., Linz, H., Henning, T., Feng, S., & Teague, R. 2017a, A&A, 605, A61

Beuther, H., Mottram, J. C., Ahmadi, A., et al. 2018, A&A, 617, A100

Beuther, H., Schilke, P., Gueth, F., et al. 2002a, A&A, 387, 931

Beuther, H. & Shepherd, D. 2005, in Astrophysics and Space Science Library, Vol. 324, Astrophysics and Space Science Library, ed. M. S. N. Kumar, M. Tafalla, & P. Caselli, 105

Beuther, H., Walsh, A., Schilke, P., et al. 2002b, A&A, 390, 289

Beuther, H., Walsh, A. J., Johnston, K. G., et al. 2017b, A&A, 603, A10

Beuther, H., Zhang, Q., Hunter, T. R., Sridharan, T. K., & Bergin, E. A. 2007b, A&A, 473, 493

Beuther, H., Zhang, Q., Sridharan, T. K., & Chen, Y. 2005, ApJ, 628, 800

Bhandare, A., Kuiper, R., Henning, T., et al. 2018, arXiv, A95

Bik, A., Henning, T., Stolte, A., et al. 2012, ApJ, 744, 87

Bik, A. & Thi, W. F. 2004, A&A, 427, L13

Boehm-Vitense, E. 1981, ARA&A, 19, 295
Boley, P. A., Linz, H., van Boekel, R., et al. 2013, A&A, 558, A24
Bonnell, I. A., Bate, M. R., Clarke, C. J., & Pringle, J. E. 1997, MNRAS, 285, 201
Bonnell, I. A., Bate, M. R., Clarke, C. J., & Pringle, J. E. 2001, MNRAS, 323, 785
Bonnell, I. A., Bate, M. R., & Zinnecker, H. 1998, MNRAS, 298, 93
Bonnell, I. A., Larson, R. B., & Zinnecker, H. 2007, in Protostars and Planets V, ed. B. Reipurth, D. Jewitt, & K. Keil, 149
Bonnell, I. A., Vine, S. G., & Bate, M. R. 2004, MNRAS, 349, 735
Bosco, F., Beuther, H., Ahmadi, A., et al. 2019, A&A, 629, A10
Boucher, D., Burie, J., Bauer, A., Dubrulle, A., & Demaison, J. 1980, Journal of Physical and Chemical Reference Data, 9, 659
Bowman, J. D., Rogers, A. E. E., Monsalve, R. A., Mozdzen, T. J., & Mahesh, N. 2018, Nature, 555, 67
Bradley, L., Sipocz, B., Robitaille, T., et al. 2016, Photutils: Photometry tools
Breen, S. L., Ellingsen, S. P., Caswell, J. L., & Lewis, B. E. 2010, MNRAS, 401, 2219
Burke, B. F. & Graham-Smith, F. 2014, An Introduction to Radio Astronomy
Caratti o Garatti, A., Stecklum, B., Garcia Lopez, R., et al. 2017, Nature Physics, 13, 276
Cesaroni, R., Beuther, H., Ahmadi, A., et al. 2019, A&A, 627, A68
Cesaroni, R., Galli, D., Lodato, G., Walmsley, C. M., & Zhang, Q. 2007, in Protostars and Planets V, 197–212
Cesaroni, R., Galli, D., Lodato, G., Walmsley, M., & Zhang, Q. 2006, Nature, 444, 703
Cesaroni, R., Sánchez-Monge, Á., Beltrán, M. T., et al. 2017, A&A, 602, A59
Chabrier, G. 2003, Publications of the Astronomical Society of the Pacific, 115, 763
Chen, H.-R., Welch, W. J., Wilner, D. J., & Sutton, E. C. 2006, ApJ, 639, 975
Chen, H.-R. V., Keto, E., Zhang, Q., et al. 2016, ApJ, 823, 125
Chernin, L. & Masson, C. 1993, ApJ, 403, L21
Chini, R., Hoffmeister, V. H., Nasseri, A., Stahl, O., & Zinnecker, H. 2012, MNRAS, 424, 1925
Choi, Y. K., Hachisuka, K., Reid, M. J., et al. 2014, ApJ, 790, 99
Clark, B. G. 1980, A&A, 89, 377
Collings, M. P., Anderson, M. A., Chen, R., et al. 2004, MNRAS, 354, 1133
Commerçon, B., Teyssier, R., Audit, E., Hennebelle, P., & Chabrier, G. 2011, A&A, 529, A35
Courant, R., Friedrichs, K., & Lewy, H. 1967, IBM Journal of Research and Development, 11, 215
Crowther, P. A. 2005, in IAU Symposium, Vol. 227, Massive Star Birth: A Crossroads of Astrophysics, ed. R. Cesaroni, M. Felli, E. Churchwell, & M. Walmsley, 389–396
Crowther, P. A. 2007, ARA&A, 45, 177
Csengeri, T., Bontemps, S., Wyrowski, F., et al. 2018, A&A, 617, A89
Cyganowski, C. J., Whitney, B. A., Holden, E., et al. 2008, AJ, 136, 2391
Davies, B., Hoare, M. G., Lumsden, S. L., et al. 2011, MNRAS, 416, 972
Davis, C. J., Moriarty-Schieven, G., Eislöffel, J., Hoare, M. G., & Ray, T. P. 1998, AJ, 115, 1118
De Buizer, J. M., Liu, M., Tan, J. C., et al. 2017, ApJ, 843, 33
di Francesco, J., Evans, N. J., I., Caselli, P., et al. 2007, in Protostars and Planets V, ed. B. Reipurth, D. Jewitt, & K. Keil, 17
Dobbs, C. L., Bonnell, I. A., & Clark, P. C. 2005, MNRAS, 360, 2
Draine, B. T. 2011, Physics of the Interstellar and Intergalactic Medium (Princeton University Press)
Dreher, J. W. & Welch, W. J. 1981, ApJ, 245, 857

Dullemond, C. P. 2012, ASCL, ascl:1202.015
Elmegreen, B. G. 1991, ApJ, 378, 139
Elmegreen, B. G. 1994, ApJ, 433, 39
Evans, II, N. J. 1999, ARA&A, 37, 311
Fallscheer, C., Beuther, H., Zhang, Q., Keto, E., & Sridharan, T. K. 2009, A&A, 504, 127
Feng, S., Beuther, H., Henning, T., et al. 2015, A&A, 581, A71
Feng, S., Beuther, H., Semenov, D., et al. 2016, A&A, 593, A46
Frank, A., Ray, T. P., Cabrit, S., et al. 2014, in Protostars and Planets VI, ed. H. Beuther, R. Klessen, C. Dullemond, & T. Henning (Univ. of Arizona Press, Tucson), 451–474
Gammie, C. F. 2001, ApJ, 553, 174
Gaume, R. A., Goss, W. M., Dickel, H. R., Wilson, T. L., & Johnston, K. J. 1995, ApJ, 438, 776
Gerner, T., Beuther, H., Semenov, D., et al. 2014, A&A, 563, A97
Gieser, C., Semenov, D., Beuther, H., et al. 2019, arXiv e-prints, arXiv:1910.05081
Ginsburg, A., Koch, E., Robitaille, T., et al. 2019, radio-astro-tools/spectral-cube: v0.4.4
Ginsburg, A. & Mirocha, J. 2011, PySpecKit: Python Spectroscopic Toolkit
Girichidis, P., Federrath, C., Banerjee, R., & Klessen, R. S. 2011, MNRAS, 413, 2741
Goddi, C., Zhang, Q., & Moscadelli, L. 2015, A&A, 573, A108
Goldreich, P. & Lynden-Bell, D. 1965, MNRAS, 130, 125
Goodman, A. A., Benson, P. J., Fuller, G. A., & Myers, P. C. 1993, ApJ, 406, 528
Green, S. 1986, ApJ, 309, 331
Hachisuka, K., Brunthaler, A., Menten, K. M., et al. 2006, ApJ, 645, 337
Harries, T. J., Douglas, T. A., & Ali, A. 2017, MNRAS, 471, 4111
Hartmann, L. 2009, Accretion Processes in Star Formation: Second Edition
Haworth, T. J., Glover, S. C. O., Koepferl, C. M., Bisbas, T. G., & Dale, J. E. 2018, New Astronomy Reviews, 82, 1
Henkel, C., Wilson, T. L., & Bieging, J. 1982, A&A, 109, 344
Hennebelle, P. & Chabrier, G. 2011, in IAU Symposium, Vol. 270, Computational Star Formation, ed. J. Alves, B. G. Elmegreen, J. M. Girart, & V. Trimble, 159–168
Hennebelle, P. & Teyssier, R. 2008, A&A, 477, 25
Herbig, G. H. 1960, ApJS, 4, 337
Hildebrand, R. H. 1983, QJRAS, 24, 267
Hoare, M. G., Kurtz, S. E., Lizano, S., Keto, E., & Hofner, P. 2007, in Protostars and Planets V, ed. B. Reipurth, D. Jewitt, & K. Keil, 181
Högbom, J. A. 1974, Astronomy and Astrophysics Supplement Series, 15, 417
Hosokawa, T. & Omukai, K. 2009, ApJ, 691, 823
Hunter, T. R., Brogan, C. L., MacLeod, G., et al. 2017, ApJ, 837, L29
Ilee, J. D., Cyganowski, C. J., Brogan, C. L., et al. 2018, ApJ, 869, L24
Ilee, J. D., Cyganowski, C. J., Nazari, P., et al. 2016, MNRAS, 462, 4386
Ilee, J. D., Wheelwright, H. E., Oudmaijer, R. D., et al. 2013, MNRAS, 429, 2960
Jankovic, M. R., Haworth, T. J., Ilee, J. D., et al. 2019, MNRAS, 482, 4673
Jeans, J. H. 1928, Astronomy and cosmogony
Jiménez-Serra, I., Martín-Pintado, J., Caselli, P., et al. 2009, ApJ, 703, L157
Johnson, B. M. & Gammie, C. F. 2003, ApJ, 597, 131
Johnston, K. G., Robitaille, T. P., Beuther, H., et al. 2015, ApJ, 813, L19
Kahn, F. D. 1974, A&A, 37, 149

Kennicutt, Robert C., J. 1989, ApJ, 344, 685
Keto, E. 2003, ApJ, 599, 1196
Keto, E. & Klaassen, P. 2008, ApJ, 678, L109
Keto, E. & Wood, K. 2006, ApJ, 637, 850
Keto, E. R. 1991, ApJ, 371, 163
Keto, E. R., Welch, W. J., Reid, M. J., & Ho, P. T. P. 1995, ApJ, 444, 765
Kim, W.-T. & Ostriker, E. C. 2001, ApJ, 559, 70
Klaassen, P. D., Johnston, K. G., Urquhart, J. S., et al. 2018, A&A, 611, A99
Klassen, M., Pudritz, R. E., Kuiper, R., Peters, T., & Banerjee, R. 2016, ApJ, 823, 28
Kölligan, A. & Kuiper, R. 2018, A&A, 620, A182
Kratter, K. & Lodato, G. 2016, ARA&A, 54, 271
Kratter, K. M. & Matzner, C. D. 2006, MNRAS, 373, 1563
Kratter, K. M., Matzner, C. D., Krumholz, M. R., & Klein, R. I. 2010, ApJ, 708, 1585
Kraus, S., Hofmann, K.-H., Menten, K. M., et al. 2010, Nature, 466, 339
Kroupa, P. 2002, Science, 295, 82
Krumholz, M. R. 2006, ApJ, 641, L45
Krumholz, M. R., Klein, R. I., & McKee, C. F. 2007, ApJ, 665, 478
Krumholz, M. R., Klein, R. I., McKee, C. F., Offner, S. S. R., & Cunningham, A. J. 2009, Science, 323, 754
Kuiper, R. & Hosokawa, T. 2018, A&A, 616, A101
Kuiper, R., Klahr, H., Beuther, H., & Henning, T. 2010, ApJ, 722, 1556
Kuiper, R., Klahr, H., Beuther, H., & Henning, T. 2011, ApJ, 732, 20
Kuiper, R., Klahr, H., Dullemond, C., Kley, W., & Henning, T. 2010, A&A, 511, A81
Kuiper, R. & Klessen, R. S. 2013, A&A, 555, A7
Kuiper, R., Turner, N. J., & Yorke, H. W. 2016, ApJ, 832, 40
Kuiper, R. & Yorke, H. W. 2013, ApJ, 772, 61
Kuiper, R., Yorke, H. W., & Turner, N. J. 2015, ApJ, 800, 86
Kurtz, S., Churchwell, E., & Wood, D. O. S. 1994, ApJS, 91, 659
Lada, C. J. 1987, in IAU Symposium, Vol. 115, Star Forming Regions, ed. M. Peimbert & J. Jugaku, 1
Laor, A. & Draine, B. T. 1993, ApJ, 402, 441
Larson, R. B. & Starrfield, S. 1971, A&A, 13, 190
Lee, C.-F., Ho, P. T. P., Li, Z.-Y., et al. 2017, Nature Astronomy, 1, 0152
Leurini, S., Codella, C., Zapata, L., et al. 2011, A&A, 530, A12
Loren, R. B. & Mundy, L. G. 1984, ApJ, 286, 232
Lumsden, S. L., Hoare, M. G., Urquhart, J. S., et al. 2013, ApJS, 208, 11
Maret, S., Hily-Blant, P., Pety, J., Bardeau, S., & Reynier, E. 2011, A&A, 526, A47
Martins, F., Schaerer, D., & Hillier, D. J. 2005, A&A, 436, 1049
Masunaga, H. & Inutsuka, S.-i. 2000, ApJ, 531, 350
Masunaga, H., Miyama, S. M., & Inutsuka, S.-i. 1998, ApJ, 495, 346
Maud, L. T., Cesaroni, R., Kumar, M. S. N., et al. 2019, A&A, 627, L6
Maud, L. T., Cesaroni, R., Kumar, M. S. N., et al. 2018, A&A, 620, A31
Maud, L. T., Moore, T. J. T., Lumsden, S. L., et al. 2015, MNRAS, 453, 645
Maury, A. J., André, P., Testi, L., et al. 2019, A&A, 621, A76
McKee, C. F. & Ostriker, E. C. 2007, ARA&A, 45, 565
McKee, C. F. & Tan, J. C. 2002, Nature, 416, 59

McKee, C. F. & Tan, J. C. 2003, ApJ, 585, 850
Mestel, L. 1963, MNRAS, 126, 553
Meyer, D. M. A., Kuiper, R., Kley, W., Johnston, K. G., & Vorobyov, E. 2018, MNRAS, 473, 3615
Meyer, D. M.-A., Vorobyov, E. I., Kuiper, R., & Kley, W. 2017, MNRAS, 464, L90
Mignone, A., Bodo, G., Massaglia, S., et al. 2007, ApJS, 170, 228
Mignone, A., Zanni, C., Tzeferacos, P., et al. 2012, ApJS, 198, 7
Molinari, S., Brand, J., Cesaroni, R., & Palla, F. 1996, A&A, 308, 573
Molinari, S., Testi, L., Brand, J., Cesaroni, R., & Palla, F. 1998, ApJ, 505, L39
Möller, T., Bernst, I., Panoglou, D., et al. 2013, A&A, 549, A21
Möller, T., Endres, C., & Schilke, P. 2017, A&A, 598, A7
Morgan, W. W. & Keenan, P. C. 1973, ARA&A, 11, 29
Moscadelli, L. & Goddi, C. 2014, A&A, 566, A150
Moscadelli, L., Reid, M. J., Menten, K. M., et al. 2009, ApJ, 693, 406
Moscadelli, L., Sánchez-Monge, Á., Goddi, C., et al. 2016, A&A, 585, A71
Moscadelli, L., Sanna, A., & Goddi, C. 2018, in IAU Symposium, Vol. 336, Astrophysical Masers: Unlocking the Mysteries of the Universe, ed. A. Tarchi, M. J. Reid, & P. Castangia, 201–206
Motte, F., Bontemps, S., & Louvet, F. 2018, Annual Review of Astronomy and Astrophysics, 56, 41
Motte, F., Bontemps, S., Schilke, P., et al. 2007, A&A, 476, 1243
Mottram, J. C. 2008, PhD thesis, University of Leeds (UK
Mottram, J. C., Hoare, M. G., Urquhart, J. S., et al. 2011, A&A, 525, A149
Müller, H. S. P., Schlöder, F., Stutzki, J., & Winnewisser, G. 2005, Journal of Molecular Structure, 742, 215
Müller, H. S. P., Thorwirth, S., Roth, D. A., & Winnewisser, G. 2001, A&A, 370, L49
Myers, A. T., McKee, C. F., Cunningham, A. J., Klein, R. I., & Krumholz, M. R. 2013, ApJ, 766, 97
Nakano, T. 1989, ApJ, 345, 464
Norberg, P. & Maeder, A. 2000, A&A, 359, 1025
Norris, R. P., Whiteoak, J. B., Caswell, J. L., Wieringa, M. H., & Gough, R. G. 1993, ApJ, 412, 222
Ohashi, N., Hayashi, M., Ho, P. T. P., & Momose, M. 1997a, ApJ, 475, 211
Ohashi, N., Hayashi, M., Ho, P. T. P., et al. 1997b, ApJ, 488, 317
Ossenkopf, V. & Henning, T. 1994, A&A, 291, 943
Oya, Y., Moriwaki, K., Onishi, S., et al. 2018, ApJ, 854, 96
Oya, Y., Sakai, N., López-Sepulcre, A., et al. 2016, ApJ, 824, 88
Palla, F. & Stahler, S. W. 1993, ApJ, 418, 414
Peretto, N., André, P., & Belloche, A. 2006, A&A, 445, 979
Pickett, H. M., Poynter, R. L., Cohen, E. A., et al. 1998, J. Quant. Spec. Radiat. Transf., 60, 883
Pineda, J. E., Zhao, B., Schmiedeke, A., et al. 2019, ApJ, 882, 103
Portegies Zwart, S. F., Makino, J., McMillan, S. L. W., & Hut, P. 1999, A&A, 348, 117
Pudritz, R. E., Ouyed, R., Fendt, C., & Brandenburg, A. 2007, in Protostars and Planets V, ed. B. Reipurth, D. Jewitt, & K. Keil (Univ. of Arizona Press, Tucson), 277–294
Qin, S.-L., Schilke, P., Wu, J., et al. 2015, ApJ, 803, 39
Rathborne, J. M., Jackson, J. M., Chambers, E. T., et al. 2005, ApJ, 630, L181
Reid, M. J., Argon, A. L., Masson, C. R., Menten, K. M., & Moran, J. M. 1995, ApJ, 443, 238
Rosen, A. L., Krumholz, M. R., McKee, C. F., & Klein, R. I. 2016, MNRAS, 463, 2553
Rybizki, J. & Just, A. 2015, MNRAS, 447, 3880
Rygl, K. L. J., Brunthaler, A., Sanna, A., et al. 2012, A&A, 539, A79

Safronov, V. S. 1960, Annales d'Astrophysique, 23, 979
Sakai, N., Sakai, T., Hirota, T., et al. 2014, Nature, 507, 78
Salpeter, E. E. 1955, ApJ, 121, 161
Sana, H., Le Bouquin, J. B., Lacour, S., et al. 2014, ApJS, 215, 15
Sánchez-Monge, Á. 2011, PhD thesis, Universitat de Barcelona, Spain
Sánchez-Monge, Á., Beltrán, M. T., Cesaroni, R., et al. 2014, A&A, 569, A11
Sandell, G., Goss, W. M., Wright, M., & Corder, S. 2009, ApJ, 699, L31
Sanna, A., Kölligan, A., Moscadelli, L., et al. 2019, A&A, 623, A77
Sanna, A., Moscadelli, L., Surcis, G., et al. 2017, A&A, 603, A94
Scalo, J. M. 1986, Fund. Cosmic Phys., 11, 1
Schilke, P., Walmsley, C. M., Pineau des Forets, G., & Flower, D. R. 1997, A&A, 321, 293
Schuller, F., Menten, K. M., Contreras, Y., et al. 2009, A&A, 504, 415
Seifried, D., Banerjee, R., Pudritz, R. E., & Klessen, R. S. 2013, MNRAS, 432, 3320
Seifried, D., Sánchez-Monge, Á., Walch, S., & Banerjee, R. 2016, MNRAS, 459, 1892
Shchekinov, Y. A. & Sobolev, A. M. 2004, A&A, 418, 1045
Shirley, Y. L. 2015, PASP, 127, 299
Shu, F. H., Adams, F. C., & Lizano, S. 1987, ARA&A, 25, 23
Smith, N. & Morse, J. A. 2019, MNRAS, 489, 268
Spitzer, L. 1978, Physical processes in the interstellar medium
Sridharan, T. K., Beuther, H., Schilke, P., Menten, K. M., & Wyrowski, F. 2002, ApJ, 566, 931
Stahler, S. W. & Palla, F. 2005, The Formation of Stars
Steer, D. G., Dewdney, P. E., & Ito, M. R. 1984, A&A, 137, 159
Strom, S. E. 1972, PASP, 84, 745
Teague, R. & Foreman-Mackey, D. 2018, Research Notes of the American Astronomical Society, 2, 173
Thompson, A. R., Moran, J. M., & Swenson, George W., J. 2017, Interferometry and Synthesis in Radio Astronomy, 3rd Edition
Tobin, J. J., Hartmann, L., Bergin, E., et al. 2012, ApJ, 748, 16
Toomre, A. 1964, ApJ, 139, 1217
Turner, J. L. & Welch, W. J. 1984, ApJ, 287, L81
Urquhart, J. S., Morgan, L. K., Figura, C. C., et al. 2011, MNRAS, 418, 1689
Urquhart, J. S., Thompson, M. A., Morgan, L. K., et al. 2007, A&A, 467, 1125
Vink, J. S., Heger, A., Krumholz, M. R., et al. 2015, Highlights of Astronomy, 16, 51
Walborn, N. R., Howarth, I. D., Lennon, D. J., et al. 2002, AJ, 123, 2754
Walmsley, M. 1995, in Revista Mexicana de Astronomia y Astrofisica Conference Series, ed. S. Lizano & J. M. Torrelles, Vol. 1, 137
Weisz, D. R., Johnson, L. C., Foreman-Mackey, D., et al. 2015, ApJ, 806, 198
Wheelwright, H. E., Oudmaijer, R. D., de Wit, W. J., et al. 2010, MNRAS, 408, 1840
Williams, J. P., Blitz, L., & McKee, C. F. 2000, in Protostars and Planets IV, ed. V. Mannings, A. Boss, & S. Russell (Univ. of Arizona Press, Tucson), 97
Wilner, D. J., Reid, M. J., & Menten, K. M. 1999, ApJ, 513, 775
Wilson, T. L., Rohlfs, K., & Hüttemeister, S. 2013, Tools of Radio Astronomy
Wilson, T. L. & Rood, R. 1994, ARA&A, 32, 191
Wolfire, M. G. & Cassinelli, J. P. 1987, ApJ, 319, 850
Wyrowski, F., Schilke, P., Walmsley, C. M., & Menten, K. M. 1999, ApJ, 514, L43
Xu, Y., Li, J. J., Reid, M. J., et al. 2013, ApJ, 769, 15

Xu, Y., Reid, M. J., Menten, K. M., et al. 2009, ApJ, 693, 413

Xu, Y., Reid, M. J., Zheng, X. W., & Menten, K. M. 2006, Science, 311, 54

Yorke, H. W. & Sonnhalter, C. 2002, ApJ, 569, 846

Zapata, L. A., Garay, G., Palau, A., et al. 2019, ApJ, 872, 176

Zapata, L. A., Rodríguez-Garza, C., Rodríguez, L. F., Girart, J. M., & Chen, H.-R. 2011, ApJ, 740, L19

Zhang, Q., Ho, P. T. P., & Ohashi, N. 1998, ApJ, 494, 636

Zhang, S., Hartmann, L., Zamora-Avilés, M., & Kuznetsova, A. 2018, MNRAS, 480, 5495

Zinchenko, I., Liu, S.-Y., Su, Y.-N., & Wang, Y. 2018, Research in Astronomy and Astrophysics, 18, 093

Zinnecker, H. & Yorke, H. W. 2007, ARA&A, 45, 481

Acknowledgements

As I close this extraordinary chapter of my life, I am filled with immense feelings of gratitude for all those who held my hand on this journey. First and foremost, my advisor and mentor, Henrik Beuther, without whom this work would not have been possible. Thank you for your timely and constructive critique of my work and for your cheerful enthusiasm for our projects which was very motivating. Your supervision has been a perfect combination of useful, patient, and encouraging guidance while allowing me to develop scientific independence. Aside from sharing your valuable knowledge so generously, you also taught me that it is possible to be a successful researcher while having a healthy work-life balance. For these and many more, I am so very thankful.

I wish to express my deep gratitude to Thomas Henning for allowing me to work in his department and for serving on my thesis committee, providing me with invaluable advice. My sincere thanks goes to Kees Dullemond for refereeing this thesis as well as serving as a member of my thesis committee, and to other members of my defence committee, Sabine Reffert and Björn Malte Schäfer. I would like to thank Ralph Pudritz for sharing his time and expertise with me and for steering me in the right direction. Your enthusiasm for science is inspiring. I am grateful to my go-to theorist, Rolf Kuiper, for answering my many many questions in long email chains, while traveling to/from conferences, and whenever you were at the institute. Thanks for your patience and sharing your theoretical knowledge in a way that would be easy to understand.

My heartfelt appreciation goes to all the past and current members of the Beuther group with whom I came into contact, and from whom I have learned a great deal of astrophysics from large to small scales at our group meetings and spontaneous hallway discussions. I extend this gratitude also to Hendrik Linz and Dima Semenov. Being part of a large collaboration like CORE has been extremely rewarding and I would like to thank each and every member of our team for their constructive feedback on my work. In particular, I would like to give many thanks to Peter Schilke, Álvaro Sánchez-Monge, and Thomas Möller for sharing their expertise about the *XCLASS* software with me.

I feel very privileged to have been a member of the International Max Planck Research School (IMPRS). Thanks to all the IMPRS-HD students who made the past few years very enjoyable, and to Christian Fendt for making it possible. I would like to thank my friends and fellow students at the Max Planck Institute for Astronomy for making our workplace such a fun space and for all the unforgettable memories drinking coffee, solving puzzles, playing snowball fights, and many more. A special shout-out goes to the official and honourary members of office 225. I cannot wait to see where life takes you all, and look forward to many adventures with you in the future. Steffi, thanks for being such a great friend and keeping me company during the writing of this thesis. I also appreciate all the support I have received from my friends abroad, especially Stefany who always knows how to cheer me up.

Last but certainly not least, I would like to thank my parents and brother for always being there for me with love and support. I am also grateful to my chosen family, the Klettkes, for always cheering me on. Your encouragement and interest in my work means a lot. Finally, to the person who has had the most profound impact in my life: Micah, thank you for following me to Heidelberg, for sharing your life with me, for being there for the happy moments and helping me through the tough times. This work would certainly not have been possible without your unwavering support. For all that you have done for me in the past few years and especially the past year I will be forever grateful. I cannot wait for our continued journey and adventures in the Netherlands and beyond.